# Three Studies of Organic Molecules Adsorbed on Copper Surfaces

Thesis submitted in accordance with the requirements of the University of Liverpool for the degree of Doctor in Philosophy by *Emile Durant.*

September 2021

# Preface

This thesis covers the original work that I have undertaken over the course of my PhD since October 2016 in the research group of Prof. Mats Persson at the Surface Science Research Centre, University of Liverpool. This work entails three projects involving theoretical modelling of organic molecules adsorbed to copper surfaces. Each of these projects was motivated by experimental scanning tunnelling microscopy results. I did not take part in these experiments, and the experimental collaborators are clearly stated in the text. Unless stated otherwise, all results in this thesis were obtained by me.

**Emile Durant**

September 2021

# Abstract

The experimental motivation behind all three projects in this thesis was scanning tunnelling microscopy (STM) images of organic molecules adsorbed to copper surfaces. Density functional theory (DFT) techniques were used to model the adsorption scenarios. The three projects concerned a flipping reaction of formaldehyde on Cu(110), the adsorption of racemic (*RS*) flurbiprofen (FBF) to Cu(110) and the tautomerization of oxa-hemiporphycene (OHPc) to Cu(111). In the case of the formaldehyde adsorbed to Cu(110), three stable adsorbed structures were found. These three structures, known as $\eta_1$, $\eta_2$, and $\eta_3$ had adsorption energy values of -0.52 eV ($\eta_1$), -0.87 eV ($\eta_2$) and -0.64 eV ($\eta_3$). The $\eta_3$ structure was identified as the only flipping species due to the similarity between simulated and experimental STM images and the calculated minimum energy path (MEP) with a corresponding small tunnelling barrier height of 20 meV. This flipping reaction was attributed to quantum mechanical tunnelling of the carbon atom of the formaldehyde molecule.

For *RS*-FBF adsorbed to Cu(110), each island contained only *R*- or *S*-FBF. Surprisingly, each island contained only one rotation domain boundary, either side of which existed a self-assembled monolayer. These monolayers consisted of molecules adsorbed into a chiral unit cell. The molecules either side of the boundary were oriented at 180° to each other. Each enantiomer also existed as both *cis* and *trans* isomers. The gas phase *cis* and *trans* molecules were essentially degenerate ($\Delta E$ = 3 meV). However, for the adsorbed species, *trans*-FBF was the energetically preferred species, being more stable than its *cis* counterpart in adsorption energy by 0.14 eV in the monolayer.

For OHPc adsorbed to Cu(111), molecular switching with voltage pulses (~ 0.75 V) allowed tautomerization between the *trans* and *right cis* structure. Experimental STM showed that most adsorbed molecules were in the *trans* state when deposited on the Cu(111) at 7 K. Only the gas phase energy differences between the tautomers were convincing enough to explain this, as the *trans* structure was significantly more stable than the *right cis* structure ($\Delta E$ = 0.15 eV). Theory and experiment both confirmed that the adsorbed molecules aligned along the [211] direction. An adsorbed tautomer oriented at 180° to another did not cause a great difference in adsorption energy.

# Contents

# Abbreviations

| | |
|---|---|
| BZ | Brillouin zone |
| DFT | Density functional theory |
| DOS | Density of states |
| FBF | Flurbiprofen |
| GGA | Generalized gradient approximation |
| HOMO | Highest occupied molecular orbital |
| LDA | Local density approximation |
| LDOS | Local density of states |
| LEED | Low energy electron diffraction |
| LUMO | Lowest unoccupied molecular orbital |
| OHPc | (22)-Oxa-hemiporphycene |
| PAW | Projector augmented wave |
| PBE | Perdew-Burke-Ernzerhof |
| PDOS | Projected density of states |
| RAIRS | Reflection absorption infrared spectroscopy |
| STM | Scanning tunnelling microscopy/ microscope |
| UHV | Ultrahigh vacuum |
| XC | Exchange-correlation |

# Chapter 1

# Introduction

## 1.1: The Aim of this Thesis

The original work of this thesis consists of three projects. These three projects are all theoretical in nature, and include the study of a flipping reaction of adsorbed formaldehyde on Cu(110) (Chapter 4), enantiomeric separation of racemic flurbiprofen (FBF) on Cu(110) (Chapter 5) and the tautomerization of oxa-hemiporphycene (OHPc) on Cu(111) (Chapter 6).

All the aforementioned adsorbed molecules are organic, and the copper (Cu) surfaces are flat. The motivation behind the theoretical studies were STM experiments. These experiments allowed the molecular orbitals of the adsorbed species to be viewed on the adsorption surface. However, these STM experiments allowed neither the positions of the adsorbed nuclei, nor the energetics of the absorbed species to be accurately determined. Therefore, theoretical modelling techniques were required to add further knowledge and understanding of the experimental results. The conclusions drawn from the original studies of the three systems in this thesis, were drawn mostly from theoretical modelling. The aim of this thesis is to explain the energetics governing the experimental observations for each system studied. This is because the experiments alone could not explain these observations.

In Chapter 4, the flipping reaction of adsorbed formaldehyde on Cu(110) occurred spontaneously at a temperature less than 10 K. This indicated that below 10 K, the reaction was independent of temperature and hence governed by heavy-atom quantum mechanical tunnelling. This had not been previously observed for formaldehyde. Thus, the work offered further insights into heavy-atom tunnelling, which is observed far less frequently than hydrogen-atom tunnelling. The work covered in Chapter 4 resulted in publication.[1]

In Chapter 5, when the racemic FBF adsorbed onto Cu(110), the molecules were separated into enantiomerically pure islands containing either only *R*-, or *S*-FBF. Each island contained two domains of molecules. The molecules in one domain were oriented at 180° to those in the other. This meant that there was only one rotation domain boundary per island. This was quite a novel and exciting experimental observation that merited further investigation. The theoretical work in Chapter 5 was able to adequately explain why there was only one rotation domain boundary per island. Therefore, the work of Chapter 5 would be potentially useful in the future as a starting point for systems of racemic organic molecules that separate into enantiomerically pure islands when adsorbed, that contain only one rotation domain boundary.

The OHPc described in Chapter 6 is a molecule that was synthesized very recently in 2018 as a derivative of hemiporphycene (a derivative of porphycene, which is in turn a derivative of porphyrin).[2] OHPc is a low-symmetry molecule, and was adsorbed to the Cu(111) surface for the work in Chapter 6. There had been no previous study of the tautomerization of this molecule between its *cis* and *trans* states when this molecule is adsorbed to a surface. In contrast, there have been considerable similar studies of other more symmetrical porphyrin derivatives when adsorbed to a surface. The work in Chapter 6 reveals some strong and novel insights into the tautomerization of this asymmetric porphyrin derivative when it is adsorbed to a surface.

## 1.2: Crystal Lattices

### 1.2.1: Introduction

In this thesis, molecules adsorb on copper surfaces in the solid state. Each surface is a single crystal of copper with very few defects, unlike most objects made of copper which are polycrystalline.[3] The concepts of real and reciprocal space are required for the study of crystalline lattices. These are introduced in Subsections 1.2.2 and 1.2.3, respectively. The unit cell of the copper lattice adopts a face-centred cubic (*fcc*) structure.[3] This is introduced in Subsection 1.2.4. This *fcc* structure can be cut along various planes to make other surfaces. These cut surfaces of interest, are the *fcc*(110) and *fcc*(111) surfaces, these are introduced in Subsection 1.2.5. It is these copper *fcc*(110) and *fcc*(111) upon which the molecules adsorb in Chapters 4 – 6.

### 1.2.2: Real Space

A crystalline structure has translational symmetry.[4] Translational symmetry means that one can identify a regular set of points, each of which has an identical environment. These regular points are repeated under translation. These points are known as the lattice points. A three-dimensional lattice is built up from these lattice points. Within this lattice, a unit cell may be defined. This unit cell is a parallelepiped with its origin at a lattice point. The edges of the parallelepiped are defined by three non-coplanar basis vectors, given by $\mathbf{a}_1$, $\mathbf{a}_2$ and $\mathbf{a}_3$.[4] The magnitudes of these vectors are known as the lattice parameters of the unit cell. The whole lattice can be generating by the stacking of the unit cells in three-dimensional space. This three-dimensional space is known as *real space.*[5] A vector that represents a translation between lattice points is known as a lattice vector. Each unit cell has eight corners.[4] Therefore, there is only point lattice per unit cell. Such a cell is defined as a primitive unit cell. Any unit cell containing two or more lattice points is said to be non-primitive. In this case, the other lattice points are not positioned at the corners of the cell. A cell that has lattice points at the centres of all it faces is designated the lattice symbol *F.* The cell is said to be *F*-centred. Such a cell would have four lattice points.

The focus from this point forward will be on cubic unit cells. This is all that is relevant to adequately deal with the copper structures that are used for the projects in this thesis. For a cubic unit cell described by cartesian coordinates, the basis vectors are mutually perpendicular and of equal magnitude, i.e. $|\mathbf{a}_1| = |\mathbf{a}_2| = |\mathbf{a}_3| = a$, where $a$ is known as the lattice parameter. Only one lattice parameter is needed to characterize cubic unit cells. Lattice parameters are material dependent. For copper, experiments indicate that $a$ is approximately 3.6 Å.[2] A schematic of a cubic unit cell is shown below in Fig. 1.1.

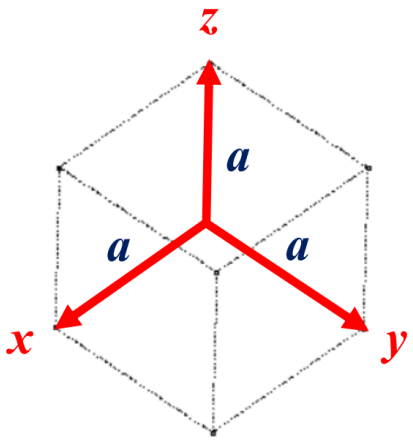


**Figure 1.1:** A cubic unit cell with one of its corners at the origin of a three-dimensional set of cartesian coordinate axes ($x$, $y$, $z$). These axes are also the lattice vectors in each of the $x$, $y$ and $z$ directions. The length of each lattice vector is $a$.

### 1.2.3: Reciprocal Space

Reciprocal space is required to study the energetics of a surface or a surface-adsorbate system. The reciprocal space is defined in terms of the reciprocal lattice. This is a special coordinate system that is useful in defining the Brillouin zone (see Subsection 1.2.4). In general, for a lattice represented by basis vectors $\mathbf{a}_1$, $\mathbf{a}_2$ and $\mathbf{a}_3$, the reciprocal lattice basis vectors are written as $\mathbf{b}_1$, $\mathbf{b}_2$ and $\mathbf{b}_3$, respectively. These reciprocal lattice basis vectors are related to the basis vectors as:[4]

$$\mathbf{b}_1 = \frac{\mathbf{a}_2 \times \mathbf{a}_3}{\mathbf{a}_1 \cdot \mathbf{a}_2 \times \mathbf{a}_3}, \tag{1.2a}$$

$$\mathbf{b}_2 = \frac{\mathbf{a}_3 \times \mathbf{a}_1}{\mathbf{a}_1 \cdot \mathbf{a}_2 \times \mathbf{a}_3}, \tag{1.2b}$$

and

$$\mathbf{b}_3 = \frac{\mathbf{a}_1 \times \mathbf{a}_2}{\mathbf{a}_1 \cdot \mathbf{a}_2 \times \mathbf{a}_3}. \tag{1.2c}$$

For a deeper understanding of the reciprocal lattice, the reader is advised to consult Ref. [6].

### 1.2.4: The Brillouin Zone

A Brillouin zone is a Wigner-Seitz primitive unit cell in the reciprocal lattice. A Wigner-Seitz (primitive) cell around a lattice point is defined as the locus of the spatial points that are closer to the lattice point than to any of the other lattice points. The first Brillouin zone is defined as the smallest volume that is entirely enclosed by the planes which are the perpendicular bisectors of the reciprocal lattice vectors, as drawn from the origin. The geometry of the Brillouin zone will not be discussed further here. However, the interested reader is advised to consult Ref. [6] for further information on the Brillouin zone.

### 1.2.5: The Face-Centred Cubic Structure

The face-centred cubic (*fcc*) structure is shown below in Fig. 1.2.

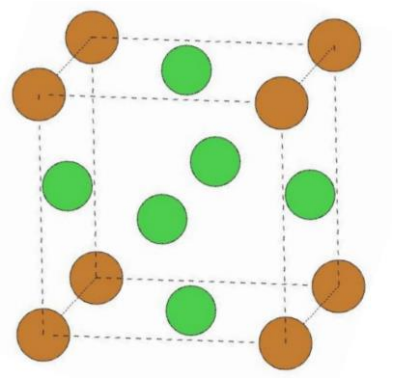

**Figure 1.2:** The *fcc* structure shown within its unit cell. In this schematic, there is a brown-coloured atom at each corner of the cube. There is a green-coloured atom at the centre of each cube face. (Image based on information given in Ref. [4]).

In the case of the *fcc* copper lattice, both the brown- and the green-coloured atoms of Fig. 1.2 would be copper. The different colours in Fig. 1.2 have been used to clearly distinguish between atoms on the corners and the faces of the unit cell.

1.2.6: The *fcc*(110) and *fcc*(111) Surfaces

Cutting the *fcc* structure shown in Fig. 1.2, parallel to the (110) and (111) planes, yields the corresponding *fcc* surfaces. For more information on the (110) and (111) planes and surface, refer to Ref. [7]. For copper, these surfaces are known as Cu(110) and Cu(111), respectively, and are shown below in Fig. 1.3.

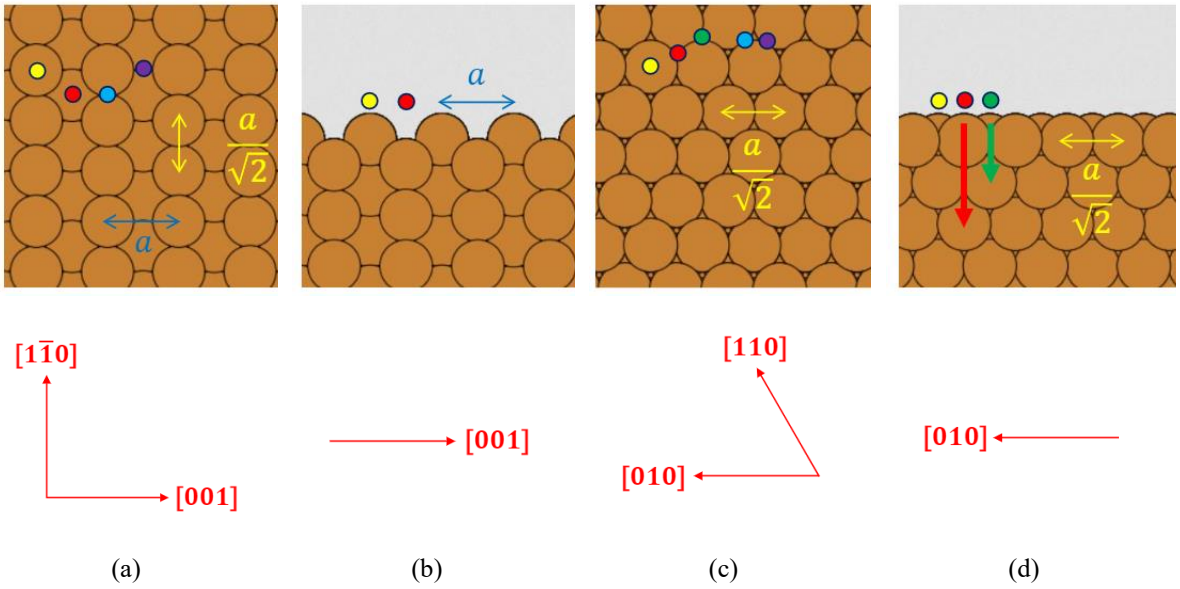


**Figure 1.3:** Shown in (a) and (b) is the top and side view, respectively, of the Cu(110) slab. The long- and short-bridge distances are shown by the blue and yellow arrowed lines, respectively. The lattice constant (approximately 3.6 Å for copper), is given by *a*. The long- and short bridge distances are equal to *a* and $a/\sqrt{2}$, respectively. The various adsorption sites on the Cu(110) surface are shown by the coloured spots. These sites are called the *top* (yellow), *hollow* (red), *long-bridge (LB)* (purple) and *short-bridge* (*SB)* site (cyan). Shown in (c) and (d) is the top and side view, respectively, of the Cu(111) slab. The distance shown by the yellow arrowed line is equal to $a/\sqrt{2}$, i.e. the same as that for the yellow arrowed line in (a). The various adsorption sites on the Cu(111) surface are shown by the coloured spots. These sites are called the *top* (yellow), *face-centred cubic (fcc)* (red), *hexagonal-close packed (hcp)* (green) and *bridge* site (blue and purple). The crystallographic directional indices for Cu(110) and Cu(111) are shown by the red arrows in (a – b) and (c – d), respectively.

The *bridge* sites shown by the blue and purple spots in Fig. 1.3 (c) are the same on the bare Cu(111) surface. However, in different initial geometries prior to optimization with DFT, the asymmetric OHPc molecule of Chapter 6 was positioned differently relative to these two *bridge* sites. In Chapter 6 the blue and purple spots in Fig 1.3 (c) will be referred to as the '*left-bridge*' and '*right-bridge*' sites, respectively. Now, the notation for describing the unit cells of Chapter 4 – 6 is introduced here. Two vectors $\mathbf{a}_1$ and $\mathbf{a}_2$, are chosen to define the smallest possible surface unit cell. These two vectors are denoted as are displayed below in Fig. 1.4 for both the Cu(110) and Cu(111) surfaces.

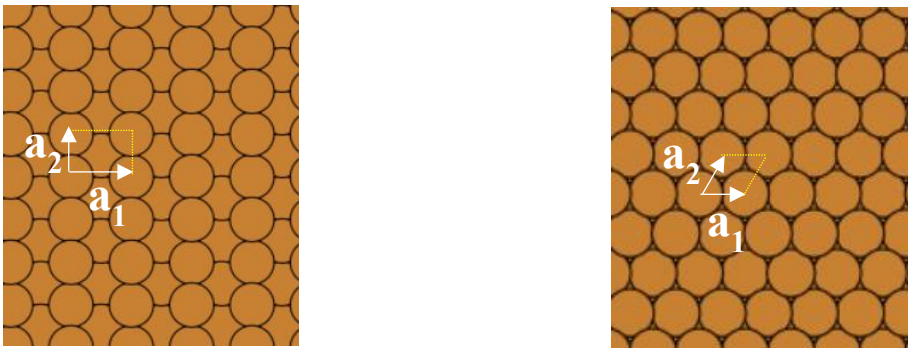


(a) (b)

**Figure 1.4:** The vectors $\mathbf{a}_1$ and $\mathbf{a}_2$ are shown by the white arrows for the Cu(110) and Cu(111) surfaces in (a) and (b), respectively. The yellow dashed lines sketch out the rest of the unit cell as defined by these vectors.

The convention in Fig. 1.4 is that in going from $\mathbf{a}_1$ to $\mathbf{a}_2$, one must rotate anticlockwise.[8] Comparing the lengths of $\mathbf{a}_1$ and $\mathbf{a}_2$ in Fig 1.4(a) with Fig. 1.3(a) indicates that $|\mathbf{a}_1| = a$ and $|\mathbf{a}_2| = a/\sqrt{2}$. A similar comparison of Fig. 1.4(b) with Fig. 1.3 (c) indicates that $|\mathbf{a}_1| = |\mathbf{a}_2| = a/\sqrt{2}$. Larger unit cells than those shown in Fig. 1.4 can be defined in terms of the $\mathbf{a}_1$ and $\mathbf{a}_2$ vectors using matrix notation.[8] In matrix notation, two other vectors $\mathbf{b}_1$ and $\mathbf{b}_2$ are constructed from $\mathbf{a}_1$ and $\mathbf{a}_2$.[8] Note that these $\mathbf{b}_1$ and $\mathbf{b}_2$ vectors are not related to those of Eq. (1.2a) – (1.2c). Wood's notation is a simpler alternative to matrix notation that can be used when the angle between $\mathbf{b}_1$ and $\mathbf{b}_2$ is the same as that between $\mathbf{a}_1$ and $\mathbf{a}_2$.[8]

The vectors $\mathbf{b}_1$ and $\mathbf{b}_2$ are related to $\mathbf{a}_1$ and $\mathbf{a}_2$ by an equation of the form

$$\begin{pmatrix} b_1 \\ b_2 \end{pmatrix} = M \begin{pmatrix} a_1 \\ a_2 \end{pmatrix}, \tag{1.3}$$

where $M$ is a matrix relating the magnitudes of $\mathbf{a}_1$ and $\mathbf{a}_2$ to $\mathbf{b}_1$ and $\mathbf{b}_2$.[8] The convention in this thesis is that in going from $\mathbf{b}_1$ to $\mathbf{b}_2$, one must rotate anticlockwise. To illustrate how this matrix is constructed, the unit cells of this thesis are considered. Firstly, the unit cells used in Chapter 4 are shown below in Fig. 1.5.

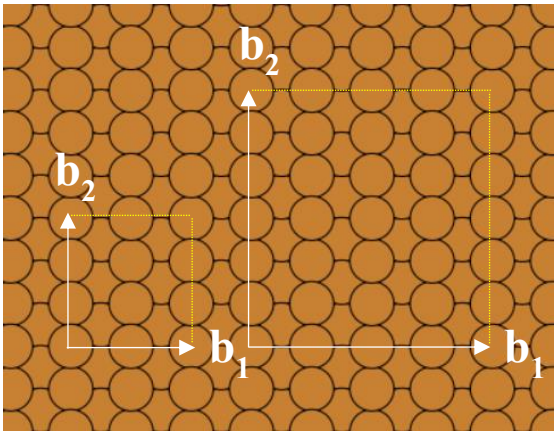


**Figure 1.5:** The Cu(110) surface with the $\mathbf{b}_1$ and $\mathbf{b}_2$ vectors for the unit cells used in Chapter 4. The yellow dashed lines sketch out the rest of the unit cell as defined by these vectors.

Comparing the $\mathbf{b}_1$ and $\mathbf{b}_2$ vectors for leftmost unit cell of Fig. 1.5 with the $\mathbf{a}_1$ and $\mathbf{a}_2$ vectors of Fig. 1.4 (a), one sees that

$$\mathbf{b}_1 = 2\mathbf{a}_1 \tag{1.4a}$$

and

$$\mathbf{b}_2 = 3\mathbf{a}_2. \tag{1.4b}$$

Similarly for the rightmost unit cell of Fig. 1.5, one has

$$\mathbf{b}_1 = 4\mathbf{a}_1 \tag{1.5a}$$

and

$$\mathbf{b}_2 = 6\mathbf{a}_2 \tag{1.5b}$$

Combining the information in Eqs. (1.4a) – (1.4b) means that the leftmost unit cell of Fig. 1.5 can be expressed as

$$\begin{pmatrix} b_1 \\ b_2 \end{pmatrix} = \begin{pmatrix} 2 & 0 \\ 0 & 3 \end{pmatrix} \begin{pmatrix} a_1 \\ a_2 \end{pmatrix}, \tag{1.6}$$

by use of Eq. (1.3). Similarly, combining the information in Eqs. (1.5a) – (1.5b) gives

$$\begin{pmatrix} b_1 \\ b_2 \end{pmatrix} = \begin{pmatrix} 4 & 0 \\ 0 & 6 \end{pmatrix} \begin{pmatrix} a_1 \\ a_2 \end{pmatrix}, \tag{1.7}$$

for the rightmost unit cell. In Wood's notation, the unit cells given by Eqs. (1.6) and (1.7) can be more simply expressed as the '(2 × 3)' and '(4 × 6)' cells, respectively. Wood's notation will be used from this point forward for both these unit cells occurring in Chapter 4.

Secondly, the smallest unit cells used in Chapter 5 are shown below in Fig. 1.6. Construction of the larger unit cells in Chapter 5 is done simply by multiplying the $\mathbf{b}_1$ and $\mathbf{b}_2$ lengths by integer values. These larger cells are shown and discussed in Chapter 5.

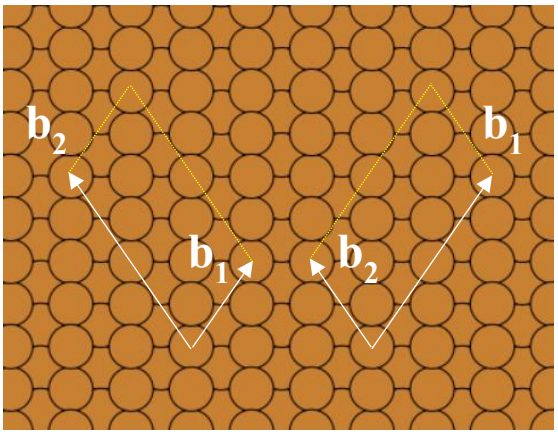


**Figure 1.6:** The Cu(110) surface with the $\mathbf{b}_1$ and $\mathbf{b}_2$ vectors for the unit cells used in Chapter 5. The yellow dashed lines sketch out the rest of the unit cell as defined by these vectors.

Comparing the $\mathbf{b}_1$ and $\mathbf{b}_2$ vectors for leftmost unit cell of Fig. 1.6 with the $\mathbf{a}_1$ and $\mathbf{a}_2$ vectors of Fig. 1.4 (a), one sees that

$$\mathbf{b}_1 = \mathbf{a}_1 + 2\mathbf{a}_2 \tag{1.8a}$$

and

$$\mathbf{b}_2 = -2\mathbf{a}_1 + 4\mathbf{a}_2 \tag{1.8b}$$

Similarly for the rightmost unit cell of Fig. 1.6, one has

$$\mathbf{b}_1 = 2\mathbf{a}_1 + 4\mathbf{a}_2 \tag{1.9a}$$

and

$$\mathbf{b}_2 = -\mathbf{a}_1 + 2\mathbf{a}_2. \tag{1.9b}$$

Combining the information in Eqs. (1.8a) – (1.8b) means that the leftmost unit cell of Fig. 1.6 can be expressed as

$$\begin{pmatrix} b_1 \\ b_2 \end{pmatrix} = \begin{pmatrix} 1 & 2 \\ -2 & 4 \end{pmatrix} \begin{pmatrix} a_1 \\ a_2 \end{pmatrix}, \tag{1.10}$$

by use of Eq. (1.3). Similarly, combining the information in Eqs. (1.9a) – (1.9b) gives

$$\begin{pmatrix} b_1 \\ b_2 \end{pmatrix} = \begin{pmatrix} 2 & 4 \\ -1 & 2 \end{pmatrix} \begin{pmatrix} a_1 \\ a_2 \end{pmatrix}, \tag{1.11}$$

for the rightmost unit cell. For both unit cells in Fig. 1.6, the angle between $\mathbf{b}_1$ and $\mathbf{b}_2$ is not the same as that between $\mathbf{a}_1$ and $\mathbf{a}_2$, Therefore, Wood's notation will not be used for these cells. However, when reference is made to these cells in the text, the leftmost and rightmost cells will henceforth be denoted to as '(1, 2; -2, 4)' and '(2, 4; -1, 2)', respectively. Finally, the unit cells used in Chapter 6 are shown below in Fig. 1.7.

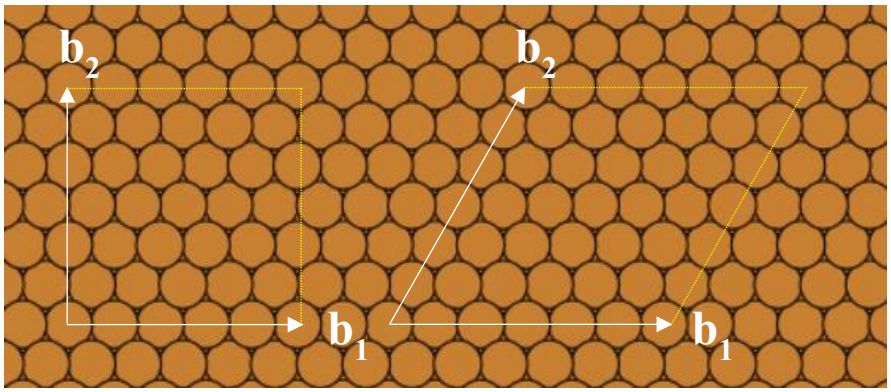


**Figure 1.7:** The Cu(111) surface with the $\mathbf{b}_1$ and $\mathbf{b}_2$ vectors for the unit cells used in Chapter 6. The yellow dashed lines sketch out the rest of the unit cell as defined by these vectors.

Comparing the $\mathbf{b}_1$ and $\mathbf{b}_2$ vectors for leftmost unit cell of Fig. 1.7 with the $\mathbf{a}_1$ and $\mathbf{a}_2$ vectors of Fig. 1.4 (b), one sees that

$$\mathbf{b}_1 = 5\mathbf{a}_1 \tag{1.12a}$$

and

$$\mathbf{b}_2 = -3\mathbf{a}_1 + 6\mathbf{a}_2. \tag{1.12b}$$

Similarly for the rightmost unit cell of Fig. 1.7, one has

$$\mathbf{b}_1 = 6\mathbf{a}_1 \tag{1.13a}$$

and

$$\mathbf{b}_2 = 6\mathbf{a}_2 \tag{1.13b}$$

Combining the information in Eqs. (1.12a) – (1.12b) means that the leftmost unit cell of Fig. 1.5 can be expressed as

$$\begin{pmatrix} b_1 \\ b_2 \end{pmatrix} = \begin{pmatrix} 5 & 0 \\ -3 & 6 \end{pmatrix} \begin{pmatrix} a_1 \\ a_2 \end{pmatrix}, \tag{1.14}$$

by use of Eq. (1.3). Similarly, combining the information in Eqs. (1.13a) – (1.13b) gives

$$\begin{pmatrix} b_1 \\ b_2 \end{pmatrix} = \begin{pmatrix} 6 & 0 \\ 0 & 6 \end{pmatrix} \begin{pmatrix} a_1 \\ a_2 \end{pmatrix}, \tag{1.15}$$

for the rightmost unit cell. For the leftmost unit cell in Fig. 1.7, the angle between $\mathbf{b}_1$ and $\mathbf{b}_2$ is not the same as that between $\mathbf{a}_1$ and $\mathbf{a}_2$. Therefore, Wood's notation will not be used for this cell. However, when reference is made to this cell in the text, this cell will henceforth be denoted to as '(5, 0; -3, 6)'. In Wood's notation, the rightmost cell of Fig. 1.7 can be more simply expressed as the '(6 × 6)' cell. Wood's notation will be used from this point forward for this cell.

## 1.3: The Adsorption of Organic Molecules on Copper Surfaces

### 1.3.1: Introduction

In this thesis, each organic molecule in Chapters 4 – 6, is adsorbed to either a Cu(110) or Cu(111) surface. Copper surfaces are experimentally useful. This is because phenomena such as quantum tunnelling and tautomerization, can be easily studied on copper. Copper is also much cheaper to purchase than gold or platinum, for instance. The adsorbed organic molecules in this thesis can either be found as self-assembled monolayers (Chapter 5) or as isolated on the surface (Chapters 4 and 6). The self-assembled monolayers occur without the guidance from an external source. Instead, it is a spontaneous molecular organization occurring under near thermodynamic equilibrium. These organization result in structurally stable and well-defined arrangements by means of non-covalent intermolecular interactions.

### 1.3.2: The Distinction between Chemisorption and Physisorption

When a molecule adsorbs onto a surface, it is said to either chemisorb[9] or physisorb[10] to the surface. In chemisorption, the adsorbed molecule (adsorbate) is chemically bonded to the surface. This bonding is caused by a chemical reaction between the adsorbate and the surface. Therefore, chemisorption can be characterized by a non-negligible change in the electronic state of the adsorbate. In the case of physisorption, there is a negligible change in the electronic structure of the adsorbate, which in turn means that the adsorbate would not chemically bond to the surface. The weaker adsorption mechanism (physisorption) is typically due to van der Waals or induced electrostatic dipole interactions. The concepts of chemisorption and physisorption will be important in studying the adsorption characteristics of the surface-bonded organic molecules in Chapters 4 – 6 of this thesis.

### 1.3.3: Interactions of Functional Groups with Cu(110) and Cu(111) Surfaces

The functional groups of organic molecules tend to anchor to preferred sites on the Cu(110) and Cu(111) surfaces. The literature on this is vast. Therefore, the discussion here is confined to the molecules and their associated functional groups of the systems of interest in this thesis. Namely, these are the aldehyde group (R-CHO) in Chapter 4, the carboxylic acid group (R-COOH) in Chapter 5, as well as the secondary amine ($R_2N$-H) and imine ($R_2C$=NR) groups in Chapter 6. Here, R represents a group of carbon and hydrogen atoms of any size. The $R_2$ before an atom means that two different R groups are bonded to this atom.

Lone pairs of electrons in an atom tend to be helpful in anchoring an organic molecule to a metal surface, such as copper. This is because these electrons interact with the metal *d*-states to form bonding states. Oxygen has a high electronegativity with respect to the copper surface. In the formaldehyde molecule, the oxygen atom has two lone pairs of electrons with which to anchor the molecule to the Cu(110) surface.[11] This results in three stable formaldehyde structures found anchored to different adsorption sites of the Cu(110). This will be explored in greater depth in Chapter 4.

Earlier studies have shown that the COOH group of a molecule, deprotonates to $COO^-$ upon adsorption to the Cu(110) surface.[12-14] This $COO^-$ group is known as the *carboxylate* group. The oxygen atoms of this group collectively contain 5 lone pairs of electrons (with 3 lone pairs on the deprotonated $O^-$ atom. As might be expected, the high electronegativity of the oxygen atoms along with the 5 lone pairs of electrons resulted in a strong anchoring of the FBF molecule to the surface by the oxygen atoms of the $COO^-$ group. It was also found that the oxygen atoms of this carboxylate group prefer to anchor themselves over two adjacent top sites separated by the short-bridge distance (see Fig. 1.3 (a – b)). This was also found in the research covered in Refs. [12-14]. This will be explored further in Chapter 5.

Previous studies have shown that the lone pairs of the nitrogen atoms in imine functional groups within porphyrin and porphycene structures are strongly bonded to the top sites of the Cu(111) surface.[11, 15-21] (see Fig. 1.3 (c - d)). This was also found to be the case for the OHPc, which has two nitrogen atoms in an imine functional group, and the other in a secondary amine group (see Fig. 6.1). The two imine groups anchor the molecule to the surface, whereas the amine nitrogen atom and the oxygen atom move away from the surface upon adsorption, indicating that they are less likely to be involved in anchoring the molecule to the Cu(111) surface. This will be explored further in Chapter 6.

## 1.4: References


[1] C. Lin, E Durant, M. Persson, M. Rossi and T. Kumagai, *J. Phys. Chem. Lett.*, 2019, **10**, 645-649, DOI: 10.1021/acs.jpclett.8b03806.

[2] J Ostapko, A Kelm, M Kijak, B Leśniewska and J. Waluk, *PubMed*, 2018, **24**(39), 9884-9891, DOI: 10.1002/chem.201801293.

[3] Copper Development Association Inc., https://www.copper.org/resources/properties/atomic_properties.html, (accessed January 2021).

[4] R.M. Martin, *Electronic structure: Basic theory and practical methods*, Cambridge University Press, Cambridge, 1st edn, 2004, Chapter 4, pp 73 – 77.

[5] F. Giustino, *Materials Modelling using Density Functional Theory*, Oxford University Press, Oxford, 1st edn, 2014, Appendix C, pp 247.

[6] F. Giustino, *Materials Modelling using Density Functional Theory*, Oxford University Press, Oxford, 1st edn, 2014, Appendix D, pp 255-257.

[7] Chemistry LibreTexts, https://chem.libretexts.org/Bookshelves/Physical_and_Theoretical_Chemistry_Textbook_Maps/Book%3A_Surface_Science_(Nix)/01%3A_Structure_of_Solid_Surfaces/1.03%3A_Surface_Structures-_fcc_Metals, (accessed January 2021).

[8] Chemistry LibreTexts, https://chem.libretexts.org/Bookshelves/Physical_and_Theoretical_Chemistry_Textbook_Maps/Book%3A_Surface_Science_(Nix)/06%3A_Overlayer_Structures_and_Surface_Diffraction/6.01%3A_Classification_of_Overlayer_Structures, (accessed August 2021).

[9] C.T. Rettner and D.J. Auerbach, J. C. Tully and A. W. Kleyn, *J. Phys. Chem*, 1996, **100** (31), 13021–33, DOI: 10.1021/jp9536007.

[10] E. Zaremba and W. Kohn, *Phys. Rev. B*, 1977, **15**, 1769, DOI: 10.1103/PhysRevB.15.1769.

[11] A. Nilsson and L. G.M. Pettersson, *Chemical Bonding at Surfaces and Interfaces*, Elsevier, 2008, pp 57-142.

[12] A. Robin, L. Marnell, J. Bjork, M.S. Dyer, P.S. Bermudez, S. Haq, S.D. Barrett, M. Persson, A. Minoia, R. Lazzaroni and R. Raval, *J. Phys. Chem. C*, 2009, **113**(30), 13223–13230, DOI: 10.1021/jp9017579.

[13] T.W. White, D.A. Duncan, S. Fortuna, Y-L. Wang, B. Moreton, T-L. Lee, P. Blowey, G. Constantini, D.P Woodruff, *Surface Science*, 2018, **668**, 134 – 143, DOI: 10.1016/j.susc.2017.10.025.

[14] G. R. Darling, M. Forster, C. Lin, N. Liu, R. Raval and A. Hodgson, *Phys. Chem. Chem. Phys.*, 2017, DOI: 10.1039/C7CP00622E.

[15] T. Kumagai, J. N. Ladenthin, Y. Litman, M. Rossi, L. Grill, S. Gawinkowski, J. Waluk and M. Persson, *J. Chem. Phys.*, 2018, **148**, 102330, DOI: 10.1063/1.5004602.

[16] M. Koch, M. Pagan, M. Persson, S. Gawinkowski, J.Waluk and T. Kumagai, *J. Am. Chem. Soc*., **139**, 12681–12687, 2017, 10.1021/jacs.7b06905.

[17] L. J. Lauhon and W. Ho, *Phys. Rev. Lett.,* **85**, 4566–4569, 2000, DOI: 10.1103/PhysRevLett.85.4566.

[18] E. Vogel, M. Kocher, H. Schmickler, and J. Lex, *Angew. Chem. Int. Ed*., **25**, 257–259, 1986, DOI: 10.1002/anie.198602571.

[19] J. Waluk, *Chem. Rev.*, **117**, 2447–2480, 2017, DOI: 10.1021/acs.chemrev.6b00328.

[20] P. Fita, L. Grill, A. Listkowski, H. Piwonski, S. Gawinkowski, M. Pszona, ´ J. Sepioł, E. Mengesha, T. Kumagai, and J. Waluk, *Phys. Chem. Chem. Phys.*, **19**, 4921–4937, 2017, DOI: 10.1039/C6CP07955E.

[21] T. Kumagai, F. Hanke, S. Gawinkowski, J. Sharp, K. Kotsis, J. Waluk, M. Persson, and L. Grill, *Phys. Rev. Lett.*, **111**, 246101, 2013, DOI: 10.1103/PhysRevLett.111.246101.

# Chapter 2

# Experimental Background

## 2.1: Introduction

For the systems studied in this thesis, all the experiments were carried out on clean flat copper surfaces under ultrahigh vacuum (UHV) conditions. The experimental techniques used for the systems in this thesis were scanning tunnelling microscopy (STM), reflection adsorption infrared spectroscopy (RAIRS) and low energy electron diffraction (LEED). All these experiments were carried out by experimental collaborators, acknowledged according in Chapters 4 – 6. In these chapters, STM was used to study the adsorbed organic molecule(s) to the copper surfaces. These copper surfaces were either Cu(110) (Chapters 4 and 5) or Cu(111) (Chapter 6). STM is useful because it allows the surfaces to be imaged and studied in real space at the sub-nanometer scale.[1] With STM, the atomic and molecular orbitals of the adsorbed organic species can also be imaged.[2-3] In Chapter 5, the experimental RAIRS[4] had peak at 1394 $cm^{-1}$ which grew with exposure to the racemic (*RS*)-flurbiprofen. This particular peak is known to arise from a $COO^-$ vibration. This indicates that the COOH group both *R*- and *S*-flurbiprofen molecules would deprotonate to the carboxylate group ($COO^-$).
A peak for the C=O vibration would be at ~1750 $cm^{-1}$. However, this peak was absent from all our spectra. This meant that the aforementioned deprotonation occurred at the Cu(110) surface. LEED[5] was used to determine the unit cells of the self-assembled monolayers of racemic flurbiprofen on the Cu(110) surface.

## 2.2: Scanning Tunnelling Microscopy

In a scanning tunnelling microscope (STM), there exists a metallic tip. This tip is used to study the surface in question. This surface can be conducting or semi-conducting. To study the surface with the tip, one must set the tip-surface distance to around 5 - 10 Å, then apply a bias voltage between the tip and surface. For a positive bias voltage, quantum tunnelling of electrons can occur from electronic states of the tip to those of the surface. Tunnelling in the opposite sense occurs for an applied negative bias voltage. Schematically, the idea behind quantum tunnelling is shown below in Fig. 2.1.

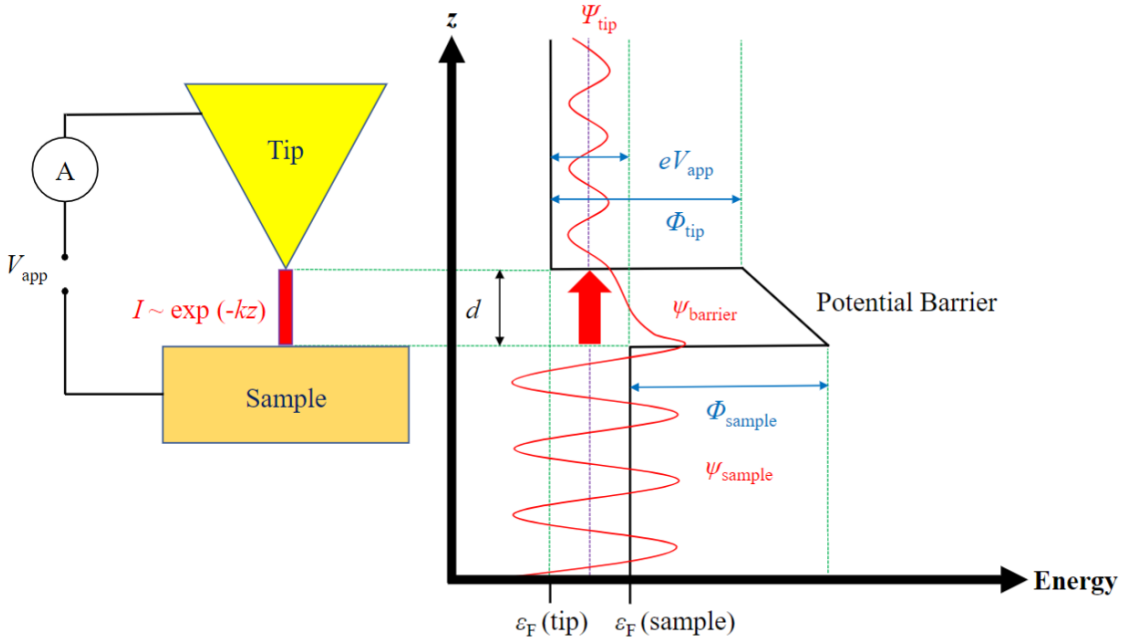


**Figure 2.1:** A schematic showing how an STM machine works. A bias voltage $V_{app}$ is applied between the tip and the sample. This causes electrons to tunnel between the tip and the sample. This produces the 'tunnelling' current $I$. Shown on the RHS of the figure is a plot of energy against tip-surface distance, $z$. The width of the barrier is given by $d$. The Fermi levels of the tip and surface are given by $\varepsilon_F$ (tip) and $\varepsilon_F$ (sample), respectively. The wavefunctions and work functions of the tip and sample are labelled on this plot. The charge on the electron is given by $e$. The characteristic decay inverse decay length of the wave function is given by $k \sim \sqrt{\Phi}$. (The schematic was constructed from information found in Ref. [6]).

Notice in Fig. 2.1, that the wavefunction oscillates sinusoidally either side of the potential barrier. Within the potential barrier itself, the wavefunction decays exponentially. The probability of quantum tunnelling $P$ for the scenario shown in Fig. 2.1 can be approximated by

$$P \propto e^{-2d\sqrt{2m(V-E)}/\hbar}, \tag{2.1}$$

where $d$ is barrier width, $m$ is the electronic mass, $V$ is the potential energy at the barrier height and $E$ is the total energy. The exponential decay of the wavefunction causes in turn the exponential decay of both the tunnelling probability and the STM tunnelling current with respect to the potential barrier width, $d$. The potential barrier width is related to the tip-surface distance. Atomic scale spatial image resolution can be obtained because of this exponentially dependent tunnelling probability. The STM tip-surface tunnelling current can be obtained by use of a theory developed by Bardeen for two metal layers separated by a vacuum gap.[7] This theory relates the tunnelling current to the local Fermi levels in each metal layer, the respective electronic density of states and the spatial overlap between the respective electronic wavefunctions. The result of this is that the tunnelling current is given by

$$\begin{aligned} I = \frac{2\pi e}{\hbar} \sum_{\mu\nu} \{ & f(\epsilon_\mu)\left[1 - f\left(\epsilon_\nu + eV_{\text{app}}\right)\right] \\ & - f(\epsilon_\nu)\left[1 - f\left(\epsilon_\mu + eV_{\text{app}}\right)\right]\} \left|M_{\mu\nu}\right|^2 \delta\left(\epsilon_\mu - \epsilon_\nu\right), \end{aligned} \tag{2.2}$$

where $f(\varepsilon)$ is the Fermi-Dirac thermal occupations. The bias voltage applied to the sample is given by $V_{\text{app}}$ (as per Fig. 2.1). $M_{\mu\nu}$ is the tunnelling matrix element between the tip and sample states, given by $\psi_\mu$ and $\psi_\nu$, respectively. In the absence of quantum tunnelling, $\varepsilon_\mu$ is the energy of state $\psi_\mu$. In Eq. (2.2), the convention is that the potential is positive at the STM tip so that under a negative bias, electrons tunnel from the tip into the sample. The corresponding tunnelling current $I$, is a function of both the sample's electronic structure and the tip-sample distance, if one assumes that the tip has a constant local density of states (LDOS). This mapping of the sample's electronic structure also allows the STM to topographically map the sample's molecular orbitals. The Fermi-Dirac thermal occupation expression in Eq. (2.2) $f(\varepsilon)$, is given by

$$f(\epsilon) = \frac{1}{\exp\left(\frac{\epsilon - \epsilon_{\mathrm{F}}}{k_B T}\right) + 1}, \tag{2.3}$$

where $k_{\mathrm{B}}$ is the Boltzmann constant, $\varepsilon_{\mathrm{F}}$ is the Fermi energy and $T$ is the temperature. The Fermi-Dirac function given by Eq. (2.3) gives the probability that on average, an electronic state of energy $\varepsilon$ will be occupied at temperature $T$.[8] The tunnelling matrix elements $M_{\mu\nu}$, of Eq. (2.2) are given by

$$M_{\mu\nu} = \frac{1}{2}\int d\mathbf{S}\,.\left(\psi_\mu^* \nabla\, \psi_\nu - \ \psi_\nu \nabla \psi_\mu^*\right). \tag{2.4}$$

The integral in Eq. (2.4) runs over a surface which separates the sample and tip. In Eq. (2.2), the Dirac delta $\delta\left(\epsilon_\mu - \epsilon_\nu\right)$, is only non-zero when $\epsilon_\mu \approx \epsilon_\nu$ in order to guarantee that the energy of an electron is conserved during the process of quantum tunnelling. Tunnelling is only permitted if the states on the other side are unoccupied. Therefore, the current $I$ is proportional to the number of unoccupied states, given by:[6]

$$\text{Number of unoccupied states } = \sum_\nu [1 - f(\epsilon_\nu)]. \tag{2.5}$$

The squared matrix elements $\left|M_{\mu\nu}\right|^2$, in Eq. (2.2) select only tunnelling events involving a constructive interference between the tip and sample wavefunctions.[6] The bias voltage $V_{\mathrm{app}}$ in Eq. (2.2) acts to offset the local Fermi levels. This modifies the opportunity for electrons to tunnel.[6] At a non-zero bias, the tunnelling electrons can excite single or multiple vibrational excitations when $|eV_{\mathrm{app}}|$ is larger than the excitation energy. This excitation will introduce a change of the slope of $I$ versus $eV_{\mathrm{app}}$ at this excitation energy.[9] Furthermore, this inelastic process is able to induce single-molecule chemistry by bond activation followed by barrier crossing.[10] This is known as tunnelling-induced vibrational excitation.

In STM experiments, it is important to consider the effects of tip shape and picking up molecules. These will be briefly discussed here in turn. Firstly, it was found that the shape of an STM tip can be quite arbitrary on the atomic scale, provided that the tip has only one atom at its apex. This is because it is this atom that gives the essential contribution to the tunnelling current.[11]

Secondly, it is difficult to determine if an STM tip has picked up a molecule or not during the experiment. In some experiments, molecules are deliberately picked up to improve resolution. The intention for this is often either to get tunnelling from different orbitals, or to manipulate atoms on a surface (e.g. moving the atoms around on the surface). The effects of picking up a molecule can either improve or degrade the resolution of an STM image by tunnelling into or from different states. Usually, a clean tip is considered to have the character of an s orbital. However, when some aromatic compounds are picked up by the tip, this can change the tip character to that of a p orbital. This would result in different STM images being obtained.[12]

In principle, the character of tip states could be modified by functionalizing the tip by picking up individual atoms and molecules. It has been shown that terminating the tip with metal atoms, CO, $H_2$ or organic molecules (for instance, pentacene) enhances STM image resolution.[12] It has been found that STM orbital images obtained with a CO-functionalized tip exhibit significant p wave contributions that are due to tunnelling through the $\pi$ orbitals of the CO tip.[12-13] Such images obtained by p wave tips are of greater resolution. These could be important in the study of metal-molecule complexes and molecular switches.[12] In general, experimentalists can get a vague idea as to whether a molecule has been picked up by the STM tip by applying a voltage pulse to clean the tip, then scanning a region. However, the difficulty is that there is no guarantee that a tip would not pick up the molecule again.

## 2.3: Reflection Absorption Infrared Spectroscopy

Molecular normal modes of vibration can be obtained by use of infrared (IR) spectroscopy. Reflection absorption IR spectroscopy (RAIRS) was used for the part work described in Chapter 5. RAIRS was useful due to the following advantages over other (IR) spectroscopies:[4]

1) On metal surfaces (such as the coppers ones of this thesis), the process is subject to a selection rule that only vibrational modes with a component of the dipole change perpendicular to the surface can be detected. This metal-surface selection rule can often yield important information on adsorption geometry.
2) It is a highly sensitive technique (sometimes as good as $< 10^{-4}$ monolayers).
3) It can be performed under high ambient pressures at which primarily electron-based surface spectroscopies cannot be used.
4) The results obtained from RAIRS can easily be correlated with results from other vibrational spectroscopies.

During the operational procedure of RAIRS, the metallic substrate is irradiated with IR light over a range of frequencies.[4] A photon can be absorbed by the vibration of a molecule adsorbed to the metallic substrate. But this only happens if this photon has the same frequency as the vibrational mode in question and if the resulting dynamic dipole moment is orthogonal to the substrate surface.

In RAIRS, the molecule being adsorbed on a metal surface means that the interaction of the IR radiation of the adsorbate is influenced strongly by the dielectric behaviour of the metal surface. This causes a selection rule that results in only being able to observe vibrations with a dipole moment change containing a component perpendicular to the surface. This is illustrated schematically below in Fig. 2.2.

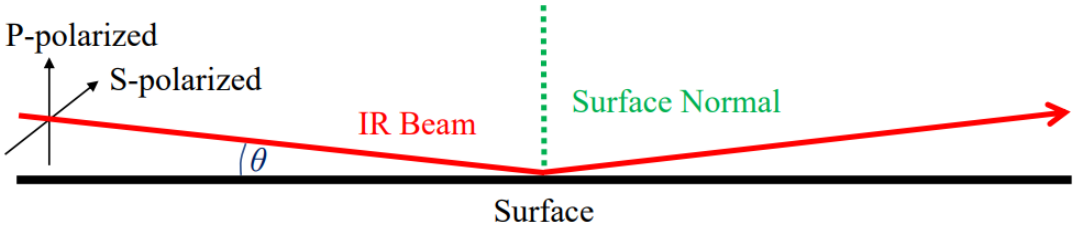


(a)

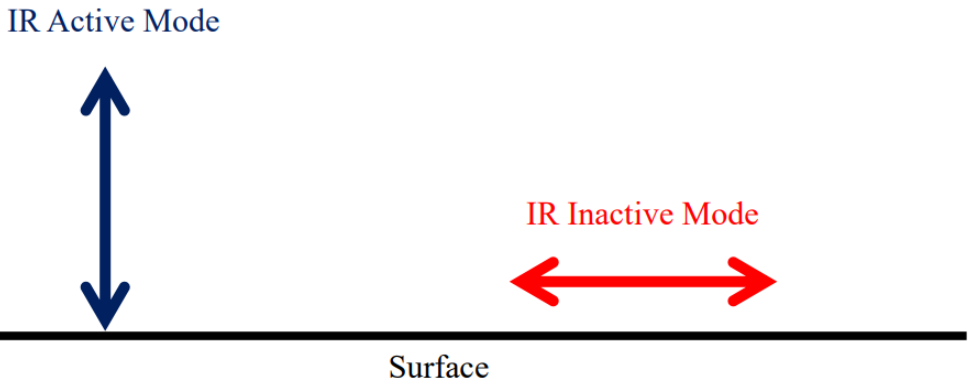


(b)

**Figure 2.2:** Schematics illustrating the fundamentals of RAIRS. As shown in (a) an IR beam is projected at a very small angle $\theta$, onto a reflective metallic surface. The P- and S-polarized vibrations are perpendicular and parallel to the substrate, respectively. In (b) the IR active mode vibrations are perpendicular to the surface (blue). The IR inactive mode vibrations are parallel to the surface (red). (The schematics in (a) and (b) were constructed from information found in Ref. [4]).

In Fig. 2.2, the IR active and inactive modes on metallic surfaces are governed by the surface dipole selection rule. This rule states that only P-polarized vibrations (perpendicular to the surface) will produce an observable absorption band. These vibrations produce a dipole change normal to the surface. Conversely, the S-polarized vibrations (parallel to the surface), will not produce such a dipole change, and hence no observable absorption band.

The physical basis for this selection rule is twofold. Firstly, the IR radiation interacts with both the adsorbate and the surface electronic states. This means that the interaction is unable to distinguish between the dipole of the adsorbate and that of the induced image dipole of the surface. For a dipole moment parallel to the surface, the effect of this is a net cancellation.

Conversely, for a dipole moment perpendicular to the surface, there is a net enhancement. Secondly, there is destructive interference of the S-polarized component of the IR beam at the surface. Therefore, there is no electric field parallel to the surface that can excite vibrational modes. In this thesis, RAIRS is used for part of the original work in Chapter 5 for the purpose of finding out whether that the COOH group of a flurbiprofen molecule (the adsorbate) would be deprotonated to $COO^-$ upon its adsorption on the Cu(110) surface.

## 2.4 Low Energy Electron Diffraction

Low energy electron diffraction (LEED) is a technique that can be used to determine the surface structure of single-crystalline materials.[14] A schematic of the LEED experimental procedure is shown below in Fig. 2.3.

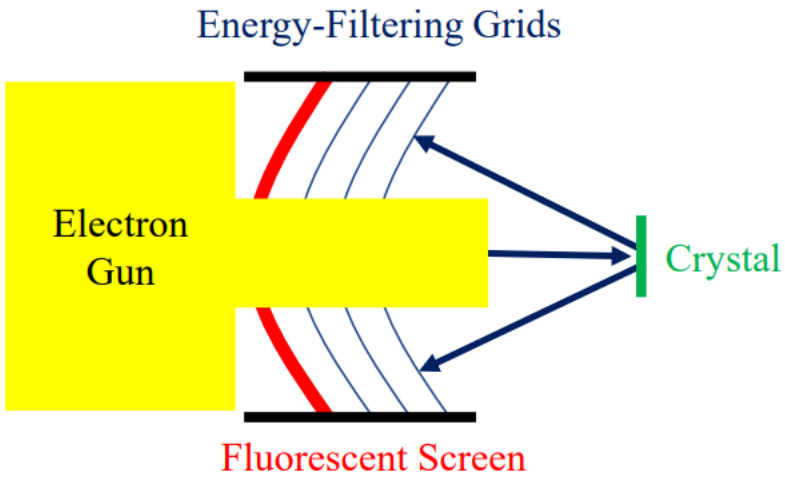


**Figure 2.3:** A schematic illustrating the typical LEED set up. The electron gun bombards the crystal (surface) at normal incidence with a collimated low-energy electron beam (20 – 200 eV). Then, the resultant diffracted electrons are studied as spots on the fluorescent screen. It is only the elastically scattered electrons that contribute to the diffraction pattern. The lower energy (secondary) electrons are removed by the energy-filtering grids in front of the fluorescent screen. (The schematics was constructed from information found in Ref. [14]).

In Chapter 5, LEED was used to find the monolayer unit cells associated with the adsorption of racemic flurbiprofen on Cu(110). In this case, the single-crystalline material was the Cu(110) surface.

## 2.5: References


[1] G. Binnig, H. Rohrer, C. Gerber and E. Weibel, *Phys. Rev. Lett*., 1982, **49**, 57-61, DOI: doi.org/10.1103/PhysRevLett.49.57.

[2] S. Chiang, *Chemical Reviews*, 1997, **97**, 1083-1096, DOI: 10.1021/cr940555a.

[3] J. Repp, G. Meyer, S. M. Stojkovic, A. Gourdon and C. Joachim, *Phys. Rev. Lett*., 2005, **94**, 026803-026806, DOI: 10.1103/PhysRevLett.94.026803.

[4] P. Hollins, *Encycl. Anal. Chem*., 2006, **3**, 107−192, DOI: 10.1002/9780470027318.a5605.

[5] D. Diehl, J. Ledieu, N. Ferralis, A. W. Szmodis and R. McGrath, *J. Phys.: Condens. Matter*, 2003, **15**, R63–R81, DOI: 10.1088/0953-8984/15/3/201.

[6] F. Giustino, *Materials Modelling using Density Functional Theory*, Oxford University Press, Oxford, 1st edn, 2014, Chapter 5, pp 80-83.

[7] J. Bardeen, *Phys. Rev. Lett*, 1961, **6**, 57, DOI: 10.1103/PhysRevLett.6.57.

[8] F. Giustino, *Materials Modelling using Density Functional Theory*, Oxford University Press, Oxford, 1st edn, 2014, Chapter 5, pp 81-82.

[9] B.C. Stipe, M.A. Rezaei and W. Ho, *Science*, 1998, **280**, 1732, DOI: 10.1126/science.280.5370.1732.

[10] B.C. Stipe, M.A. Rezaei, W. Ho, S. Gao, M.Persson and B.I. Lundqvist, *Phys. Rev. Lett*, 1997, **78**, 4410, DOI: 10.1103/PhysRevLett.78.4410.

[11] S. Watanabe and M. Aono. *Journal of Vacuum Science & Technology B: Microelectronics and Nanometer Structures Processing, Measurement, and Phenomena*, 1994, **12**, 2167, DOI: 10.1116/1.587733.

[12] L. Gross, N. Moll, F. Mohn, A. Curioni, G. Meyer, F. Hanke and M. Persson, *Phys. Rev. Lett.*, 2011,**107**, 086101, DOI: 10.1103/PhysRevLett.107.086101.

[13] A. Gustafsson, N. Okabayashi, A. Peronio, F.J. Giessibl, and M. Paulsson, *Phys. Rev. B*, 1997, 96, 085415, DOI: 10.1103/PhysRevB.96.085415**.**

[14] K. Oura, V. G. Lifshifts, A. A. Saranin, A. V. Zotov and M. Katayama (2003). *Surface Science*. Springer-Verlag, Berlin, Heidelberg, New York, pp 1–45.

# Chapter 3

## Theoretical Background

### 3.1: Introduction

The original work in Chapters 4 – 6 is derived from theoretical modelling. This modelling is employed to aid the interpretation and understanding of the experimental results. The theoretical modelling and experimental techniques allow insights from different perspectives into a system in question. In the theoretical modelling approach, a model is known (or assumed) of a system, such that predictions are made about the properties of a system. In contrast, in the experimental approach, the properties of the system are taken as known, but the system model that would explain these properties is unknown. Using both theoretical modelling and experimental techniques together on a system, allows the theoretical modelling to help to explain and understand the experimental results. It also allows the experimental results to help confirm or refute the validity of a given theoretical model. Therefore, the combined use of theoretical modelling and experimental techniques is powerful. The experimental techniques used have already been described in Chapter 2. This chapter serves to introduce the reader to the theoretical modelling used for the projects in this thesis.

All the theoretical modelling techniques used in this thesis, are or are based upon, density functional theory (DFT) by Hohenberg, Kohn and Sham. This DFT is based upon quantum mechanics. For a many-atom (*N*-atom) system, the Schrödinger equation would need to be solved for an *N*-electron wavefunction. When *N* is large, this is almost impossible to solve analytically or in a computationally inexpensive manner. DFT alleviates this problem because it is a good compromise between accuracy and efficiency. It is for this reason that DFT and DFT based calculations are used to model the systems in this thesis. In DFT, all the ground state properties of a given system can be obtained by the electron density of the system alone. In principle, DFT is exact in the ground state. However, a quantity known as the exchange-correlation (XC) functional would have to be exactly known. This functional can only be approximated to various degrees of precision and accuracy.

Accurate approximation of this functional is crucial in order to understand and accurately model a given system. Currently the standard approach is semi-local DFT used with the generalized gradient approximation (GGA). In the GGA, both the density and the gradient of the density are contained in the XC functional. The GGA is widely used because it has been successfully used to model bulk materials, molecular internal structures as well as the adsorption of atoms and small molecules on surfaces. However, the disadvantage of semi-local DFT is that it does not account for van der Waals (vdW) interactions. These vdW interactions are very prevalent between and within organic molecules (such as those studied in this thesis). Hence, they must be accounted for. In general, various methods are used to correct the XC functional to account for vdW interactions.

## 3.2: Time-Independent Density Functional Theory

### 3.2.1: Time-Independent Many-Body Quantum Mechanics

The Coulomb interaction between a pair of electrons is repulsive. The Coulomb interaction between a pair of nuclei is also repulsive. The Coulomb interaction is attractive between an electron and a nucleus. Materials are held together by the balance of the repulsive and attractive Coulomb interactions. Firstly, the Coulomb interaction potential energy between two electrons at positions $\mathbf{r}_i$ and $\mathbf{r}_j$, is given by[1]

$$E_{\mathrm{ee}} = \frac{e^2}{4\pi\epsilon_0 \left|\mathbf{r}_i - \mathbf{r}_j\right|}, \tag{3.1}$$

where $e$ is the electronic charge, and $\varepsilon_0$ is the permittivity of free space. Secondly, the interaction potential energy between two nuclei at at positions $\mathbf{R}_I$ and $\mathbf{R}_J$, is given by

$$E_{\mathrm{nn}} = \frac{Z_I Z_J e^2}{4\pi\epsilon_0 \left|\mathbf{R}_I - \mathbf{R}_J\right|}, \tag{3.2}$$

where $Z_I$ and $Z_J$ are the atomic numbers of nuclei $I$ and $J$, respectively. Finally, the interaction potential between an electron at position $\mathbf{r}_i$ and a nucleus at position $\mathbf{R}_I$, is given by

$$E_{\text{en}} = -\frac{Z_I e^2}{4\pi\epsilon_0 |\mathbf{r}_i - \mathbf{R}_I|}. \tag{3.3}$$

Notice that the energies in Eqs. (3.1) and (3.2) are positive. This indicates that these energies are due to a repulsive Coulomb force. Conversely, the energy in Eq. (3.3) is negative, indicating an attractive Coulomb force. One can see from Eqs. (3.1) – (3.3), that the Coulomb interaction potential energies are inversely proportional to distance. For the systems in this thesis, the Born-Oppenheimer approximation[2] is applied. This is because the nuclei masses are much greater than the electronic mass. Therefore, the nuclei can be considered immobile and only the electronic motion needs to be considered.

For modelling the electronic properties of materials, the Born-Oppenheimer approximation has proven to be adequate in many cases. To begin modelling the electronic properties of materials, the starting point is the many-body Schrödinger equation.[3] The systems studied in this thesis are in the ground state. These systems also do not vary appreciably with time. Therefore, one can use the time-independent many-body Schrödinger equation. Applying the Born-Oppenheimer approximation to this equation gives

$$\left\{ -\frac{\hbar^2}{2m_{\text{e}}} \sum_{i=1}^{N} \nabla_i^2 + \frac{e^2}{4\pi\epsilon_0} \sum_{i \neq j} \frac{1}{|\mathbf{r}_i - \mathbf{r}_j|} + \sum_{i=1}^{N} v(\mathbf{r}_i) \right\} \Psi(\mathbf{r}_1, \mathbf{r}_2, \ldots, \mathbf{r}_N) = E\Psi(\mathbf{r}_1, \mathbf{r}_2, \ldots, \mathbf{r}_N), \tag{3.4}$$

for a system of $N$ electrons. The many-electron wavefunction is given by $\Psi$, and the external potential $v$, is Coulomb potential of the nuclei, as experienced by the electrons. This potential can be expressed as

$$v(\mathbf{r}) = -\frac{Z_I e^2}{4\pi\epsilon_0} \sum_{I=1}^{M} \frac{1}{|\mathbf{r} - \mathbf{R}_I|} \tag{3.5}$$

where the sum is up to the *M*th nucleus, for an electron at position **r**. These equations can look a tad cumbersome at first glance. Therefore, it is helpful to use atomic units. In atomic units, $\hbar = e = m_e = 1$. One can then rewrite Eq. (3.4) as

$$\left\{ -\frac{1}{2}\sum_{i=1}^{N}\nabla_i^2 + \sum_{i\neq j}\frac{1}{|\mathbf{r}_i - \mathbf{r}_j|} + \sum_{i=1}^{N} v(\mathbf{r}_i) \right\} \Psi(\mathbf{r}_1, \mathbf{r}_2, \ldots, \mathbf{r}_N) = E\Psi(\mathbf{r}_1, \mathbf{r}_2, \ldots, \mathbf{r}_N). \tag{3.6}$$

Similarly, Eqs (3.1) – (3.3), and (3.5) can also be expressed easily in atomic units. From this point onwards, all derivations and calculations will be done in atomic units. The Schrödinger equation given by Eq. (3.6) would be very challenging to solve analytically, or very computationally expensive to solve numerically for a many-electron system.

One way to alleviate this difficulty is to use density functional theory (DFT). DFT allows the quantum properties of a system to be calculated from the electron density,[4] rather than by an explicit calculation of Ψ and *E* in Eq. (3.6). This significantly reduces the difficulty of determining the quantum properties of a system. The development of DFT begins with a discussion of the Hohenberg-Kohn theorems[4] and the Kohn-Sham equations.[5]

### 3.2.2: The Hohenberg-Kohn Theorems and the Kohn-Sham Equations

The two Hohenberg-Kohn theorems apply to any configuration of electrons, moving under the influence of an external potential. In Eq. (3.6), this external potential is given by $v(\mathbf{r})$. The proofs of these two theorems are beyond the scope of this text. However, for these proofs, please consult Ref. [4].

**Theorem 1:** The total energy of the electronic system is a unique functional of the electron density.[4]

**Theorem 2:** The true ground state electron density is that which uniquely yields the true ground state energy.[4]

The electron density is denoted as $n(\mathbf{r})$. The total energy functional is denoted as $E[n(\mathbf{r})]$. To make this less cumbersome, $E[n(\mathbf{r})]$ will henceforth be expressed as $E[n]$. For an inhomogeneous electron gas, $E[n]$ is given by

$$E[n] = \int v(\mathbf{r}) n(\mathbf{r}) d\mathbf{r} + \frac{1}{2} \int \frac{n(\mathbf{r}) n(\mathbf{r}')}{|\mathbf{r} - \mathbf{r}'|} d\mathbf{r} d\mathbf{r}' + G[n], \tag{3.7}$$

where the second term is the Coulomb energy and $G[n]$ is an unknown functional of $n(\mathbf{r})$. From the Hohenberg-Kohn theorem, $E[n]$ has a minimum only for the correct ground state electron density. The functional $G[n]$ can be split into the sum of two other functionals as

$$G[n] \stackrel{\text{def}}{=} T_{\text{s}}[n] + E_{\text{xc}}[n], \tag{3.8}$$

where $T_{\text{s}}[n]$ is the kinetic energy of a fictitious system of non-interacting electrons, and $E_{\text{xc}}[n]$ is the exchange-correlation energy of the interacting system of electrons. Combining Eqs. (3.7) and (3.8) gives

$$E[n] = T_{\text{s}}[n] + \int v(\mathbf{r}) n(\mathbf{r}) d\mathbf{r} + \frac{1}{2} \int \frac{n(\mathbf{r}) n(\mathbf{r}')}{|\mathbf{r} - \mathbf{r}'|} d\mathbf{r} d\mathbf{r}' + E_{\text{xc}}[n]. \tag{3.9}$$

The exchange-correlation energy $E_{xc}[n]$, is the only term in Eq. (3.9) that cannot be determined exactly. However, there exist several approximations for $E_{xc}[n]$. For further details on the approximations of $E_{xc}[n]$, see Section 3.5. To find an expression for the ground state total energy, one must minimize $E[n]$ with respect to $n(\mathbf{r})$. This minimization is done for a fixed number of electrons. The variational principle can be applied to Eq. (3.9) in order to minimize $E[n]$. Therefore, an electron density $n$, needs to be found that satisfies

$$\frac{\delta E[n]}{\delta n(\mathbf{r})} = \frac{\delta T_s[n]}{\delta n(\mathbf{r})} + \phi(\mathbf{r}) + \mu_{xc}(\mathbf{r}) = \mu, \tag{3.10}$$

where

$$\phi(\mathbf{r}) = v(\mathbf{r}) + \int \frac{n(\mathbf{r}')}{|\mathbf{r} - \mathbf{r}'|} d\mathbf{r}', \tag{3.11}$$

and

$$\mu_{xc}[n] = \frac{\delta E_{xc}[n]}{\delta n(\mathbf{r})}. \tag{3.12}$$

In Eq. (3.12), $\mu_{\mathrm{xc}}[n]$ is the exchange-correlation contribution to the chemical potential of an electron gas with density $n(\mathbf{r})$. For a system of non-interacting electrons moving in an effective external potential, one also obtains Eq. (3.10). Hence, for a given value of $\psi_i$ and $\mu_{\mathrm{xc}}$, the electron density that satisfies Eq. (3.10) can be found by solving the one-electron Schrödinger equation

$$\left\{-\frac{1}{2}\nabla^2 + \{\phi(\mathbf{r}) + \mu_{\mathrm{xc}}[n]\}\right\}\psi_i(\mathbf{r}) = \epsilon_i(\mathbf{r})\psi_i \tag{3.13}$$

and

$$n(\mathbf{r}) = \sum_{i=1}^{N} |\psi_i(\mathbf{r})|^2, \tag{3.14}$$

where $N$ is the total number of electrons. Eqs. (3.11) – (3.14) must be solved self-consistently.[5] The first step in this self-consistent procedure is to assume an electron density $n(\mathbf{r})$. Secondly, $\psi_i(\mathbf{r})$ and $\mu_{\mathrm{xc}}$ are calculated from Eqs. (3.11) and (3.12), respectively. A new electron density $n(\mathbf{r})$ is then calculated from Eqs. (3.13) and (3.14). In each iteration of this procedure, the energy calculated is given by

$$E = \sum_{i}^{N} \epsilon_i - \frac{1}{2}\int \frac{n(\mathbf{r})n(\mathbf{r}')}{|\mathbf{r}-\mathbf{r}'|} d\mathbf{r}d\mathbf{r}' + E_{\mathrm{xc}}[n] - \frac{1}{2}\int n(\mathbf{r})\,\mu_{\mathrm{xc}}[n]d\mathbf{r}. \tag{3.15}$$

This self-consistent loop stops only when the energy has converged with respect to the input parameters of the DFT calculation. When this self-consistent loop has stopped at the point of convergence, the energy given by Eq. (3.15) is the ground state energy for the specific final configuration of the nuclei. Eqs. (3.9) – (3.15) are known as the Kohn-Sham equations.[5] A schematic of this self-consistent procedure of solving the Kohn-Sham equations, is given below in Fig. 3.1.

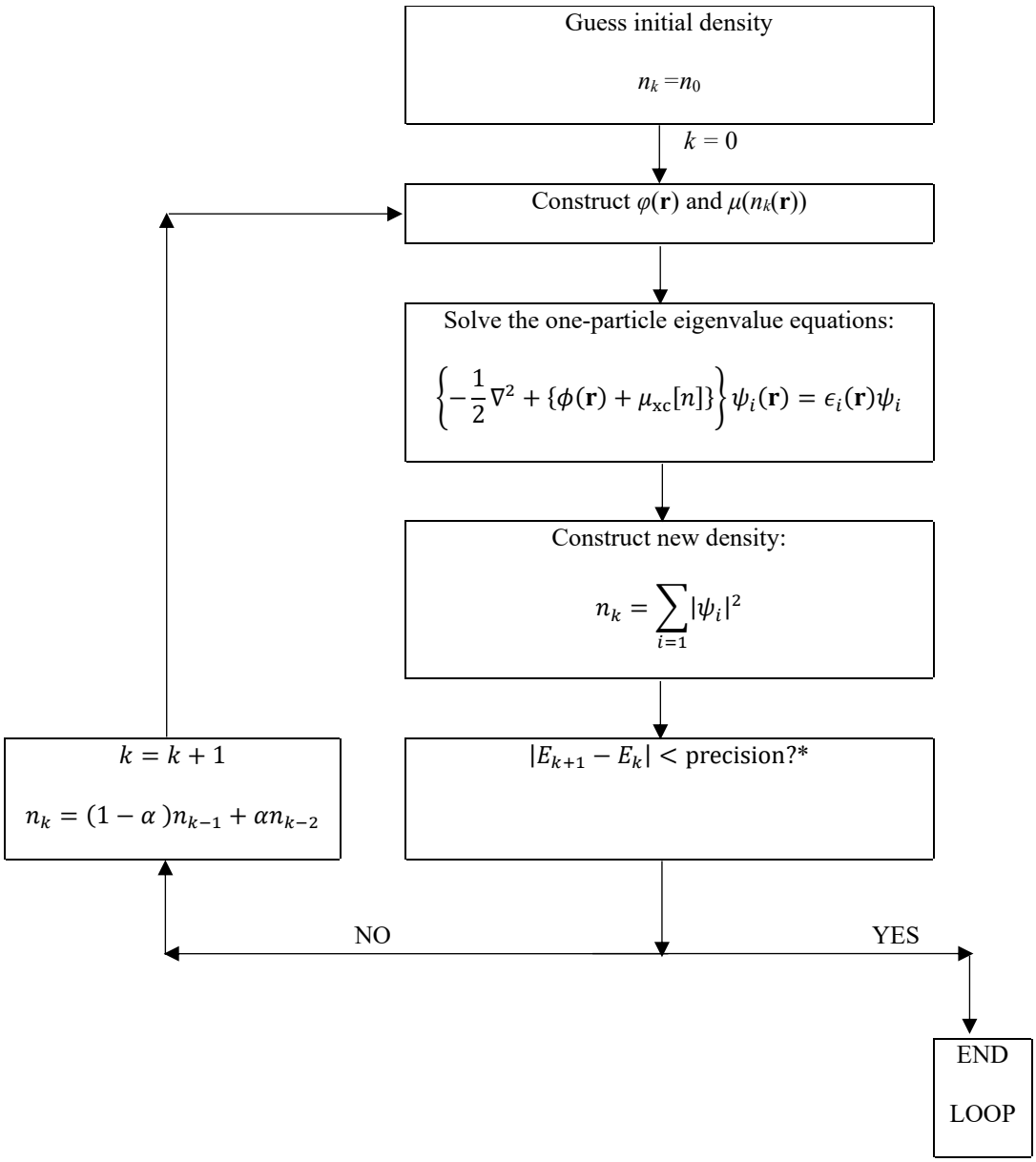


**Figure 3.1:** A flow chart of the algorithm used in DFT to solve the Kohn-Sham equations to find the minimum energy with respect to the electron density. *The precision is set to a desired tolerance that depends on the parameters required in a system being studied. (Figure derived from a schematic in Ref. [6]).

### 3.2.3: The Hellmann-Feynman Theorem and Atomic Forces

After the execution of each iteration to find the electron density (as shown in Fig. 3.1), one can update the positions of the nuclei. The positions of the nuclei need to be updated in a geometric optimization in order to obtain an estimate of the equilibrium structure of the system in question. These nuclear positions are updated by updating the atomic forces for a given electron density. For the atomic forces to be updated at each stage of the self-consistent procedure in Subsection 3.2.2, the Hellmann-Feynman theorem is applied.[7-10] This is a useful theorem in quantum mechanics. In general, the theorem states that

$$\frac{\mathrm{d}E_\lambda}{\mathrm{d}\lambda} = \left\langle \psi_\lambda \middle| \frac{\mathrm{d}\hat{H}}{\mathrm{d}\lambda} \middle| \psi_\lambda \right\rangle, \tag{3.16}$$

where $\hat{H}$ is a Hamiltonian dependent on the continuous parameter $\lambda$. The eigenfunction and eigenvalue of $\hat{H}$ are $\psi_\lambda$ and $E_\lambda$, respectively. In general, when the spatial distribution of all the electrons for a given system has been calculated by the Schrödinger equation, all the forces can be calculated by electrostatics. Taking analytical derivatives of Eq. (3.16) gives the electrostatic force experienced by the $I$th nucleus $\mathbf{F}_I$, as

$$\mathbf{F}_I = Z_I \mathbf{E}_I, \tag{3.17}$$

for atomic number $Z_I$. The electrostatic field $\mathbf{E}_I$, is given by

$$\mathbf{E}_I = Z_I \left\{ \int n(\mathbf{r}) \frac{\mathbf{r} - \mathbf{R}_I}{|\mathbf{r} - \mathbf{R}_I|^3} d\mathbf{r} - \sum_{J \neq I} Z_J \frac{\mathbf{R}_J - \mathbf{R}_I}{\left|\mathbf{R}_J - \mathbf{R}_I\right|^3} \right\}, \tag{3.18}$$

where the left and right terms within the brackets are the contributions to $\mathbf{E}_I$ from the electrons and nuclei, respectively. The electron density $n(\mathbf{r})$ appears in Eq. (3.18). This is none other than the electron density obtained by solving the Kohn-Sham equations self-consistently. At each completion of the loop, shown in Fig. 3.1, the electrostatic field in Eq. (3.18) must be updated. The procedure shown in Fig. 3.1 concerns the update of $n(\mathbf{r})$. At each update of $n(\mathbf{r})$, $\mathbf{E}_I$ in Eq. (3.18) can be updated, and hence $\mathbf{F}_I$ in Eq. (3.17) can also be updated. This in turn updates the positions of the nuclei. This procedure is shown schematically in Fig. 3.2.

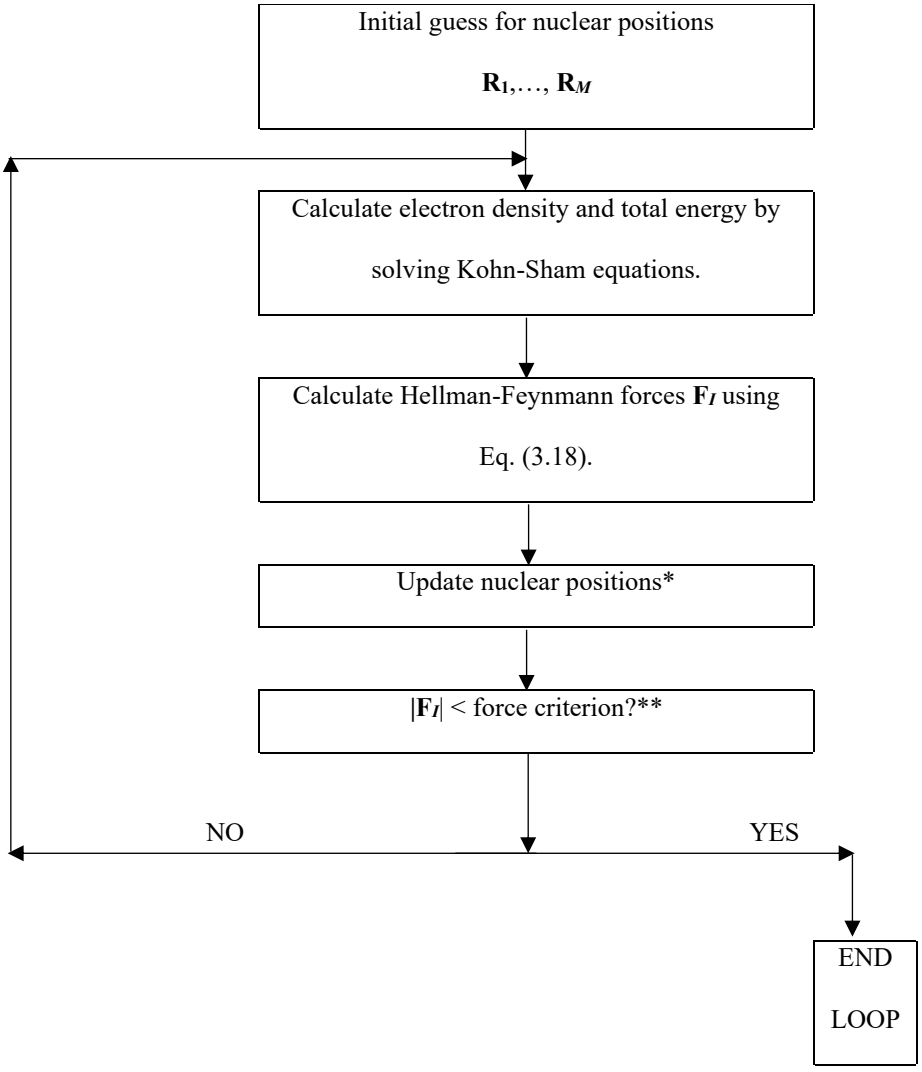


**Figure 3.2:** A flow chart for finding the equilibrium structure of a material using DFT at $T = 0$ K. *For the work in this thesis, the conjugate gradient algorithm is used to update the nuclear positions. **The force criterion is a judiciously chosen value for all $|\mathbf{F}_I|$. For all systems in this thesis, the chosen value of $|\mathbf{F}_I|$ was 0.01 eV/ Å. (Figure derived from a schematic in Ref. [11]).

For the project in Chapters 4-6 of this thesis, the electrostatic fields (and hence forces) were updated by means of the conjugate gradient algorithm. An algorithm based on the quasi-Newton method could also have been used for this purpose. However, the conjugate gradient algorithm was chosen because it has been shown to be that which, in many cases, is most efficiently implemented in VASP[12] for the purpose of updating the nuclear positions. A full coverage of the conjugate gradient algorithm is not presented here because it is a standard optimization method that is readily available in textbooks on numerical methods.[13-16] As a general note, a smaller force criterion value require greater computational expense. Therefore, the force criterion of 0.01 eV/ Å was chosen because it allowed accurate comparisons of structures with respect to energetics, whilst not being too computationally expensive.

## 3.3: Solving the Kohn-Sham Equations in VASP

### 3.3.1: Periodic Boundary Conditions

In VASP,[12] the Kohn-Sham equations are solved such that periodic boundary conditions are applied in all three Cartesian directions of the unit cell of the system being studied. An example of such applied periodic boundary conditions is shown below in Fig. 3.3.

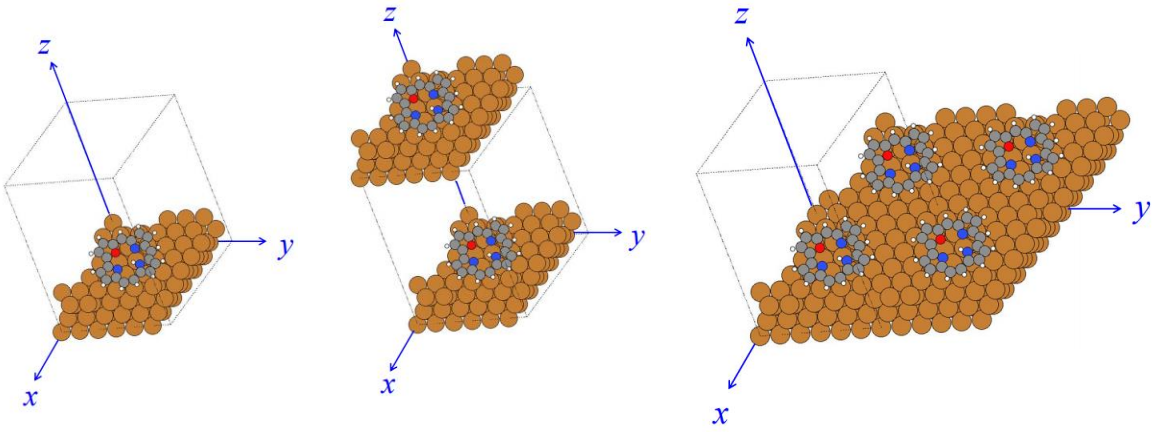


(a) (b) (c)

**Figure 3.3:** Shown is the single non-repeated unit cell (a), the unit cell repeated once in the *z*-direction (b) and the unit cell repeated once in both the *x*- & *y*-directions (c). (Figure produced by use of the *Atomic Simulation Environment* (ASE), Ref. [17]).

### 3.3.2: Plane Wave Basis Sets

VASP[12] uses plane waves as basis set over which to expand the Kohn-Sham wavefunctions in a DFT calculation. This is explored below. Rewriting Eq. (3.13) gives

$$\left\{-\frac{1}{2}\nabla^2 + V(\mathbf{r})\right\}\psi_i(\mathbf{r}) = \epsilon_i(\mathbf{r})\psi_i, \tag{3.19}$$

where $V(\mathbf{r})$ is the effective potential given by $\{\phi(\mathbf{r}) + \mu_{xc}[n]\}$ in Eq. (3.13). In a periodic material structure, the nuclei are arranged in periodic positions. This means that $V(\mathbf{r})$ must also be periodic. This means that

$$V(\mathbf{r} + \mathbf{R}) = V(\mathbf{r}), \tag{3.20}$$

where $\mathbf{R}$ is a lattice vector given by

$$\mathbf{R} = n_1\boldsymbol{a}_1 + n_2\boldsymbol{a}_2 + n_3\boldsymbol{a}_3, \tag{3.21}$$

where $n_1$, $n_2$ and $n_3$ are positive integers. The unit cell vectors of the system are given by $\mathbf{a}_1$, $\mathbf{a}_2$ and $\mathbf{a}_3$. Bloch's theorem[18] indicates that the wavefunction $\psi_{\mathbf{k}}(\mathbf{r})$ of a periodic system can be expressed as

$$\psi_{\mathbf{k}}(\mathbf{r}) = e^{i\mathbf{k}.\mathbf{r}}u_{\mathbf{k}}(\mathbf{r}), \tag{3.22}$$

where $\mathbf{k}$ is a wavevector in the first Brillouin zone[19], $e^{i\mathbf{k}.\mathbf{r}}$ is a function representing a plane wave, and $u_{\mathbf{k}}(\mathbf{r})$ is a function that has the same periodicity as the potential given by Eq. (3.20). It follows from this that

$$\psi_{\mathbf{k}}(\mathbf{r} + \mathbf{R}) = \psi_{\mathbf{k}}(\mathbf{r})e^{i\mathbf{k}.\mathbf{R}}, \tag{3.23}$$

which indicates that the wave-functions $\psi_{\mathbf{k}}(\mathbf{r}+\mathbf{R})$ and $\psi_{\mathbf{k}}(\mathbf{r})$, are the same, except for differing by the phase factor $e^{i\mathbf{k}.\mathbf{R}}$. Expanding $u_{\mathbf{k}}(\mathbf{r})$ as a series of plane waves gives

$$u_{\mathbf{k}}(\mathbf{r}) = \sum_{\mathbf{G}} \boldsymbol{c}_{\mathbf{k}}(\mathbf{G}) e^{i\mathbf{G}.\mathbf{r}}, \tag{3.24}$$

where **G** is the sum of the reciprocal lattice vectors given by

$$\mathbf{G} = \sum_{j} m_j \, \mathbf{b}_j, \tag{3.25}$$

and $\boldsymbol{c}_{\mathbf{k}}(\mathbf{G})$ are coefficients that can be varied in order to determine the lowest energy solution. In Eq. (3.25), the $m_j$ and $\mathbf{b}_j$ are positive integers and reciprocal lattice vectors of the unit cell of the system, respectively. The $\mathbf{b}_j$ are defined such that they satisfy

$$\mathbf{R}.\mathbf{G} = 2\pi q, \tag{3.26}$$

where $q$ is an integer. This means that both the wavefunction and periodic potential can also be expanded as a series of plane waves, giving

$$\psi_{\mathbf{k}}(\mathbf{r}) = \sum_{\mathbf{G}} \boldsymbol{c}_{\mathbf{k}}(\mathbf{G}) e^{i(\mathbf{k}+\mathbf{G}).\mathbf{r}}, \tag{3.27}$$

and

$$V(\mathbf{r}) = \sum_{\mathbf{G}} V(\mathbf{G}) e^{i\mathbf{G}.\mathbf{r}}, \tag{3.28}$$

respectively. The insertion of Eqs. (3.27) and (3.28) into (3.19) gives

$$\sum_{m'} H_{mm'}(\mathbf{k}) \boldsymbol{c}_{\mathbf{k}}(\mathbf{G}_{m'}) = \epsilon(\mathbf{k}) \boldsymbol{c}_{\mathbf{k}}(\mathbf{G}_m), \tag{3.29}$$

which is an eigenvalue problem where the Hamiltonian matrix elements $H_{mm'}$, are given by

$$H_{mm'} = \frac{|\mathbf{k} + \mathbf{G}_m|^2}{2} \delta_{mm'} + V(\mathbf{G}_m - \mathbf{G}_{m'}). \tag{3.30}$$

Diagonalization of the Hamiltonian matrix gives a set of discrete eigenvalues $\varepsilon_i(\mathbf{k})$, with corresponding eigenfunctions $\boldsymbol{c}_{\mathbf{k}}(\mathbf{G}_m)$. These are functions are calculated for each *k*-point in the first Brillouin zone. Eqs. (3.29) can be solved numerically. There are several methods for generating the *k*-points in the first Brillouin zone. The most common method (and that which is used in the work of this thesis), is the Monkhorst-Pack scheme.[20] An infinite number of plane waves are required for a perfect expansion of a Kohn-Sham wavefunction. However, $\boldsymbol{c}_{\mathbf{k}}(\mathbf{G}_{\boldsymbol{m}}) \rightarrow 0$ for high energy planewaves. Otherwise, the wavefunction energy would tend to infinity with increasing planewave energy.

Therefore, a planewave basis set can be truncated above a judiciously chosen cut-off energy, $E_{\text{cut}}$. Computational expense increases with increasing values of $E_{\text{cut}}$. A judiciously chosen value of $E_{\text{cut}}$ will balance both accuracy and computational expense. For this balance, the $E_{\text{cut}}$ value should be chosen such that it satisfies

$$\frac{|\mathbf{k}+\mathbf{G}|^2}{2} < E_{\text{cut}}. \tag{3.31}$$

One must perform a total energy convergence test with respect to varying $E_{\text{cut}}$, in order to judiciously choose a value of $E_{\text{cut}}$ for accurately modelling a given system. These tests are shown in Appendices A, B and C for the projects in Chapters 4, 5 and 6, respectively.

### 3.3.3: Pseudopotentials and the Projector Augmented Wave Method

Solving the Kohn-Sham equations self-consistently using planewave basis sets, can be computationally expensive. This is because the atomic core electrons are highly localized, meaning that a great many planewaves would be needed as the basis over which to expand the Kohn-Sham wavefunctions. Fortunately, the core electron contribution to bonding is usually negligible in comparison to the valence electron contribution. Thanks to this negligible core electron contribution, the computational expense can be decreased. This can be done by application of the frozen core approximation. In this approximation, the core electrons are assumed to negligibly interact with the environment. Therefore, only the valence electron wavefunctions need to be updated at each iteration of the self-consistent solving of the Kohn-Sham equations.

Valence electron wavefunctions oscillate rapidly in the vicinity of the core electrons. Outside the region of the core electrons, the core electron wavefunctions are essentially zero. This means that outside the core region, the valence electron wavefunctions are smoother. The pseudopotential approximation allows the valence electron wavefunctions to be represented by a smoother potential, such that this potential does not oscillate in the region of the core electrons. This is useful because it reduces the number of plane-waves needed in the basis set. This reduces the computational cost of a DFT calculation. A schematic of how a pseudopotential smooths out the wavefunctions oscillation in the core region, is shown below in Fig. 3.4.

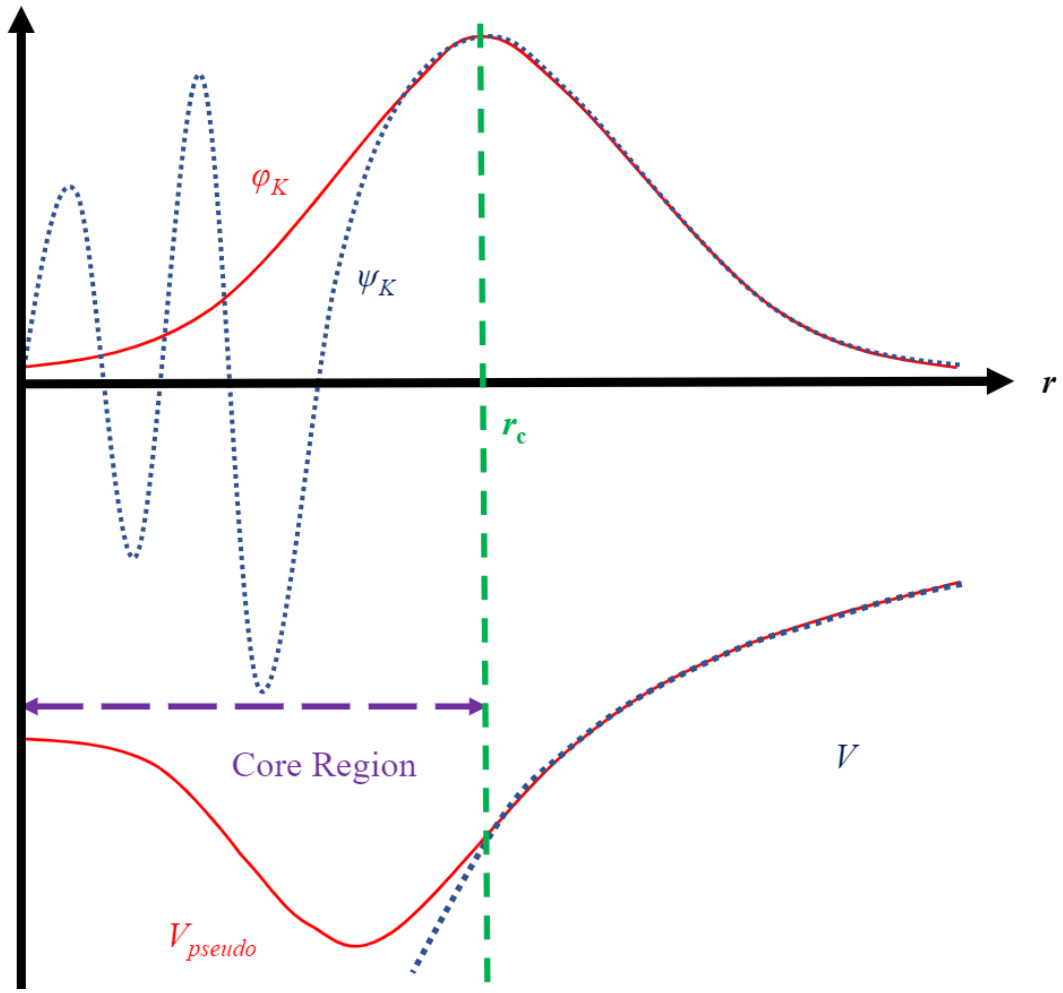


**Figure 3.4:** The true nuclear Coulomb potential ($V$) and the true electron wavefunction ($\psi_K$) are shown by the dashed blue graphs. These are approximated by the pseudopotential ($V_{pseudo}$) and the pseudo wavefunction $\varphi_K$, respectively, shown by the red graphs. The distance from the centre of the atom is given by $r$. The 'cut-off radius' of the core region occurs at $r = r_c$ (dashed green line). All the graphs are shown in real space. (Image derived from information in Ref. [21]).

Inside the core region of Fig. 3.4 ($r < r_c$), the fine details of the wavefunction near the nucleus are missing. This leads to inaccuracies in calculations. In the region $r < r_c$, $V_{pseudo}$ and the pseudo wavefunction $\varphi_K$ are poor approximations to true nuclear Coulomb potential ($V$) and the true electron wavefunction ($\psi_K$), respectively. However, for the DFT calculations for the work in this thesis, only valence electrons located in the region $r > r_c$ need to be considered. In this region, $V_{pseudo}$ and $\varphi_K$ are good approximations to $V$ and $\psi_K$, respectively.

There exist several pseudopotential approximations. The projector augmented wave (PAW) method is a generalization of the pseudopotential with linear augmented plane-wave methods.[22] This generalization allows for computational DFT calculations to be performed more efficiently. Therefore, the PAW method is used for the projects in this thesis. For a detailed coverage of the PAW method, the reader is advised to consult Ref. [22].

## 3.4: Sampling the Brillouin Zone and Dipole Corrections

### 3.4.1: Sampling the Brillouin Zone

The DFT calculation of many properties requires an integration of functions over the Brillouin zone. Two such properties are densities of states and charge densities. These integrated functions over the Brillouin zone adopt the following form:

$$f(\mathbf{r}) = \frac{\Omega_{\mathrm{BZ}}}{(2\pi)^3}\int_{\mathrm{BZ}} F(\mathbf{k})d\mathbf{k} = \sum_j \omega_j F(\mathbf{k}_j), \tag{3.32}$$

where $\Omega_{\mathrm{BZ}}$ is the cell volume and $F(\mathbf{k})$ is the Fourier transform of $f(\mathbf{r})$.[20] The $\omega_j$ are weighting factors in the summation approximation on the right-hand side of Eq. (3.32).[20] The $\mathbf{k}_j$ are known as *k*-vectors. These are related to another set of quantities known as *k*-points. There are various methods of sampling the Brillouin zone with these *k*-points. The method employed for the projects in this thesis is that of Monkhorst and Pack.[20] In this method, the *k*-points ($n_j$) are uniformly distributed in reciprocal space, and are related to the *k*-vectors $\left(\mathbf{k}_{n_1 n_2 n_3}\right)$ as

$$\mathbf{k}_{n_1 n_2 n_3} = \sum_j^3 \frac{2n_j - N_j - 1}{2N_j}\mathbf{b}_j, \tag{3.33}$$

where $n_j$ = 1, 2, 3, …, $N_j$. $N_j$ is the total number of *k*-points along a given direction in reciprocal space. The primitive vectors of the reciprocal lattice are given by $\mathbf{b}_j$. The sum in Eq. (3.33) exactly integrates a periodic function that possesses Fourier components only extending as far as $N_j\mathbf{R}_j$ in each direction. $\mathbf{R}_j$ is the translation vector of the crystal indicating the lattice periodicity in the *j*th direction. For cubic crystals, choosing $N_j$ to be even usually results in a more sufficient sampling of the Brillouin zone.

In general, the three values of $N_j$ are multiplied together to give the *k*-point mesh as $N_1 \times N_2 \times N_3$. For the projects in this thesis, the organic molecules adsorb to the Cu(110) and Cu(111) surfaces. In the case of these surfaces, if $N_1$ and $N_2$ are the *k*-points corresponding to the lattice vectors spanning the adsorption (*xy*) plane, then $N_3$ is *k*-point corresponding to the lattice vector perpendicular to this plane (i.e. in the *z*-direction). A vacuum distance is given to separate the molecule-surface system from its repeated structure in the *z*-direction due to the periodic boundary conditions, akin to the situation shown in Fig. 3.3(b). In this situation, one can choose $N_3 = 1$. This reduces the *k*-point mesh to $N_1 \times N_2 \times 1$, which is less computationally expensive. The energy bands in the direction normal to the surface are flat. Hence, these bands vary negligibly with respect to $\mathbf{k}_{n_3}$. This justifies the choice of $N_3 = 1$.

For accurately modelling chemical systems, the values of these $N_1$ and $N_2$ need to be judiciously selected. A good choice of values for $N_1$ and $N_2$ values, yields a *k*-point mesh that can be used to obtain accurate modelling of a system, whilst minimizing computational expense. Computational expense increases with increasing values of $N_j$. To get good values for $N_1$ and $N_2$, one must perform a total energy convergence test with respect to varying $N_1$ and $N_2$. These tests are shown in Appendices A, B and C for the projects in Chapters 4, 5 and 6, respectively. For gas phase configurations, the energy bands in each direction are flat. Therefore, in this case one can choose $N_1 = N_2 = N_3 = 1$. Hence, one can sample a supercell containing a molecule in the gas phase, with a *k*-point mesh of $1 \times 1 \times 1$.

### 3.4.2: Dipole Corrections

In this thesis, adsorbate molecules are placed upon one side of the Cu(110) or Cu(111) surface. When a molecule is placed on one side of a slab in this manner, the periodic boundary conditions employed by VASP[12] can be problematic. This is because a DFT calculation can result in a slab that possesses a non-negligible net dipole moment. This net dipole moment gives rise to an electric field which corrupts the electron density of the slab, which in turn gives an inaccurate slab energy. A dipole correction technique introduced by Neugebauer and Scheffler[23] (later improved by Bengtsson),[24] is used to alleviate this problem.

## 3.5: Approximating the Exchange-Correlation Functional

At this stage, the only ingredient that is missing in a DFT calculation, is an approximation for the exchange-correlation functional. It was mentioned in Subsection 3.2.2 that there exist several approximations for the exchange-correlation functional. The most primitive of these is the local density approximation (LDA),[5] described below.

### 3.5.1: The Local Density Approximation

The exchange-correlation functional in the LDA, $E_{\mathrm{xc}}^{\mathrm{LDA}}[n]$, is taken to be dependent only on the density $n$ at each point in space of a homogeneous electron gas. The expression for $E_{\mathrm{xc}}^{\mathrm{LDA}}[n]$ is given by

$$E_{\mathrm{xc}}^{\mathrm{LDA}}[n] = \int n(\mathbf{r})\, \epsilon_{\mathrm{xc}}^{\mathrm{hom}}[n] d^3\mathbf{r}, \tag{3.34}$$

where $\epsilon_{\mathrm{xc}}^{\mathrm{hom}}[n]$ is the exchange-correlation energy per electron for a homogeneous electron gas of density $n(\mathbf{r})$. This gas is characterized uniquely by the Wigner-Seitz radius $r_s$. This is the radius of a sphere that contains one electron on average. The expression for $r_s$ given by

$$r_s(n) = \left(\frac{3}{4\pi n}\right)^{\frac{1}{3}} = \frac{1.919}{k_{\mathrm{F}}}, \tag{3.35}$$

where $k_{\mathrm{F}}$ is the Fermi wavevector for the homogeneous electron gas, given by

$$k_{\mathrm{F}} = (3\pi^2 n)^{\frac{1}{3}}. \tag{3.36}$$

The total exchange-correlation energy is the sum of the exchange and correlation energies, i.e.

$$E_{\mathrm{xc}}^{\mathrm{LDA}} = E_{\mathrm{x}}^{\mathrm{LDA}} + E_{\mathrm{c}}^{\mathrm{LDA}}. \tag{3.37}$$

In Eq. (3.37), the exchange energy $E_{\mathrm{x}}^{\mathrm{LDA}}[n]$, is given by

$$E_{\mathrm{x}}^{\mathrm{LDA}}[n] = \int n(\mathbf{r})\, \epsilon_{\mathrm{x}}^{\mathrm{hom}}[n] d^3\mathbf{r}, \tag{3.38}$$

where $\epsilon_{\mathrm{x}}^{\mathrm{hom}}[n]$ is the exchange energy per electron, given by

$$\epsilon_{\mathrm{x}}^{\mathrm{hom}}[n] = A_{\mathrm{x}} n^{\frac{1}{3}}. \tag{3.39}$$

In Eq. (3.39), $A_{\mathrm{X}} = -(3/4)(3/\pi)^{1/3}$. Similarly, the correlation energy $E_{\mathrm{c}}^{\mathrm{LDA}}[n]$, is given by

$$E_{\mathrm{c}}^{\mathrm{LDA}}[n] = \int n(\mathbf{r})\, \epsilon_{\mathrm{c}}^{\mathrm{hom}}[r_s(\mathbf{r})] d^3\mathbf{r}, \tag{3.40}$$

where $\epsilon_{\mathrm{c}}^{\mathrm{hom}}[n]$ is the correlation energy per electron. This quantity cannot be analytically calculated except in the limits of high and low density, for which $r_s \to 0$ and $r_s \to \infty$, respectively. Monte Carlo calculations have provided numerical approximations of $\epsilon_{\mathrm{c}}^{\mathrm{hom}}[n]$ for intermediate values of $r_s$ The generalized gradient approximation (GGA) is an improvement on the LDA. This approximation is discussed below in Subsection 3.5.2.

### 3.5.2: The Generalized Gradient Approximation to the Exchange-Correlation Functional

In the generalized gradient approximation (GGA),[25] the exchange energy $E_{\mathrm{x}}^{\mathrm{GGA}}[n]$, is given by

$$E_{\mathrm{x}}^{\mathrm{GGA}}[n] = \int n(\mathbf{r})\, \epsilon_{\mathrm{x}}^{\mathrm{hom}}[n] F_{\mathrm{x}}[s(\mathbf{r})] d^3\mathbf{r}. \tag{3.41}$$

where $F_{\mathrm{x}}$ is known as the exchange enhancement factor. This factor 'enhances' the LDA exchange energy, resulting in a better exchange energy approximation. The enhancement factor also depends on the parameter $s(\mathbf{r})$, which is given by.

$$s(\mathbf{r}) = \frac{|\boldsymbol{\nabla}\, n(\mathbf{r})|}{2k_{\mathrm{F}} n(\mathbf{r})}. \tag{3.42}$$

Eq. (3.42) indicates that unlike $E_{\mathrm{x}}^{\mathrm{LDA}}[n]$, $E_{\mathrm{x}}^{\mathrm{GGA}}[n]$ also depends on the gradient of $n(\mathbf{r})$. The exchange-correlation energy $E_{\mathrm{xc}}^{\mathrm{GGA}}[n]$, is expressed as

$$E_{\mathrm{xc}}^{\mathrm{GGA}}[n] = \int n(\mathbf{r})\, \epsilon_{\mathrm{x}}^{\mathrm{hom}}[n] F_{\mathrm{xc}}[r_s(\mathbf{r}), s(\mathbf{r})] d^3\mathbf{r}, \tag{3.43}$$

for the non-spin-polarized case, where $F_{\mathrm{xc}}$ is the exchange-correlation enhancement factor. The limiting behaviours of $F_{\mathrm{xc}}$ are

$$F_{\mathrm{xc}}[r_s, s = 0)] = F_{\mathrm{xc}}^{\mathrm{hom}}(r_s), \qquad F_{\mathrm{xc}}[r_s = 0, s)] = F_{\mathrm{x}}(s). \tag{3.44}$$

$F_{\mathrm{xc}}$ can be analytically evaluated, or by fitting parameters to experimental data. There are several flavours of GGA, with the Perdew-Burke-Ernzerhofer (PBE)[26] flavour being one of the most useful. For the organic molecule adsorbed species studied in this thesis, van der Waals (vdW) interactions become important. The exchange-correlation energy for such situations cannot be adequately modelled by the LDA or the GGA. Corrections to the exchange-correlation that account for these vdW interactions, are covered below in Subsection 3.5.3.

### 3.5.3: Van der Waals Corrections to the Exchange-Correlation Functional

There are several versions of the van der Waals density functional (vdW-DF) to the exchange-correlation functional. The discussion here begins with the Langreth-Lundqvist vdW-DF.[26-27] For this vdW-DF, the correlation energy is given by

$$E_{\mathrm{c}}[n] = E_{\mathrm{c}}^{0}[n] + E_{\mathrm{c}}^{\mathrm{nl}}[n]. \tag{3.45}$$

The value of $E_{\mathrm{c}}^{0}[n]$ is that given by $E_{\mathrm{c}}^{\mathrm{LDA}}[n]$. In the LDA, the correlation is local. The value of $E_{\mathrm{c}}^{\mathrm{nl}}[n]$ is the non-local correlation energy contribution due to the vdW interactions. This is given by

$$E_{\mathrm{c}}^{\mathrm{nl}}[n] = \frac{1}{2}\int n(\mathbf{r})\Phi(\mathbf{r},\mathbf{r}')\, n(\mathbf{r}')d^{3}\mathbf{r}d^{3}\mathbf{r}', \tag{3.46}$$

where Φ is a kernel dependent on |**r** – **r'**| and the densities in the neighbourhoods of **r** and **r'**. The vdW-corrected total energy is given by

$$E_{\mathrm{vdW}} = E_{\mathrm{GGA}} - E_{\mathrm{c,GGA}} + E_{\mathrm{c,LDA}} + E_{\mathrm{c}}^{\mathrm{nl}}, \tag{3.47}$$

where $E_{\mathrm{c,GGA}}$ and $E_{\mathrm{c,LDA}}$ are the correlation energies given by the GGA and LDA, respectively. $E_{\mathrm{c}}^{\mathrm{nl}}$ is given by Eq. (3.44). An empirical approach to account for the vdW interactions was introduced by Grimme.[28] This approach adds a pair wise interaction between all the atoms in the system. For *N* atoms, the total dispersion energy $E_{\mathrm{disp}}^{\mathrm{tot}}$, is

$$E_{\text{disp}}^{\text{tot}} = \sum_{i=1}^{N} \sum_{j>i}^{N} V(R_{ij}), \tag{3.48}$$

where $V(R_{ij})$ is a pair potential between atoms $i$ and $j$, and $R_{ij}$ is the distance between these two atoms. This pair potential is given by

$$V(R_{ij}) = -f_{\text{damp}}(R_{ij}) \frac{C_{6,ij}}{R_{ij}^6}, \tag{3.49}$$

where $C_{6,ij}$ is the '$C_6$ coefficient' governing the interaction strength between atoms $i$ and $j$. The quantity $f_{\text{damp}}$ is a damping function approximately equal to 1 or 0, for large or small atomic separations, respectively. The force contribution on atom $i$ due to the $C_6$-correction are equal to the negative gradient of Eq. (3.49), i.e.

$$F_i = -\nabla_i V(R_{ij}) = C_{6,ij} \frac{\vec{R}_j - \vec{R}_i}{R_{ij}^7} \left[ \frac{6 f_{\text{damp}}}{R_{ij}} - f'_{\text{damp}}(R_{ij}) \right]. \tag{3.50}$$

The thesis projects in Chapters 4 – 6 use vdW exchange-correlation functionals that are developed further than that given by the Langreth-Lundqvist vdW-DF. Namely, the functionals used for these projects are the optB86b-vdW (Chapter 5) and vdW-DF-cx functionals (Chapters 4 and 6). These functionals are discussed below in Subsections 3.5.4 and 3.5.5, respectively.

### 3.5.4: The optB86b-vdW Functional

The optB86b-vdW XC-functional[29-32] has been used successfully in theoretical modelling of numerous previous DFT studies requiring accurate adsorption energies on transition metals when bonding to the surface is dominated by strong covalent or ionic bonding, along with strong vdW interaction contributions.[33] This functional was used specifically in Chapter 5 for the modelling of FBF on Cu(110).

At the start of the project, it was very difficult to predict the dominant interaction contribution(s). Therefore, the optB86b-vdW functional was an ideal choice due to its high degree of accuracy across different bonding scenarios. This was especially important too given the current lack of literature concerning flurbiprofen adsorption on metal surfaces

This functional has also been accurate in modelling the adsorption of molecules containing a carboxylate ($COO^-$) group to the Cu(110) surface (he reader should refer to Chapter 5 for the references that link to these studies). In Chapter 5, the flurbiprofen molecule uses the carboxylate group to anchor itself to the Cu(110) surface. Use of the optB86b-vdW functional yielded the typical Cu-O distance of 1.9 – 2.0 Å for the molecule-surface system.[34-36] This was a promising start to using this functional to model the adsorption scenarios of Chapter 5. The value of the copper lattice constant as calculated by optB86b-vdW functional was 3.60 Å. The experimental value is 3.60 – 3.61 Å.[37] The percentage difference between these values is 0.28%, which is very low.

### 3.5.5: The vdW-DF-cx Functional

The vdW-DF-cx XC-functional[29-30, 38] was used to correct for the vdW interactions of Chapters 4 and 6. This functional has performed very well by resolving many of the internal consistency problems related to overestimation of separation distances. The functional provides a good account of systems beyond the vdW regime, for instance, covalent solids and systems with mixed binding characteristics. The result of this is that using the vdW-DF-cx functional very often yields interaction energies that approach chemical accuracy.[39] This functional also performs excellently when used to calculate barrier heights in the MEPs resulting from NEB calculations.[40-41] Accurate NEB calculations were required in both Chapters 4 and 6. Therefore, the vdW-DF-cx functional was considered the most appropriate functional to use for this purpose. The value of the copper lattice constant as calculated by vdW-DF-cx functional is 3.579 Å. The experimental value is 3.60 – 3.61 Å.[37] The percentage difference between these values is 0.585 – 0.862%, which is very low.

## 3.6: Finding the Equilibrium Structure of a System

### 3.6.1: Reaction Equation and Calculated Adsorption Energy

For the projects in this thesis, an organic molecule is adsorbed to a copper (Cu) surface. The reaction equation for this is

$$n(\text{molecule}) + \text{Cu} \rightarrow n(\text{molecule})\backslash\text{Cu}, \tag{3.51}$$

where $n$ is the number of molecules, and molecule\Cu represents the adsorbed molecules on the Cu surface. The adsorption energy, $E_{\text{ads}}$ corresponding to Eq. (3.51) is

$$E_{\text{ads}} = \frac{E[n(\text{molecule})\backslash\text{Cu}] - \{nE[(\text{molecule})] + E[\text{Cu}]\}}{n}. \tag{3.52}$$

In some of the adsorption reactions in this thesis, the molecule deprotonates upon adsorption to give off hydrogen gas. In this case, the reaction equation becomes

$$n(\text{molecule}) + \text{Cu} \rightarrow n(\text{molecule})\backslash\text{Cu} + \frac{n}{2}\text{H}_2, \tag{3.53}$$

with $E_{\text{ads}}$ given by

$$E_{\text{ads}} = E[n(\text{molecule})\backslash\text{Cu}] + nE[\text{H}_2] - \{nE[(\text{molecule})] + E[\text{Cu}]\}. \tag{3.54}$$

Eqs. (3.51) – (3.54) apply to adsorbed molecule(s) within a supercell. The adsorption energy per molecule for a system, can be calculated by dividing Eq. (3.52) or (3.54) by *n.* In order to find the configuration of an adsorbed molecule-surface system that is likely to best model the system found by experiment, a search of the potential energy surface (PES) is necessary. This is discussed below in Subsection 3.6.2.

### 3.6.2: The Potential Energy Surface

In this thesis, the equilibrium structure of a molecule adsorbed to a surface, is defined as that ground-state configuration occurring at the global minimum of the potential energy surface (PES). The PES is the potential energy of the system as a function of the atomic positions. To find the global minimum of the PES, various configurations of the molecule-surface must be set up and optimized by DFT calculations. The ground-state energies of these DFT optimized configurations will correspond to the energy minima of the PES. If enough initial configurations of the molecule on the surface are set up, these energy minima will contain both local minima and the global minimum of the PES. If the PES search can be judged to be adequately exhaustive, then the lowest minimum energy can be taken as likely to be the global minimum of the system.

## 3.7: Modes of Vibration

### 3.7.1: The Harmonic Approximation

Atomic and molecular vibrations involve very small displacements away from the nuclei equilibrium positions. In this thesis, it is necessary to simulate the vibrational modes of equilibrium structures. Comparing theoretical modelling of vibrations with the corresponding experimental data, allows further support that an equilibrium structure being modelled can actually reproduce the corresponding experimental vibrational results. In this thesis, the harmonic approximation[42] is used to simulate the molecular vibrational modes. This subsection covers the main principles of the harmonic approximation, as applied to the study of molecular vibrational modes. The time-dependent position of each nucleus $\mathbf{R}_I(t)$ can be expressed as

$$\mathbf{R}_I(t) = \mathbf{R}_I^0 + \mathbf{u}_I(t), \tag{3.55}$$

where $\mathbf{R}_I^0$ is the time-independent equilibrium position and $\mathbf{u}_I(t)$ is the displacement away from the equilibrium position. Newton's second law can be used to express the partial derivatives of the total energy $U$, with respect to $\mathbf{u}_I(t)$, as

$$M_I \ddot{\mathbf{u}}_I(t) = -\frac{\partial U}{\partial \mathbf{u}_I}. \tag{3.56}$$

The total energy $U$ can be written in terms of a Taylor expansion as

$$U(\mathrm{R}_1, \ldots, \mathrm{R}_M) = U(\mathbf{R}_1^0, \ldots, \mathbf{R}_M^0) + \frac{\partial U}{\partial R_{I\alpha}} u_{I\alpha} + \frac{1}{2} \frac{\partial^2 U}{\partial R_{I\alpha} \partial R_{J\beta}} u_{I\alpha} u_{J\beta}, \tag{3.57}$$

where $R_{I\alpha}$ is the coordinate of the $I$th nucleus along the Cartesian direction $\alpha$. The expansion has used the Einstein convention for the summation over repeated indices. Eq. (3.57) can be expressed more simply as

$$U(\mathrm{R}_1, \ldots, \mathrm{R}_M) = U_0 - F_{I\alpha} u_{I\alpha} + \frac{1}{2} \frac{\partial^2 U}{\partial R_{I\alpha} \partial R_{J\beta}} u_{I\alpha} u_{J\beta}, \tag{3.58}$$

where $U_0 = U(\mathbf{R}_1^0, \ldots, \mathbf{R}_M^0)$ and $F_{I\alpha}$ is the atomic force on the $I$th nucleus in direction $\alpha$. The so-called 'Born-von Karman' force constants are defined as

$$K_{I\alpha,J\beta} = \frac{\partial^2 U}{\partial R_{I\alpha} \partial R_{J\beta}}. \tag{3.59}$$

The constants $K_{I\alpha,J\beta}$ are independent of time because they are evaluated at the nuclear equilibrium positions. For these equilibrium positions, $F_{I\alpha} = 0$. Therefore, combining Eqs. (3.58) and (3.59) yields

$$U = U_0 + \frac{1}{2} K_{I\alpha,J\beta}\, u_{I\alpha} u_{J\beta}. \tag{3.60}$$

Eq. (3.60) defines the harmonic approximation. With some algebra, one can show that

$$M_I \ddot{u}_{I\alpha} = -K_{I\alpha,J\beta} u_{J\beta}. \tag{3.61}$$

Dividing Eq. (3.61) by $\sqrt{M_I}$, and introducing a factor of $\sqrt{M_J}$and $1/\sqrt{M_J}$ gives

$$\sqrt{M_I}\ddot{u}_{I\alpha} = \frac{-K_{I\alpha,J\beta}\sqrt{M_J}}{\sqrt{M_I M_J}} u_{J\beta}. \tag{3.62}$$

Defining the 'mass-weighted' displacements $v_{I\alpha}$, as

$$v_{I\alpha} = \sqrt{M_I} u_{I\alpha}, \tag{3.63}$$

allows Eq. (3.62) to be rewritten as

$$\ddot{v}_{I\alpha} = -\frac{K_{I\alpha,J\beta}}{\sqrt{M_I M_J}}\, v_{J\beta}. \tag{3.64}$$

Eq. (3.64) represents the motion of 3$M$ springs that are interconnected by the Born-von Karman force constants. The 'dynamical matrix' is defined as

$$D_{I\alpha,J\beta} = \frac{K_{I\alpha,J\beta}}{\sqrt{M_I M_J}}, \tag{3.65}$$

which means that Eq. (3.64) can be expressed as

$$\ddot{v}_{I\alpha} = -D_{I\alpha,J\beta}\, v_{J\beta}. \tag{3.66}$$

Eq. (3.66) can be rewritten as

$$\ddot{\mathbf{v}} = \underline{\mathbf{D}}\mathbf{v}, \tag{3.67}$$

where **v** is the 3$M$-dimensional matrix with the $v_{I\alpha}$ as components. The dynamical matrix is diagonalized by solving the secular equation given by Eq. (3.68) below.

$$\det(\underline{\mathbf{D}} - \omega^2\underline{\mathbf{I}}) = 0. \tag{3.68}$$

In Eq. (3.68), the eigenvalues of the dynamical matrix are given by $\omega$ and $\underline{\mathbf{I}}$ is the identity matrix of size (3$M$) × (3$M$). The dynamical matrix can be expressed explicitly in terms of total energy as

$$D_{I\alpha}u_{I\alpha} = \frac{1}{\sqrt{M_I M_J}} \frac{\partial^2 U}{\partial R_{I\alpha}\partial R_{J\beta}}, \tag{3.69}$$

or in terms of forces as

$$D_{I\alpha}u_{I\alpha} = -\frac{1}{\sqrt{M_I M_J}} \frac{\partial F_{I\alpha}}{\partial R_{J\beta}}. \tag{3.70}$$

The forces $F_{I\alpha}$ in Eq. (3.70) can be evaluated by the method of finite differences as

$$D_{I\alpha}u_{I\alpha} = -\frac{1}{\sqrt{M_I M_J}} \frac{F_{I\alpha}\left(R^0_{J\beta} + u\right) - F_{I\alpha}\left(R^0_{J\beta} - u\right)}{2u} + O(u^2). \tag{3.71}$$

In Eq. (3.71), $F_{I\alpha}\left(R^0_{J\beta} \pm u\right)$ represents the force acting on nucleus $I$ along the direction $\alpha$, such that all nuclei, except $J$, are in their equilibrium positions. Nucleus $J$ has been displaced along direction $\beta$ by a small distance, $\pm u$.

### 3.7.2: Zero-Point Energy Corrections

The lowest possible energy state of a system is known as the 'zero-point energy'. This is often abbreviated as the 'ZPE'. Quantum mechanics shows that this ZPE, $(E_{\text{tot}})_{\text{min}}$ is given by

$$(E_{\text{tot}})_{\text{min}} = U_0 + \sum_{\nu} \frac{\hbar\omega_{\nu}}{2}. \tag{3.72}$$

where $U_0$ is the minimum of the potential energy surface. Eq. (3.72) indicates the ground-state energy of any atomic system is slightly higher than $U_0$. The additional energy $\sum_{\nu} \frac{\hbar\omega_{\nu}}{2}$. cannot be ignored in thermochemical reactions.[43]

## 3.8: The Tersoff-Hamann Approximation

It is possible to simulate STM images to allow further insights into the degree of support between a computationally derived theoretical model and an STM experimental observation. In order to do this, the Tersoff-Hamann approximation[44-45] is used for all such STM images simulations in this thesis.

The Tersoff-Hamann approximation is twofold. Firstly, one applies the Bardeen approximation[46] to derive the $M_{\mu\nu}$ matrix elements of Eq. (2.2). Secondly, one assumes that the STM tip is spherical with an s orbital at the apex (although this has been relaxed in more recent work which projects the DOS onto a "tip" p or d orbital).[47-48] However, the spherical tip with the s orbital is assumed for the calculations in this thesis. The local density of states (LDOS) at the STM tip, $\rho(\mathbf{r}_{\text{tip}}, \epsilon)$, is given by

$$\rho(\mathbf{r}_{\text{tip}}, \epsilon) = \sum_{\mu\mathbf{K}} |\psi_{\mu\mathbf{K}}(\mathbf{r}_{\text{tip}})|^2 \ \delta(\epsilon - \epsilon_{\mu\mathbf{K}}). \tag{3.76}$$

In Eq. (3.76), the wavevectors **K**, are in the surface Brillouin zone. For each vector **K**, there exist several eigenstates labelled by $\mu$. For each $\mu$ and **K**, the sample wavefunctions and energies are given by $\psi_{\mu\mathbf{K}}$ and $\epsilon_{\mu\mathbf{K}}$, respectively. In the framework of DFT, these wavefunctions are given by the Kohn-Sham wavefunctions in the vacuum region. For calculational convenience, one can scale the Fermi energy to zero. One can then show that the tunnelling current *I* is directly proportional to the integrated sample LDOS, i.e.

$$I(V, \mathbf{r}_{\text{tip}}) \propto \int_0^V \rho(\epsilon, \mathbf{r}_{\text{tip}}) d\epsilon \tag{3.77}$$

Differentiating Eq. (3.77) with respect to the bias voltage *V* gives

$$\frac{dI}{dV}(V, \mathbf{r}_{\text{tip}}) \propto \rho(\epsilon_F + eV, \mathbf{r}_{\text{tip}}) = \sum_{\mu\mathbf{K}} |\psi_{\mu\mathbf{K}}(\mathbf{r}_{\text{tip}})|^2 \delta(\epsilon_{\text{F}} + eV - \epsilon_\alpha), \tag{3.78}$$

The $\mathbf{r}_{\text{tip}}$ position is in the vacuum region. Here, the one-electron potential is constant. The assumption of a spherical STM tip and a tunnelling current that is proportional to the LDOS is what constitutes the Tersoff-Hamann approximation.[44-45] The calculation of the LDOS in Eq. (3.76) can be simplified by extrapolation of the vacuum tails of $\psi_{\mu\mathbf{K}}$ from a position called the matching plane ($z = z_{\text{m}}$), in the vacuum region.

This extrapolation is done because the tails of the electronic wavefunctions are exponentially small in the vacuum region and are not well-converged in the DFT calculations. These tails tend to be noisy since they give a very small contribution to the total energy. The matching plane is measured perpendicularly to the adsorption surface, and is given by

$$z_{\mathrm{m}} = z_{\mathrm{s}} + d_{\mathrm{m}}, \tag{3.79}$$

where $z_s$ is the height of the first surface layer and $d_m$ is known as the matching distance. In this thesis, the plane of the surface is denoted as the *xy* plane. Quantities measured perpendicularly to the *xy* plane are described as being along the *z* direction. The criterium of choice of matching distance (and hence of matching plane) is that this distance should be in the vacuum region.

The vacuum region can be identified by observing a derived plot of the variation with respect to distance in the $z$ direction, of the laterally averaged electrostatic potential. This electrostatic potential is essentially constant in the vacuum region. This is shown schematically in Fig. 3.5.

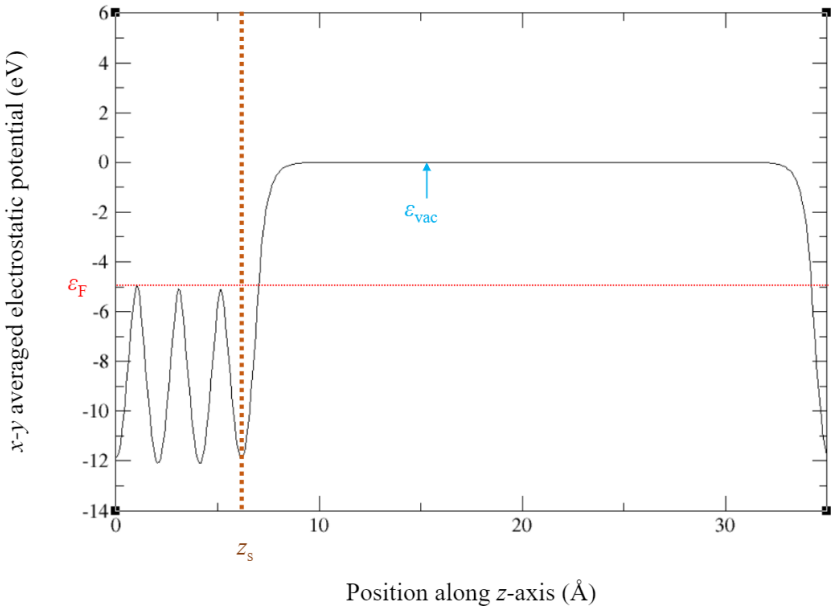


(a)

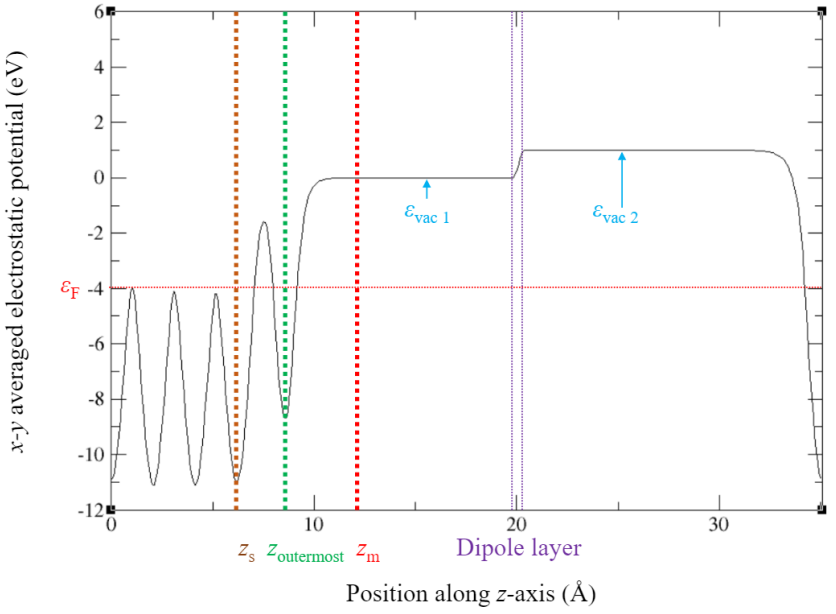


(b)

**Figure 3.5:** Plots of *x-y* averaged electrostatic potential vs position along *z*-axis for an optimized bare Cu(111) slab (a) and an OHPc\Cu(111) adsorbate-surface system (b). The coordinate of the outermost atom of adsorbate molecule is $z_{outermost}$. The dipole layer in (b) is artificial. The $\varepsilon_{vac\ 2}$ energy is the vacuum energy above the dipole layer and is equal to 1.00 eV relative to $\varepsilon_{vac\ 1}$. $\varepsilon_{vac}$ and $\varepsilon_{vac\ 1}$ have both been scaled to zero. The Fermi energy and work function are given by $\varepsilon_F$ and $\Phi$, respectively. $\Phi = \varepsilon_{vac} - \varepsilon_F = 4.95$ eV (a) and $\Phi = \varepsilon_{vac\ 1} - \varepsilon_F = 3.99$ eV (b).

The dipole layer in Fig. 3.5 (b) is due to the artificial dipole moment that VASP uses to oppose that of the whole (adsorbate-surface) system. This is so that the total dipole moment in the direction perpendicular to the surface will be zero. This has the effect of cancelling out the induced electric field due to the periodic boundary conditions as previously described in Subsection 3.4.2. The schematics shown in Fig. 3.5 are an example corresponding to calculations in Chapter 6 of this thesis. Other such plots from Chapters 4 – 6 contained similar features. These have not been shown as their presence would be superfluous. Now, the extrapolation of the LDOS into the vacuum region yields the following expression for $\psi_{\mu\mathbf{K}}$, in atomic units:

$$\psi_{\mu\mathbf{K}}(\boldsymbol{r}) = \sum_{\mathbf{G}} \psi_{\mu\mathbf{K}+\mathbf{G}}\,(\mathbf{R}, z_{\mathrm{m}}) \exp\left[-\sqrt{2\left(\Phi - \epsilon_{\mu\mathbf{K}}\right) + (\mathbf{G}+\mathbf{K})^2}\,(z - z_{\mathrm{m}})\right], \qquad z > z_{\mathrm{m}}, \tag{3.80}$$

where **R** and **G** are the position vectors and reciprocal lattice vectors, respectively, in the matching plane $z_{\mathrm{m}}$. The energy $\epsilon_{\mu\mathbf{K}}$ is referenced with respect to the Fermi levl $\epsilon_{\mathrm{F}}$. The work function of the sample is denoted by $\Phi$, which is related to the vacuum and Fermi energies by

$$\Phi = \epsilon_{\mathrm{vac}} - \epsilon_{\mathrm{F}} \tag{3.81}$$

In summary, a topographic STM image can be generated by a contour plot of tip-surface distances for a constant tunnelling current, as given by Eq. (3.77). The bias voltage is chosen to be the same as that of experiment, and the other quantities involved are evaluated accordingly by one's knowledge of the adsorbate-surface system being studied.

Even though the Tersoff-Hamann approximation is employed for all STM image simulation in this thesis, a brief discussion of a more accurate method follows. The Tersoff Hamann approximation can be improved such that the tunnelling current $I$ in Eq. (3.77) can be calculated more accurately without the use of the perturbation theory in Bardeen's approximation. For instance, the tip is a semi-infinite chain of spherical potential wells oriented perpendicularly to the surface of the sample. However, the sample surface is arbitrary. The wavefunction of the entire system is obtained by a matching procedure. This matching procedure allows the tunnelling current to be determined.

For a small bias voltage, the result is similar to that of the Tersoff-Hamann approximation, with the tunnelling conductance $\sigma$, proportional to the LDOS of the surface. However, the current is renormalized to include multiple reflections to all orders. The relationship can be described as $\sigma \propto \rho(\mathbf{r}_{\mathrm{tip}}, E_{\mathrm{F}})/D$, where $\rho$ and $E_{\mathrm{F}}$ are the LDOS and Fermi level in the STM tip. $D$ is a quantity that depends on the electronic structures of both the tip and the sample. As the tip-surface distance increases, $D$ approaches unity, resulting in the result of the Tersoff-Hamann approximation. $D$ can be smaller or greater than unity, resulting in a relative decrease or increase, respectively, of the tunnelling current. This effect can be significant in the interpretation of STM images.[49]

## 3.9: The Projected Density of States on an Atomic or Molecular Orbital

In Section 3.8, the constant LDOS at the STM tip in the Tersoff-Hamann approximation was described for the purpose of the simulation of STM images. This gives a contour plot of different tip-surface distances for constant tip LDOS and constant tunnelling current for a given bias voltage. This contour plot can then be compared to the corresponding experimental STM image at the same bias voltage. In both cases of theory and experiment, the STM image is built up from the STM tip moving over the atomic or molecular orbitals of the system.

However, these calculations just serve as a purpose of comparing the theoretical model to the experimental results in order to give further evidence for or against the validity of a theoretical model candidate equilibrium structure. The calculations in the Tersoff-Hamann equation do not offer many further insights into the bonding of an adsorbate onto a surface. One can get further insights into this by considering the projected density of states (PDOS) of the isolated adsorbate Kohn-Sham wavefunctions on the adsorbate-surface system Kohn-Sham wavefunctions. The isolated adsorbate should be in the same geometric configuration as it is when adsorbed to the surface.[50] Calculating the PDOS allows further study of bonding character. The expression for the PDOS of an isolated adsorbate orbital with wavefunction $\psi_{a\mathbf{K}}$ is defined as[50]

$$\rho_{\mathrm{a}}(\epsilon) = \sum_{\mu}\sum_{\mathbf{K}} \left|\langle \psi_{a\mathbf{K}} | \psi_{\mu\mathbf{K}} \rangle\right|^2 w_{\mathbf{K}} \delta(\epsilon - \epsilon_{\mu\mathbf{K}}), \tag{3.82}$$

where $w_{\mathbf{K}}$ are $k$-points weights. In Eq. (3.82), $\left|\langle \psi_{a\mathbf{K}} | \psi_{\mu\mathbf{K}} \rangle\right|^2 = 1$. In practice, a gaussian broadening of the density of states replaces the delta function, $\delta(\epsilon - \epsilon_{\mu\mathbf{K}})$.[50]

## 3.10: The Nudged Elastic Band Method

### 3.10.1: Minimum Energy Paths

The nudged elastic band (NEB) method[51] is a technique used to identify the minimum energy path (MEP) between one stable arrangement of atoms to another. The NEB method is used in Chapters 4 and 6. The saddle point of the MEP is the maximum in the potential energy in one dimension, and a minimum in all others. This maximum defines the activation energy barrier for the rearrangement process being studied. The NEB method works by DFT optimizing a judiciously chosen number of intermediate images along the reaction pathway between the initial and final stable atomic arrangements. These images are joined together by 'elastic bands' with an associated 'spring constant.' In the NEB method, this elastic band is minimized such that the perpendicular spring force component, and the parallel true force component are projected outwards. This means that the force on image *i*, $\mathbf{F}_i^0$, is given by

$$\mathbf{F}_i^0 = -\boldsymbol{\nabla} V(\mathbf{R}_i)|_\perp + (\mathbf{F}_i^s \cdot \hat{\boldsymbol{\tau}}_\parallel)\hat{\boldsymbol{\tau}}_\parallel \tag{3.83}$$

where $\mathbf{R}_i$ is the reaction coordinate of image *i* and $\hat{\boldsymbol{\tau}}_\parallel$is the unit tangent to the reaction pathway. The spring force is given by $\mathbf{F}_i^s$. The perpendicular component of the gradient of the potential *V* along the reaction pathway, $\boldsymbol{\nabla} V(\mathbf{R}_i)|_\perp$, can be expressed as

$$\boldsymbol{\nabla} V(\mathbf{R}_i)|_\perp = \boldsymbol{\nabla} V(\mathbf{R}_i) - [\boldsymbol{\nabla} V(\mathbf{R}_i) \cdot \hat{\boldsymbol{\tau}}_\parallel]\hat{\boldsymbol{\tau}}_\parallel. \tag{3.84}$$

The projection of the perpendicular component of $\boldsymbol{\nabla} V(\mathbf{R}_i)$ and the parallel component of $\mathbf{F}_i^s$ is referred to as 'nudging.' These projections make the NEB method useful. This is because the force projections decouple the path dynamics from the particular distribution of the chosen images in the discrete representation of the path. Then, the spring force does not interfere with the optimization of the images in the direction perpendicular to the path. This means that the optimized configuration of the images satisfies

$$\boldsymbol{\nabla} V(\mathbf{R}_i)|_{\perp} = \mathbf{0}. \tag{3.85}$$

Eq. (3.85) indicates that all the optimized images will lie on the MEP. Moreover, the spring force affects only the image distribution in the path. Therefore, the spring constants can be chosen quite arbitrarily. The decoupling of the path optimization and the discrete representation of the path is essential in order to ensure the convergence of the path to the MEP.

### 3.10.2: The IDPP Algorithm

Before running an NEB calculation, it is useful to create the images so that they form a good initial guess of the reaction pathway between the initial and final states of a system. In this thesis, the image dependent pair potential (IDPP) algorithm[52] is used for this purpose. The NEB method finds a discrete representation of the MEP. Firstly, the atomic coordinates of the endpoint stable structures at the energy minima are used to generate an initial path. This initial path is a guess. Here, $r = \{r_1, r_2, \ldots, r_N\}$ represents the vector of $3N$ coordinates of the atoms in a given arrangement. The initial and final stable configurations are denoted by $r_\alpha$ and $r_\beta$, respectively. The starting guess for the reaction pathway is typically a linear interpolation of the Cartesian coordinates of the two endpoint configurations. The number of intermediate images between these two structures is denoted as $(p - 1)$. The linear interpolation path most commonly used as the initial path in NEB calculations, is given by

$$r_{L,i}^{\kappa} = r_i^{\alpha} + \frac{\kappa\left(r_i^{\beta} - r_i^{\alpha}\right)}{p}, \tag{3.86}$$

where $r_i$ is the coordinates of atom $i$. The image number along the path is given by $\kappa$. The image number along the path runs from 1 to ($p$ – 1). The minimization (optimization) process of an NEB calculation adjusts the coordinates of the ($p$ – 1) images until the images lie on the MEP. During this process, the coordinates of the endpoint structures are unchanged. The IDPP method is a way of automatically creating a path with physically reasonable distances between pairs of images, whilst increasing the probability that the initial path would lie close to the MEP. Therefore, using the IDPP algorithm rather than linear interpolation is usually much less computationally expensive.

In the IDPP method, an interpolation of all pair distances between atoms is performed for each of the images along the path. These pair distances yield target values for the initial path to match as closely as possible. In image $\kappa$, the interpolated distance between atoms $i$ and $j$ is $d_{ij}^{\kappa}$, and is given by

$$d_{ij}^{\kappa} = d_{ij}^{\alpha} + \frac{\kappa\left(d_{ij}^{\beta} - d_{ij}^{\alpha}\right)}{p}, \tag{3.87}$$

where for a given upper index ($\alpha$ or $\beta$), the distance between atoms $i$ and $j$ for a given atomic configuration is given by

$$d_{ij} = \sqrt{\sum_{\sigma}\left(r_{i,\sigma} - r_{j,\sigma}\right)^2}, \qquad \sigma = x, y, z. \tag{3.88}$$

The number of atomic degrees of freedom is $3N - 6$. The number of atomic pair distances is $N(N-1)/2$. Therefore, the number of atomic degrees of freedom is much less than the number of atomic pair distances. This means that the interpolated values of the atomic coordinates cannot rigorously satisfy the constraints. Therefore, a compromise must be made. For each image, one can define an objective function. This is done by summing the squared deviation of each pair distance from the target values. This function is given by $S_{\kappa}^{\mathrm{IDPP}}(r)$, and is given by

$$S_{\kappa}^{\mathrm{IDPP}}(r) = \sum_{i}^{N} \sum_{i>j}^{N} w(d_{ij}) \left( d_{ij}^{\kappa} - \sqrt{\sum_{\sigma} (r_{i,\sigma} - r_{j,\sigma})^2} \right)^2 . \tag{3.89}$$

In Eq. (3.89), $w(d_{ij})$ is a weighting function that is used in order to place more emphasis on the shorter interpolated distances. This weighting function is useful because the energy of an atomic systems strongly increases when two atoms come close together. In image $\kappa$, the force that acts on atom $I$ is given by

$$F_i^{\kappa}(r) = -\nabla_i S_{\kappa}^{\mathrm{IDPP}}(r). \tag{3.90}$$

After the application of the NEB optimization with all spring constants chosen to be equal, a path is obtained such that all the images are evenly distributed. This is known as the 'IDPP path'. The IDPP path approximation of the NEB usually requires much less computational iterations than for the MEP as approximated by using linear interpolation as the initial guess.

### 3.10.3: Calculating the Length of the Minimum Energy Path

The path length *s* of an MEP obtained from *N* images is given by

$$s = \sum_{\sigma=0}^{N} \sqrt{\sum_{I} \left(\mathbf{R}_I\,(\sigma+1) - \mathbf{R}_I\,(\sigma)\right)^2}\,. \tag{3.91}$$

In Eq. (3.91), the outer sum is over image $\sigma$, where $\sigma = 0$ and $\sigma = N + 1$ are the initial and final configurations, respectively. The inner sum is over atoms *I*, where $\mathbf{R}_I\,(\sigma)$ is the position vector of atom *I* in image $\sigma$. In general, this sum is over all atoms in the system. $\Delta D_{\text{mol}}$ is the corresponding path length when the inner sum is over all the atoms in the molecule. $\Delta D_{\text{H}}$ is the MEP length when only the H atom is included, for instance, in a hydrogen atom transfer reaction. This is given by

$$\Delta D_{\text{H}} = \sqrt{\left(\boldsymbol{R}_{\mathbf{H}}\,(N+1) - \boldsymbol{R}_{\text{H}}\,(0)\right)^2}. \tag{3.92}$$

Eqs. (3.91) and (3.92) are derived from calculating Euclidean distance in high-dimensional space.

### 3.10.4: Testing for Stable structures and Transition Structures

After carrying out an NEB calculation, it is necessary to access the accuracy of the calculated MEP. In the harmonic approximation outlined in Section 3.7, a stable structure will have no imaginary frequencies in the calculated modes of vibration.[51-52] The two endpoint structures of an NEB calculation should be stable structures. The transition structure to be assessed at the saddle point of an MEP is known as 'first order' if it has only one imaginary frequency in the calculated modes of vibration. [51-52] First order saddle points represent 'proper transition structures.' MEPs with first order saddle points (representing proper transition structures) are likely to be physically viable. In contrast, MEPs with higher order saddle points are likely to be unphysical.

## 3.11: References


[1] F. Giustino, *Materials Modelling using Density Functional Theory*, Oxford University Press, Oxford, 1st edn, 2014, Chapter 2, pp 19.

[2] M. Born and R. Oppenheimer, *Annalen der Physik*, 1927, **389**, 457, DOI: 10.1002/andp.19273892002.

[3] E. Schrödinger, *Annalen der Physik*, 1926, **385**, 437, DOI: 10.1002/andp.19263851302.

[4] P. Hohenberg and W. Kohn, *Phys. Rev.*, 1964, **136**, B864, DOI: 10.1103/PhysRev.136.B864.

[5] W. Kohn and L. J. Sham, *Phys. Rev.*, L. J. 1965, **140**, A1133, DOI: 10.1103/PhysRev.140.A1133.

[6] F. Giustino, *Materials Modelling using Density Functional Theory*, Oxford University Press, Oxford, 1st edn, 2014, Chapter 3, pp 19.

[7] P. Ehrenfest, *Z. Phys.*, 1927, **45**, 455, DOI: 10.1007/BF01329203.

[8] W. Pauli. *Handbuch der SPhysik*, 1933, Springer, Berlin, pp 83 – 272.

[9] H. Hellmann, *Einfuhrung in die Quantumchemie*, 1937, Franz Duetsche, Leipzig.

[10] R. P. Feynmann, *Phys. Rev.*, 1939, **56**, 340, DOI: 10.1103/PhysRev.56.340.

[11] F. Giustino, *Materials Modelling using Density Functional Theory*, Oxford University Press, Oxford, 1st edn, 2014, Chapter 4, pp 64.

[12] G. Kresse and J. Furthmüller,. *Phys. Rev. B: Condens. Matter Mater. Phys.*, 1996, **54**, 11169– 11186, DOI: 10.1103/PhysRevB.54.11169.

[13] J.M. Thijssen, *Computational Physics*, Cambridge University Press, Cambridge, 2000,

[14] W. H. Press and S. A. Teukolsky, *Numerical Recipes*, Cambridge University Press, Cambridge, 1992.

[15] M. T. Heath, *Scientific Computing: An introductory Survey*, McGraw-Hill, New York, 1997.

[16] P.E. Gill, W. Murray and M.H. Wright, *Practical Optimization*, Academic Press, London, EDITION, 1981.

[17] S. Bahn and K. Jacobson, *Computing in Science & Engineering*, 2002, **4**, 56 – 66. DOI: 10.1109/5992.998641.

[18] F. Bloch, *Z. Phys.*, 1929, **52**, 555, DOI: 10.1007/BF01339455.

[19] C. Kittel, *Introduction to solid state physics*, Wiley, New York, 5th edn, 1976.

[20] H. J. Monkhorst and J. D. Pack, *Phys. Rev. B*, 1976, **13**, 5188 – 5192, DOI: 10.1103/PhysRevB.13.5188.

[21] F. Giustino, *Materials Modelling using Density Functional Theory*, Oxford University Press, Oxford, 1st edn, 2014, Appendix E, pp 260.

[22] G. Kresse and D. Joubert, *Phys. Rev. B: Condens. Matter Mater. Phys.* 1999, **59**, 1758– 1775, DOI: 10.1103/PhysRevB.59.1758.

[23] J. Neugebauer and M. Scheffler, *Phys. Rev. B*, 1992, **46**, 16067-16080, DOI: 10.1103/PhysRevB.46.16067.

[24] L. Bengtsson, *Phys. Rev. B*, 1999, **59**, 12301-12304, DOI: 10.1103/PhysRevB.59.12301.

[25] M. Fuchs, M. Bockstedte, E. Pehlke, and M. Scheffler, *Phys. Rev. B*, 1998, **57**, 2134-2145, DOI: 10.1103/PhysRevB.57.2134.

[26] J. P. Perdew, K. Burke and M. Ernzerhof, *Phys. Rev. Lett.*, 1996, **77**, 3865, DOI: 10.1103/PhysRevLett.77.3865.

[27] B. Hammer, L. B. Hansen and J. K. Nørskov, *Phys. Rev. B*, 1999, **59**, 7413-7421, DOI: 10.1103/PhysRevB.59.7413.

[28] S. Grimme, *J. Comp. Chem.*, 2006, **27**, 1787, DOI: 10.1002/jcc.20495.

[29] M. Dion, H. Rydberg, E. Schröder, D. C. Langreth, and B. I. Lundqvist, *Phys. Rev. Lett.*, 2004, **92**, 246401-246404, DOI: 10.1103/PhysRevLett.92.246401.

[30] G. Roman-Pérez and J. M. Soler, *Phys. Rev. Lett*., 2009, **103**, 096102, DOI: 10.1103/PhysRevLett.103.096102.

[31] J. Klimes, D. R. Bowler and A. J. Michaelides, *Phys.: Condens. Matter*, 2010, **22**, 022201, DOI: 10.1088/0953-8984/22/2/022201.

[32] J. Klimes, D. R. Bowler and A. J. Michaelides, *Phys. Rev. B*, 2011, **83,** 195131, DOI: 10.1103/PhysRevB.83.195131.

[33] A.J.R. Hensley, K. Ghale, C. Rieg, T. Dang, E. Anderst, F. Studt, C. T. Campbell, J. McEwen, Y. Xu, *J. Phys. Chem. C.*, 2017, **121**, 9, 4937–4945, DOI: 10.1021/acs.jpcc.6b10187.

[34] L. Barbosa, P. Sautet, *J. Am. Chem. Soc*., 2001, **123**, 6639–6648, DOI: 10.1021/ja004336k.

[35] D. Woodruff, C.F. McConville, A.L.D. Kilcoyne, Th. Lindner, J. Somers, M. Somers, M. Surman, G. Paolucci and A. M. Bradshaw, *Surf. Sci.*, 1988, **201**, 228.

[36] M.D. Crapper, C.E. Riley and D.P. Woodruff, *Surf. Sci.*, 1987, **184**, 121.

[37] H. W. King, *Crystal structures and lattice parameters of allotropes of the elements*, in CRC Handbook of Chemistry and Physics, ed. W. M. Haynes, CRC Press, 97$^{th}$ edn, 2017, Chapter 12, pp 16.

[38] K. Berland and P. Hyldgaard, *Phys. Rev. B: Condens. Matter Mater. Phys.*, 2014, **89**, 035412, DOI: 10.1103/PhysRevB.89.03541.

[39] L. Gharaee, P. Erhart and P. Hyldgaard, *Phys. Rev. B*, 2017, **95**, 085147, 10.1103/PhysRevB.95.085147, DOI: 10.1103/PhysRevB.95.085147.

[40] M. Koch, M. Pagan, M. Persson, S. Gawinkowski, J. Waluk and T. Kumagai, *J. Am. Chem. Soc*., **139**, 12681–12687, 2017, DOI: 10.1021/jacs.7b06905

[41] T. Kumagai, J. N. Ladenthin, Y. Litman, M. Rossi, L. Grill, S. Gawinkowski, J.Waluk and M. Persson, *J. Chem. Phys.,* **148**, 102330, 2018, DOI: 10.1063/1.5004602.

[42] F. Giustino, *Materials Modelling using Density Functional Theory*, Oxford University Press, Oxford, 1st edn, 2014, Chapter 7, pp 106 – 112.

[43] F. Giustino, *Materials Modelling using Density Functional Theory*, Oxford University Press, Oxford, 1st edn, 2014, Chapter 8, pp 139.

[44] J. Tersoff and D. R. Hamann, *Phys. Rev. Lett.*, 1983, **50**, 1998 – 2001, DOI: 10.1103/PhysRevLett.50.1998.

[45] J. Tersoff and D. R. Hamann, *Phys. Rev. B*, 1985, **31**, 805 – 813, DOI: 10.1103/PhysRevB.31.805.

[46] J. Bardeen, *Phys. Rev. Lett.*, 1961, **6**, 57 – 59, DOI: 10.1103/PhysRevLett.6.57.

[47] C.J. Chen, *Phys. Rev. B*, 1990, **42**, 8841, DOI: 10.1103/PhysRevB.42.8841.

[48] C. J. Chen, *Phys. Rev. Lett.*, 1990, **65**, 448, DOI: 10.1103/PhysRevLett.65.448.

[49] W. Sacks and C. Noguera, *Journal of Vacuum Science & Technology B: Microelectronics and Nanometer Structures Processing, Measurement, and Phenomena*, (1991), **9**, 488-491, DOI: 10.1116/1.585552.

[50] N. Lorente and M. Persson, *Faraday Discuss.*, 2000, **117**, 277-290, DOI: 10.1039/B002826F.

[51] G. Henkelman, B. P. Uberuaga and H. A. Jónsson, *J. Chem. Phys.* 2000, **113**, 9901– 9904, DOI: 10.1063/1.1329672.

[52] S. Smidstrup, A. Pedersen, K. Stokbro and H. Jónsson, *J. Chem. Phys.* 2014, **140**, 214106, DOI: 10.1063/1.4878664.

# Chapter 4

# Insights into a Flipping Reaction of Adsorbed Formaldehyde on Cu(110)

## 4.1: Introduction

In this chapter, DFT calculations are applied in order to study the flipping of two mirror-reflected states of formaldehyde adsorbed on the Cu(110) surface.[1] This chapter serves as an extension to that which was already published in Ref. [1]. The motivation for this study was low temperature STM experiments that first observed this flipping reaction.[1] These experiments found that the flipping reaction was independent of temperature below 10 K. This indicated that quantum mechanical tunnelling governed the reaction. Although the entire formaldehyde molecule tunnelled between states during the reaction, we can refer to this as 'carbon tunnelling.' This is because the carbon atoms were displaced as much as the hydrogen atoms during the reaction (~1 Å), whereas the oxygen atom anchored the molecule to the surface. In other words, the dominant heavy-atom contribution to the tunnelling was from the carbon atom.

There has been much study into hydrogen atom tunnelling.[2-12] However, carbon atom tunnelling whilst studied in some depth,[13-28] is still much less understood. This original work concerning the flipping of formaldehyde on Cu(110)[1] provides another situation in which carbon atom tunnelling can be studied. This contributes towards an enhanced understanding of quantum tunnelling for heavier atoms. All theoretical calculations in this chapter were based on DFT. The details surrounding these calculations are covered in Section 4.2.

There was a previous DFT study of formaldehyde adsorption on Cu(110) by Sakong and Groß.[29] This study used the GGA approximation, with the use of the Perdew–Wang (PW91) functional.[30] This functional did not account for dispersion interactions, and this study predated the common use of van der Waals exchange-correlation functionals.

In contrast, the study outlined in this chapter and our previous publication[1] did account for dispersion interactions (see Section 4.2). In our earlier publication,[1] we used the same $\eta_1$ and $\eta_2$ notation as used by Sakong and Groß.[29] We also found a new stable species that we designated as $\eta_3$. However, our study differs somewhat from this early DFT study of this adsorption system. These comparisons are further discussed at relevant positions within the text.

## 4.2: Computational Details

Periodic DFT calculations were performed using version 5 of VASP.[31] The PAW method[32] was used to treat the electron-ion core interactions. The effects of exchange-correlation were handled by the vdW-DF-cx exchange-correlation functional[33-35] which includes van der Waals interactions. The plane cut-off energy was set at 400 eV. This value was found to be reasonable by convergence tests of the cut-off energy. For further details on this, refer to Appendix A, Section A1.

The gas phase formaldehyde molecule was modelled in a unit cell of size (11 × 11 × 11) Å$^3$. This cell was adequately sized in order to isolate each molecule from its periodic images due to the periodic boundary conditions. This cell was sampled with a (1 × 1 × 1) *k*-point mesh. The adsorbed formaldehyde molecule and the Cu(110) surface were represented in super cells using (2 × 3) and (4 × 6) surface unit cells, where the surface was represented by a Cu slab with five layers and a vacuum region of about 25 Å.

During the geometrical optimizations, the bottom two layers of the Cu slab were constrained at the calculated lattice constant of 3.579 Å.[36] These geometrical optimizations were performed until the ionic forces were less than 0.01 eV/ Å. Dipole corrections were applied in all calculations in order to decouple the dipole-dipole interactions between the periodic images of adsorbed formaldehyde structures in the perpendicular direction to the Cu(110) surface.

The larger (4 × 6) unit cell was used only for the purpose of simulating STM images in order to avoid overlapping images between neighbouring cells due to the periodic boundary conditions. The topographic STM images were simulated using the Tersoff-Hamann approximation at a constant LDOS.[37-38] For all other theoretical modelling of adsorbed formaldehyde, the (2 × 3) unit cell was used. The (2 × 3) and (4 × 6) unit cells are shown below in Fig. 4.1.

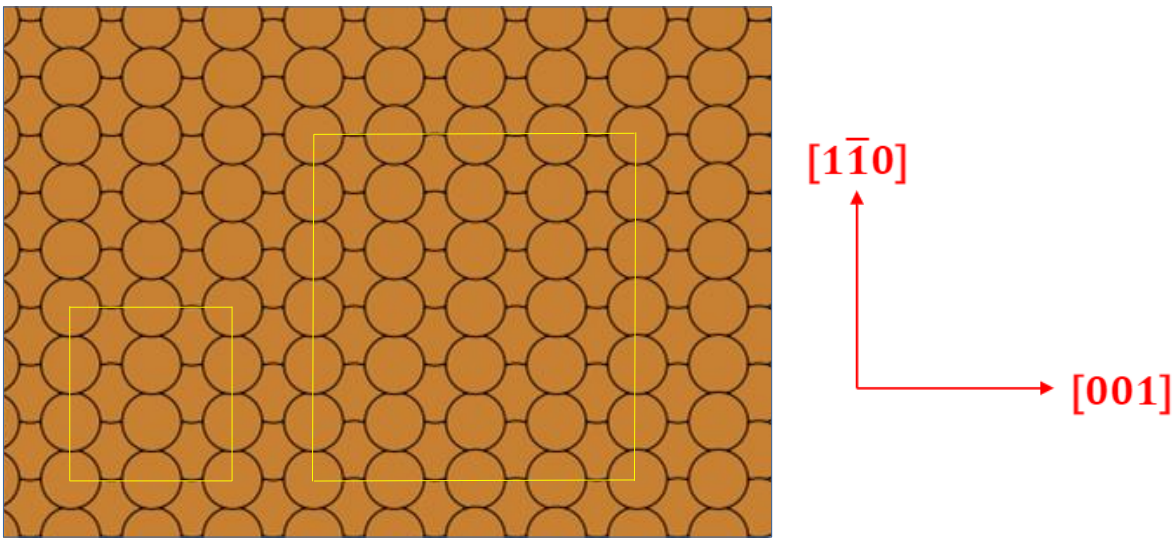


**Figure 4.1:** The (2 × 3) (LHS) and (4 × 6) unit cell (RHS) on the Cu(110) surface. The Cu(110) directional indices are shown by the red arrows.

The Brillouin zones of the (2 × 3) and (4 × 6) cells shown in Fig. 4.1 were sampled with (6 × 6 × 1) and (3 × 3 ×1) *k*-point meshes, respectively. The estimated error in $E_{ads}$ for this *k*-point sampling was found to be 0.01 eV, which is the estimated error in $E_{ads}$ for all results in this chapter. For further details on the convergence test for this, refer to Appendix A, Section A1. In contrast, the study by Sakong and Groß[29] mostly used a (2 × 2) surface unit cell with a vacuum region of 12 Å, a plane cut-off energy of 350 eV and a (16 × 16 × 1) Monkhorst-Pack *k*-point mesh. In their calculations, the Cu(110) slabs were five layers thick with uppermost two Cu layers fully optimized. The estimated precision of their results was also 0.01 eV. Their parameters are very different to those of our study, but they are mentioned here to provide some helpful background to the reader.

Now, we turn our attention back to the original work being described in this chapter. The molecule-surface bond was studied using the calculated partial density of states (PDOS) for the *d* waves of the coordinated Cu atom of the bare surface and the *p* waves of the C atom of the adsorbed and isolated formaldehyde molecule. The molecule-surface bond was studied using the calculated projected density of states (PDOS) on the HOMO and LUMO of the isolated formaldehyde molecule using the method described in Ref. [38].

The harmonic approximation was used to calculate the vibrational modes of each adsorbed formaldehyde configuration in order to determine a given structure's stability. The force constant matrix was generated from the calculated forces using finite differences where the displacement of the atoms was 0.02 Å. A structure was determined as stable if its vibrational modes contained only real frequencies. These frequencies were also used to calculate the zero-point energy (ZPE) corrections to the energy barriers.

The minimum energy paths (MEPs), the transition structure and associated potential energy barriers between a pair of equilibrium configurations were calculated using the nudged elastic band (NEB) method.[39-40] The image-dependent pair potentials (IDPP) algorithm[41] was used to set up the intermediate images between the pair of equilibrium structures. The images were geometrically optimized until the forces were less than 0.01 eV/ Å. A saddle point of a converged NEB calculation was determined as a proper transition structure if its vibrational modes contained only one imaginary frequency. This would mean that the associated MEP would be likely to be physically viable. Tunnelling rates and probabilities for each mirror-reflected adsorbed formaldehyde configuration were estimated by use of the WKB approximation along the MEP in isoinertial coordinates.

## 4.3: Results and Discussion

Firstly, the search for equilibrium structures of the adsorbed formaldehyde that are relevant for the observed flipping reaction are presented. Secondly, this is followed by a discussion of the nature of the molecule-surface bond based on the calculated projected density of electronic states (PDOS) of these structures. Thirdly, the simulated STM images of these structures are compared to the observed experimental images. Finally, calculated minimum energy paths (MEPs), energy barriers and transition structures are presented. The adsorption energy per molecule, $E_{ads,}$ is defined as the formation energy for the adsorption reaction,

$$CH_2O + Cu(110) \rightarrow CH_2O/Cu(110), \quad (4.1)$$

and is simply given by

$$E_{ads} = E[CH_2O/Cu(110)] - \{E[CH_2O] + E[Cu(110)]\}. \quad (4.2)$$

Here $E[CH_2O/Cu(110)]$, $E[CH_2O]$,and $E[Cu(110)]\}$ are the calculated total energies for the molecule adsorbed on the Cu(110) slab, the molecule in the gas phase and the bare Cu(110), respectively.

### 4.3.1: Molecule in the Gas Phase

The optimized gas phase structure of formaldehyde is shown below in Fig. 4.2.

(a) (b)

**Figure 4.2:** Top (a) and side view (b) of the optimized gas phase of formaldehyde.

In Fig. 4.2, the molecule is symmetrical about the C=O axis. The calculated C-H bond lengths are both 1.12 Å. The C=O bond length is 1.21 Å. These calculated bond lengths are in very good agreement with the experimental values given in Ref. [42]. In order to later discuss the molecule-surface bonding, we will now discuss the intramolecular bonding based on the character of the calculated molecular orbitals (MOs).

The C valence orbitals are found to form three $sp^2$ hybrids and a $p_z$ orbital perpendicular to the molecular plane (*xy*-plane). The lowest lying MO is predominantly an O 2s orbitals and the next two MOs are bonding C $sp^2$ orbitals with the two H 1s orbitals. The fourth MO is a bonding $\sigma$ MO formed between the remaining C $sp^2$ orbital and the O $p_y$ orbital along the molecular axis (*y*-axis). The fifth MO is a bonding $\pi$ MO formed between the C and O $p_z$ orbitals. The sixth MO is the highest occupied MO (HOMO) and is a non-bonding O $p_x$ orbital. Finally, the lowest unoccupied MO (LUMO) is an anti-bonding $\pi$ MO formed between the C and O $p_z$ orbitals.

### 4.3.2: Equilibrium Structures on Cu(110)

In order to identify the possible equilibrium structure behind the flipping reaction of the adsorbed formaldehyde molecule, an extensive search of possible equilibrium structures of the adsorbed molecule was carried out by using a more or less exhaustive set of initial configurations in the geometrical optimization.

The following four different adsorption sites for the O atom of the formaldehyde molecule were included: *hollow*, *top*, *short-bridge* (*SB*) and *long-bridge* (*LB*) sites. For a reminder of where these sites are located on the Cu(110) surface, refer to Chapter 1, Fig. 1.3(a).

The C=O molecular axis was tilted away from the surface normal along two different directions; one along the [100] direction and one where the projection of the molecular axis on the surface plane makes an angle of $45^0$ with respect to the [100] direction. This is illustrated further below in Fig. 4.3.

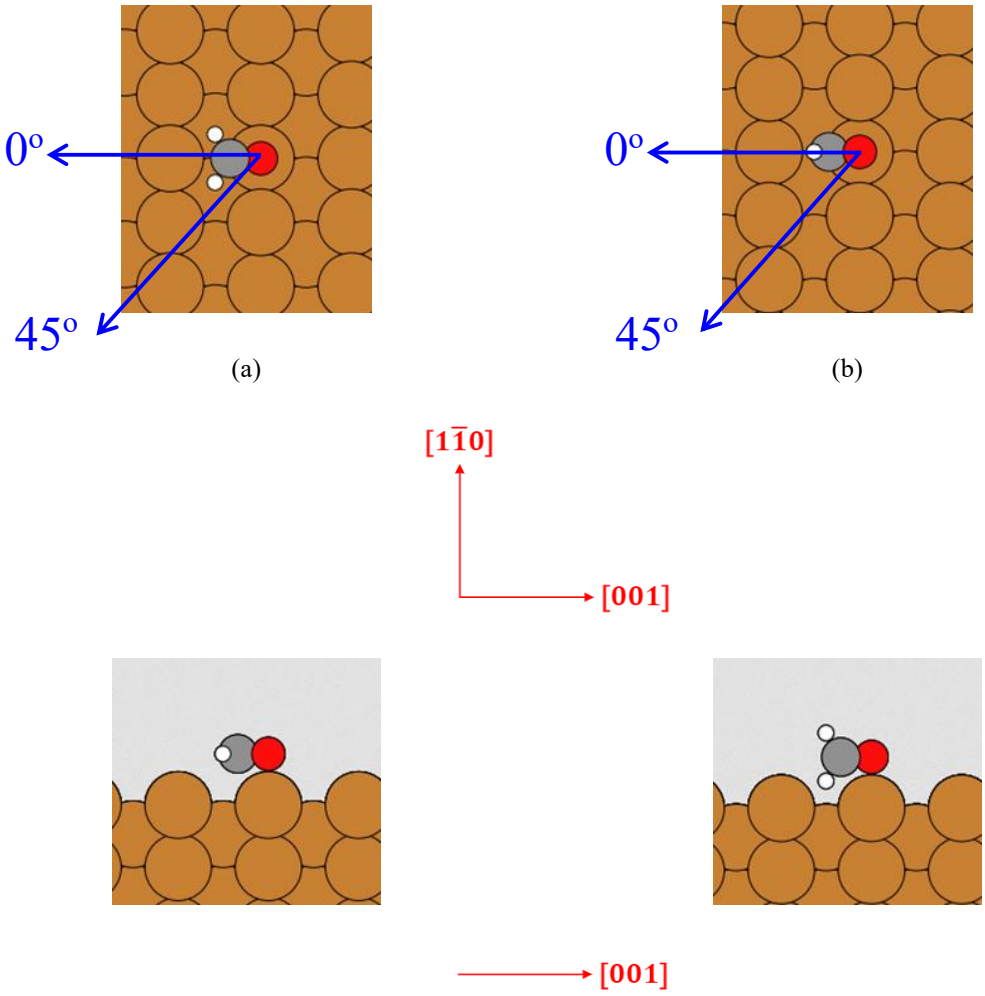


**Figure 4.3:** Shown in (a) and (b) are top views of a formaldehyde molecule with the O atom positioned above the top site of the Cu(110) surface, prior to DFT optimization. The H atoms of the molecule are either in the plane (a) or out of the plane spanned by the C=O molecular axis and the surface normal (b). In (a) and (b), the C=O molecular axes are aligned parallel to the [001] direction. This is referred to as the '0°' alignment, as indicated by the blue arrow in this direction. When the C=O axis rotated at '45° to the '0°' alignment, it is referred to the '45°' alignment. The Cu(110) crystallographic directional indices for the top and side views are shown with each schematic by the red arrows below (a – b) and (c – d), respectively.

The initial molecular configurations shown in Fig. 4.3 (a) and (c) is denoted by [*top*, 0°, in]. The configurations shown in Fig. 4.3 (b) and (d) is denoted by [*top*, 0°, out]. If these were in the '45°' instead of the '0°' alignment with respect to the Cu(110) surface, one would instead have signatures of [*top*, 45°, in] and [*top*, 45°, out], respectively.

The initial configurations are denoted in the following manner: the adsorption site, the angle $\phi$ (either 0° or 45°) and configuration of the hydrogen atoms (either in or out of plane). This resulted in 16 different initial configurations. The 16 initial configurations, as well as their resulting final structures and adsorption energetics are shown below in Table 4.1. All final configurations here denoted here as $\Lambda_i$. This designation includes both stable and unstable structures. The stables structures that were found and published in Ref. [1] were simply denoted by the $\eta_j$ signature, as per the previous study of this system by Sakong and Groß.[29] This is because the other $\Lambda_i$ structures did not need to be discussed in our publication, Ref. [1].

| **Initial Configuration** | **Final Configuration** | **$E_{ads}$ (eV)** | **Initial Configuration** | **Final Configuration** | **$E_{ads}$ (eV)** |
|---|---|---|---|---|---|
| **[*hollow*, 0°, in]** | $\Lambda_1$ ($\eta_2$) | -0.87 | **[*SB*, 0°, in]** | $\Lambda_1$ ($\eta_2$) | -0.87 |
| **[*hollow*, 45°, in]** | $\Lambda_1$ ($\eta_2$) | -0.87 | **[*SB*, 45°, in]** | $\Lambda_6$ ($\eta_3$) | -0.64 |
| **[*hollow*, 0°, out]** | $\Lambda_2$ | -0.34 | **[*SB*, 0°, out]** | $\Lambda_2$ | -0.34 |
| **[*hollow*, 45°, out]** | $\Lambda_1$ ($\eta_2$) | -0.87 | **[*SB*, 45°, out]** | $\Lambda_6$ ($\eta_3$) | -0.64 |
| **[*LB*, 0°, in]** | $\Lambda_3$ | -0.49 | **[*top*, 0°, in]** | $\Lambda_7$ | -0.42 |
| **[*LB*, 45°, in]** | $\Lambda_1$ ($\eta_2$) | -0.87 | **[*top*, 45°, in]** | $\Lambda_6$ ($\eta_3$) | -0.64 |
| **[*LB*, 0°, out]** | $\Lambda_4$ ($\eta_1$) | -0.52 | **[*top*, 0°, out]** | $\Lambda_4$ ($\eta_1$) | -0.52 |
| **[*LB*, 45°, out]** | $\Lambda_5$ | -0.52 | **[*top*, 45°, out]** | $\Lambda_4$ ($\eta_1$) | -0.52 |

**Table 4.1**: Initial configurations [site, $\phi$, H atom orientation] labelled alongside the final DFT relaxed configurations denoted by $\Lambda_i$. The stable final structures are labelled in red. In parentheses next to the $\Lambda_i$ signatures, are the corresponding $\eta_j$ configurations that were described in Ref. [1].

From Table 4.1, the only stable structures are $\Lambda_1(\eta_2)$, $\Lambda_4(\eta_1)$, $\Lambda_5$ and $\Lambda_6(\eta_3)$. Their stabilities were confirmed by their vibrational modes containing no imaginary frequencies. The $\Lambda_4(\eta_1)$ and $\Lambda_5$ structures have the same adsorption energy. Structurally they are very similar. They were found to be marginally stable, differing only in the very low energy vibrational modes of about 3-10 meV corresponding to a vibrational motion of the H atoms out of the plane spanned by the C=O molecular axis and the surface normal. The $\Lambda_4(\eta_1)$ and $\Lambda_5$ structures are compared further in Appendix A, Section A.2. There, it is shown that the potential energy surface is very shallow around $\Lambda_4$, although the time-averaged configuration will correspond to the $\Lambda_4(\eta_1)$ structure. From this point onwards in this chapter, only the stable $\eta_j$ configurations of Ref. [1] will be discussed. Therefore, the $\Lambda_i$ signature will be dropped as it is no longer needed. The $\eta_1$, $\eta_2$, and $\eta_3$ structures are shown below in Fig. 4.4.

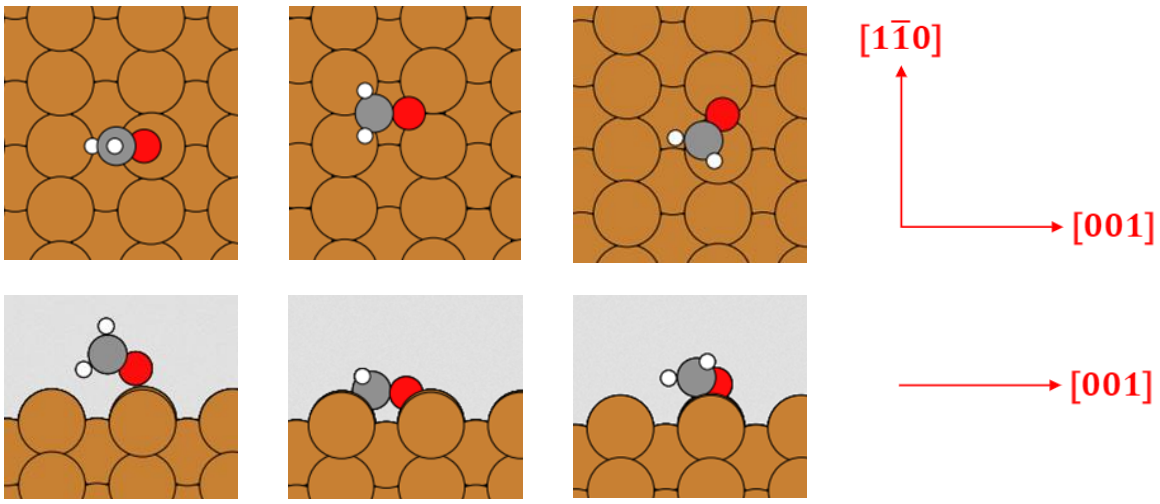


**Figure 4.4:** The top and side views of the DFT optimized $\eta_1$ (a), $\eta_2$ (b), and $\eta_3$ configuration (c), are shown on the top and bottom rows, respectively. The side views are as seen along the [1$\bar{1}$0] direction. The Cu(110) crystallographic directional indices are shown by the red arrows for the top and side views, along the top and bottom rows of the figure, respectively. $E_{ads}$ = -0.52 eV (-0.55 eV) ($\eta_1$), -0.87 eV (-0.93 eV) ($\eta_2$) and -0.64 eV (-0.66 eV) ($\eta_3$). The $E_{ads}$ values without parentheses were for optimizations in the (2 × 3) cell. The values with parentheses were for optimizations in the (4 × 6) cell.

The adsorption energetics of the stable structures of Fig. 4.4 are displayed below in Table 4.2, along with the ZPEs of their vibrational modes and the nearest neighbour distances between each molecular atom and the Cu(110) surface.

| **Structure** | $E_{ads}$ **(eV)** | **ZPE (eV)** | **C-Cu (Å)** | **H-Cu (Å)** | **O-Cu (Å)** |
|---|---|---|---|---|---|
| $\eta_2$ | -0.87 (-0.93) | 0.725 (0.726) | 2.17 (2.17) | 2.09 (2.10) | 2.00 (2.00) |
| $\eta_3$ | -0.64 (-0.66) | 0.738 (0.740) | 2.08 (2.08) | 2.62 (2.62) | 2.02 (2.02) |
| $\eta_1$ | -0.52 (-0.55) | 0.724 (0.728) | 2.95 (2.95) | 2.44 (2.50) | 2.06 (2.05) |

**Table 4.2**: $E_{ads}$ and ZPEs of the final stable equilibrium structures. These are listed along with the nearest neighbour C-Cu, H-Cu and O-Cu distances in the DFT optimized configurations. The structures are listed in order of increasing $E_{ads}$ (i.e. in order of decreasing structural stability). The values without parentheses were for optimizations in the (2 × 3) cell. The values with parentheses were for optimizations in the (4 × 6) cell.

As shown by the energetics in Table 4.2, $\eta_2$ has the strongest molecule-surface bond, whereas $\eta_1$ has the weakest molecule-surface bond. This behaviour is also reflected by their O-Cu distances, which increase with increasing $E_{ads}$, and the increasingly weaker molecule-surface bond. The rather small magnitudes of $E_{ads}$ below 1 eV show that the molecule-surface bond is weak, even for the $\eta_2$ structure. There is no other obvious trend between $E_{ads}$ and the other quantities listed in Table 4.2. The calculated C-H and C=O bond lengths within the molecule are listed for the three structures in Table 4.3.

| **Structure** | **C-H$^1$ (Å)** | **C-H$^2$ (Å)** | **C=O (Å)** |
|---|---|---|---|
| $\eta_2$ | 1.13 (1.12) | 1.13 (1.12) | 1.39 (1.39) |
| $\eta_3$ | 1.11 (1.11) | 1.11 (1.11) | 1.30 (1.31) |
| $\eta_1$ | 1.12 (1.12) | 1.11 (1.11) | 1.23 (1.23) |
| Gas Phase | 1.12 | 1.12 | 1.21 |

**Table 4.3**: C-H and C=O bond lengths of the final stable equilibrium structures. The C-H$^1$ and C-H$^2$ bond lengths are those corresponding to that the left- and right-most H atom for a configuration, as shown in Fig. 4.4. For the gas phase and $\eta_2$ structures, the C-H$^1$ and C-H$^2$ bond lengths are the same due to symmetry. The values without parentheses were for optimizations in the (2 × 3) cell. The values with parentheses were for optimizations in the (4 × 6) cell.

One can see from Table 4.3 that there are much larger changes in the C=O bond length than in the C-H bond length changes. The C=O bond length increases, which corresponds to a weakening of the C=O bond. The C=O bond is at its shortest in the gas phase. This behaviour reflects that an increase of the molecule-surface bonding is at the expense of the intramolecular C=O bond, and is a manifestation of the principle of the conservation of bond order.[43]

4.3.3: Calculated Projected Density of States

An analysis of the bonding of formaldehyde to the Cu(110) surface was done by calculating the projected density of states (PDOS) of the Kohn-Sham wavefunctions of the isolated formaldehyde adsorbate onto the adsorbate-surface system Kohn-Sham wavefunctions. The general method for this calculation was covered in Section 3.9. The calculated PDOS on the frontier orbitals of formaldehyde is shown below in Fig. 4.5 for the $\eta_1$, $\eta_2$ and $\eta_3$ structures.

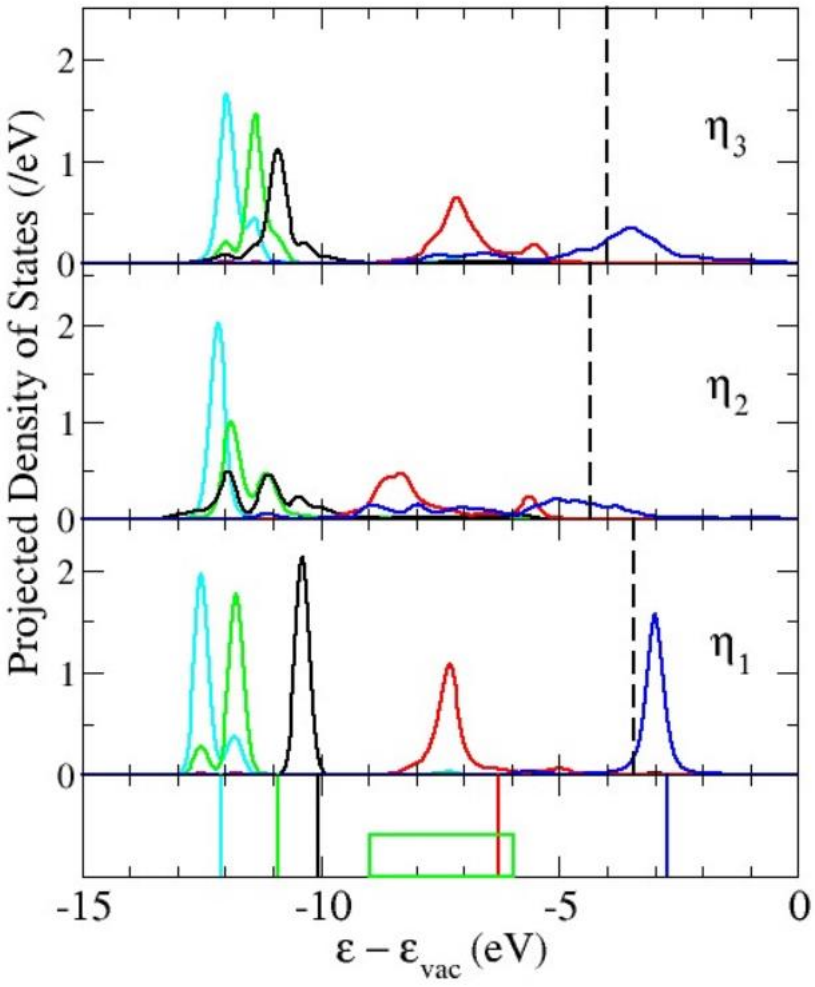


**Figure 4.5**. Calculated PDOS on the HOMO (red) and LUMO (dark blue) of formaldehyde for the $\eta_1$, $\eta_2$ and $\eta_3$ structures. The HOMO-1, HOMO-2 and HOMO-3 are shown in black, green and light blue, respectively. The vertical bars in the bottom panel are the PDOS for the gas phase. The energy range of the Cu d band is shown by the green rectangle in the bottom panel. The alignment of these plots is such that vacuum energy ($\varepsilon_{vac}$) set to zero in the lateral average electrostatic potential perpendicular to the surface. Fermi energies are indicated by vertical dashed lines. The broadening for the PDOS is 0.2 eV.

As discussed in Section 4.3.1, the HOMO is a non-bonding O $p_x$ orbital in the molecular plane and perpendicular to the molecular axis, while the LUMO is an anti-bonding π MO. As shown in Fig. 4.5, the HOMO and LUMO of $\eta_1$ is relatively weakly perturbed by their interaction with the Cu metal states. However, there is a notable downward energy shift of the HOMO, corresponding to the non-bonding O $p_x$ orbital, which a suggests the formation of a dative bond.

In contrast, the HOMO and the LUMO of the $\eta_2$ structure and the $\eta_3$ structure are interacting strongly with the Cu metal states. This interaction is much stronger for $\eta_2$ than for $\eta_3$. They show a large broadening and downward shift and the LUMO becomes partially occupied. Since the LUMO is an anti-bonding π MO, this results in an increase of the C-O bond length. The partial occupation of the LUMO is almost complete for $\eta_2$, while it is more or less singly occupied for $\eta_3$, and the corresponding C-O bond length is less extended than for $\eta_2$. The double-peaked structure of the PDOS on HOMO with a peak in the energy range of the Cu d band shows that HOMO mixes with the Cu d states, with this interaction being the strongest for $\eta_2$, and weakest for $\eta_1$.

Finally, the increase of the interaction of the frontier orbitals with $\eta_1$, $\eta_3$, and $\eta_2$ is reflected by the corresponding trend of the decrease of the adsorption energy. In order to make an assignment of the experimentally observed species to our calculated structures, we will now turn to our simulated topographical STM images, then make a comparison of these with original experimental STM images.

4.3.4: Simulation of STM Images and Comparison to Experiment

The simulated topographical STM images for the $\eta_1$, $\eta_2$ and $\eta_3$ structures are shown in Fig 4.6. A characteristic feature of all images is the pronounced protrusion centred more or less above the C atom. In contrast to the image of the $\eta_3$ structures, there is a depression on the O side in the images of the $\eta_2$ and $\eta_3$ structures.

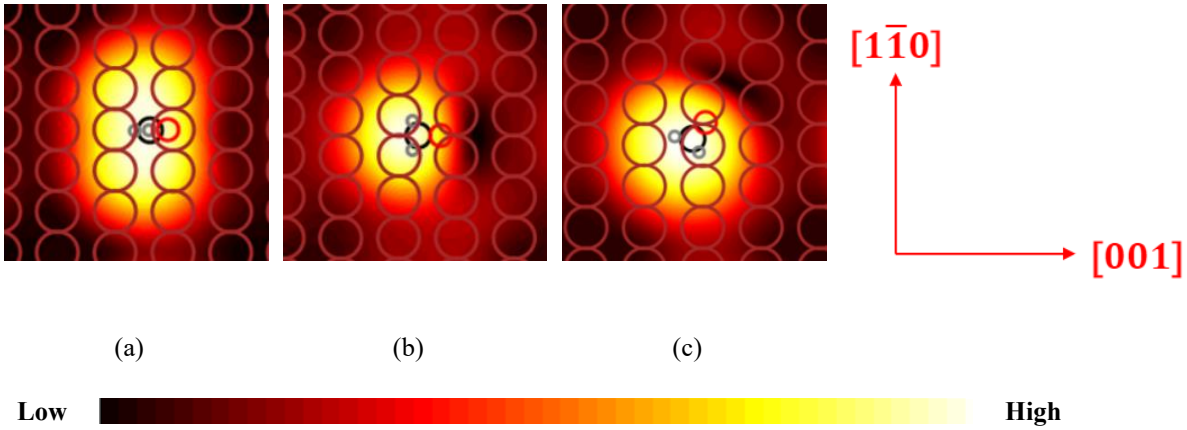


**Figure 4.6:** Simulated topographical STM images of the $\eta_1$ (a), $\eta_2$ (b), and $\eta_3$ structure (c) at a bias voltage of +10 mV. The average STM tip-surface distances are 10.0 Å (a), 7.5 Å (b) and 8.7 Å (c). The formaldehyde molecule and the top layer of the Cu(110) surface are superimposed upon each image. The brown, black, grey and red coloured circles represent the Cu, C, H and O atoms, respectively. The Cu(110) directional indices are shown by the red arrows. Shown at the bottom of the figure is a spectrum for the tip-surface distance. 'Low' means that the tip is close to the surface, and 'high' means that the tip is far from the surface.

The simulated STM images of Fig. 4.6 can now be compared to the experimental STM images of adsorbed formaldehyde shown below in Fig. 4.7. Three different structures $O_{pa}$, $P_{pd}$, and $O_{pb}$ of adsorbed formaldehyde were observed following dehydrogenation of an adsorbed methoxy molecule by inelastic electron tunnelling at 4.5 K. The images of $O_{pa}$ and $O_{pb}$ show both an oval protrusion and are very similar. They only differ by the protrusion of $O_{pa}$ is of lower apparent height than that of $O_{pb}$. Furthermore, only $O_{pb}$ among the observed structures shows a spontaneous flipping between two mirror-reflected configurations. In contrast, the image of $P_{pd}$ shows a pair of protrusion and depression. The resemblance of this image with the simulated image of $\eta_2$ structure suggests an assignment of $P_{pd}$ to the $\eta_2$ structure.

Furthermore, this assignment is corroborated by $\eta_2$ being the most stable structure, with $O_{pa}$ and $O_{pb}$ being kinetically stable at low temperatures. The images of $O_{pa}$ and $O_{pb}$ are consistent with the simulated images of the $\eta_1$ and $\eta_3$ structure but cannot be straightforwardly discriminated yet. This problem will be resolved in Section 4.3.5 from the calculation of energy barriers for the flipping of the molecule.

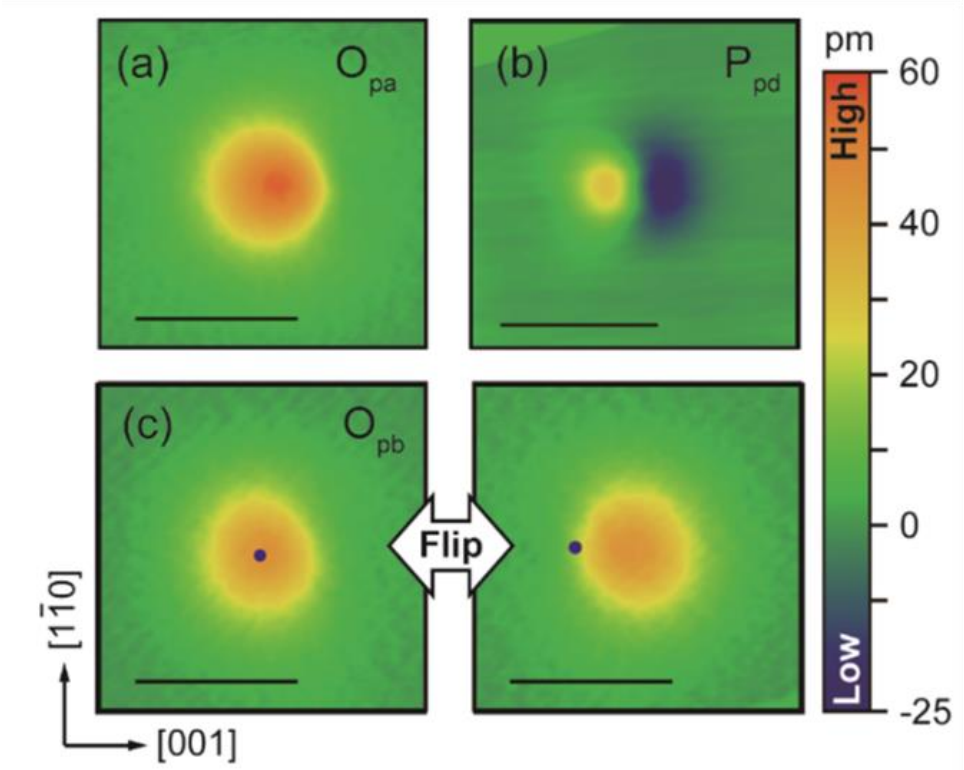


**Figure 4.7:** Experimental STM images of three different adsorption configurations $O_{pa}$ (a), $P_{pd}$ (b) and $O_{pb}$ (c). The two mirror-reflected configurations of formaldehyde on Cu(110) are for $O_{pb}$ in (c). The $P_{pd}$ and $O_{pb}$ species have been identified previously.[27] The scale bar (black horizontal line) in (a – c) is 1 nm. All images were obtained at the same bias voltage of +10 mV, at a temperature of 4.5 K.
(Figure taken from Ref. [1]).

4.3.5: The Energy Barriers between Mirror-Reflected Configurations

In this section, we present estimated tunnelling rates for the flipping reaction between each pair of mirror-reflected $\eta_1$ and $\eta_3$ structures based on calculated potential energy barriers for these reactions. These energy barriers were observed from the minimum energy path (MEP) for this reaction, which was found by application of the NEB method. The resulting MEPs are shown below in Fig. 4.8.

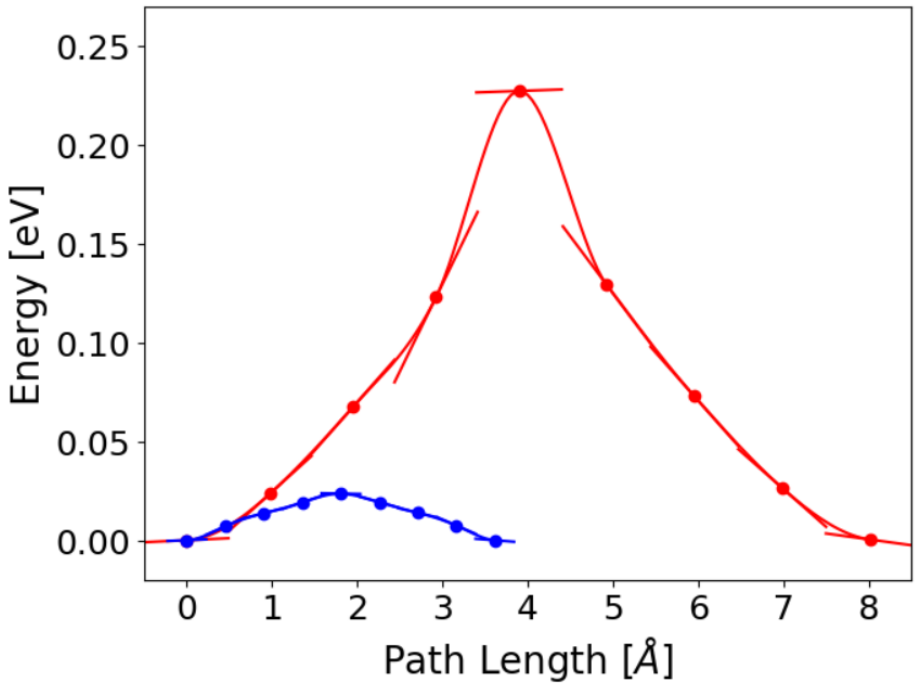


**Figure 4.8:** MEPs of the flipping reactions of the $\eta_1$ (red) and $\eta_3$ (blue) structures on the Cu(110) surface. The images and the calculated energy gradients along the MEP are indicated by solid circles and bars, respectively. In either calculated MEP, the mirror-reflected structures are represented by the left-most and right-most points. The transition structure of each MEP is shown by the saddle point in either graph. Both MEP lengths were calculated by use of Eq. (3.91) with atoms from the molecule and the two outermost Cu surface layers included.

As shown in Fig. 4.8, the calculated MEPs are symmetric around the saddle points. The flipping of the $\eta_1$ takes place in the molecular plane of the $\eta_1$ structure, whereas the flipping of the $\eta_3$ involves more or less a rotation around the surface normal.[1] The calculated vibrational modes of the saddle point for $\eta_1$ in Fig. 4.8 contained two modes with imaginary frequencies. Hence this not a proper transition structure. This means that the calculated MEP for the $\eta_1$ flipping is unlikely to be physically viable. In contrast, the calculated vibrational modes of the saddle point for $\eta_3$ in Fig. 4.8 contained only one mode with an imaginary frequency. Hence this is a proper transition structure. This means that the calculated MEP for the $\eta_3$ flipping is likely to be physically viable. These saddle points will be used to estimate the associated tunnelling probabilities.

There is an order of magnitude difference between the calculated barrier heights of about 227 and 24 meV for the flipping reactions of $\eta_1$ and $\eta_3$, respectively. Furthermore, the path length along the MEP between the two mirror-reflected configurations is about twice as large for $\eta_1$ than for $\eta_3$. These differences will have a large effect on the tunnelling rates for the two flipping reactions. The tunnelling rates, $R_t$, for the two flipping reactions were estimated from the MEPs in iso-inertial (mass-scaled) coordinates using the one-dimensional WKB approximation for the tunnelling probability $P_0$.

The mass-scaled position vector of atom $I$ with position vector $\mathbf{R}_I$ and mass $m_I$ is defined as $(m_H/m_I)^{1/2}\,\mathbf{R}_I$. In terms of the mass-scaled position vectors, the mass of the atoms in the kinetic energy will all be equal to the mass, $m_H$, of the hydrogen atom. The change in zero-point energies (ZPEs) between the equilibrium and the transition structures was included and resulted in an effective barrier height $D_{eff}$. $R_t$ was obtained from $P_0$ using the frequency of the vibrational mode in the equilibrium structure along the MEP as the attempt frequency. The resulting $D_{eff}$. $R_t$ and $P_0$ are shown in Table 4.4.

| Configuration | $D_{eff}$ (meV) | $\Delta s$ (Å) | $R_t$ ($s^{-1}$) | $P_0$ |
|---|---|---|---|---|
| $\eta_1$ | 214 (215) | 7.80 | $2.0 \times 10^{-56}$ ($2.0 \times 10^{-63}$) | $6 \times 10^{-70}$ ($5 \times 10^{-77}$) |
| $\eta_3$ | 20 (21) | 3.62 | $6.0 \times 10^{-2}$ ($1.5 \times 10^{-3}$) | $3 \times 10^{-14}$ ($8 \times 10^{-16}$) |

**Table 4.4:** MEP effective barrier heights ($D_{eff}$) and lengths ($\Delta s$) between the two mirror-reflected $\eta_1$ and $\eta_3$ configurations, and estimated tunnelling rates ($R_t$) and tunnelling probabilities ($P_0$) for the corresponding flipping reactions. Values for the deuterated formaldehyde species ($CD_2O$) are shown in parentheses. (Table taken from Ref. [1]).

As shown in Table 4.4, the ZPE correction on the barrier height is relatively small and $D_{eff}$ is still about 10 times larger for the flipping reaction of $\eta_1$ than for $\eta_3$. This large difference in barrier heights has a huge effect on $P_0$, being many orders of magnitude smaller for $\eta_1$ than for $\eta_3$. The resulting $R_t$ for $\eta_1$ is completely negligible. Hence tunnelling for the flipping reaction of $\eta_1$ can be ruled out.

In contrast, $R_t$ for $\eta_3$ is about the same order of magnitude as the observed temperature-independent rate of about $10^{-2}$ $s^{-1}$ below 10 K. Furthermore, the estimated $R_t$ for $CH_2O$ and $CD_2O$ give a kinetic isotope effect (KIE) of about 40. This is in reasonable agreement with the observed KIE of about 10, considering the simplicity of the approximation for $R_t$ and the limited accuracy of DFT calculations to describe potential energy barriers. Here, the KIE is primarily caused by the mass difference since the difference between $D_{eff}$ is small. Thus, these results give substantial support that $O_{pb}$, can be assigned to $\eta_3$.

## 4.4: Conclusion

A somewhat surprising result is the low symmetry of $\eta_3$ compared to the $\eta_1$ and $\eta_2$ structures. The magnitudes of the adsorption energies are relatively small, less than 1 eV and their magnitudes increase with the elongation of the C=O bond length. As mentioned in Section 6.1, in the previous study by Sakong and Groß,[29] three different adsorption geometries were identified. These included a physisorbed species with a large molecule-surface distance of about 3 Å, a slightly more strongly bound $\eta_1$ species with an adsorption energy of -0.21 eV and a more strongly bound $\eta_2$ species with an adsorption energy of -0.63 eV. In our study, no attempt was specifically made to study physisorbed species. This is because they do not form a directed bond with the surface atoms, and are expected to be highly mobile on the surface.

Our $\eta_2$ species has the same adsorption geometry as their $\eta_2$ species. In the case of their $\eta_1$ species, the adsorption geometry was not specified except for the adsorption site being the short-bridge site, which makes it difficult to make a definite correspondence to our $\eta_3$ species. No species corresponding to our $\eta_1$ structure was identified in their study. In our study, the most stable of the three $\eta_j$ structures was $\eta_2$.[1] The $\eta_2$ was assigned to the $P_{pd}$ by comparison of the simulated and experimental STM features. The fact that no flipping reaction occurs for $P_{pd}$ is consistent with the relatively large calculated adsorption energy of -0.87 eV for the $\eta_2$ structure.

Conversely, the experimental $O_{pa}$ and $O_{pb}$ species were difficult to assign to a simulated STM in a straightforward manner. However, analysis of the flipping mechanism of the mirror-reflected $\eta_1$ and $\eta_3$ configurations allowed identification of the $O_{pa}$ and $O_{pb}$ species. The MEP of $\eta_1$ was constrained in the symmetry plane spanned by the surface normal and the [001] direction. This reaction for $\eta_1$ occurred by means of a vertical wagging motion of the formaldehyde molecule. The MEP of $\eta_3$ occurred by means of an azimuthal rotation of the $CH_2$ group. The vibrational spectrum of the saddle point of the $\eta_3$ MEP had one imaginary frequency. Hence this could be assigned to a transition structure. The potential energy barrier of $\eta_3$ is just ~24 meV. This is about 10 times smaller than that for $\eta_1$.

When the change in ZPE of the real vibrational modes between the equilibrium and transition structure along the reaction coordinate of $\eta_3$ is included, the effective barrier becomes ~20 and ~21 meV for $CH_2O$ and $CD_2O$, respectively. The barrier is very small and allows for carbon tunnelling in the flipping direction. At the experimental temperature of 4.5 K, the thermal population of excited states was negligible for all vibrational modes. This is because all vibrational modes have energies greater than ~7 meV. One can see from Table 4.4 that tunnelling probability allows $\eta_3$ to undergo the flipping process. In the same way, one can see that the tunnelling probability for $\eta_1$ is completely negligible.

In summary of all these findings, the tunnelling species $O_{pb}$ was assigned to $\eta_3$, and $O_{pa}$ to $\eta_1$. In previously observed reactions involving carbon tunnelling, the carbon atom displacement was very small (~0.1 Å),[44] resulting in a very narrow barrier that permits tunnelling. For the case of the formaldehyde flipping in this work, the carbon displacement of approximately 1.1 Å between the two mirror-reflected states is significantly larger. However, the barrier is very small, which hence puts forward another interesting scenario for carbon tunnelling. The difference in tunnelling rate between $CH_2O$ and $CD_2O$ is mostly due to mass difference. This is because the effective barrier height difference is small in the WKB approximation.

## 4.5: References


[1] C. Lin, E Durant, M. Persson, M. Rossi and T. Kumagai, *J. Phys. Chem. Lett.*, 2019, **10**, 645-649, DOI: 10.1021/acs.jpclett.8b03806.

[2] R. P. Bell, *Proc. R. Soc. London, Ser. A*, 1933, **139**, 466– 474, DOI: 10.1098/rspa.1933.0031.

[3] R. Bell, *The Tunneling Effect in Chemistry*, Chapman and Hall: London and New York, 1980.

[4] J. T. Hynes, J. P. Klinman, H. Limbach and R. L. Schowen, *Hydrogen-Transfer Reactions*; Wiley-VCH, 2007.

[5] R. A. More O'Ferrall, *J. Phys. Org. Chem.*, 2010, **23**, 559, DOI: 10.1002/poc.1746.

[6] J. P. Klinman and A. Kohen, *Annu. Rev. Biochem.* 2013, **82**, 471– 496, DOI: 10.1146/annurev-biochem-051710-133623.

[7] L. J. Lauhon and W. Ho, *Phys. Rev. Lett.*, 2000, **85**, 4566– 4569, DOI: 10.1103/PhysRevLett.85.4566.

[8] T. Kumagai, M. Kaizu, S. Hatta, H. Okuyama, T. Aruga, I. Hamada and Y. Morikawa, *Phys. Rev. Lett.*, 2008, **100**, 166101– 166104, DOI: 10.1103/PhysRevLett.100.166101.

[9] X. Meng, J. Guo, J. Peng, J. Chen, Z. Wang, J-R. Shi, X-Z. Li, E-G. Wang and Y. Jiang, *Nat. Phys.*, 2015, **11**, 235– 239, DOI: 10.1038/nphys3225.

[10] M. Koch, M. Pagan, M. Persson, S. Gawinkowski, J. Waluk, and T, Kumagai, *J. Am. Chem. Soc.*, 2017, **139**, 12681– 12687, DOI: 10.1021/jacs.7b06905.

[11] T. Kumagai, J. N. Ladenthin, Y. Litman, M. Rossi, L. Grill, S. Gawinkowski, J. Waluk and M. Persson, *J. Chem. Phys.*, 2018, **148**, 102330, DOI: 10.1063/1.5004602.

[12] J. N. Ladenthin, T. Frederiksen, M. Persson, J. C. Sharp, S. Gawinkowski, J. Waluk and T. Kumagai, *Nat. Chem.*, 2016, **8**, 935– 940, DOI: 10.1038/nchem.2552.

ss[13] B. K. Carpenter, *J. Am. Chem. Soc.*, 1983, **105**, 1700– 1701, DOI: 10.1021/ja00344a073.

[14] A. M. Orendt, B. R. Arnold, J. G. Radziszewski, J. C. Facelli, K. D. Malsch, H. Strub, D. M Grant, D. M. and J. Michl, *J. Am. Chem. Soc.*, 1988, **110**, 2648– 2650, DOI: 10.1021/ja00216a049.

[15] R. Lefebvre and N. Moiseyev, *J. Am. Chem. Soc.*, 1990, **112**, 5052– 5054, DOI: 10.1021/ja00169a008.

[16] P. S. Zuev, R. S. Sheridan, T. V. Albu, D. G. Truhlar, D. A. Hrovat and W. T. Borden, *Science*, 2003, **299**, 867– 870, DOI: 10.1126/science.1079294.

[17] H. Sekiya, Y. Nagashima, T. Tsuji, Y. Nishimura, A. Mori, and H. Takeshita, *J. Phys. Chem.* 1991, **95**, 10311– 10317, DOI: 10.1021/j100178a015.

[18] R. L. Redington, T. E. Redington, T. A. Blake, R. L. Sams and T. J. Johnson, *J. Chem. Phys.*, 2005, **122**, 224311, DOI: 10.1063/1.1897367.

[19] H. Inui, K. Sawada, S. Oishi, K. Ushida and R. J. McMahon, *J. Am. Chem. Soc.* 2013, **135**, 10246– 10249, DOI: 10.1021/ja404172s.

[20] M. Ertelt, D. A. Hrovat, W. T. Borden and W. Sander, *Chem. – Eur. J.*, 2014, **20**, 4713– 4720, DOI: 10.1002/chem.201303792.

[21] T. Schleif, J. Mieres-Perez, S. Henkel, M. Ertelt, W. T. Borden and W. Sander, *Angew. Chem., Int. Ed.*, 2017, **56**, 10746– 10749, DOI: 10.1002/anie.201704787.

[22] M. J. Vetticatt and D. A. Singleton, *Org. Lett.*, 2012, **14**, 2370– 2373, DOI: 10.1021/ol300789a.

[23] C. Doubleday, R. Armas, D. Walker, C. V. Cosgriff and E. M. Greer, *Angew. Chem., Int. Ed.*, 2017, **56**, 13099– 13102, DOI: 10.1002/anie.201708489.

[24] A. J. Heinrich, C. P. Lutz, J. A.; Gupta and D. M. Eigler, *Science*, 2002, **298**, 1381– 1387, DOI: 10.1126/science.1076768.

[25] J. Repp, G. Meyer, K. H. Rieder and P. Hyldgaard, *Phys. Rev. Lett.*, 2003, **91**, 206102, DOI: 10.1103/PhysRevLett.91.206102.

[26] J. A. Stroscio and R. J. Celotta, *Science*, 2004, **306**, 242– 247, DOI: 10.1126/science.1102370.

[27] C. Nacci, S. Fölsch, K. Zenichowski, J. Dokić, T. Klamroth and P. Saalfrank, *Nano Lett.*, 2009, **9**, 2996– 3000, DOI: 10.1021/nl901419g.

[28] Y. Kitaguchi, A. Shiotari, H. Okuyama, S. Hatta, and T. Aruga, *J. Chem. Phys.*, 2011, **134**, 174703, DOI: 10.1063/1.3589256, DOI: 10.1063/1.3589256.

[29] S. Sakong, and A. Groß, *J. Catal.*, 2005, **231**, 420– 429, DOI: 10.1016/j.jcat.2005.02.009.

[30] J.P. Perdew, J.A. Chevary, S.H. Vosko, K.A. Jackson, M.R. Pederson, D.J. Singh ad C. Fiolhais, *Phys. Rev. B*, 1992, **46**, 6671, DOI: 10.1103/PhysRevB.46.6671.

[31] G. Kresse and J. Furthmüller,. *Phys. Rev. B: Condens. Matter Mater. Phys.*, 1996, **54**, 11169– 11186, DOI: 10.1103/PhysRevB.54.11169.

[32] G. Kresse and D. Joubert, *Phys. Rev. B: Condens. Matter Mater. Phys.* 1999, **59**, 1758– 1775, DOI: 10.1103/PhysRevB.59.1758.

[33] M. Dion, H. Rydberg, E. Schröder, D. C. Langreth, and B. I. Lundqvist, *Phys. Rev. Lett.*, 2004, **92**, 246401-246404, DOI: 10.1103/PhysRevLett.92.246401.

[34] G. Roman-Pérez and J. M. Soler, *Phys. Rev. Lett*., 2009, **103**, 096102,

DOI: 10.1103/PhysRevLett.103.096102.

[35] K. Berland and P. Hyldgaard, *Phys. Rev. B: Condens. Matter Mater. Phys.*, 2014, **89**, 035412,

DOI: 10.1103/PhysRevB.89.035412.

[36] L. Gharaee, P. Erhart and P. Hyldgaard, *Phys. Rev. B*, 2017, **95**, 085147, 10.1103/PhysRevB.95.085147,

DOI: 10.1103/PhysRevB.95.085147.

[37] J. Tersoff and D. R. Hamann, *Phys. Rev. Lett.*, 1983, **50**, 1998 – 2001, DOI: 10.1103/PhysRevLett.50.1998.

[38] N. Lorente and M. Persson, *Faraday Discuss.*, 2000, **117**, 277-290, DOI: 10.1039/B002826F.

[39] G. Mills, H. Jónsson and G. K. Schenter, *Surf. Sci.*, 1995, **324**, 305– 337,

DOI: 10.1016/0039-6028(94)00731-4.

[40] G. Henkelman, B. P. Uberuaga and H. A. Jónsson, *J. Chem. Phys.*, 2000, **113**, 9901– 9904,

DOI: 10.1063/1.1329672.

[41] S. Smidstrup, A. Pedersen, K. Stokbro and H. Jónsson, *J. Chem. Phys.*, 2014, **140**, 214106,

DOI: 10.1063/1.4878664.

[42] L.V. Gurvich, I. V. Veyts, and C. B. Alcock, Thermodynamic Properties of Individual Substances, Fourth Edition, Hemisphere Pub. Co., New York, 1989.

[43] E. Shustorovich, The Bond-Order Conservation Approach to Chemisorption and Heterogeneous Catalysis: Applications and Implications, *Advances in Catalysis*, 1990, **37**, 101-163,

DOI: 10.1016/S0360-0564(08)60364-8.

[44] W. T. Borden, *WIREs Comput. Mol. Sci.*, 2016, **6**, 20– 46, DOI: 10.1002/wcms.1235.

# Chapter 5

# Chiral Separation of Racemic Flurbiprofen on Cu(110)

## 5.1: Introduction

This chapter covers our DFT study of the adsorption of the chiral pharmaceutical flurbiprofen (FBF) on the Cu(110) surface This study was motivated by the recent surface science experiments of this system by the group headed by R. Raval at the University of Liverpool. They found some very interesting chiral behavior of this system that needs to be explained using DFT calculations. FBF is a non-steroidal anti-inflammatory drug (NSAID) used to treat several conditions related to fever, inflammation, pain and stiffness. In such treatments, the *S* enantiomer is some thousand times more active than the *R* enantiomer.[1] Studies have shown that unlike many other profens (including ibuprofen), *R*-FBF hardly inverts to *S*-FBF in humans.[2] Hence, it would be very beneficial to reduce the cost of separating both *R*- and *S*-FBF from the racemic (*RS*) mixture, which is the usual product of industrial synthesis.

There has been a great research effort towards separating racemic compounds into their pure enantiomers. This is most important for pharmaceutical compounds, where following the thalidomide tragedy, legislation has resulted in some 75% of new drugs going to market as single enantiomers.[3-6] It is possible to produce single enantiomers by the introduction of a chiral centre during some stage of the synthesis or by separation of racemic compounds. In the latter case, one of the most effective methods is the preferential crystallization of one enantiomer over the other. This method is only applicable to molecules that form conglomerates (a mixture of homochiral crystallites). Unfortunately, few chiral compounds do this.

However, surface science methods, and particularly scanning tunnelling microscopy (STM), have been extensively used for studying chiral molecules on surfaces.[7-15] Using STM, the Raval group at the University of Liverpool found that racemic FBF separates into enantiomerically pure islands on the Cu(110) surface. Each island contains two rotation domains, where the molecules in one domain are oriented at 180° with respect to those in the other domain. It is unusual that each enantiomerically pure island has only one rotation domain boundary. This observation raised questions as to how and why these boundaries form. We attempted to answer these questions by use of DFT calculations. It is well established from other studies that intermolecular interactions such as hydrogen bonding, steric repulsions and van der Waals interactions are important in controlling chiral assembly.[16-23] It has also been established from recent work that upon a surface, the footprints adopted by individual adsorbed molecules play a crucial role in the determination of the organization of the adsorbed molecules.[24-26] For instance, in racemic systems containing an equal population left- and right-handed molecules, the adsorption footprints have a strong influence in determining whether the system would organize into an ordered heterochiral array, distinct homochiral domains segregated from each other, or as a solid solution with the enantiomers randomly arranged.[27-28] Now, we turn our attention back towards this new study of FBF adsorbed to the Cu(110) surface. Schematics of *R*- and *S*-FBF molecules are shown below in Fig. 5.1.

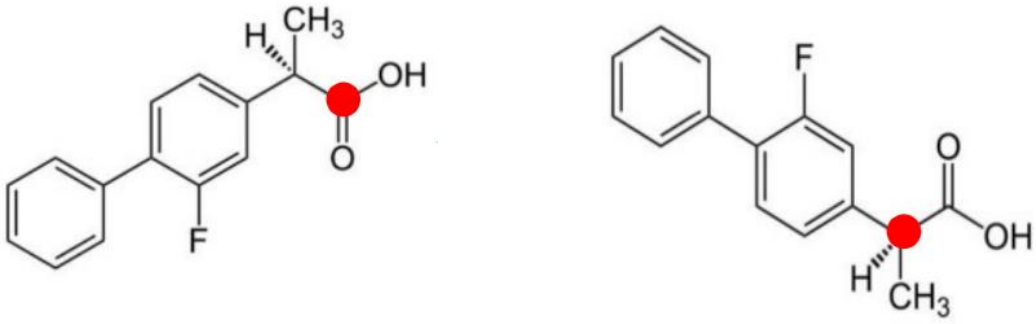


(a) (b)

**Figure 5.1:** Schematics of *trans*-*R*- (a) and *S*-FBF (b). The chiral centre is at the C-atom of each molecule which is shown by the red dots. (Structure schematics provided by C. L. Pang).

The enantiomers shown in Fig. 5.1 are in their *trans* configurations because the F atom and $CH_3$ group are on opposite sides of the molecule with respect to the phenyl rings. Conversely, the *cis* configurations have the F and $CH_3$ groups on the same side. Experimental reflection absorption infrared spectroscopy (RAIRS) indicated that the COOH group of the FBF molecule deprotonated to $COO^-$ upon adsorption to the Cu(110) surface (see Appendix B, Section B.3). The surface unit cells of the domains of monolayers of the FBF enantiomers were determined from low energy electron diffraction (LEED) and are shown in Fig. 5.2.

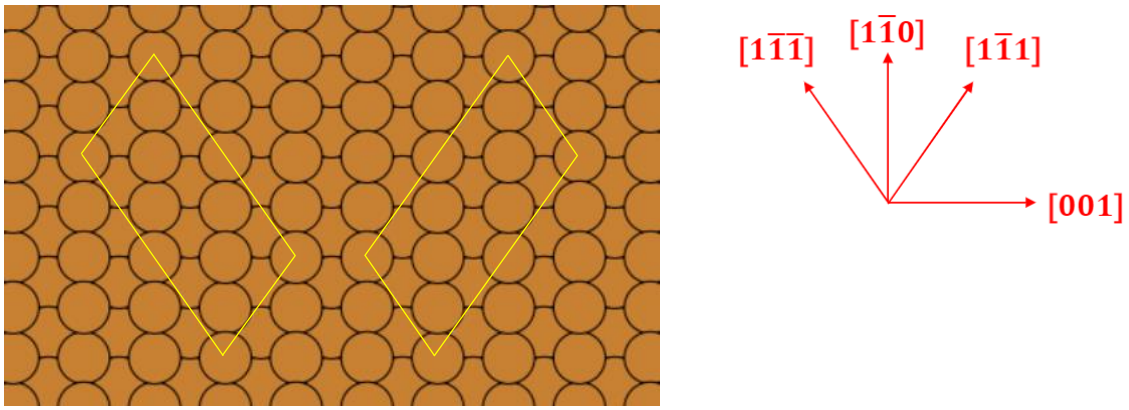


**Figure 5.2:** The surface unit cells of the monolayers of *R*- and *S*-FBF molecules on the Cu(110) surface. The unit cells on the left and righthand sides correspond to the *R*-and *S*-FBF monolayers, respectively. In matrix notation, these unit cells are denoted as '(1, 2; -2, 4)' and '(2, 4; -1, 2)', respectively. The Cu(110) crystallographic directional indices are shown by the red arrows.

It is evident from Fig 5.2 that the unit cells are simply related by a reflection through a line along the [1$\bar{1}$0] direction. The rest of this chapter is organized as follows. The details of density functional calculations are described in Section 5.2, The results and the discussions are presented in Section 5.3, which covers the molecule in the gas phase, monolayer adsorption of the *cis* and *trans* FBF enantiomers, which includes a study of the role of adsorbate-adsorbate versus adsorbate-substrate interactions in the formation of the monolayers. The nature of the formation of the rotation domain boundary is also presented in this section. Finally, the chapter finishes by concluding remarks in Section 5.4.

## 5.2: Computational Details

The geometric structures and the total energies of FBF adsorbed on the Cu(110) surface, were calculated with DFT using the version 5 of VASP.[29] These calculations were performed with the optB86b-vdW exchange-correlation functional[30-31] to include van der Waals interactions. The PAW method was used to treat the electron-ion core interactions.[32] The Cu(110) surface was approximated by a supercell of four Cu layers with atoms in the bottom two layers fixed at the calculated lattice constant of 3.60 Å. A vacuum region of 30 Å was used between the Cu(110) supercells. The cut-off energy was set at 400 eV. The convergence testing with respect to cut-off energy, is shown in Appendix B, Subsection B.1.2. Dipole corrections perpendicular to the Cu(110) surface were applied in all DFT calculations in order to sufficiently decouple periodic images of adsorbed structures of FBF in the surface unit cells. The adsorption energy per molecule, $E_{\text{ads}}$, of $n$ FBF molecules within a surface cell is here defined as the formation energy of the adsorption reaction,

$$n\text{FBF} + \text{Cu}(110) \rightarrow n\text{FBF}(-\text{H})^{*}/\text{Cu}(110) + \frac{1}{2}n\text{H}_2\,, \tag{5.1}$$

as,

$$nE_{\text{ads}} = E[n\text{FBF}(-\text{H})^{*}/\text{Cu}(110)] + \frac{n}{2}E[\text{H}_2] - \{nE[\text{FBF}] + E[\text{Cu}(110)]\}. \tag{5.2}$$

Here, $E[n\text{FBF}(-\text{H})^{*}/\text{Cu}(110)]$, $E[\text{H}_2]$, $E[\text{FBF}]$ and $E[\text{Cu}(110)]$ are the total energies of the adsorbed deprotonated molecules on the Cu slab, $H_2$ and FBF in the gas-phase, and the bare Cu(110) slab, respectively. The FBF and $H_2$ molecules in the gas phase were modelled in supercells of sizes (25 × 25 × 25) Å$^3$ and (11 × 11 × 11) Å$^3$, respectively. Each supercell was sampled with a (1 × 1 × 1) *k*-point mesh. Due to the reflectional symmetry between the *R*- and *S*-FBF enantiomers, and between their associated unit cells in Fig. 5.2., it was possible to arbitrarily choose either unit cell for the modelling of the monolayer adsorption scenarios. The (2, 4; -1, 2) cell (corresponding to *S*-FBF adsorption) in Fig. 5.2 was chosen arbitrarily for this purpose. This unit cell will henceforth be referred to as either the '(1 × 1)' or the '*S*-(1 × 1)' cell. The (1, 2; -2, 4) unit cell (corresponding to *R*-FBF adsorption) was not used in any of the modelling described in this chapter.

The Brillouin zone of the *S*-(1 × 1) cell was sampled with a (3 × 6 × 1) *k*-point mesh. Two larger unit cells were also required to separate periodic images in order to model the adsorption behaviour at the rotation domain boundary. The first of these cells is denoted as the '(3 × 1)' cell, since it is the *S*-(1 × 1) cell extended by a factor of 3 in the $[1\bar{1}\bar{1}]$ direction. The second is denoted as the '(3 × 2)' cell, since it is this (1 × 1) cell extended by a factor of 3 in the $[1\bar{1}\bar{1}]$ direction, and a factor of 2 in the $[1\bar{1}1]$ direction. The (3 × 1) and (3 × 2) cells are shown below in Fig. 5.3 below, along with the (1 × 1) cell for comparison.

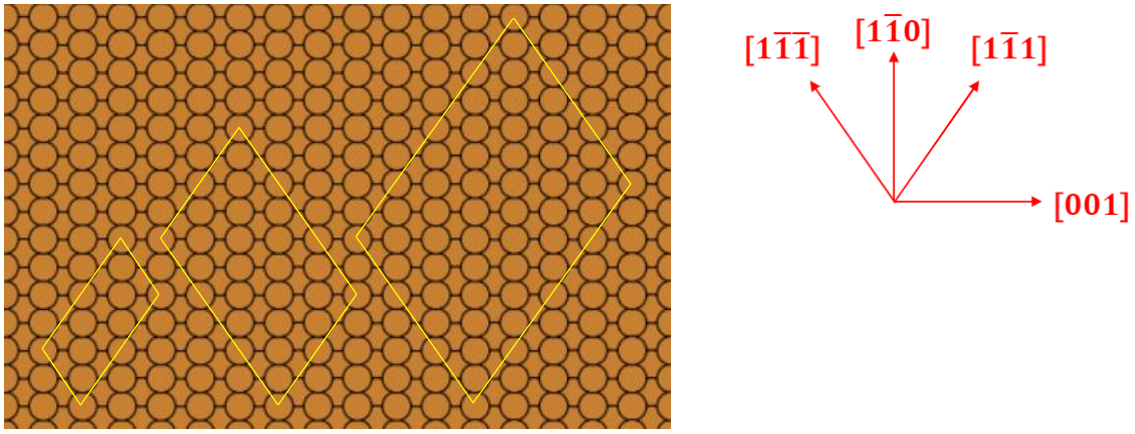


**Figure 5.3:** The (1 × 1) (left), (3 × 1) (middle) and (3 × 2) unit cell (right) on the Cu(110) surface. The Cu(110) crystallographic directional indices are shown by the red arrows.

The Brillouin zones of the (3 × 1) and (3 × 2) cells of Fig.5.3 were sampled with (3 × 2 × 1) and (5 × 5 × 1) *k*-point meshes, respectively. Some of the $E_{ads}$ differences were small in the (3 × 2) cell which was used to investigate different coverages of FBF on the Cu(110) surface. Therefore, more *k*-points were used for the (3 × 2) cell due to the higher precision required to investigate these small energy differences.

The estimated error in $E_{ads}$ for both the (1 × 1) and (3 × 1) cells was 0.02 eV. The (3 × 1) cell was sampled with the (3 × 2 × 1) *k*-point mesh so that the Brillouin zone of the (3 × 1) cell was sampled with the same the *k*-point density as for the (1 × 1) cell, namely $(108/A_{BZ})$ Å$^2$ where $A_{BZ}$ is the area of the surface Brillouin zone of the unit cell. The estimated error in $E_{ads}$ for the (3 × 2) cell was 0.01 eV. For the convergence testing with respect to *k*-points, refer to Appendix B, Subsection B.1.1. The topographic STM images were simulated using the Tersoff-Hamann approximation at a constant LDOS.[33-34]

## 5.3: Results and Discussion

### 5.3.1: Molecule in the Gas Phase

The optimised geometric structure of the *cis*- and *trans*-FBF molecules in the gas phase for the *S* enantiomer are shown below in Fig. 5.4. The *cis* structure was found to be marginally more stable than the *trans* structure by 3 meV.

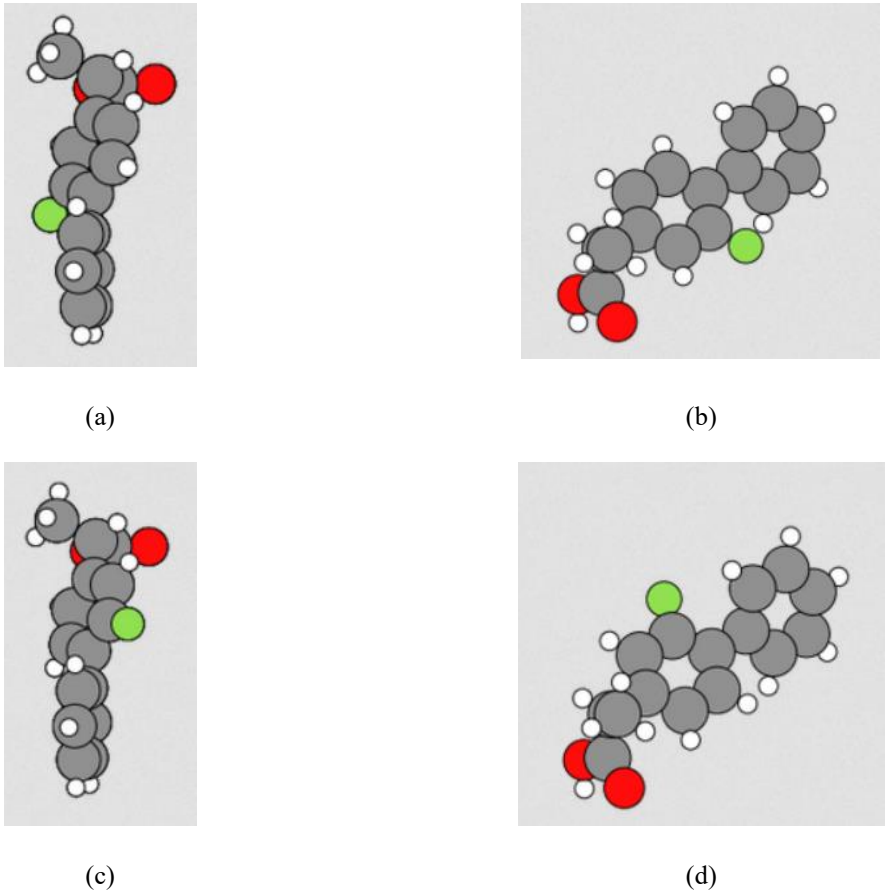

(a) (b)

(c) (d)

**Figure 5.4:** Calculated equilibrium structure of *cis*- and *trans*-*S*-FBF molecules in the gas phase. Shown in (a) and (b) are the top and side views, respectively, of *cis*-*S*-FBF. Shown in (c) and (d) are the top and side views, respectively, of *trans*-*S*-FBF. The carbon, fluorine, hydrogen and oxygen atoms are shown in dark grey, green, white and red, respectively. The *cis*-*S*-FBF was more stable than the *trans*-*S*-FBF by $\Delta E = 3$ meV.

One can see from Fig. 5.4 that the value of $\Delta E = 3$ meV means that the *cis* and *trans* gas phases are almost degenerate. Next, we turn to the adsorption of FBF within a rotation domain, i.e. within a monolayer either side of the rotation domain boundary.

5.3.2: Monolayer Adsorption of *cis*- and *trans*-*S*-FBF

We begin by presenting our study of the adsorption of *cis*-*S*-FBF in the (1 × 1) unit cell. The initial configuration for the geometrical optimization is shown below in Fig. 5.5 (a). The resulting optimized structure is shown in Fig. 5.5 (b) with an adsorption energy, $E_{ads}$ = -3.08 eV. This structure will be denoted as [*S*, *cis*, monolayer, original].

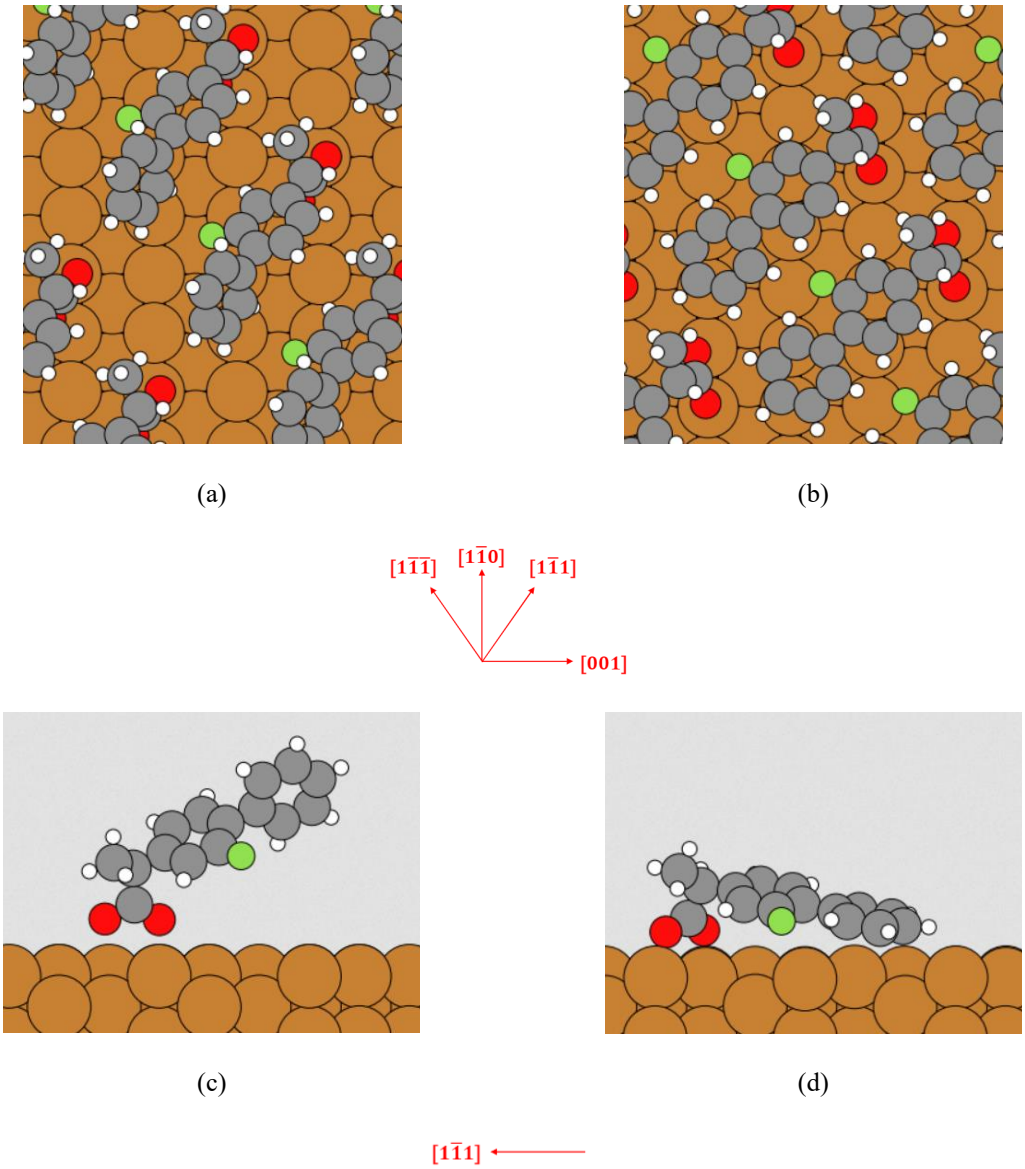


**Figure 5.5:** Shown in (a) and (b) are the top views of the non-optimized and optimized configurations of [*S*, *cis*, monolayer, original]. The side views in (c) and (d) correspond to (a) and (b), respectively. The Cu(110) crystallographic directional indices are shown by the red arrows below the top and side views. $E_{ads}$ = -3.08 eV.

In order to explore the potential energy surface further, the geometrical optimizations of initial configurations were obtained by rigidly rotating the molecule in the [*S*, *cis*, monolayer, original] configuration, in the surface plane by intervals of 10º from 0º to 360º. This procedure is illustrated below in Fig. 5.6.

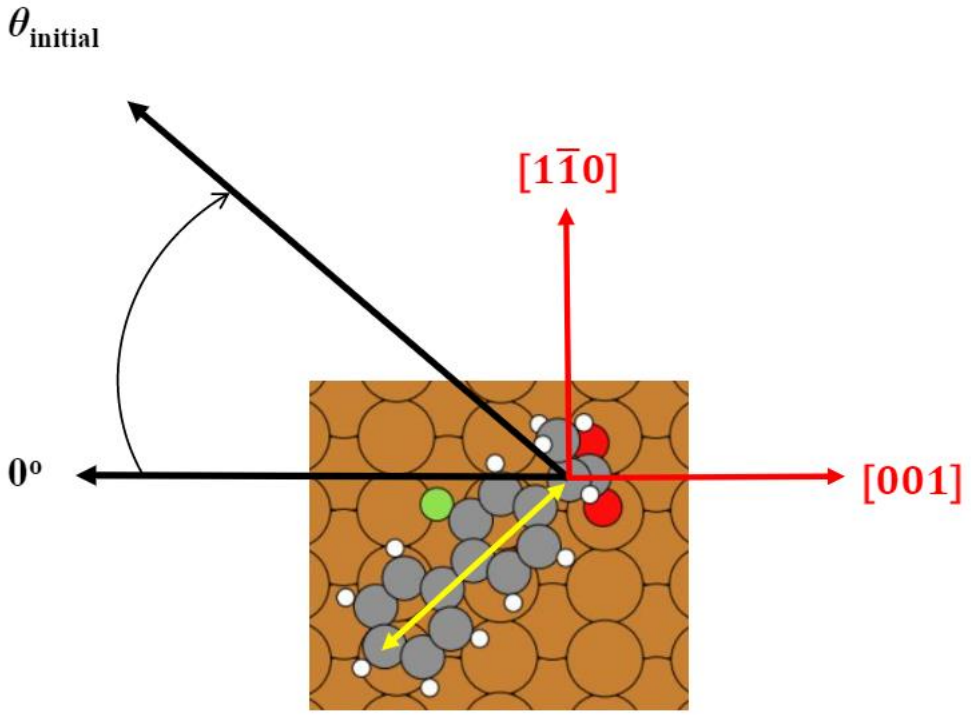


**Figure 5.6:** FBF molecule in the [*S*, *cis*, monolayer, original] configuration and the definition of the angle of orientation. The orientation of the molecule is given by the 'spine' of the molecule as defined by the double-arrowed yellow line. These arrows point from the carbon atom defining the chiral centre of the molecule, to the carbon atom furthest away from this. This reference orientation of the molecule is indicated by the black arrow-line labelled by '0º'. The other black arrow-line represents an arbitrary orientation of the molecule, defined by its angle '$\theta_{initial}$.' The horizontal and vertical Cu(110) crystallographic directional indices are shown by the red arrows centred on the molecule's chiral centre.

With reference to Fig 5.6, the first step in making these molecular rotations was to rotate the molecular spine of the [*S*, *cis*, monolayer, original] structure about the surface normal passing through the chiral centre, until the spine was parallel with the '0°' orientation.

Secondly, initial configurations of the molecule for the geometrical optimizations were obtained by rotating the molecule in incremental steps of 10°. These configurations will henceforth be denoted as [*S*, *cis*, monolayer, $\theta_{initial}$], where $\theta_{initial}$ is the orientational angle of the rotated molecule. The resulting variation of the adsorption energies of the optimized structures with $\theta_{initial}$ is shown in Table 5.1.

| $\theta_{initial}^{(o)}$ | $E_{ads}$ (eV) | $\theta_{initial}^{(o)}$ | $E_{ads}$ (eV) |
|---|---|---|---|
| **0** | -2.56 | **110** | -3.00 |
| **-10** | -2.56 | **120** | -2.24 |
| **-20** | -2.48 | **130** | -2.25 |
| **-30** | -3.08 | **140** | -3.08 |
| **-40** | -3.08 | **150** | -3.08 |
| **-50** | -3.08 | **160** | -2.70 |
| **-60** | -3.08 | **170** | -2.70 |
| **-70** | -2.25 | **180** | -2.70 |
| | | **190** | -2.27 |

**Table 5.1:** Resulting adsorption energies $E_{ads}$ as obtained from geometrical optimization of the [*S*, *cis*, monolayer, $\theta_{initial}$] configurations. Energy values labelled in red correspond to the minimum value of $E_{ads}$.

Some of the chosen values for $\theta_{initial}$ resulted in initial configurations having overlapping atoms across the (1 × 1) unit cell boundaries. Such configurations with overlapping atoms are unphysical. Hence these configurations were not studied, and the corresponding values of $\theta_{initial}$ are missing from Table 5.1. All optimized structures of [*S*, *cis*, monolayer, $\theta_{initial}$] in Table 5.1 with $E_{ads}$ values in red, have structures and $E_{ads}$ values equivalent to [*S*, *cis*, monolayer, original]. This structure will henceforth be denoted as [*S*, *cis*, monolayer].

Next, we turn to presentation of our study of the adsorption of *trans*-*S*-FBF on Cu(110) in the (1 × 1) cell. An initial configuration of the adsorbed *trans*-*S*-FBF for the geometrical optimization was obtained by exchanging the positions of the F atom and the H atom on either side of the 'spine' of the [*S*, *cis*, monolayer] configuration, as shown in Fig. 5.7. The geometrical optimization of this initial configuration resulted in the structure shown in Fig. 5.8 with $E_{ads}$ = -3.22 eV and will henceforth be denoted as [*S*, *trans*, monolayer, original].

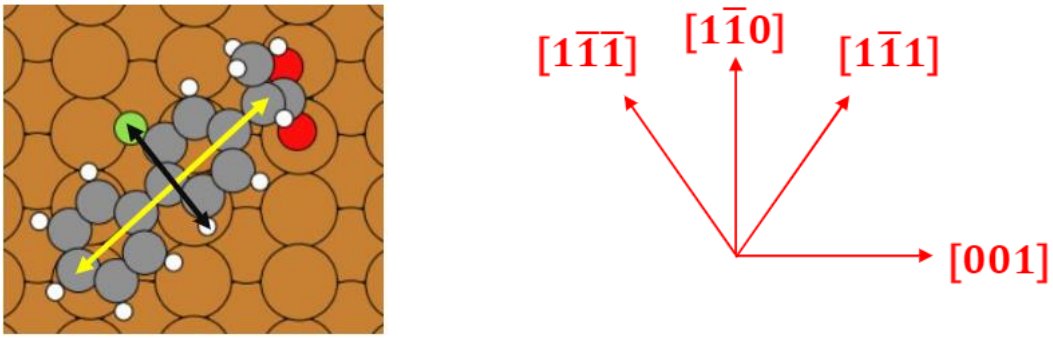


**Figure 5.7:** Construction of initial *trans* configuration from [*S*, *cis*, monolayer]. The spine of the molecule is shown as in Fig. 5.6. Exchanging the positions of the F and H atoms, as indicated by the black arrows, puts the F atom on the opposite side of the molecular spine, which changes the FBF molecule from a *cis*, to a *trans* configuration. The Cu(110) crystallographic directional indices are shown by the red arrows.

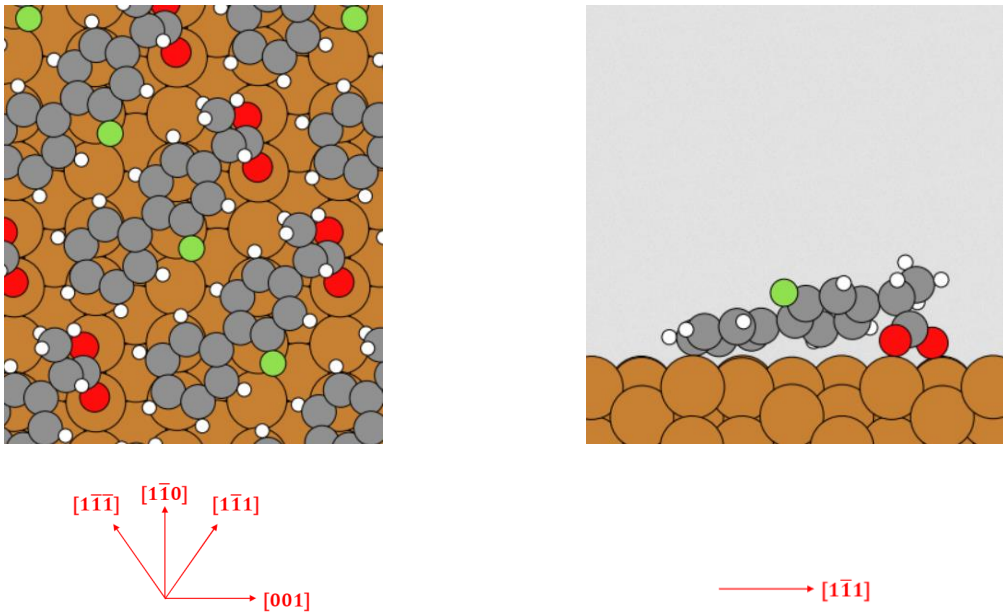


(a) (b)

**Figure 5.8:** Top (a) and side view (b) of the optimized [*S*, *trans*, monolayer, original] structure. The Cu(110) crystallographic directional indices are shown by the red arrows below each illustration. $E_{ads}$ = -3.22 eV.

As for [*S*, *cis*, monolayer, original], the [*S*, *trans*, monolayer, original] was demonstrated to be the equilibrium structure, using the same procedure as for the adsorbed *cis*-FBF. The initial set of configurations [*S*, *trans*, monolayer, $\theta_{initial}$] was generated in the same manner as for the [*S*, *cis*, monolayer, $\theta_{initial}$ ] configurations. The resulting adsorption energies obtained from the geometrical optimization of this set of initial configurations are shown in Table 5.2.

| $\theta_{initial}^{(o)}$ | $E_{ads}$ (eV) | $\theta_{initial}^{(o)}$ | $E_{ads}$ (eV) |
|---|---|---|---|
| **0** | -2.78 | **110** | -2.49 |
| **-10** | -2.79 | **120** | -2.85 |
| **-20** | -2.56 | **130** | -2.85 |
| **-30** | -3.22 | **140** | -3.22 |
| **-40** | -3.22 | **150** | -3.22 |
| **-50** | -3.22 | **160** | -2.81 |
| **-60** | -3.22 | **170** | -2.81 |
| **-70** | -2.41 | **180** | -2.71 |
| | | **190** | -2.71 |

**Table 5.2:** Same as for Table 5.1, but for the [*S*, *trans*, monolayer, $\theta_{initial}$].

As for Table 5.1, any missing angles in Table 5.2 correspond to the unphysical situation of overlapping atoms across unit cell boundaries. All optimized structures of [*S*, *trans*, monolayer, $\theta_{initial}$] in Table 5.2 with $E_{ads}$ values in red, have structures and $E_{ads}$ values equivalent to [*S*, *trans*, monolayer, original]. This structure will henceforth be denoted as [*S*, *trans*, monolayer].

5.3.3: Monolayer Adsorption of *cis*- and *trans*-*R*-FBF in the *S*-(1 × 1) Cell

Here, we present our study of the adsorption of *R*-FBF in the *S*-(1 × 1) cell on Cu(110), which was carried out in the same manner as for *S*-FBF. Firstly, an initial structure was generated by placing *cis*-*R*-FBF in this (1 × 1) cell and is shown in Fig. 5.9 (a) and (b). The geometrically optimized structure with $E_{ads}$ = -2.48 eV will henceforth be denoted as [*R*, *cis*, monolayer, original].

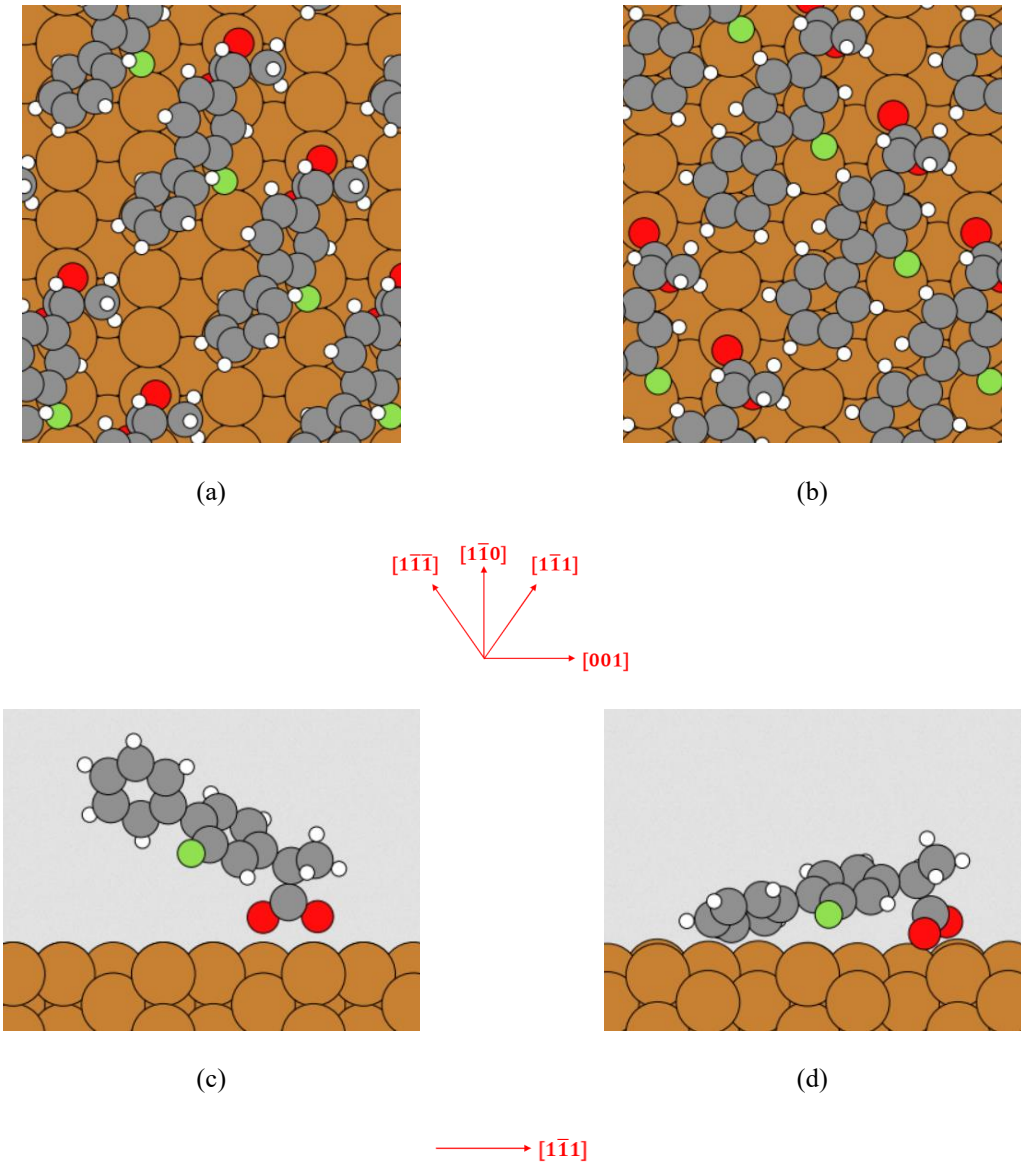


**Figure 5.9:** Shown in (a) and (b) are the top views of the non-optimized and optimized configurations of [*R*, *cis*, monolayer, original]. The side views in (c) and (d) correspond to (a) and (b), respectively. The Cu(110) crystallographic directional indices are shown by the red arrows below the top and side views. $E_{ads}$ = -2.48 eV.

In the same manner as for *S*-FBF, initial configurations were generated by rigid rotations of variations were made of [*R*, *cis*, monolayer, original]. These structures will henceforth be collectively denoted as [*R*, *cis*, monolayer, $\theta_{initial}$]. The resulting adsorption energies obtained from the geometrical optimization of this set of initial configurations are shown in Table 5.3.

| $\theta_{initial}$ (o) | $E_{ads}$ (eV) | $\theta_{initial}$ (o) | $E_{ads}$ (eV) |
|---|---|---|---|
| **0** | -2.97 | **110** | -2.24 |
| **-10** | -2.97 | **120** | -2.48 |
| **-20** | -2.97 | **130** | -2.97 |
| **-30** | -2.97 | **140** | -2.97 |
| **-40** | -2.97 | **150** | -2.97 |
| **-50** | -2.97 | **160** | -2.97 |
| **-60** | -2.48 | **170** | -2.36 |
| **-70** | -2.48 | **180** | -2.36 |
| **-80** | -2.48 | **190** | -2.77 |

**Table 5.3:** Same as for Table 5.1, but for [*R*, *cis*, monolayer, $\theta_{initial}$].

As for Tables 5.1 – 5.2, any missing angles in Table 5.3 correspond to the unphysical situation of overlapping atoms across unit cell boundaries. All optimized structures of [*R*, *cis*, monolayer, $\theta_{initial}$] in Table 5.3 with $E_{ads}$ values in red, correspond to the structure shown below in Fig. 5.10. This equilibrium structure will henceforth be referred to as [*R*, *cis*, monolayer] and differs from [*R*, *cis*, monolayer, original] with respect to orientation, and is more stable.

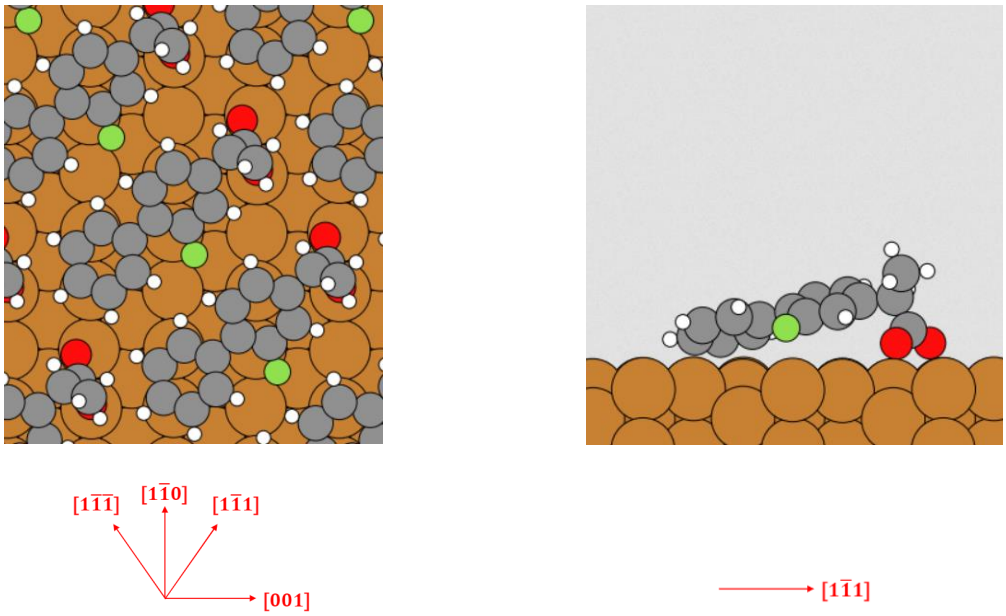


(a) (b)

**Figure 5.10:** Top (a) and side view (b) of the optimized [*R*, *cis*, monolayer] structure. The Cu(110) crystallographic directional indices are shown by the red arrows below each illustration. $E_{ads}$ = -2.97 eV.

Finally, we present our study of *trans*-*R*-FBF in the (1 × 1) cell on the Cu(110), which proceeds in the same way as for *trans*-*S*-FBF. The initial structure was obtained from [*R*, *cis*, monolayer] by exchanging the F and H atom positions of the [*R*, *cis*, monolayer] structure in the same manner as for *cis*-*S*-FBF in Subsection 5.3.2. This geometrically optimized structure is shown in Fig. 5.11 and will henceforth be denoted as [*R*, *trans*, monolayer, original].

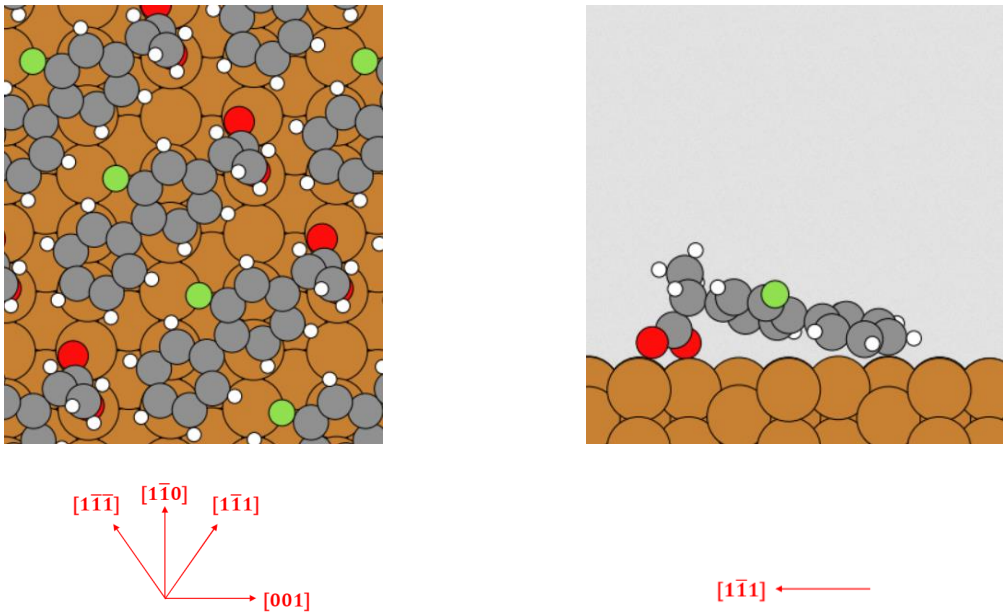


(a) (b)

**Figure 5.11:** Top (a) and side view (b) of the optimized [*R*, *trans*, monolayer, original] structure. The Cu(110) crystallographic directional indices are shown by the red arrows below each illustration. $E_{ads}$ = -3.13 eV.

In the same manner as for *S*-FBF, initial configurations were generated by rigid rotations variations of [*R*, *trans*, monolayer, original] . These structures will henceforth be collectively denoted as [*R*, *trans*, monolayer, $\theta_{initial}$]. The resulting adsorption energies obtained from the geometrical optimization of this set of initial configurations are shown in Table 5.4.

| $\theta_{initial}^{(o)}$ | $E_{ads}$ (eV) | $\theta_{initial}^{(o)}$ | $E_{ads}$ (eV) |
|---|---|---|---|
| **0** | -2.50 | **110** | -2.42 |
| **-10** | -2.50 | **120** | -3.04 |
| **-20** | -2.47 | **130** | -2.40 |
| **-30** | -3.13 | **140** | -3.13 |
| **-40** | -3.13 | **150** | -3.13 |
| **-50** | -3.13 | **160** | -2.69 |
| **-60** | -3.13 | **170** | 2.69 |
| **-70** | -2.50 | **180** | -2.50 |
| **-80** | -2.42 | **190** | -1.62 |

**Table 5.4:** Same as Table 5.1, but for the [*R, trans*, monolayer, $\theta_{initial}$] structures.

As for Tables 5.1 – 5.3, any missing angles in Table 5.4 correspond to the unphysical situation of overlapping atoms across unit cell boundaries. All optimized structures of [*R*, *trans*, monolayer, $\theta_{initial}$] in Table 5.4 with $E_{ads}$ values in red, have structures and $E_{ads}$ values equivalent to [*R*, *trans*, monolayer, original]. This structure will henceforth be denoted as [*R*, *trans*, monolayer]. In the next subsection, the energetics of the four monolayer equilibrium structures of *R*- and *S*-FBF will be compared.

5.3.4: Comparison of the Monolayer Equilibrium Structure Energetics

At this stage, the four (1 × 1) monolayer structures of adsorbed the *cis* and *trans* isomers of the *R* and *S* enantiomers of adsorbed FBF molecule have been obtained ready for comparison. For comparison, the top and side views of these monolayer structures are reproduced in Figs. 5.12 and 5.13, respectively, and the adsorption energetics of these structures are displayed in Table 5.5. Firstly, the top views are presented below in Fig. 5.12.

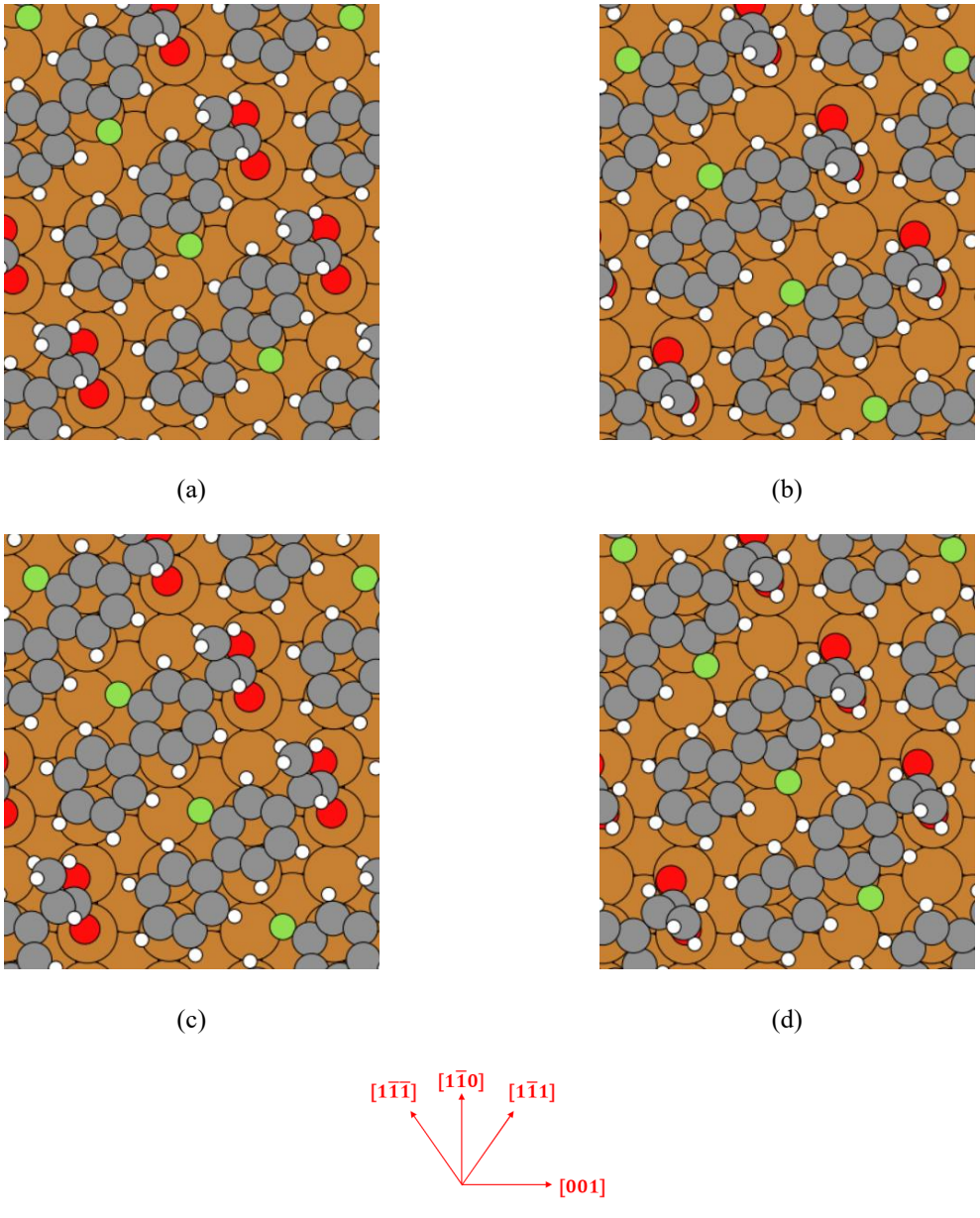


**Figure 5.12:** Top views of the [*S*, *trans*, monolayer] (a), [*R*, *trans*, monolayer] (b), [*S*, *cis*, monolayer] (c) and [*R*, *cis*, monolayer] structure (d). $E_{ads}$ = -3.22 eV (a), -3.13 eV (b), -3.08 eV (c) and -2.97 eV (d). The Cu(110) crystallographic directional indices are shown by the red arrows.

Secondly, the top views are presented below in Fig. 5.13.

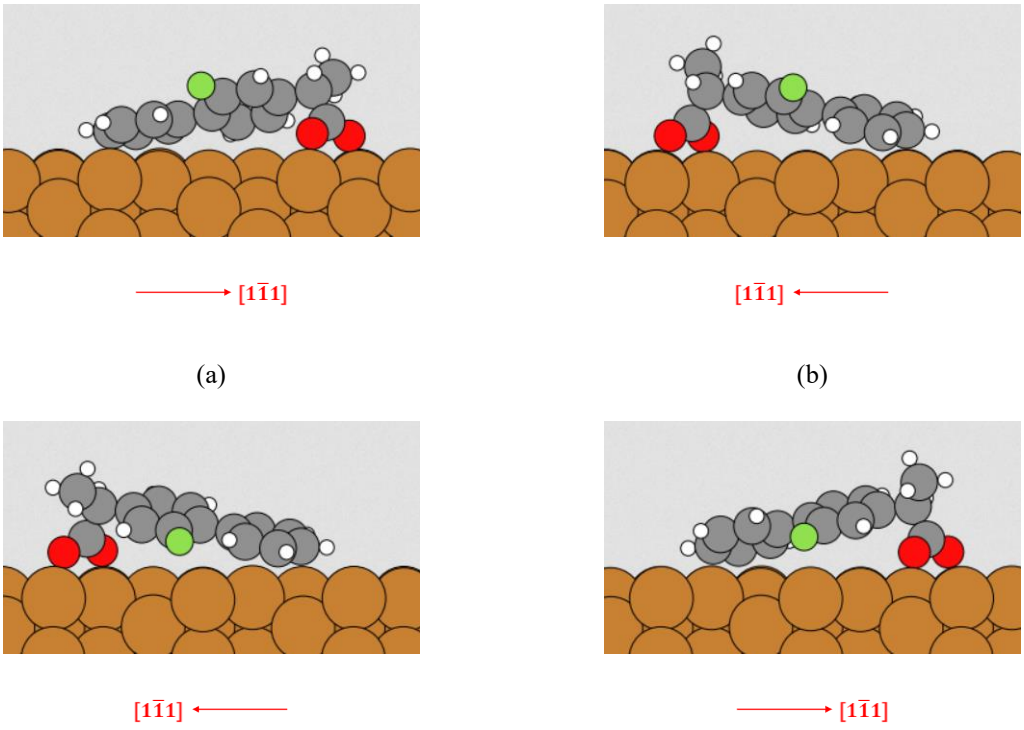


**Figure 5.13:** Side views of the [*S*, *trans*, monolayer] (a), [*R*, *trans*, monolayer] (b), [*S*, *cis*, monolayer] (c) and [*R*, *cis*, monolayer] structure (d). $E_{ads}$ = -3.22 eV (a), -3.13 eV (b), -3.08 eV (c) and -2.97 eV (d). The Cu(110) crystallographic directional indices are shown by the red arrows with each illustration.

Finally, the energetics of Figs. 5.12 and 5.13 are compared below in Table 5.5.

| **Equilibrium Structure** | **$E_{ads}$ (eV)** | **$\Delta E_{ads}$ (eV)** |
|---|---|---|
| [*S*, *trans*] | -3.22 | 0.00 |
| [*R*, *trans*] | -3.13 | 0.09 |
| [*S*, *cis*] | -3.08 | 0.14 |
| [*R*, *cis*] | -2.97 | 0.25 |

**Table 5.5:** Comparison of the adsorption energetics of the (1 × 1) monolayer structures. The structure signatures have been abbreviated for clarity by omitting 'monolayer' in the signature. The values of $\Delta E_{ads}$ (eV) are quoted relative to value of $E_{ads}$ for [*S*, *trans*], which is the most stable of the four structures.

As shown from the energetics in Table 5.5, the *trans* isomer for a given enantiomer is preferentially adsorbed into the (1 × 1) cell. Furthermore, [*S*, *trans*, monolayer] is the most stable monolayer structure. This finding corroborates the observation of enantiomeric selectivity that the rotational domains consist only of *S* enantiomers in *S*-(1 × 1) unit cells or *R* enantiomers in *R*-(1 × 1) unit cells (by reflectional symmetry). The new finding from this study is that *trans*-FBF preferentially adsorbs in the (1 × 1) monolayer structure rather than *cis*-FBF. Before investigating the origin of the relative stabilities of the four monolayer structures, we provide further corroboration for [*S*, *trans*, monolayer] being the most structure by making a comparison between simulated and experimental STM images in the next subsection.

5.3.5: Simulation of STM Images and Comparison to Experiment

Further corroboration of [*S*, *trans*, monolayer] being the observed equilibrium structure in a rotational domain comes from a comparison between simulated and experimental topographical STM images of this structure and the rotational domain, respectively. These images are shown in Fig. 5.14.

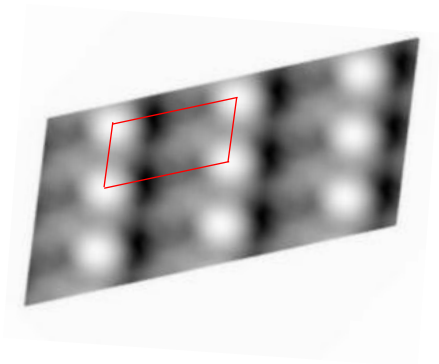

(a)

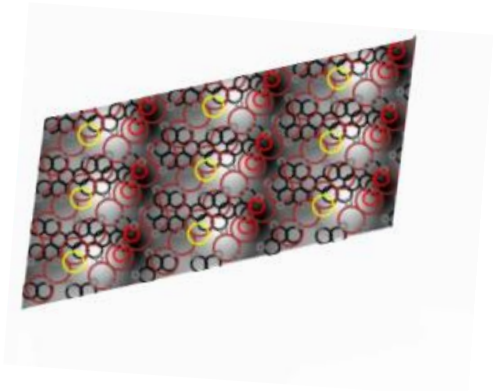

(b)

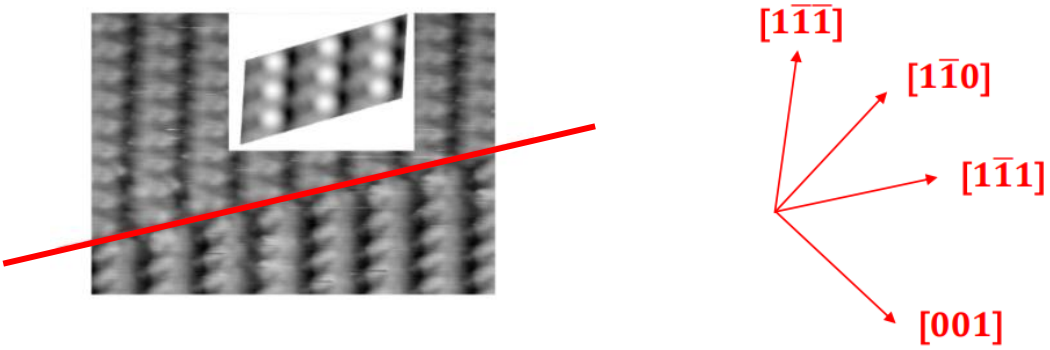


(c)

**Figure 5.14:** The simulated (a-b) and experimental (c), topographical STM images of the [*S*, *trans*, monolayer] structure. The images in (a - b) are repeated three times in both the [1$\bar{1}\bar{1}$] and [1$\bar{1}$1] directions to show their appearance in the monolayer. The *S*-(1 × 1) unit cell is shown in (a). The top layer of the Cu(110) surface and the FBF molecules are superimposed in (b). The Cu, F, H and O atoms are represented by the brown, yellow, grey and red circles, respectively. In (c), the experimental STM image is superimposed by the simulated image in (a) and the red line along the [1$\bar{1}$1] direction depicts the rotation domain boundary. All were obtained at the same bias voltage of +0.15 V. The average tip-surface distance is 9.4 Å for the simulated image. (Experimental STM image provided by C. L. Pang and R. Raval).

The simulated image of the FBF molecule in this monolayer structure shows a characteristic protrusion with a bright spot and a weaker tail. Notice that the atomic overlay in Fig. 5.14 (b) shows that this protrusion occurs between the molecules. This indicates that molecular orbitals exist mostly between the atomic positions of neighbouring molecules. This behaviour illustrates that the image is determined by electronic states and not the atoms. The shape and orientation of the protrusion in the simulated image is in good agreement with the protrusion in the experimental image. Before investigating the nature and origin of the boundary between two domains, we return to an investigation of the origin of the relative stabilities of the four monolayer structures.

### 5.3.6: Origin of the Monolayer Structure and the Chiral Selectivity

Here, we investigate the molecule-surface and molecule-molecule interactions behind the formation of the monolayer in order to better understand the origin behind the chiral selectivity and the monolayer structure. This investigation is based on total energy calculations of single monomers and monomer chains in the (3 × 2) cell. In order to have accurate values for total energy differences, we have also calculated the monolayer structures in the (3 × 2) cell, based on the monolayer structures obtained in the (1 × 1) cell.

The adsorption energetics of the monolayer in the (3 × 2) cell are shown in Table 5.6. The higher *k*-point density in the sampling of the SBZ for the (3 × 2) cell makes the calculated $E_{ads}$ slightly larger than for the (1 × 1) cell, but the relative adsorption energies are well converged. The *S* enantiomers are more stable by about 0.10 eV than the *R* enantiomers, and the *trans* isomers are more stable by about 0.14 eV than the *cis* isomers. Note that in the gas phase, the *cis* structure is slightly more stable than the *trans* structure by 3 meV. This very small energetic difference means that the gas phase *cis* and *trans* isomers are essentially degenerate. Therefore, all these energy differences for the adsorbed molecules are caused by molecule-surface and molecule-molecule interactions. The trend of $E_{ads}$ over the enantiomers and isomers is not caused by the repulsive dipole-dipole interactions between the molecules. The corresponding interaction energy $E_{dd}$ per molecule is given by

$$E_{dd} = \sum_{\boldsymbol{R}\neq\mathbf{0}} \frac{\Delta\mu^2}{R^3} \ , \qquad (5.3)$$

where $\Delta\mu$ is the adsorbate-induced perpendicular dipole moment per molecule and the sum is over the surface lattice vectors.[35] $\Delta\mu$ calculated as

$$\Delta\mu = \mu_{\text{whole system}} - \mu_{\text{bare surface}}, \tag{5.4}$$

where $\mu_{\text{whole system}}$ and $\mu_{\text{bare surface}}$ are the dipole moments of the whole system (adsorbed molecule and surface) and the bare surface, respectively. As shown in Table 5.6, the calculated values of $E_{\text{dd}}$ are too small to account for the calculated trend of $E_{\text{ads}}$ over the different enantiomers and isomers.

| | **[*S*, *trans*]** | **[*R*, *trans*]** | **[*S*, *cis*]** | **[*R*, *cis*]** |
|---|---|---|---|---|
| $E_{\text{ads}}$ **(eV)** | -3.25 (-3.22) | -3.15 (-3.13) | -3.11 (-3.08) | -3.00 (-2.97) |
| $\Delta E_{\text{ads}}$ **(eV)** | 0.00 (0.00) | 0.10 (0.09) | 0.14 (0.14) | 0.25 (0.25) |
| $\Delta\mu$ **(eÅ)** | 0.32 (0.32) | 0.31 (0.32) | 0.39 (0.40) | 0.38 (0.38) |
| $E_{\text{dd}}$ **(eV)** | 0.022 | 0.021 | 0.033 | 0.031 |

**Table 5.6:** Adsorption energetics of the monolayer. $\Delta E_{\text{ads}}$ is quoted relative to $E_{\text{ads}}$ for [*S*, *trans*]. $\Delta\mu$ is the adsorbate-induced perpendicular dipole moment per molecule. $E_{\text{dd}}$ is the dipole-dipole interaction energy as defined in Eq. (5.3). The values were obtained for the (3 × 2) cell, whereas the values within the parentheses were obtained for the (1 × 1) cell.

As shown by the side views of the molecules in Fig. 5.13, the geometries of the isomers show some notable differences. The F atom is closer to the surface for the *cis* isomers than for the *trans* isomers. As shown by the top views of the molecules in Fig 5.12, the adsorbed *S*- and *R*-enantiomers are not simply related by a reflection in the surface plane due to the different orientations of the methyl group with respect to the carboxyl group for the adsorbed enantiomers. The orientations of the molecular axis with respect to the rows of the Cu atoms are very similar for all monomers. This orientation of the molecular axis maximizes the distance between the molecular axes of two neighbouring molecules since they are nearly perpendicular to the direction between two nearest neighbouring adsorption sites.

Note that it would be possible to form a monolayer with a higher coverage if the adsorption sites of two neighbouring molecules would be on the same row, but that would force the molecules closer to each other, which could make the molecule-molecule interaction less favourable. This suggestion is supported by our result for the dimer chains in the next subsection. In order to show the different surface coverages within the (3 × 2) cell, the optimized [*S*, *trans*] structures are shown as an example.

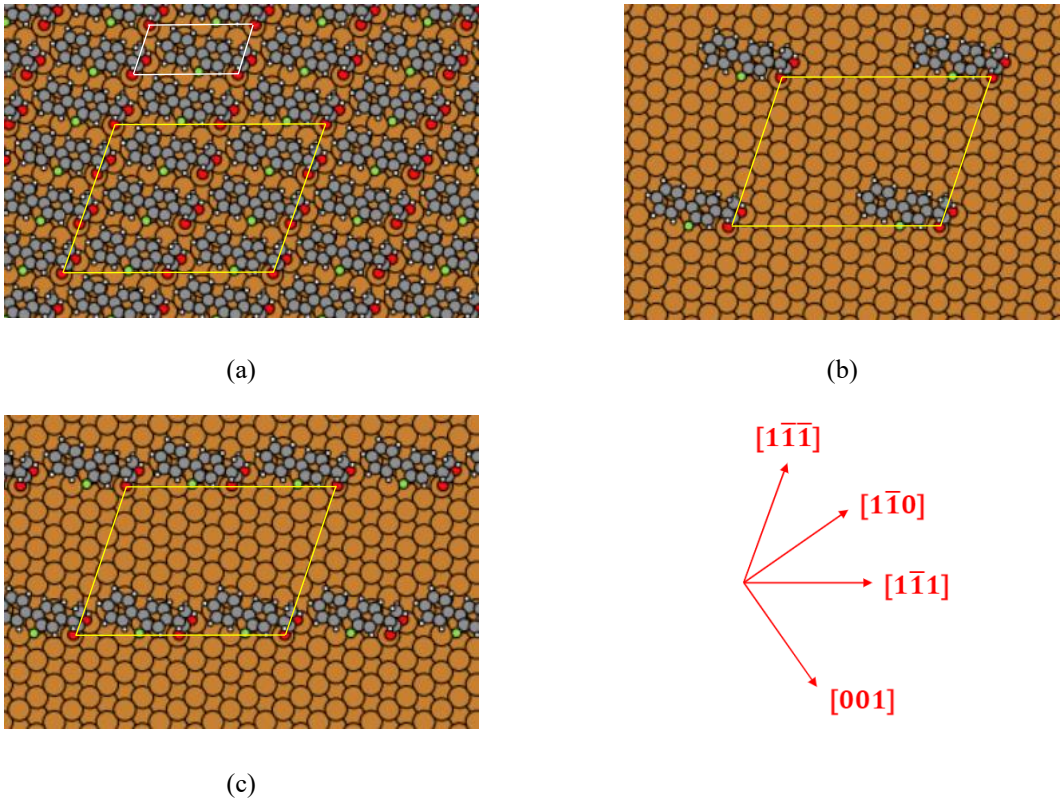


**Figure 5.15:** The optimized [*S*, *trans*] structure in the monolayer (a), as an isolated monomer (b), and as a monomer chain (c). The (3 × 2) cell is shown in (a – c) by the yellow parallelogram. In (a), the (1 × 1) cell is shown by the white parallelogram for comparison. The Cu(110) crystallographic directional indices are shown by the red arrows.

In Fig. 5.15 (c), the monomer chain structure is constructed of a single monomer of FBF that is repeated only along the [1$\bar{1}$1] direction to form an infinite chain of monomers. This chain of monomers has the same periodicity of the (1 × 1) cell along the [1$\bar{1}$1] direction. Side views of the [*S*, *trans*] and the other equilibrium structures in the (3 × 2) cell are shown below in Fig. 5.16. The side views are most useful here as they show the differences and similarities of the adsorbed molecular structures better than the top views.

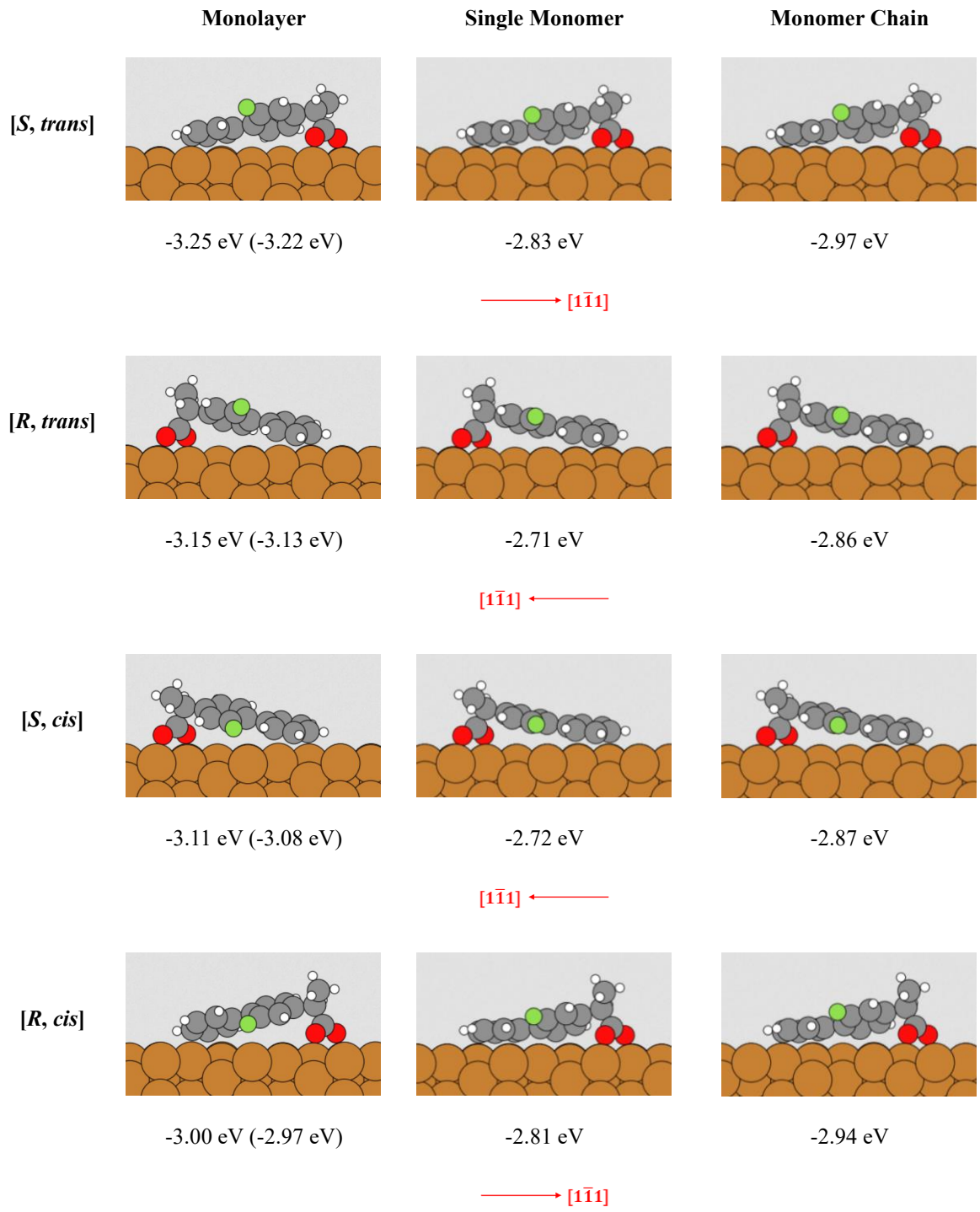


**Figure 5.16:** Side views of an adsorbed molecule in the monolayer, single adsorbed molecule and an adsorbed molecule in monomer chains. All configurations shown are in the (3 × 2) cell. The Cu(110) crystallographic directional indices are shown by the red arrows. The adsorption energy per molecule ($E_{ads}$) values are shown below each structure. The values within the parentheses for the monolayer structures were obtained for the (1 × 1) cell.

As shown in Fig 5.16, comparison of the side views of the resulting molecular geometries of these structures with the molecular geometry of the monolayer structure indicates that the geometries are all very similar for a given isomer, except for *cis*-*R*-FBF. Furthermore, the orientations of the molecules with respect to the Cu rows have not changed from their orientation in the monolayer.

In Tables 5.7 and 5.8, we show the calculated adsorption energetics for the single isomers and monomers chains in the (3 × 2) cell. These structures were obtained by geometric optimization starting from the molecular geometries in the monolayer. These structures were shown schematically for the *trans*-*S*-FBF in Fig. 5.15 as an example in order to show the different molecular coverages within the (3 × 2) cell.

| | **[*S*, *trans*]** | **[*R*, *trans*]** | **[*S*, *cis*]** | **[*R*, *cis*]** |
|---|---|---|---|---|
| $E_{ads}$ **(eV)** | -2.83 | -2.71 | -2.72 | -2.81 |
| $\Delta E_{ads}$ **(eV)** | 0.00 | 0.12 | 0.11 | 0.02 |
| $\Delta\mu_z$ **(eÅ)** | 0.67 | 0.60 | 0.67 | 0.71 |
| $E_{dd}$ **(eV)** | 0.005 | 0.004 | 0.005 | 0.006 |

**Table 5.7:** Same as for Table 5.6, but for isolated monomer structures. The values were obtained for the (3 × 2) cell.

| | **[*S*, *trans*]** | **[*R*, *trans*]** | **[*S*, *cis*]** | **[*R*, *cis*]** |
|---|---|---|---|---|
| $E_{ads}$ **(eV)** | -2.97 | -2.86 | -2.87 | -2.94 |
| $\Delta E_{ads}$ **(eV)** | 0.00 | 0.11 | 0.10 | 0.03 |
| $\Delta\mu_z$ **(eÅ)** | 0.58 | 0.53 | 0.59 | 0.61 |
| $E_{dd}$ **(eV)** | 0.011 | 0.010 | 0.013 | 0.013 |

**Table 5.8:** Same as for Table 5.7, but for the monomer chains.

A notable finding is the result that the trend of $\Delta E_{ads}$ over the enantiomers and isomers for the single monomer and the monomer chains in the (3 × 2) cell are essentially the same as for in the monolayer, except for the *cis*-*R*-FBF. In the limit of zero coverage corresponding to an isolated adsorbed molecule, the adsorption energies of the same isomer of the *S* and *R* enantiomers should be degenerate, since the Cu(110) surface is not a chiral surface. The small changes in the energy differences between $\Delta E_{ads}$ of a single enantiomer in the (3 × 2) cell and the corresponding enantiomer in the monolayer suggests then that calculated geometries of the single enantiomer in the (3 × 2) cell are metastable.

As will be discussed below, the monolayer geometries arise due to the strong attractive interactions between the molecules in the monolayer. Finally, $\boldsymbol{\Delta\mu}$ is larger for the single molecule in the (3 × 2) cell and the monomer chain than for the molecule in the monolayer, but the resulting $E_{dd}$ are still smaller than for the monolayer due to their smaller coverages. As shown in Table 5.6, there are strong attractive interactions between molecules in the monolayer. The interaction energies $E_{\mathrm{int}}$ per molecule were obtained as the $E_{ads}$ difference between the single molecule in the (3 × 2) cell and a molecule in the monolayer. These interaction energies for the different monomers are similar in magnitude and much larger than the differences between the molecule-substrate interaction energies given by $\Delta E_{ads}$ for the single molecules in the (3 × 2) cell. This behaviour suggests that the strong attractive molecule-molecule interactions force the *S* and *R* enantiomers into geometries with substantial energy differences resulting in chiral selectivity. As also shown in Table 5.9, a large fraction of the molecule-molecule interaction is due to the van der Waals interaction between the molecules. The contribution $E_{\mathrm{int,\ vdW}}$ per molecule from the van der Waals interactions to $E_{\mathrm{int}}$ is given by

$$E_{\mathrm{int,\ vdW}} = (\,E_{\mathrm{vdW}}((3\times2)\ \mathrm{monolayer}) - E_{\mathrm{vdW}}(\mathrm{Cu}(110))/6 - (E_{\mathrm{vdW}}\big((3\times2)\mathrm{molecule}\big) - E_{\mathrm{vdW}}(\mathrm{Cu}(110)), \tag{5.4}$$

where $E_{\mathrm{vdW}}((3\times2)\ \mathrm{monolayer})$, $E_{\mathrm{vdW}}\big((3\times2)\mathrm{molecule}\big)$ and $E_{\mathrm{vdW}}(\mathrm{Cu}(110))$ are the van der Waals energies of the monolayer in the (3 × 2) cell, single molecule in the (3 × 2) cell and the bare Cu(110) surface in the (3 × 2) cell, respectively.

Furthermore, we have decomposed the interaction energies into perpendicular and parallel contributions with respect to the molecular axis. The perpendicular interaction energy, $E_{\text{int, perp}}$, per molecule is simply defined as the $E_{\text{ads}}$ difference between the single molecule in the (3 × 2) cell and a molecule in the monomer chain and the parallel interaction energy, $E_{\text{int ,par}}$, per molecule is just then the remaining part $E_{\text{int}}$ - $E_{\text{int, perp}}$. Not surprisingly, $E_{\text{int, perp}}$ is the dominant contribution to $E_{\text{int}}$. $E_{\text{int, par}}$ is about half the value of $E_{\text{int, perp}}$ and is essentially equal for the four monomers.

The interactions between adsorbed molecules will in general have both substrate-mediated and direct contributions. Here, the direct interaction is defined as the interaction energy between protonated molecules in the gas phase, but in the same geometry as on the surface. The molecules have been protonated in order to avoid interaction between unpaired electrons of two separate molecules. As shown by a comparison of the results for interaction energies in Tables 5.9 and 5.10, the interaction between the adsorbed molecules is to a large part, a direct molecule-molecule interaction. This result is consistent with the large contribution for the van der Waals interaction to the interaction between the adsorbed molecules.

| | **[*S*, *trans*]** | **[*R*, *trans*]** | **[*S*, *cis*]** | **[*R*, *cis*]** |
|---|---|---|---|---|
| $E_{\text{int}}$ **(eV)** | -0.42 | -0.44 | -0.39 | -0.19 |
| $E_{\text{int, vdW}}$ **(eV)** | -0.22 | -0.47 | -0.43 | 0.14 |
| $E_{\text{int, par}}$ **(eV)** | -0.28 | -0.29 | -0.24 | -0.06 |
| $E_{\text{int, perp}}$ **(eV)** | -0.14 | -0.15 | -0.15 | -0.13 |

**Table 5.9:** Breakdown of the interaction energy $E_{\text{int}}$, into its vdW, parallel and perpendicular components for each *cis* and *trans* enantiomer equilibrium structure in the monolayer. The values shown were obtained for the (3 × 2) cell, and the energy definitions are given above in the text.

| | [*S*, *trans*] | [*R*, *trans*] | [*S*, *cis*] | [*R*, *cis*] |
|---|---|---|---|---|
| $E_{int}$ (eV) | -0.50 (-0.47) | -0.42 (0.45) | -0.46 (-0.47) | -0.64 (-0.62) |
| $E_{int, par}$ (eV) | -0.12 (-0.11) | -0.07 (-0.07) | -0.09 (-0.09) | -0.13 (-0.12) |
| $E_{int, perp}$ (eV) | -0.38 (-0.36) | -0.35 (-0.38) | -0.37 (-0.38) | -0.51 (-0.50) |

**Table 5.10:** Interaction energetics of protonated gas-phase monolayers. The values correspond to the *up* configuration, whereas the values within the parentheses correspond to the *down* configuration.
(Refer to Fig. 5.17 for the definition of the *up* and *down* configuration).

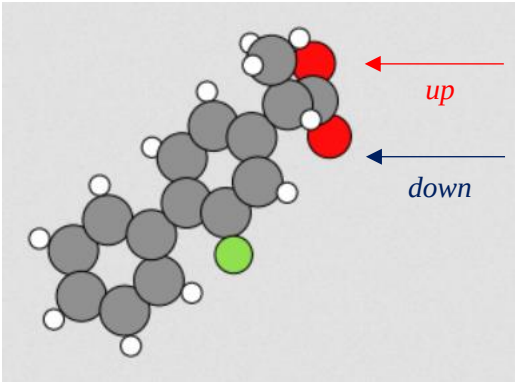


**Figure 5.17:** A single molecule of FBF. This is protonated by placing a hydrogen atom at distance $z$ = -1 Å below either the *up*, or the *down* oxygen atom.

In Fig. 5.17, the *up* configuration corresponds to protonation of the oxygen atom nearest the methyl group. The *down* configuration is protonation of the other oxygen atom. All interaction energetics of protonated gas-phase configurations are calculated from structures that are constructed in the way shown in Fig. 5.17. These structures are geometrically optimized in the (3 × 2) cell, with all atoms fixed, except for the hydrogen atom(s) protonating the molecule(s) in either the *up* or the *down* configuration. In conclusion, we find that the strong attractive van der Waals interaction favours a high coverage monolayer phase where the surface unit cell is chiral and forces the adsorbed enantiomers in configurations that results in a chiral selectivity.

## 5.3.7: Formation of the Rotation Domain Boundary

The STM experiments indicated that there is only one domain wall in an enantiomerically pure island. The molecules in the domains on either side of the domain wall were found to be orientated at 180° relative to each other. Here, we investigate the molecule-molecule interaction behind the formation of this domain wall based on total energy calculations of dimer chains in (3 × 1) and (3 × 2) cells and isolated dimers in a (3 × 2) cell. These cell sizes were chosen in order to adequately isolate neighbouring images of the dimer chains and isolated dimers due to the periodic boundary conditions.

Furthermore, this choice of cells restricts our study to domain walls along the observed direction. The interaction energies of the molecules in the dimer chains were extracted from total energy calculations of isolated dimer chains in a (3 × 2) cell. All these calculations were limited to homodimers of either *cis* or *trans* isomers of the *S*-enantiomer since the two isomers of the *R*-enantiomer were less stable.

The initial configurations of the dimer chains were based on equilibrium geometries of the molecules in the monolayer and the molecules in the dimers were placed either with parallel or anti-parallel orientations and at different displaced configurations. There are three inequivalent relative orientations of the molecule in the dimer, which are noted by '66', '69' and '96'. The orientation '66' means that the molecules are not rotated and are parallel with respect to each other, whereas the orientation '69' or '96' means that they molecules in the dimer unit are oriented at $180^0$ with respect to each other and the F atoms of the dimer point towards or away from each other, respectively. This '66', '69' and '96' notation is used because it is a concise way of describing the aforementioned relative molecular orientations.

As illustrated in Fig 5.18, the relative displacement of the molecules in a primitive unit of the dimer chain is characterised by its footprint (*n*,*m*) where $n\mathbf{a}_{[001]} + m\mathbf{a}_{[1\bar{1}0]}$ is the relative position vector between the bridge adsorption sites of the two molecules in the dimer. Here, *n* and *m* are integers and $\mathbf{a}_{[001]}$ and $\mathbf{a}_{[1\bar{1}0]}$ are the primitive lattice vectors of the bare surface along the $[001]$ and $[1\bar{1}0]$ directions, respectively. The lowest energy structure of the possible footprints for each orientation of the dimer was then determined by geometrical optimisation and this procedure is detailed in Appendix B, Section B.2.

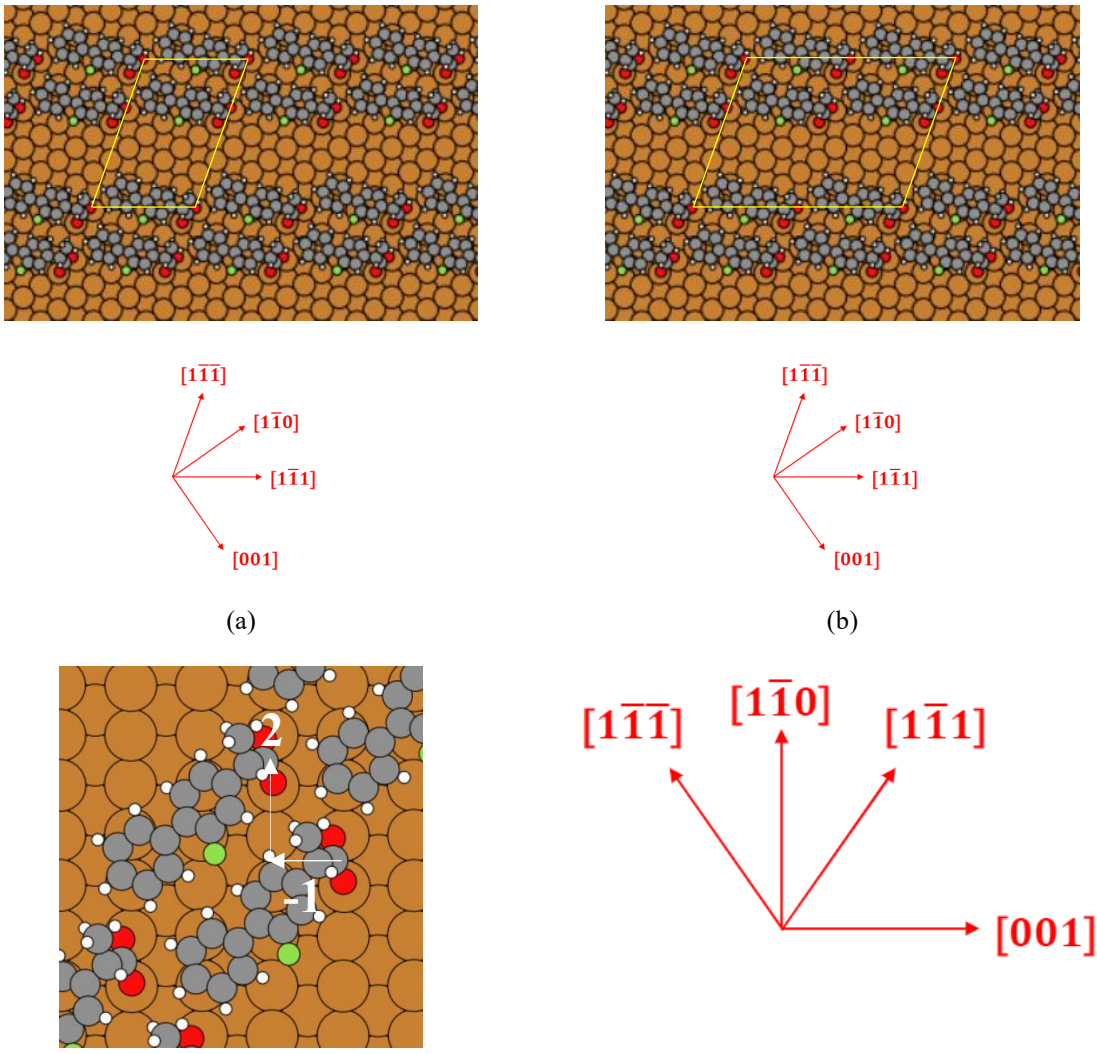


**Figure 5.18:** Illustration of a *trans*-66 dimer chain structure in the (3 × 1) cell (a) and the (3 × 2) cell (b). The footprint (-1,2) is defined by the white arrows indicating the displacements along the [001] and [1$\bar{1}$0] directions between the adsorption sites in the primitive unit of the dimer chain. Note that for a given relative orientation of the molecules in the 66 dimer chain, (*n*, *m*) and (-*n*, -*m*) represent equivalent footprints. The Cu(110) crystallographic directional indices are shown with each illustration.

Fig. 5.19 shows the top views of the lowest energy footprint (-1,2), of the *trans*- and *cis*-66 dimer chains.

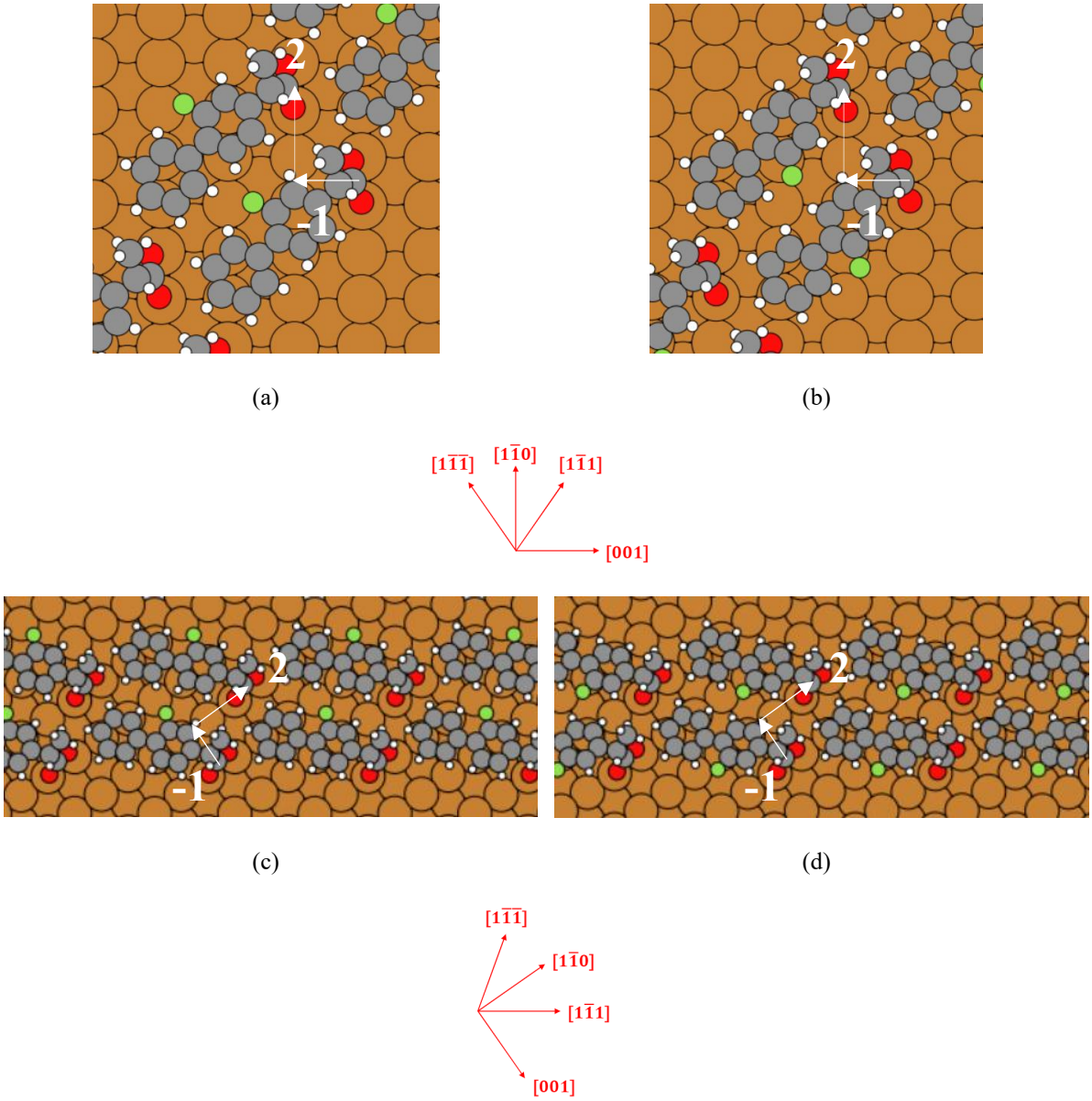


**Figure 5.19:** Top views of the *cis*- (a) and *trans*-66 dimer chain (b). The structures in (c) and (d) correspond to (a) and (b), respectively, but these show the extension of the dimer chain along the $[1\bar{1}1]$ direction. The schematics in (c) and (d) have been rotated to conserve space. The Cu(110) crystallographic directional indices corresponding to (a – b) and (c – d), are shown by the red arrows below them. The adsorption energy per molecule ($E_{ads}$) values of the *cis*- and *trans*-66 dimer chains are -2.98 eV (-2.94 eV) and -3.10 eV (-3.06 eV), respectively. The values shown within the parentheses were obtained for the (3 × 1) cell, whereas those without were for the (3 × 2) cell.

As shown in Fig. 5.19, the lowest energy footprint (-1, 2) of the *trans*- and *cis*-66 dimer chains is the same as the dimer chains in the monolayer. The side views of the molecules in these dimer chains in Fig. 5.20.

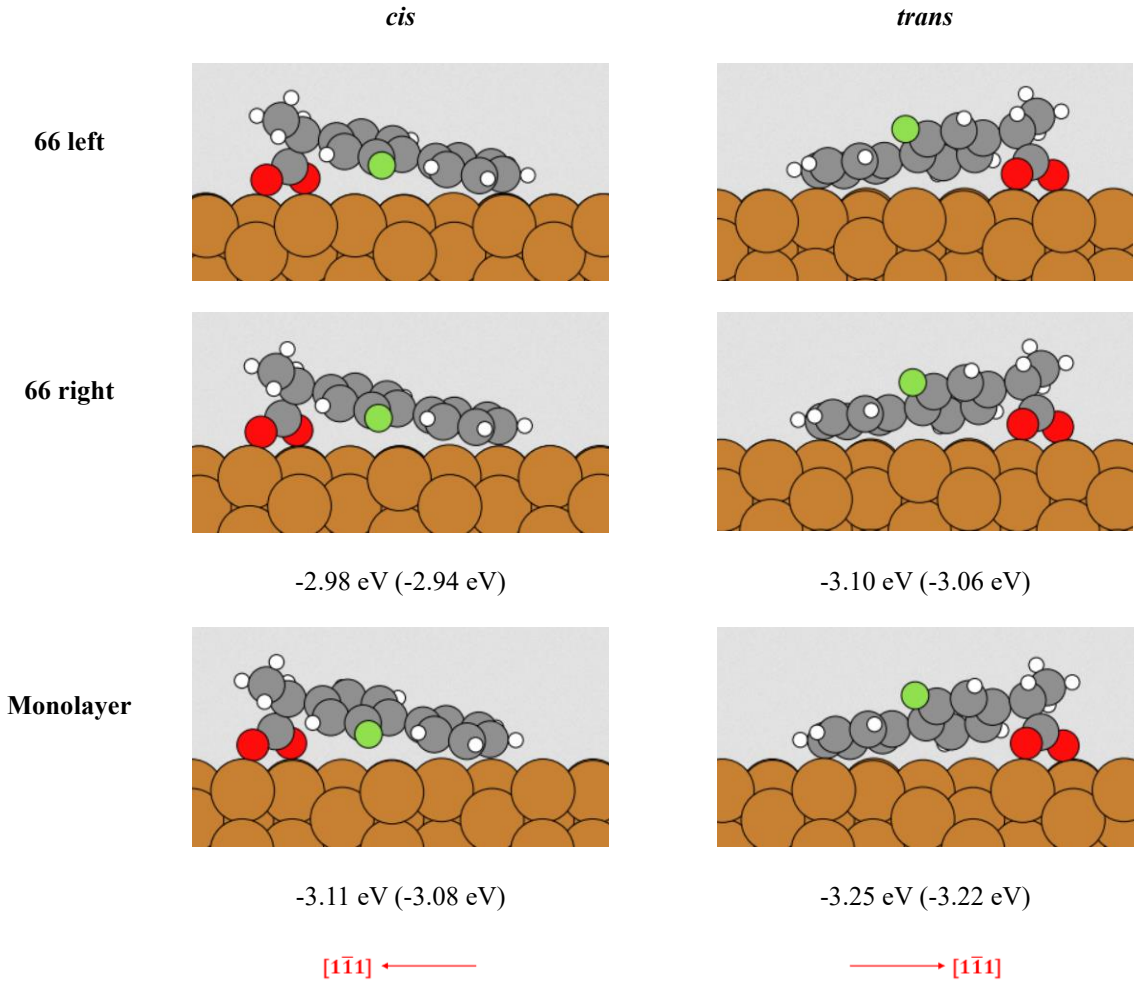


**Figure 5.20:** Side views each molecule in the *cis*- and *trans*-66 dimer chain configurations. The side views of the *cis* and *trans* monolayers have been reproduced here for comparison. The '66 left' and '66 right' configurations are not exactly the same because of symmetry breaking due to periodic boundary conditions. However, one can see that there is not an appreciable structural difference between these structures in either the *cis* or *trans* case. The adsorption energy per molecule ($E_{ads}$) values are shown below the 66 and the monolayer structures. The Cu(110) crystallographic directional indices for all the *cis* and *trans* structures are shown by the red arrows at the bottom.

Note that for a given isomer, the calculated $E_{ads}$ value is the same for both the 66 left and the 66 right structures. The values without parentheses were obtained for the (3 × 2) cell. The values within the parentheses were obtained for the (3 × 1) and (1 × 1) cells for the 66 and monolayer structures, respectively.

Fig. 5.20 shows that the geometries of the two molecules within the dimer are essentially unchanged from the corresponding geometry of the molecule in the monolayer. The energetics of the 66 dimer chains are found to be consistent with the energetics of the monolayer. As shown in Table 5.11, the relative adsorption energy of a molecule in the *trans* and the *cis* dimer chains is very close to the corresponding value for the *cis* and *trans* molecules in the monolayer shown in Table 5.6. The interaction energies between molecules in the dimer chains were obtained in a similar manner to those for the molecules in the monolayer. The interaction energy $E_{\text{int}}$ per molecule was now defined as the difference in $E_{ads}$ between a molecule in the dimer chain and a single molecule in the (3 × 2) cell.

As shown in Tables 5.6 And 5.11, $E_{\text{int}}$ is about two thirds of $E_{\text{int}}$ for the molecules in the monolayer due to the loss of neighbours of molecules in a dimer chain compared to molecules in the monolayer. The perpendicular component $E_{\text{int, perp}}$ of $E_{\text{int}}$, defined here as the $E_{ads}$ difference between a molecule in the dimer chain and a monomer chain in the (3 × 2) cell, is the row-row interaction energy. In a simple additive, nearest neighbouring row pair interaction energy model, $E_{\text{int, perp}}$ should be twice as large for the monolayer than for the dimer chain, which is borne out by the results in Tables 5.6 and 5.11. Furthermore, the remaining parallel part $E_{\text{int ,par}} = E_{\text{int}} - E_{\text{int, perp}}$, is equal to $E_{\text{int, par}}$ for the monolayer, since they turn out to be both equal to the difference in $E_{ads}$ between a molecule in the monomer chain in the (3 × 2) cell and a single molecule in the (3 × 2) cell.

| | [*S*, *trans*] | | | | [*S*, cis] | | |
|---|---|---|---|---|---|---|---|
| | **66** | **69** | **96** | | **66** | **69** | **96** |
| **Footprint** | (1, -2) | (1, 4) | (-4, -1) | (3, 0) | (1, -2) | (-4, -1) | (1, 4) |
| $E_{ads}$ **(eV)** | -3.10<br>(-3.06) | -3.12<br>(-3.07) | -2.93<br>(-2.89) | -2.91<br>(-2.88) | -2.98<br>(-2.94) | -2.88<br>(-2.85) | -3.02<br>(-2.98) |
| $\Delta E_{ads}$ **(eV)** | 0.00<br>(0.00) | -0.02<br>(-0.01) | 0.17<br>(0.17) | 0.19<br>(0.18) | 0.12<br>(0.12) | 0.22<br>(0.21) | 0.08<br>(0.08) |
| $E_{int}$ **(eV)** | -0.27 | -0.29 | -0.10 | -0.08 | -0.25 | -0.16 | -0.30 |
| $E_{int, perp}$ **(eV)** | -0.13 | -0.15 | 0.04 | 0.06 | -0.10 | -0.01 | -0.15 |
| $E_{int, par}$ **(eV)** | -0.14 | -0.14 | -0.14 | -0.14 | -0.15 | -0.15 | -0.15 |
| $E_{int, par'}$ **(eV)** | -0.22 | -0.20 | -0.13 | -0.03 | -0.24 | -0.15 | -0.20 |
| $E_{int, cross}$ **(eV)** | -0.08 | -0.06 | 0.01 | 0.11 | -0.09 | 0.00 | -0.05 |

**Table 5.11:** Energetics of dimer chains. Values within the parentheses are for the (3 × 1) cell whereas the other values are for the (3 × 2) cell. $E_{int, cross}$ is defined as the difference between $E_{int, par'}$ and $E_{int, par}$. The other interaction energies were already defined in the text.

The top and side views of the lowest energy footprints of the 69 and 96 dimer chains are shown in Figs 5.21-5.24. The top views show that the footprints are (1, 4) and (-4, -1), respectively. They are the same for the *trans* 69 and *cis* 96 dimer and the same for the *trans* 96 and *cis* 69 dimer chains. In addition, we have included the next lowest energy footprint (-3, 0) of the *trans* 96 dimer since this footprint turns out to be favourable for the isolated dimer.

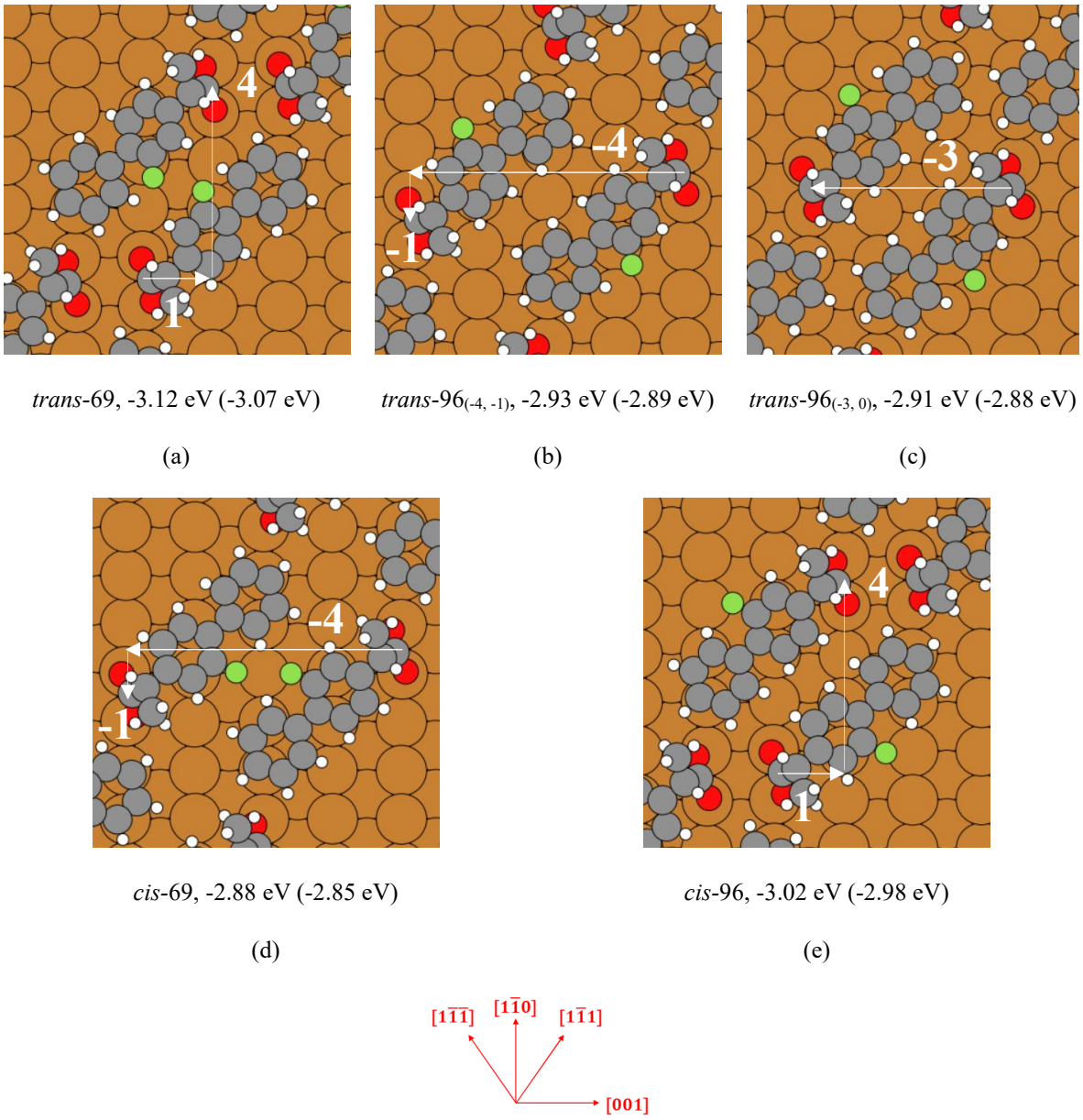


*trans*-69, -3.12 eV (-3.07 eV)

(a)

*trans*-96$_{(-4, -1)}$, -2.93 eV (-2.89 eV)

(b)

*trans*-96$_{(-3, 0)}$, -2.91 eV (-2.88 eV)

(c)

*cis*-69, -2.88 eV (-2.85 eV)

(d)

*cis*-96, -3.02 eV (-2.98 eV)

(e)

**Figure 5.21:** Top views of the dimer chain structures. The Cu(110) crystallographic directional indices are shown by the red arrows. Adsorption energies per molecule ($E_{ads}$) are shown with each structure. The values without parentheses were obtained for the (3 × 2) cell, whereas the values within the parentheses correspond to the (3 × 1) cell.

Notice from Fig. 5.21 that the *trans*-69 and *cis*-96 structures have the same (1, 4) footprint, whereas the *trans*-$96_{(-4,\,-1)}$ and *cis*-69 structures have the same (-4, -1) footprint. Fig. 5.22 shows a view of the structures in Fig. 5.21, extending along the $[1\bar{1}1]$ direction.

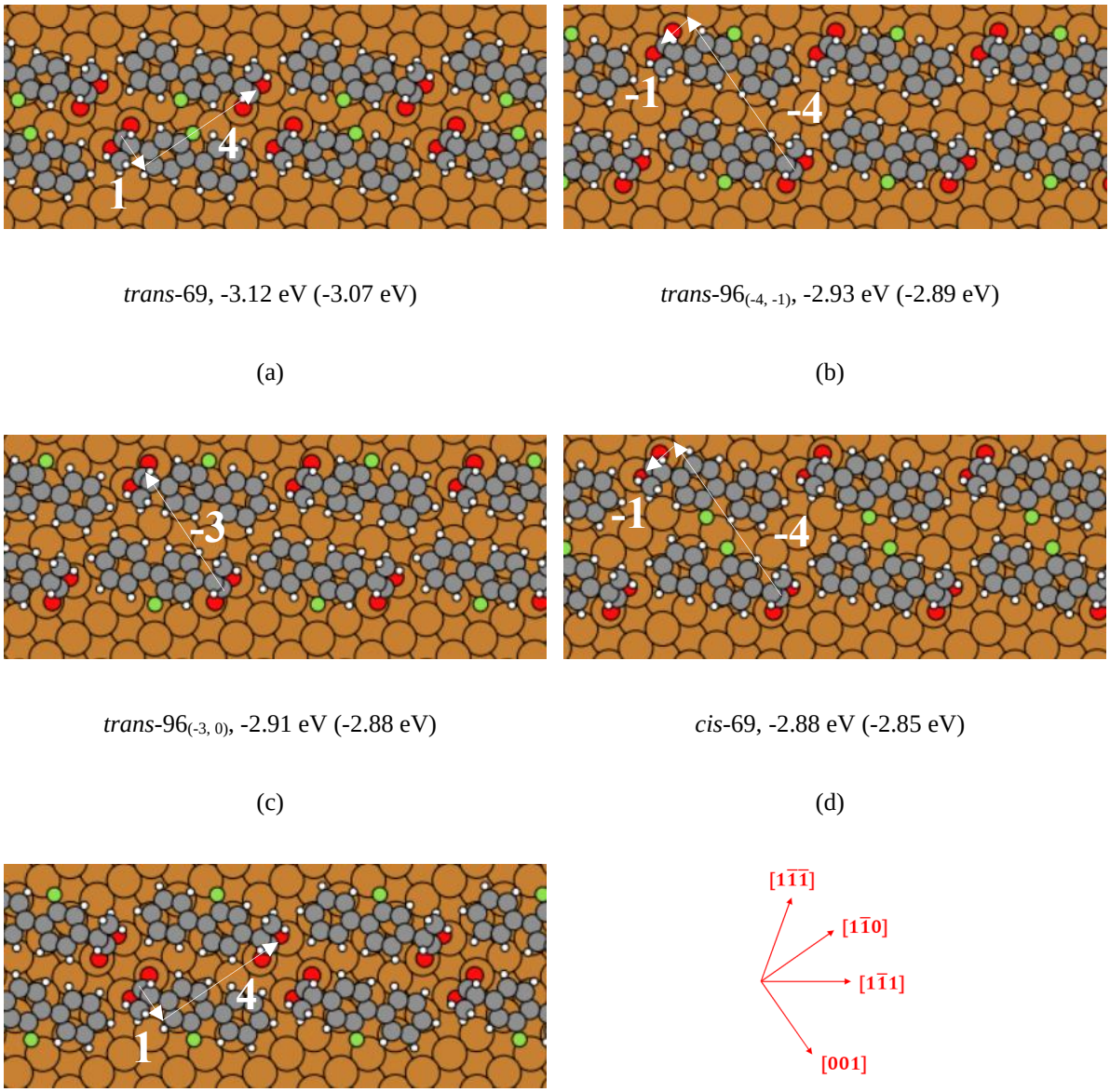


*trans*-69, -3.12 eV (-3.07 eV)

(a)

*trans*-$96_{(-4,\,-1)}$, -2.93 eV (-2.89 eV)

(b)

*trans*-$96_{(-3,\,0)}$, -2.91 eV (-2.88 eV)

(c)

*cis*-69, -2.88 eV (-2.85 eV)

(d)

*cis*-96, -3.02 eV (-2.98 eV)

(e)

**Figure 5.22:** Top views of the dimer chain structures extending along the $[1\bar{1}1]$ direction. The Cu(110) crystallographic directional indices are shown by the red arrows. Adsorption energies per molecule ($E_{ads}$) are shown with each structure. The values without parentheses were obtained for the (3 × 2) cell, whereas the values within the parentheses correspond to the (3 × 1) cell.

The side views of these structures are shown below in Figs. 5.23 and 5.24 for the *cis* and *trans* isomers, respectively.

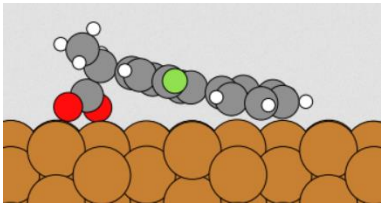

*cis*-69, -2.88 eV (-2.85 eV)

(a)

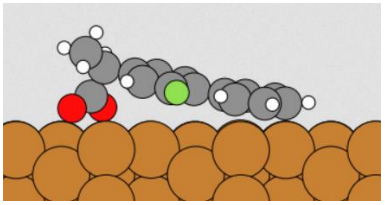

*cis*-96, -3.02 eV (-2.98 eV)

(b)

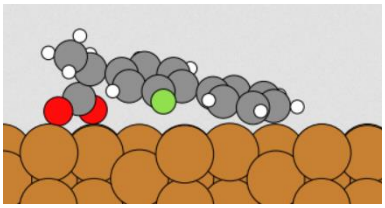

*cis* monolayer, –3.11 eV (-3.08 eV)

(c)

[1$\bar{1}$1] ←

**Figure 5.23:** Side views of the 69 and 96 *cis* dimer chain structures (a – b). The *cis* monolayer structure has also been shown here for comparison in (c). The [1$\bar{1}$1] crystallographic direction is shown by the red arrow. Adsorption energies per molecule ($E_{ads}$) are shown with each structure. The values without parentheses were obtained for the (3 × 2) cell, whereas the values within the parentheses correspond to the (3 × 1) cell for (a – b), and to the (1 × 1) cell for (c).

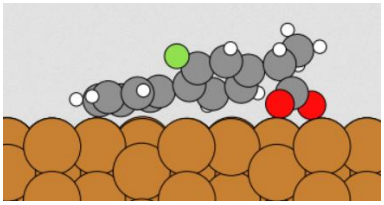

*trans*-69, -3.12 eV (-3.07 eV)

(a)

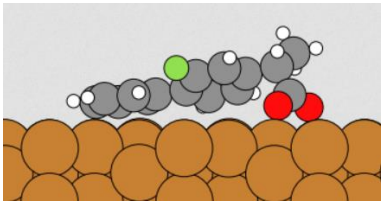

*trans*-96$_{(-4, -1)}$, -2.93 eV (-2.89 eV)

(b)

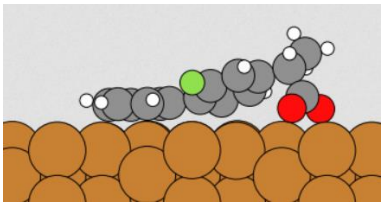

*trans*-96$_{(-3, 0)}$, -2.91 eV (-2.88 eV)

(c)

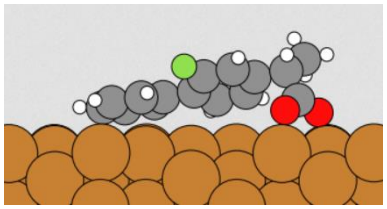

*trans* monolayer, -3.25 eV (-3.22 eV)

(d)


**Figure 5.24:** Side views of the 69 and 96 *trans* dimer chain structures (a – c). The *trans* monolayer structure has also been shown here for comparison in (d). The [1$\bar{1}$1] crystallographic direction is shown by the red arrow. Adsorption energies per molecule ($E_{ads}$) are shown with each structure. The values without parentheses were obtained for the (3 × 2) cell, whereas the values within the parentheses correspond to the (3 × 1) cell for (a – c), and to the (1 × 1) cell for (d).

A comparison of the side views of the structures in Fig. 5.23 indicates a slight trend that as the *cis* isomer structural stability increases, the fluorine atom gets closer to the surface. The same comparison for Fig. 5.24 indicates the opposite effect. Namely, the *trans* isomer structural stability appears to be enhanced by increased distance between the fluorine atom and the surface. In fact, the side views of Fig. 5.24 (a) and (d) are very similar. This indicates that the molecule in the most stable *trans*-69 dimer chain structure, is essentially the same as that in the *trans* monolayer.

The energetics for the 69 and 96 dimer chains are shown collectively in Table 5.11. The key result is the finding that there is a relatively large energy difference between $E_{ads}$ of these two orientations of the chains and that these chains are slightly more stable than a 66 chain for the same isomer. As we will discuss in the next section, this finding has important implications for the growth of the dimer row and the formation of the domain boundary. The orientation 69 of the *trans* dimer chain and the orientation 96 of the *cis* dimer chain are about 0.01 and 0.04 eV, respectively, more stable than the corresponding 66 orientation of the chains. In contrast, the orientation 96 of the *trans* dimer chain and the orientation 69 of the *cis* dimer chain are about 0.17 and 0.09 eV, respectively, less stable than the corresponding 66 orientation of the chains. As shown in Table 5.11, these energy differences can be traced back to the differences in the row-row interaction energies $E_{int,\ perp}$ of the dimer chains. A common feature of the *trans* and *cis* chains is the result that the row-row interactions are repulsive when the methyl groups of the molecules in the dimer unit of the chains face each other.

A more detailed account of the molecule-molecule interactions in the dimer chains is obtained from our results for isolated dimers in the (3 × 2) cell. The starting molecular geometries for the geometrical optimization of the isolated dimers were based on the structure of the primitive units of the dimer chain in the (3 × 2) cell. The top views of all the isolated *trans* and *cis* dimers are shown in Figs. 5.25 and 5.26, respectively and their energetics are shown in Table 5.12. The difference between adsorption energies per molecule of the *trans* and *cis* isolated dimers is essentially the same as between the dimer chain and monolayer.

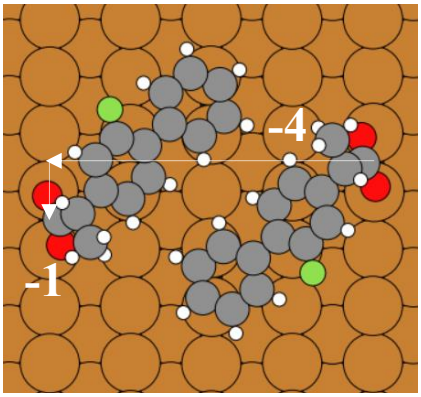


*trans*-96, (-4, -1), -2.80 eV

(a)

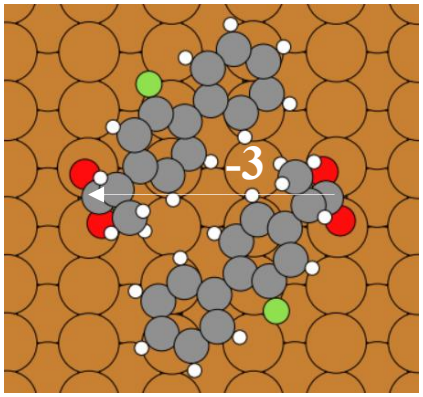


*trans*-96, (-3, 0), -2.88 eV

(b)

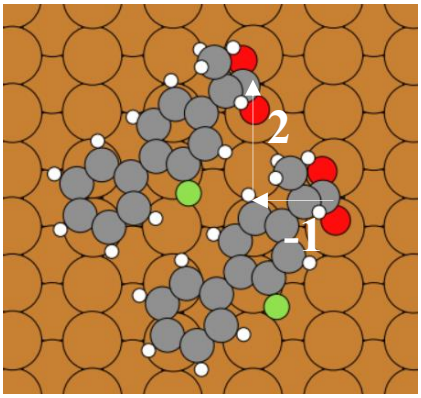


*trans*-66, (-1, 2), -2.88 eV

(c)

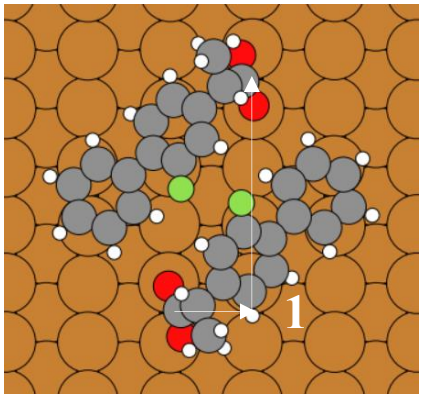


*trans*-69, (1, 4), -2.92 eV

(d)

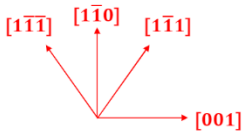


**Figure 5.25:** Top views of the isolated *trans* dimers as indicated by their orientations and footprints. The Cu(110) crystallographic directional indices are shown by the red arrows. Adsorption energies per molecule ($E_{ads}$) are shown with each structure. All these structures were optimized in the (3 × 2) cell.

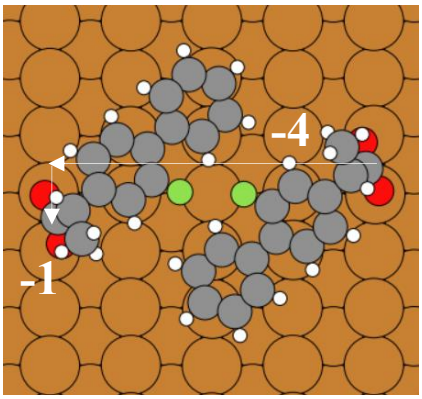


*cis*-69, (-4, -1), -2.73 eV

(a)

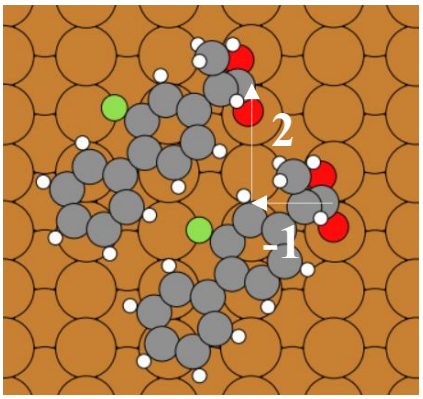


*cis*-66, (-1, 2), -2.74 eV

(b)

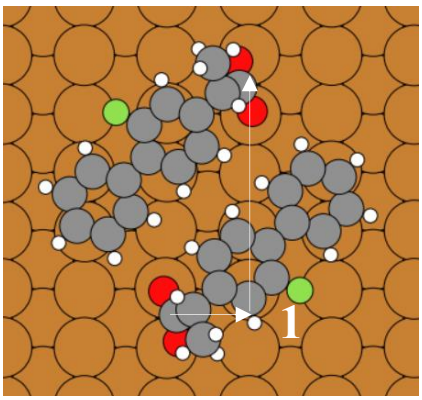


*Cis*-96, (1, 4), -2.82 eV

(c)

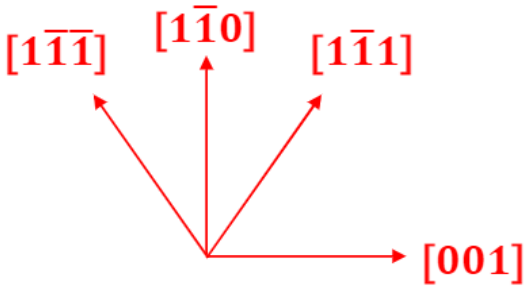


**Figure 5.26:** Same as Fig. 5.25 but for the isolated *cis* dimers.

The interaction energy per molecule $E_{int}$ for the isolated dimer is defined in analogous manner as for the dimer chain and is given by the difference of $E_{ads}$ between the isolated dimer and the isolated monomer in the (3 × 2) cell. As shown from a comparison between $E_{int}$ in Table 5.12 and $E_{int, perp}$ in Table 5.11, $E_{int, perp}$ is larger than $E_{int}$ so that the row-row interaction energy in the dimer chain is not simply given by the molecule-molecule interaction energy of the isolated dimer. This finding is reflected by the parallel interaction energy $E_{int, par'}$ of the dimer chain, which is defined as the difference of $E_{ads}$ between the dimer chain and the isolated dimer in the (3 × 2) cell, is larger than the corresponding energy $E_{int, par}$ for the monolayer.

This behaviour can be accounted for by introducing a next nearest neigbouring interaction between molecules in separate rows. The corresponding interaction energy is then given by $E_{int, cross} = E_{int, par'} - E_{int, par}$. As shown by the results for $E_{int, cross}$ in Table 5.11 and the top views of the dimer chain in Figs. 5.19 and 5.21, this interaction is negligible for the *cis* 69 and *trans* 96 (-4 ,-1) dimer chains with the largest intermolecular distances between next nearest neighbouring molecules in separate rows, attractive at closer distances for the 66, *trans* 69 with footprint (-4 ,-1) and *cis* 96 dimer chains and repulsive at the closest distance for the *trans* 96 dimer chain with footprint (-3,0).

| | [*S*, *trans*] | | | | [*S*, cis] | | |
|---|---|---|---|---|---|---|---|
| | **66** | **69** | **96** | | **66** | **69** | **96** |
| **Footprint** | (-1, 2) | (1, 4) | (-4, -1) | (-3, 0) | (-1, 2) | (-4, -1) | (1, 4) |
| $E_{ads}$ **(eV)** | -2.88 | -2.92 | -2.80 | -2.88 | -2.74 | -2.73 | -2.82 |
| $\Delta E_{ads}$ **(eV)** | 0.00 | -0.04 | 0.07 | 0.00 | 0.14 | 0.15 | 0.06 |
| $E_{int}$ **(eV)** | -0.05 | -0.09 | 0.03 | -0.05 | -0.01 | -0.01 | -0.10 |

**Table 5.12:** Energetics of isolated dimers with different relative orientation and footprints.

In the next subsection we will discuss the rotation domain boundary further.

### 5.3.8: Further Insights into the Experimental STM Observations

Here, we rationalize the observation by R. Raval and C. L. Pang, of the formation of a single domain wall in an enantiomerically pure island and its observed orientation based on our results for the molecule-molecule interaction energies in the previous section. An STM image of such a domain wall between two rotated domains of *S*-FBF molecules is shown in Fig. 5.27.

The domain wall runs along the $[1\bar{1}1]$ direction, which is also along the direction of the primitive surface lattice vector of the *S*-(1 × 1) unit cell of the domain. From a comparison of the STM image in Section 5.3.5 with the simulated image of a monolayer, we conclude that the relative orientation between the upper and the lower domains is 69.


(a)

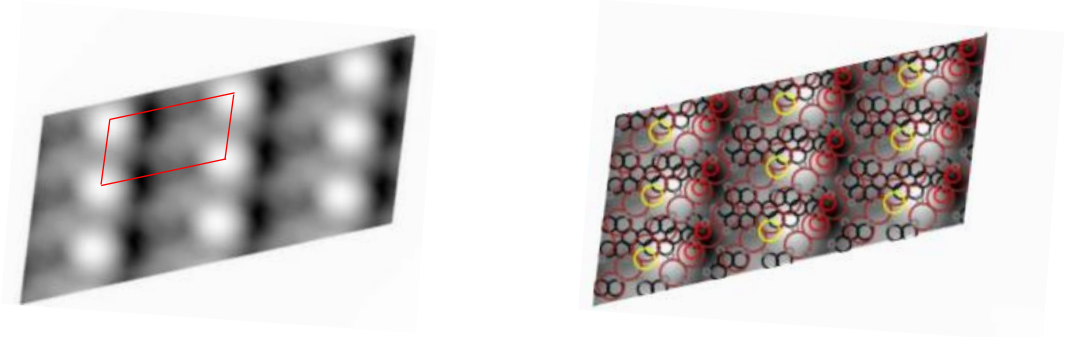

(b) (c)

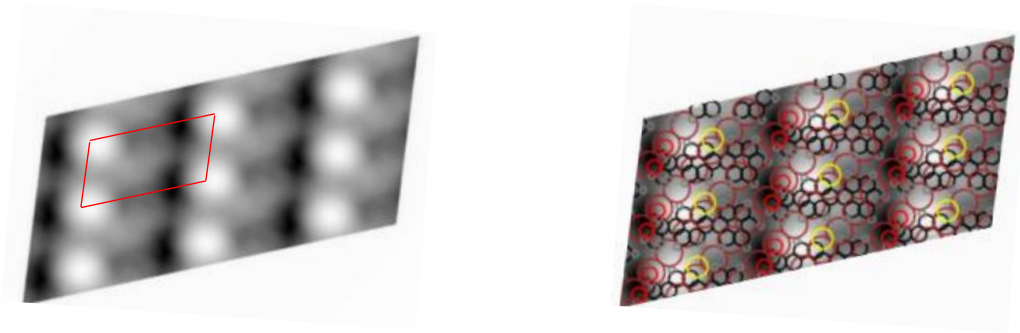

(d) (e)

**Fig. 5.27:** Shown in (a) is an experimental STM image of a domain wall between two domains of adsorbed *S*-FBF rotated by $180^0$. Shown in (b-e) are topographical STM images of the [*S*, *trans*, monolayer] structure, repeated three times in both the [$1\bar{1}\bar{1}$] and [$1\bar{1}1$] directions to show their appearance in the monolayer. The red parallelograms in (b) and (d) depict the *S*-(1 × 1) unit cell. $V_{bias}$ = +0.15 V.

(Experimental STM image in (a) provided by C. L. Pang and R. Raval).

Notice in Fig. 5.27 that the image in (c) is the same as that in (b), with the molecules and surface superimposed. Likewise, for (d) and (e) The images in (b – c) and (d – e) are oriented at $180^0$ with respect to each other. One can see from Fig. 5.27 (b) and (d) that these two images are oriented at $180^0$ to one another, whilst the *S*-(1 × 1) unit cell remained unchanged. This is due to the $C_2$ symmetry of this unit cell. The images in (c) and (e) correspond to those in (b) and (d), respectively, albeit with molecules and surface superimposed. The heads and tails of the FBF molecule between theory and experiment match at $V_{bias}$ = +0.15 V. Matching this with the molecular orientations in (b) and (d) would indicate that the fluorine atoms of molecules in monolayers on either side of the rotation domain boundary, point towards this boundary. This indicates that the domain wall has a 69 orientation.

The observation that the domain walls of islands with *S*-FBF molecules have a 69 orientation is corroborated by the following results from the calculations: (1) the monolayer with *trans* isomers of *S*-FBF has the lowest energy in the *S*-(1x1) unit cell; (2) the 69 orientation of a dimer chain along the $[1\bar{1}1]$ direction has a lower energy than its 96 orientation by about 0.18 eV per molecule. The footprint (1, 4) of the 69 dimer chain is also consistent with the observed STM image of the domain wall.

Furthermore, the formation of a domain wall in either in the lower domain with the 66 stacking pattern, or in the upper domain with a 99 stacking pattern away from the domain wall requires the domain wall to have a 96 orientation, which is more repulsive than the 66 and 99 orientations in the domains by about 0.17 eV per molecule.

## 5.4: Conclusion

In summary, it was found from STM experiments that a racemic (*RS*) mixture of flurbiprofen (FBF) adsorbed into enantiomerically pure islands on the Cu(110) surface. The experimental RAIRS indicated that the molecules were deprotonated upon adsorption, such that their COOH groups were converted to $COO^-$. This has also been observed in similar studies of adsorbed molecules that contain a COOH group.[26, 36-37] All the molecules changed structure upon adsorption. These structural changes as well as the adsorption energy values were indicative of chemisorption. Each equilibrium structure molecule was anchored by its oxygen atoms to two adjacent Cu(110) top sites, separated by the *short-bridge* distance. This anchoring phenomenon has been observed before. [26, 36]

Each island always consisted of two monolayers of FBF either side of a rotation domain boundary- molecules either side of the boundary were rotated at 180$^o$ to each other. LEED was used to find that the monolayer unit cells of *R*- and *S*-FBF were reflectionally symmetrical to one another. DFT was used in an attempt to explain this very strong feature of chiral selectivity.

The *cis* gas phase was slightly more stable than the *trans* by 3 meV. This is a very small energy difference which means that the *cis* and *trans* gas phases were almost degenerate. However, upon adsorption on the surface, the *trans* configuration of FBF was clearly preferred. For the monolayer configurations, adsorption in *S*-(1 × 1) unit cells indicated that *S*-*trans*-FBF was the most stable structure, followed by *R*-*trans*-FBF. *S*-*trans*-FBF was considerably more stable than *R*-*trans*-FBF. This indicated, along with the very small energy difference between the *cis* and *trans* gas phases, that all differences for adsorbed molecules were governed by molecule-surface and molecule-molecule interactions. Repulsive dipole-dipole interactions between molecules did not govern the adsorption energetics. The top views of the monolayer structures in Fig. 5.12 indicated that the *R* enantiomer configurations were not just reflections of the *S* enantiomers. The corresponding side views of these structures in Fig. 5.13 showed that geometries of the monolayer isomers were all substantially different from one another.

However, the side views in Fig. 5.16 showed a molecule of the [*S, trans*], [*S, cis*], [*R, trans*] and [*R, cis*] structure in the monolayer, as a single monomer, and in a chain of monomers. Except for the [*R, cis*] structure, the molecular configuration of each of these structures was found to be essentially independent of whether it was in the monolayer, as a single monomer or as a monomer chain. This lack of geometric variation for all except the [*R, cis*] structure was supported by the differences in adsorption energy. The isolated monomers are all metastable, except the [*R, cis*] case. These interaction energies between the molecules in the monolayer was found to force the *R* and *S* enantiomers into geometries with substantial energy differences, explaining the chiral selectivity. Furthermore, it was found that this interaction between adsorbed molecules was largely due to this direct molecule-molecule interaction. This was consistent with the large vdW contribution to the intermolecular interaction between the adsorbed molecules. For the rotation domain boundary, it was found that the 96 arrangement was so repulsive that it would be very unlikely to form. This explains why 96 was never experimentally observed.

This would then explain an energetic favouring of a 66 molecular stacking, or the formation of a 69 rotation domain boundary. However, 6969…6969 arrangements would be unlikely to form because such an arrangement would contain 96 configurations, which would be energetically unfavourable. This helps to explain the experimental STM observation that only one rotation domain boundary was ever formed per enantiomerically pure island of FBF adsorbed to the Cu(110) surface. It is important to reiterate that the 66 structures do not occur at the rotation domain boundary. The experimental STM images indicated that the molecules either side of the boundary were oriented at $180^{o}$ to each other, indicating that the candidate dimer pairs on either side of the boundary would occur as either 69 or 96 structures, but not the 66 structures. Therefore, the energetics strongly imply that at the domain boundary, each dimer pair was in the 69 configuration.

It was suspected at the start of the project that the enhanced stability was due to a 69 case, allowing F-H hydrogen bonding across the boundary. The F-H distances were certainly small enough for this hydrogen bonding to have occurred, and the lifting of the fluorine atoms away from the surface in the *trans*-69 case would allow more F-H bonding than if the F atom were more closely interacting with the surface, as was found for the *cis* cases. Further potential work towards this end is suggested in Chapter 7.

## 5.5: References


[1] D. Riendeau, S. Charleson, W. Cromlish, J. Mancini, E. Wong, J. Guay, *Can. J. Physiol. Pharmacol.*, 1997, **75**, 1088, PMID: 9365818.

[2] D. D. Leipold, D. Kantoci, E. D. Murray Jr., D. D. Quiggle, and W. J. Wechter, *Chirality*, 2004, **16**, 379, DOI: 10.1002/chir.20053.

[3] O. McConnell, A. Bach, C. Balibar, N. Byrne, Y. Cai, G. Carter, M. Chlenov, L. Di, K. Fan, I. Goljerm Y. He, D. Herold, M. Kagan, E. Kerns, F. Koehn, C. Kraml, V. Marathias, B. Marquez, L. McDonald, L. Nogle, C. Petucci, G. Schlingmann, G. Tawa, M. Tischler, R. T. Williamson, A. Sutherland, W. Watts, M. Young, M. Zhang, Y. Zhang, D. Zhou and D. Ho, *Chirality*, 2007, **19**, 658, DOI: 10.1002/chir.20399.

[4] B. Y. Li and D. T. Haynie, Chiral Drug Separation, in Encyclopedia of Chemical Processing, vol. 1, ed. Sunggyu Lee, 2005, Taylor & Francis, New York.

[5] H. C. Agranat and J. Caldwell, *Nature Reviews Drug Discovery*, 2002, **1**, 753, DOI: 10.1038/nrd915.

[6] R. M. Kellogg, J. W. Nieuwenhuijzen, K. Pouwer, T. R. Vries, Q. B. Broxterman[b], R. F. P. Grimbergen, B. Kaptein, R. M. La Crois, E. de Wever, K. Zwaagstra and A. C. van der Laan, *Synthesis*, 2003, **10**, 1626, DOI: 10.1055/s-2003-40508.

[7] S. M. Barlow and R. Raval, *Surf. Sci. Reports*, 2003, **50**, 201-341, DOI: 10.1016/S0167-5729(03)00015-3.

[8] C. J. Baddeley and N. V. Richardson, *Chirality at Metal Surfaces, in Scanning Tunnelling Microscopy in Surface Science*, eds. M. Bowker and P. Davies, 2010, VCH-Wiley.

[9] A. G. Mark, M. Forster, and R. Raval, *Tetrahedron: Asymmetry*, 2010, **21**, 1125-1134, DOI: 10.1016/j.tetasy.2010.05.042.

[10] M. Ortega Lorenzo, C. J. Baddeley, C. Muryn and R. Raval, *Nature*, 2000, **404**, 376 – 379, DOI: 10.1038/35006031.

[11] Q. Chen and N. V. Richardson, *Nature Materials*, 2003, **2**, 324 – 328, DOI: 10.1038/nmat878.

[12] S. Haq, N. Liu, V. Humblot, A. P. J. Jansen, and R. Raval, *Nature Chemistry*, 2009, **1**, 5, 409 – 414, DOI: 10.1038/nchem.295.

[13] C. Roth, D. Passerone and K. H. Ernst, *Chem. Commun*., 2010, **46**, 8645 – 8647. DOI: 10.1039/c0cc03060k.

[14] W. Y. Cheong and A. J. Gellman, *J. Phys. Chem. C*, 2011, **115**, 1031, DOI: 10.1021/jp105520t.

[15] S. De Feyter, A. Gesquiere, K. Wurst, D. B. Amabilino, J. Veciana, and F. C. De Schryver, *Angew. Chem. Int. Ed.*, 2001, 40, 17, 3217 – 3220, DOI: 10.1002/1521-3773.

[16] L. Perez-Garcia and D. B. Amabilino, *Chem. Soc. Rev.*, 2007, **36**, 941 – 967, DOI: 10.1039/B610714A.

[17] S. Katano, Y. Kim, H. Matsubara, T. Kitagawa and M. Kawai, *J. Am. Chem. Soc.*, 2007, **129**, 9, 2511 – 2515, DOI: 10.1021/ja065893v.

[18] P. Besenius, G. Portale, P. H. H. Bomans, H. M. Janssen, A. R. A. Palmans and E. W. Meijer, *Proc. Nat. Acad. Sci.*, 2010, **107**, 42, 17888 – 17893, DOI: 10.1073/pnas.1009592107.

[19] N. Abdurakhmanova, A. Floris, T. C. Tseng, A. Comisso, S. Stepanow, A. De Vita and K. Kern, *Nature Comm.*, 2012, **3**, 940, DOI: 10.1038/ncomms1942.

[20] A. Della Pia, M. Riello, A. Floris, D. Stassen, T. S. Jones, D. Bonifazi, A. De Vita and G. Costantini, *Acs Nano*, 2014, **8**, 12356-12364, DOI: 10.1021/nn505063w.

[21] R. Otero, M. Lukas, R. E. A. Kelly, W. Xu, E. Laegsgaard, I. Stensgaard, L. N Kantorovich and F. Besenbacher, *Science*, 2008, **319**, 312 – 315, DOI: 10.1126/science.1150532.

[22] I. Temprano, G. Thomas, S. Haq, M. S. Dyer, E. G. Latter, G. R. Darling, P. Uvdal and R. Raval, R., *J. Chem. Phys.*, 2015, **142**, 101916, DOI: 10.1063/1.4907721.

[23] P. Donovan, A. Robin, M. S. Dyer, M. Persson and R. Raval, *Chem. Euro. J.*, 2010, **16**, 11641 – 11652, DOI: 10.1002/chem.201001776.

[24] M. Forster, M. S. Dyer, M. Persson and R. Raval, *J. Am. Chem. Soc.*, 2011, **133**, 15992- 16000, DOI: 10.1021/ja202986s.

[25] M. Forster, M. S. Dyer, M. Persson and R. Raval, *J. Am. Chem. Soc.*, 2011, **131**, 10173- 10181, DOI: 10.1021/ja9020364.

[26] G. R. Darling, M. Forster, C. Lin, N. Liu, R. Raval and A. Hodgson, *Phys. Chem. Chem. Phys.*, 2017, DOI: 10.1039/C7CP00622E.

[27] R. B. Rankin and D. S. Sholl, *J. Phys. Chem. B*, 2005, **109**, 16764 – 16773, DOI: 10.1021/jp0535700.

[28] M. Forster, M. S. Dyer, M. Persson and R. Raval, *Angew. Chem. Int. Ed.*, 2010, **49**, 2344 – 2348, DOI: 10.1002/anie.200904979.

[29] G. Kresse and J. Furthmüller,. *Phys. Rev. B: Condens. Matter Mater. Phys.*, 1996, **54**, 11169– 11186, DOI: 10.1103/PhysRevB.54.11169.

[30] J. Klimes, D. R. Bowler and A. J. Michaelides, *Phys.: Condens. Matter*, 2010, **22**, 022201, DOI: 10.1088/0953-8984/22/2/022201.

[31] J. Klimes, D. R. Bowler and A. J. Michaelides, *Phys. Rev. B*, 2011, **83,** 195131, DOI: 10.1103/PhysRevB.83.195131.

[32] G. Kresse and D. Joubert, *Phys. Rev. B: Condens. Matter Mater. Phys.* 1999, **59**, 1758– 1775, DOI: 10.1103/PhysRevB.59.1758.

[33] J. Tersoff and D. R. Hamann, *Phys. Rev. Lett.*, 1983, **50**, 1998 – 2001, DOI: 10.1103/PhysRevLett.50.1998.

[34] N. Lorente and M. Persson, *Faraday Discuss.*, 2000, **117**, 277-290, DOI: 10.1039/B002826F.

[35] I. Scivetti and M. Persson, *J. of Phys: Cond. Matt.*, 2017, **35**, 355002, DOI: 10.1088/1361-648X/aa7c3a.

[36] A. Robin, L. Marnell, J. Bjork, M.S. Dyer, P.S. Bermudez, S. Haq, S.D. Barrett, M. Persson, A. Minoia, R. Lazzaroni and R. Raval, *J. Phys. Chem. C*, 2009, **113**(30), 13223–13230, DOI: 10.1021/jp9017579.

[37] T.W. White, D.A. Duncan, S. Fortuna, Y-L. Wang, B. Moreton, T-L. Lee, P. Blowey, G. Constantini, D.P Woodruff, *Surface Science*, 2018, **668**, 134 – 143, DOI: 10.1016/j.susc.2017.10.025.

# Chapter 6

# Tautomerization of Oxa-hemiporphycene Adsorbed to Cu(111)

## 6.1: Introduction

At the beginning of quantum chemistry, the quantum tunnelling of electrons was recognised and found to have a significant role in chemical and biological reactions.[1-5] Intramolecular H-atom transfer reactions (tautomerization) in organic molecules have served as a significant model for studying hydrogen dynamics.[6-8] Low temperature STM can be used to precisely control tunnelling dynamics,[9-10] including hydrogen atom diffusion.[11] Porphycene is the first synthesized structural isomer of porphyrin,[12] which has turned out to be an interesting model of intramolecular hydrogen bonding and double hydrogen atom transfer.[10, 13-15] One interesting feature of this is that tautomerization of a single porphycene molecule can be induced by various stimuli, including heat, light and electrons.[16-20]

The studies of tautomerization of porphyrin molecules and their derivatives on metal surfaces by scanning tunnelling microscopy (STM) have attracted a lot of interest in recent years.[10, 15, 21-25] This interest stems from the possibilities to measure directly hydrogen transfer rates in single, adsorbed molecules and also to induce transfer by inelastic electron tunnelling. For instance, a concerted transfer of two hydrogen atoms via quantum tunnelling in a porphycene molecule adsorbed on a Ag(110) surface was identified in a combined STM and DFT study.[10] However, all these studies have so far been limited to tautomerization of molecules involving two hydrogen atoms.

The present DFT study of single hydrogen transfer in a 22-oxa-hemiporphycene (OHPc) molecule adsorbed on a Cu(111) surface was motivated by the recent low temperature STM experiments of Jaekel and Grill.[26] This molecule has some interesting properties which makes it interesting for the study of hydrogen transfer. Following the deposition of a molecule of OHPc on the Cu(111) surface at a substrate temperature of 7 K, mostly *trans* tautomers of OHPc were observed by STM measurements. In these experiments, they were able to switch reversibly between the *trans* and a *cis* tautomer by inelastic electron tunnelling.

As shown by the schematic of OHPc in Fig. 6.1, there are two imine nitrogen atoms, one amine nitrogen atom and one oxygen atom The amine nitrogen atom for a given tautomer is that which is bonded to the hydrogen atom within the molecular cavity, forming the NH group. The H atom in the molecular cavity can be bonded to any of these three N atoms. Therefore, the tautomerization of the molecule involves only a single H atom and there are three different tautomers.

Furthermore, the different lengths of the bridges between the pyrrole groups makes the molecule asymmetric and there are in principle three different pathways for hydrogen transfer between the tautomers: *trans* ↔ *left cis* ↔ *right cis* ↔ *trans.* One key question raised by the experiments is the origin of the observation of two different voltage thresholds for hydrogen transfer which will be resolved in our DFT study.

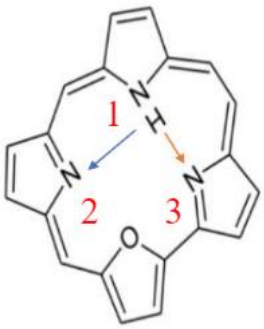


**Figure 6.1:** Schematic of the OHPc molecule in its *trans* configuration. When the H atom is instead bonded to the N atom at the position '2', as indicated by the blue arrow, this will be referred to as the *left cis* configuration. When the H atom is bonded to the N atom at the position '3', as indicated by the red arrow, this will be referred to as the *right cis* configuration. (Image of the molecular structure provided by L. Grill and S. Jaekel).

The details surrounding the DFT calculations are covered in Section 6.2. The rest of this chapter is organized as follows: the computational details for the DFT calculations (Section 6.2), followed by the results of these calculations (Section 6.3). Within Section 6.3, the gas phase, the equilibrium structures of adsorbed tautomers on the Cu(110) surface, the simulation of STM images with comparison to experiment and the energy barriers between these equilibrium structures are all investigated. This is then followed by the conclusions drawn from these calculations (Section 6.4).

## 6.2: Computational Details

Periodic DFT calculations were performed using version 5 of VASP.[27] The PAW method was used to treat the electron-ion core interactions.[28] The effects of exchange-correlation were handled by the vdW-DF-cx exchange-correlation functional[29-31] which includes vdW interactions.

The gas phase OHPc molecules (for the *trans* and each *cis* configuration) were modelled in a super cell of size (21 × 21 × 15) $Å^3$. The gas phase $H_2$ molecule was modelled in a unit cell of size (11 × 11 × 11) $Å^3$. These cells were adequately sized in order to isolate each molecule from its periodic images due to the periodic boundary conditions. Each super cell was sampled with a (1 × 1 × 1) *k*-point mesh.

The adsorbed OHPc molecule (in *trans* or either *cis* configuration) on the Cu(111) surface was represented in super cells using (5, 0; -3, 6) and (6 × 6) surface unit cells where the surface was represented by a Cu slab with four layers and a vacuum region of about 30 Å. The (5, 0; -3, 6) cell was used to find the equilibrium geometric structure. The (6 × 6) cell was used in the simulation of STM images of the equilibrium structures in order to decouple the periodic images. The (5, 0; -3, 6) and (6 × 6) unit cells are shown below in Fig. 6.2.

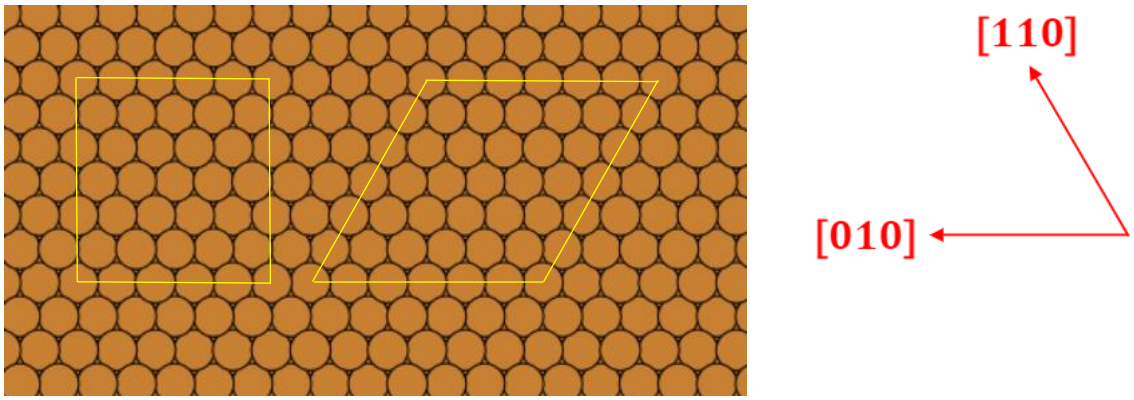


**Figure 6.2:** The (5, 0; -3, 6) (LHS) and the (6 × 6) (RHS) surface unit cell on the Cu(111) surface. The Cu(111) crystallographic directional indices are shown by the red arrows.

An estimated error in adsorption energy of less than 0.02 eV was needed for the work in this chapter. To achieve this estimated error, the Brillouin zones of the (5, 0; -3, 6) and (6 × 6) unit cells were sampled with *k*-point meshes of (8 × 8 × 1) and (12 × 12 × 1), respectively (see Appendix C, Subsection C.1.1). This meant that the number of *k*-points required to sample either cell was 8 × 8 × 1 = 64 and 12 × 12 × 1 = 144, respectively. The (5, 0; -3, 6) cell was used exclusively to find the equilibrium geometric structures. This is because sampling the Brillouin zone of the (5, 0; -3, 6) cell required only 64 *k*-points, as opposed to the 144 *k*-points needed to sample the (6 × 6) cell. This meant that achieving convergence of DFT calculations in the (5, 0; -3, 6) cell was much less computationally expensive than for the (6 × 6) cell.

The value of the plane wave cut-off energy used for all calculations in this chapter was 400 eV. The estimated errors in the adsorption energy due to $E_{cut}$ for the (5, 0; -3, 6) and (6 × 6) cells, were 0.003 and 0.007 eV, respectively (see Appendix C, Subsection C.1.2). During all the calculations, the bottom two layers of the Cu slab were constrained at the calculated lattice constant of 3.579 Å.[32] All geometrical optimizations were performed until the ionic forces were less than 0.01 eV/ Å. Dipole corrections were applied in all calculations in order to decouple the dipole-dipole interactions between the periodic images of adsorbed OHPc structures in the perpendicular direction to the Cu(111) surface.

The topographic STM images in the (6 × 6) cell were simulated using the Tersoff-Hamann approximation at constant LDOS.[33-34] The minimum energy paths (MEPs), the transition structures and associated potential energy barriers between a pair of equilibrium configurations were calculated using the climbing image, nudged elastic band (CI-NEB) method[35-37] and the FIRE optimiser as provided by the transition state tools of VASP. [27] The image-dependent pair potentials (IDPP) algorithm was used to set up the intermediate images between the pair of equilibrium structures.[38] The images were geometrically optimized until the ionic forces were less than 0.01 eV/ Å.

## 6.3: Results and Discussion

Firstly, the calculated equilibrium structures of the gas phase and the adsorbed OHPc, as obtained from geometric optimizations are presented. Secondly, the simulated STM images of these structures are compared to the observed experimental images. Finally, calculated minimum energy paths (MEPs), energy barriers and transition structures are presented.

### 6.3.1: Modelling the Gas Phase OHPc

The optimized structures of the three tautomers of OHPc in the gas phase are shown below in Fig. 6.3. There are three inequivalent ways for an H atom to bind to the N atoms of OHPc and the corresponding tautomers are called *trans*, *left cis* and *right cis* OHPc. The *left cis* OHPc and *right cis* OHPc are inequivalent due to the different number of C atoms in the bridges between the pyrrole groups in the macrocycle. All the tautomers are found to be planar.

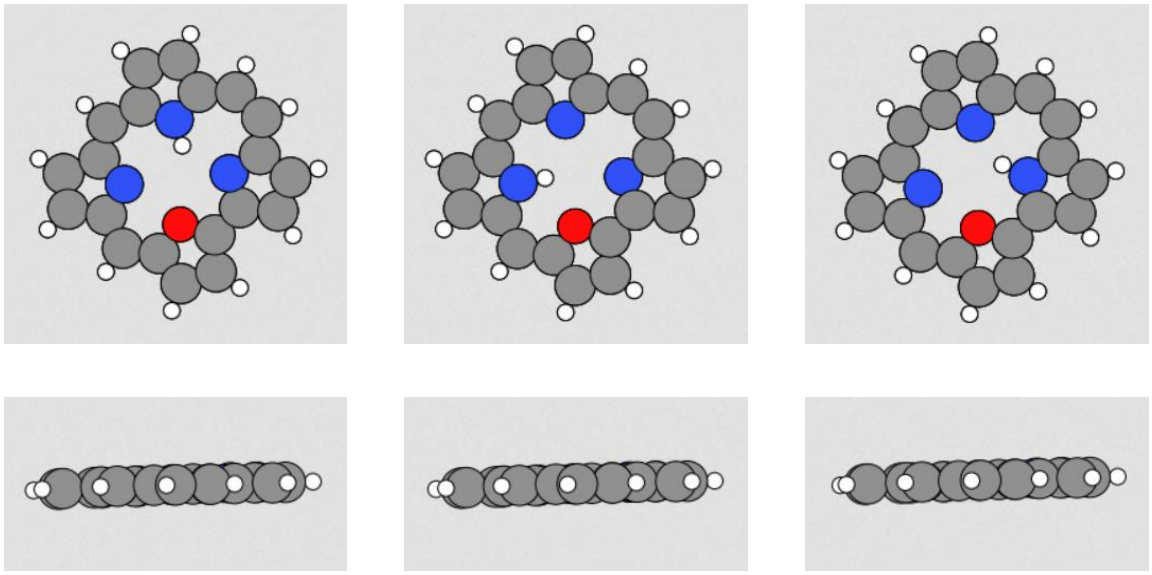

(a) (b) (c)

**Figure 6.3:** The top and side views of (a) the *trans*, (b) *left cis* and (c) right *cis* OHPc tautomers.

The relative total energies and N-N interatomic distances of the three O-HPc tautomers are summarized below in Table 6.1.

| **Tautomer** | **$\Delta E$ (eV)** | **$N^1$-$N^2$ (Å)** | **$N^1$-$N^3$ (Å)** | **$N^2$-$N^3$ (Å)** |
|---|---|---|---|---|
| *trans* | 0.00 | 3.11 [$N^1$] | 2.92 [$N^1$] | 3.99 |
| *right cis* | 0.15 | 3.18 | 2 85 [$N^3$] | 3.98 [$N^3$] |
| *left cis* | 0.28 | 2.99 [$N^2$] | 3.08 | 3.98 [$N^2$] |
| OHPc(-H) | 3.02 | 3.08 | 3.01 | 4.01 |

**Table 6.1:** Calculated relative total energies and N-N interatomic distances of the three different OHPc tautomers. The amine N atoms are labelled in red and in brackets for each structure. The $N^1$, $N^2$ and $N^3$ atoms correspond to the N atoms labelled as '1', '2' and '3' in Fig 6.1. The bottom row shows the dehydrogenation energy and the corresponding interatomic distances of the dehydrogenated OHPc.

As shown by the calculated, relative total energies in Table 6.1, the most stable tautomer is the *trans* tautomer, whereas the *left cis* tautomer is the least stable one. As also shown in Table 6.1, the dehydrogenation energy of the inner H atom of the *trans* tautomer is about 3 eV. This energy is defined as the formation energy for the dehydrogenation reaction,

$$\mathrm{OHPc}_{trans} \rightarrow \mathrm{OHPc}(-\mathrm{H}) + \frac{1}{2}\mathrm{H}_2, \tag{6.1}$$

and is then given by,

$$\Delta E = E[\mathrm{OHPc}(-\mathrm{H})] + \frac{1}{2}E[\mathrm{H}_2] - E[\mathrm{OHPc}_{trans}]. \tag{6.2}$$

Table 6.1 shows also the various interatomic distances between the N atoms in the macrocycle. A somewhat surprising result is that the $N^1$-$N^3$ interatomic distances are in many cases except for *left cis*, shorter than the $N^1$-$N^2$ interatomic distance, despite the C atom bridge between the pyrrole groups of the $N^1$ and $N^3$ atoms containing two atoms, whereas the corresponding bridge between the pyrrole groups of the $N^1$ and $N^2$ atoms contains only one atom. These distances change also substantially with the tautomer, whereas the $N^2$-$N^3$ interatomic distance shows only minor changes. As shown in Table 6.2, this behaviour of the N-N interatomic distances is also reflected in the interatomic distances between the H atom and the imine N atoms (N atoms that are not bonded to the H atom). For instance, in the case of the *trans* tautomer the $N^3$-H distance is shorter by about 0.6 Å than the $N^2$-H distance, which is expected to make the energy barrier for the hydrogen transfer from *trans* to *right cis* to be lower than the one from *trans* to *left cis*. The N-H bonding distance for amine N atoms (N atoms which are bonded to the H atom) differ slightly among the different tautomers, but do not follow simply the trend over the total energies.

| **Structure** | **$N^1$-H (Å)** | **$N^2$-H (Å)** | **$N^3$-H (Å)** |
|---|---|---|---|
| *trans* | 1.04 | 2.64 | 2.07 |
| *right cis* | 1.90 | 3.13 | 1.06 |
| *left cis* | 2.34 | 1.03 | 2.96 |

**Table 6.2:** Calculated N-H interatomic distances of the three tautomers. The $N^1$, $N^2$ and $N^3$ atoms correspond to the N atoms labelled as '1', '2' and '3' in Fig 6.1. The distances quoted in red indicate amine N atoms.

6.3.2: Equilibrium Structures of Adsorbed Tautomers of OHPc

Since *trans* OHPc is the most stable tautomer in the gas phase, the equilibrium structure of the adsorbed *trans* OHPc was first determined from structural optimisation at various different initial adsorption sites and orientations of the adsorbed molecule. The *cis* tautomers were then be modelled by moving the H atom of the NH group of the optimised *trans* tautomer, to form both the *left* and *right cis* tautomers. The resulting *cis* tautomers were then structurally optimised. The adsorption energy, $E_{\text{ads}}$, of a OHPc tautomer on Cu(111) was defined as the formation energy of the adsorption reaction equation,

$$\text{OHPc}_{trans} + \text{Cu}(111) \rightarrow \text{OHPc/Cu}(111), \tag{6.3}$$

where $\text{OHPc}_{trans}$ is the *trans* tautomer and $E_{\text{ads}}$ is then given by

$$E_{\text{ads}} = E[\text{OHPc/Cu}(111)] - \{E[\text{OHPc}_{trans}] + E[\text{Cu}(111)]\}. \tag{6.4}$$

In the dehydrogenated case, where H atom shown in Fig 6.1 was removed from the adsorbed molecule, the corresponding adsorption energy, $E_{\text{ads}}$, is defined as

$$\text{OHPc}_{trans} + \text{Cu}(111) \rightarrow \text{OHPc}(-\text{H})/\text{Cu}(111) + \tfrac{1}{2}\text{H}_2\,, \tag{6.5}$$

and $E_{\text{ads}}$ is then given by,

$$E_{\text{ads}} = E[\text{OHPc}(-\text{H})/\text{Cu}(111)] + \tfrac{1}{2}E[\text{H}_2] - \{E[\text{OHPc}_{trans}] + E[\text{Cu}(111)]\}. \tag{6.6}$$

A schematic of the initial configurations of the adsorbed *trans* tautomer in the structural optimisation is shown in Fig. 6.4. The initial adsorption sites of the *trans* tautomer in the structural optimisation compromised the four different sites where the centre-of-mass of the molecule were placed over the *fcc* and *hcp, top* and *bridge* sites of the Cu(111) surface.

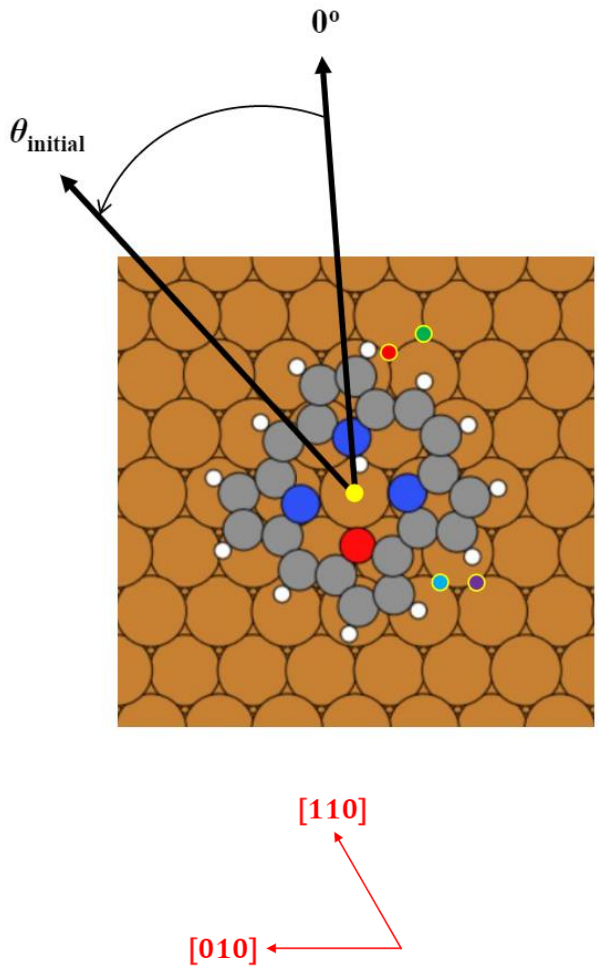


**Figure 6.4:** Schematic of the initial configurations of the adsorbed *trans* OHPc used in the geometrical optimizations. The configuration shown here is with the molecular axis at the top site with orientational angle $\theta_{initial} = 0^0$. The coloured dot represents the following adsorption sites: *top* (yellow), *hcp* (green), *fcc* (red), *left bridge* site (cyan) and *right bridge* site (purple). The $0^0$ position is the line that intersects both the molecular axis site and the N atom in the '1' position of Fig. 6.1. The Cu(111) crystallographic directional indices are shown by the red arrows.

Note that there are two *bridge* sites denoted by *left* and *right bridge* sites that are positioned differently with respect to the molecule as shown in Fig. 6.4. This is to the low symmetry of the molecule and the coordination of the Cu atom in the second layer with respect to the first layer. These *left* and *right bridge* sites were shown by the blue and purple spots, respectively, in Fig. 1.3 (c).

The *hcp* site is on top of a Cu atom in the second layer of the Cu slab. The *fcc* site is on top of a Cu atom in the third layer. Additional initial configurations of the adsorbed *trans* tautomer were obtained for each site by rotations of the molecule by an angle $\theta_{initial}$ around the surface normal over intervals of 60°. The 60° intervals were chosen in the hope that the threefold symmetry of the Cu(111) surface would be useful in reducing the number of $\theta_{initial}$ angles required for the geometric optimizations.

Many of the resulting final structures in Tables 6.3 and 6.4 turned out to be equivalent. This indicated that the 60° interval choice was reasonable. Here, $\theta_{initial} = 0^0$ corresponds to the orientation of the molecule shown in Fig. 6.4. The *fcc*, *hcp* and *top* sites have all a threefold axis of symmetry with respect to the surface, so it was sufficient to consider only $\theta_{initial} = 0°$ and 60°. The *bridge* sites do not have this axis of symmetry, so all six $\theta_{initial}$ angles (0°, 60°, 120°, 180°, 240° and 300°) needed to be included.

The initial configurations of the adsorbed *trans* tautomer derived from different orientations at their respective adsorption sites and their final geometrically optimized structures, denoted by $\Lambda_i$, where $i$ is a positive integer. The adsorption energies are shown for each initial adsorption site and $\theta_{initial}$ in Tables 6.3 - 6.4.

| **Adsorption site** | **$\theta_{initial}$ (°)** | **Final Configuration** | **$E_{ads}$ (eV)** |
|---|---|---|---|
| *Fcc* | 0 | $\Lambda_1$ | -3.69 |
| | 60 | $\Lambda_2$ | -3.69 |
| *Hcp* | 0 | $\Lambda_1$ | -3.69 |
| | 60 | $\Lambda_2$ | -3.69 |
| *top* | 0 | $\Lambda_1$ | -3.69 |
| | 60 | $\Lambda_2$ | -3.68 |

**Table 6.3:** The *fcc*, *hcp* and *top* adsorption sites and the orientational angle $\theta_{initial}$, for the initial configurations of the adsorbed *trans* OHPc, with the corresponding configurations $\Lambda_i$ and adsorption energies of the geometrically optimized structures.

As shown in Table 6.3, the geometrical optimizations of the *trans* OHPc adsorbed in the *fcc*, *hcp* and *top* sites result in two different configurations $\Lambda_1$ and $\Lambda_2$, which have essentially the same $E_{ads}$. The results for the *bridge sites* are shown below in Table 6.4.

| $\theta_{initial}$ (°) | Final Configuration | $E_{ads}$ (eV) |
|---|---|---|
| 0 | $\Lambda_1$ | -3.69 |
| 60 | $\Lambda_2$ | -3.69 |
| 120 | $\Lambda_3$ | -3.47 |
| 180 | $\Lambda_2$ | -3.69 |
| 240 | $\Lambda_1$ | -3.69 |
| 300 | $\Lambda_4$ | -3.45 |

**Table 6.4** Orientational angle $\theta_{initial}$, for the initial configuration of *trans* OHPc adsorbed in the *left bridge* site with the corresponding configuration $\Lambda_i$ and adsorption energy of the geometrically optimised structure. The results for the *right bridge* site are found to be same when comparing the same orientations of the initial configurations of the adsorbed molecule.

In the case of the initial configurations in the *bridge* site, they resulted in two additional configurations $\Lambda_3$ and $\Lambda_4$ but with a larger $E_{ads}$ than for $\Lambda_1$ and $\Lambda_2$. Thus, the most stable structures as obtained from the geometrical optimizations starting from the initial configurations in Tables 6.3 and 6.4 are $\Lambda_1$ and $\Lambda_2$ and are henceforth denoted as $\Lambda_{hcp,\ trans}$ and $\Lambda_{fcc,\ trans}$. These two equilibrium structures are very similar to one another, but are oriented at $180^0$ with respect to one another. They can be distinguished easily from each other by the position of the O atom relative to the *fcc* and *hcp* sites. The O atom of $\Lambda_{hcp,\ trans}$ is nearer to the *hcp* site than to the *fcc* site, and vice versa for $\Lambda_{fcc,\ trans}$. Firstly, the $\Lambda_{hcp,\ trans}$ and $\Lambda_{fcc,\ trans}$ structure are shown below in Fig. 6.5.

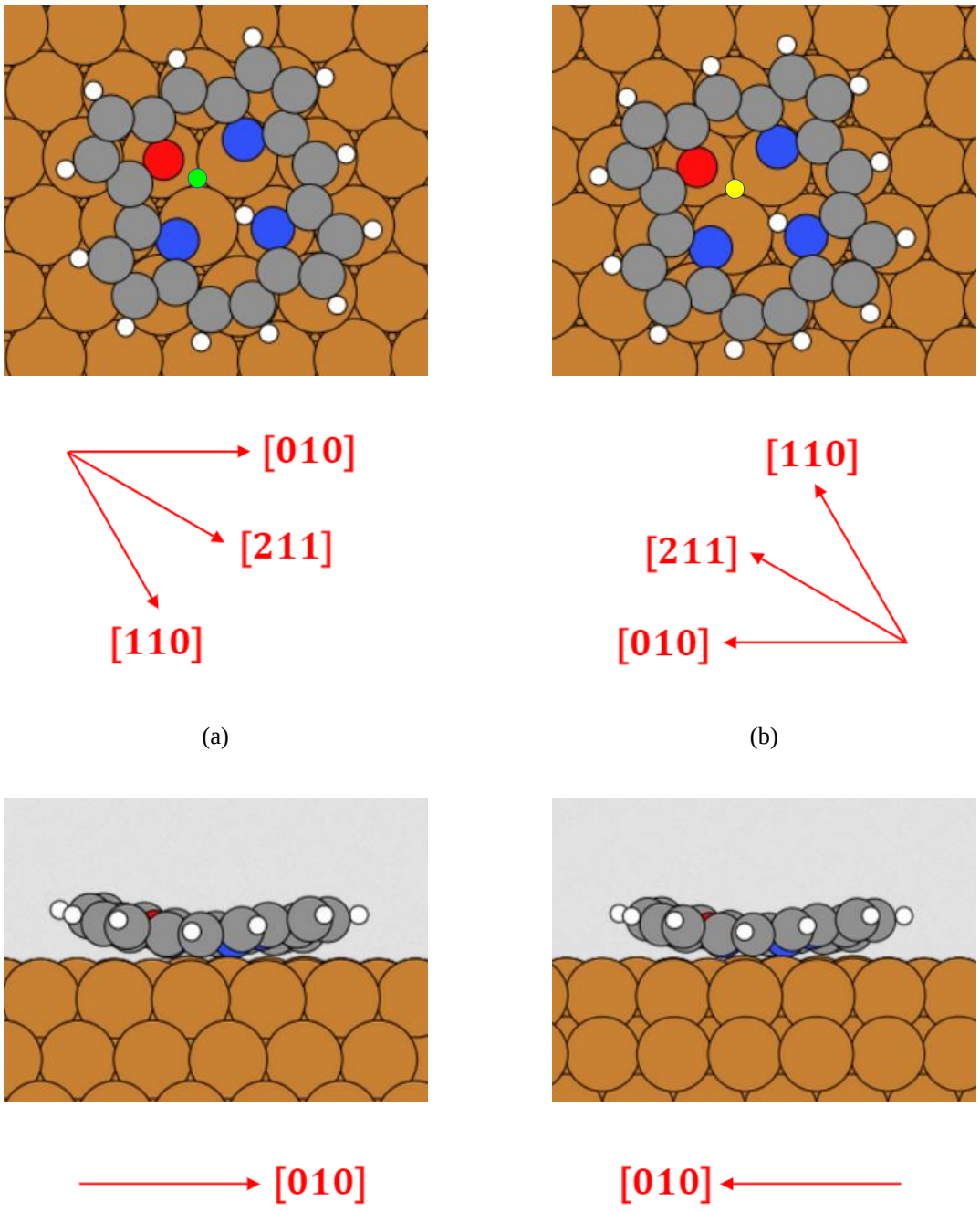


**Figure 6.5:** Top views of the $\Lambda_{hcp,\ trans}$ (a) and the $\Lambda_{fcc,\ trans}$ structure (b). The green dot in (a) is centred at the *hcp* site, whereas yellow dot in (b) is centred at the *fcc* site. Shown in (c) and (d) are the side views corresponding to (a) and (b), respectively. The Cu(111) crystallographic directional indices are shown below each schematic by the red arrows.

The initial *cis* configurations were created by translating the H atom of the NH group of $\Lambda_{hcp,\ trans}$ and $\Lambda_{fcc,\ trans}$ to close proximity of the other N atoms. The resulting *cis* structures from the geometrical optimizations are shown for the *left cis* structures ($\Lambda_{hcp,\ left\ cis}$ and $\Lambda_{fcc,\ left\ cis}$) and for the *right cis* structures ($\Lambda_{hcp,\ right\ cis}$ and $\Lambda_{fcc,\ right\ cis}$) in Figs. 6.6 and 6.7, respectively.

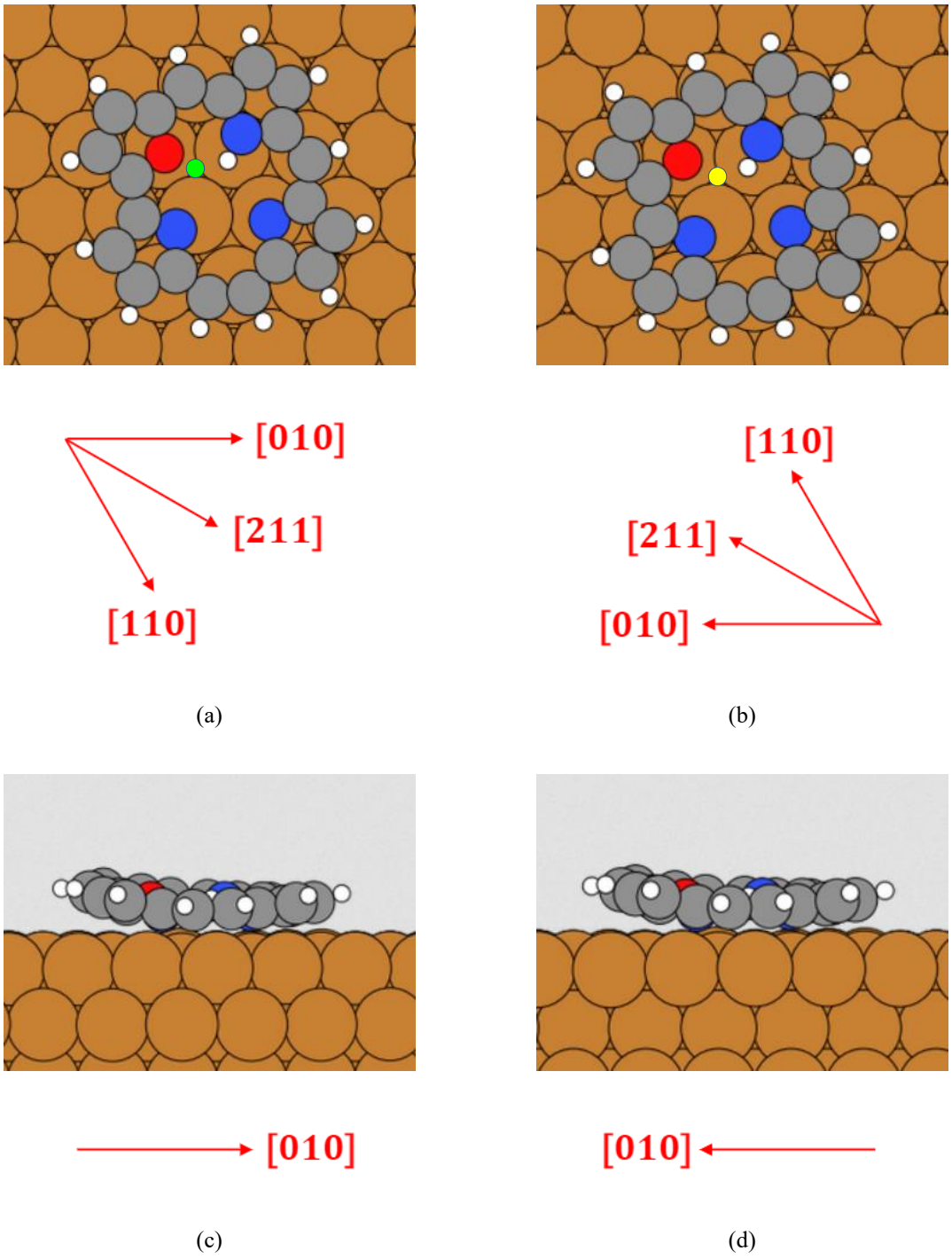


**Figure 6.6:** Same as Fig, 6.5, but for the $\Lambda_{hcp,\ left\ cis}$ (a & c) and the $\Lambda_{fcc,\ left\ cis}$ structure (b & d).

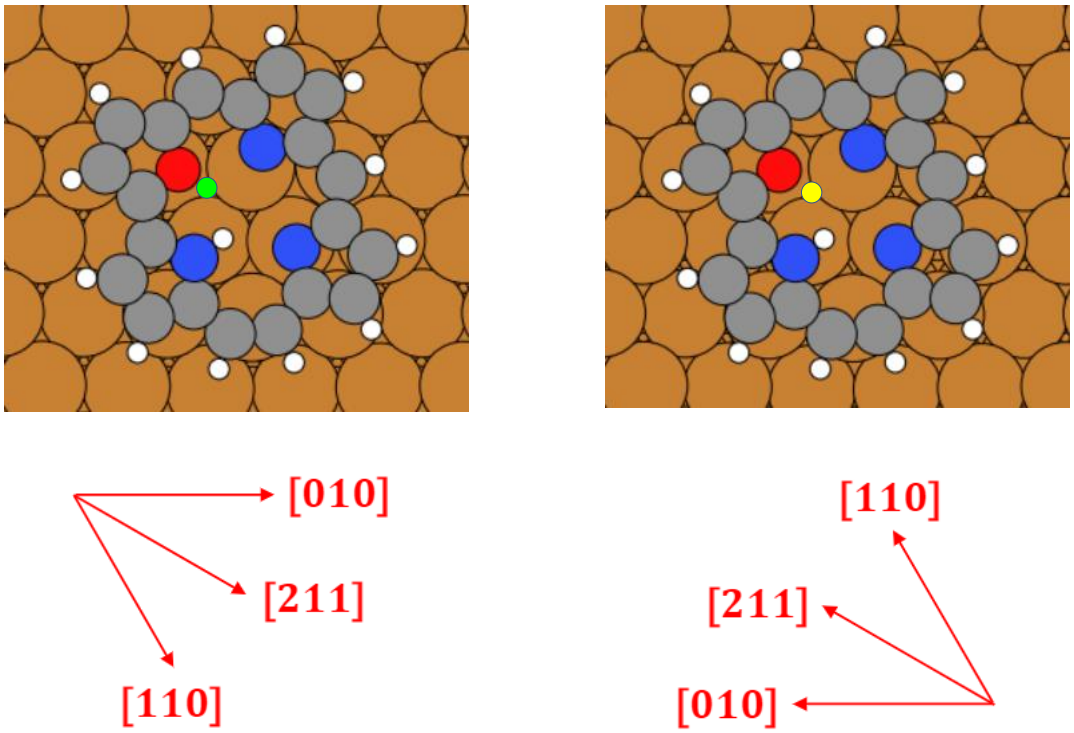


(a) (b)

s

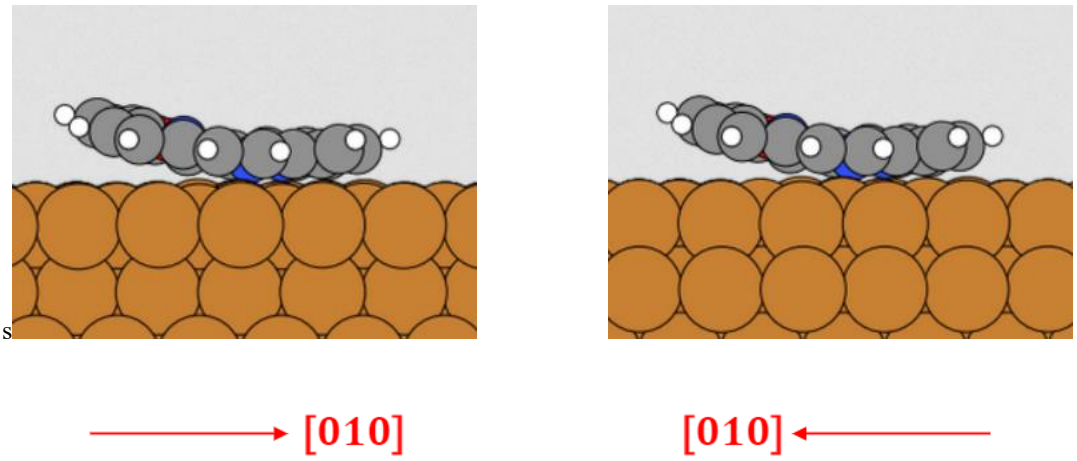


(c) (d)

**Figure 6.7:** Same as Fig, 6.5, but for the $\Lambda_{hcp,\ right\ cis}$ (a & c) and the $\Lambda_{fcc,\ right\ cis}$ structure (b & d).

Finally, the dehydrogenated structures, as obtained from geometrical optimisations following the detachment of the H atom of the NH group of $\Lambda_{hcp,\ trans}$ and $\Lambda_{fcc,\ trans}$, are shown below in Fig. 6.8.

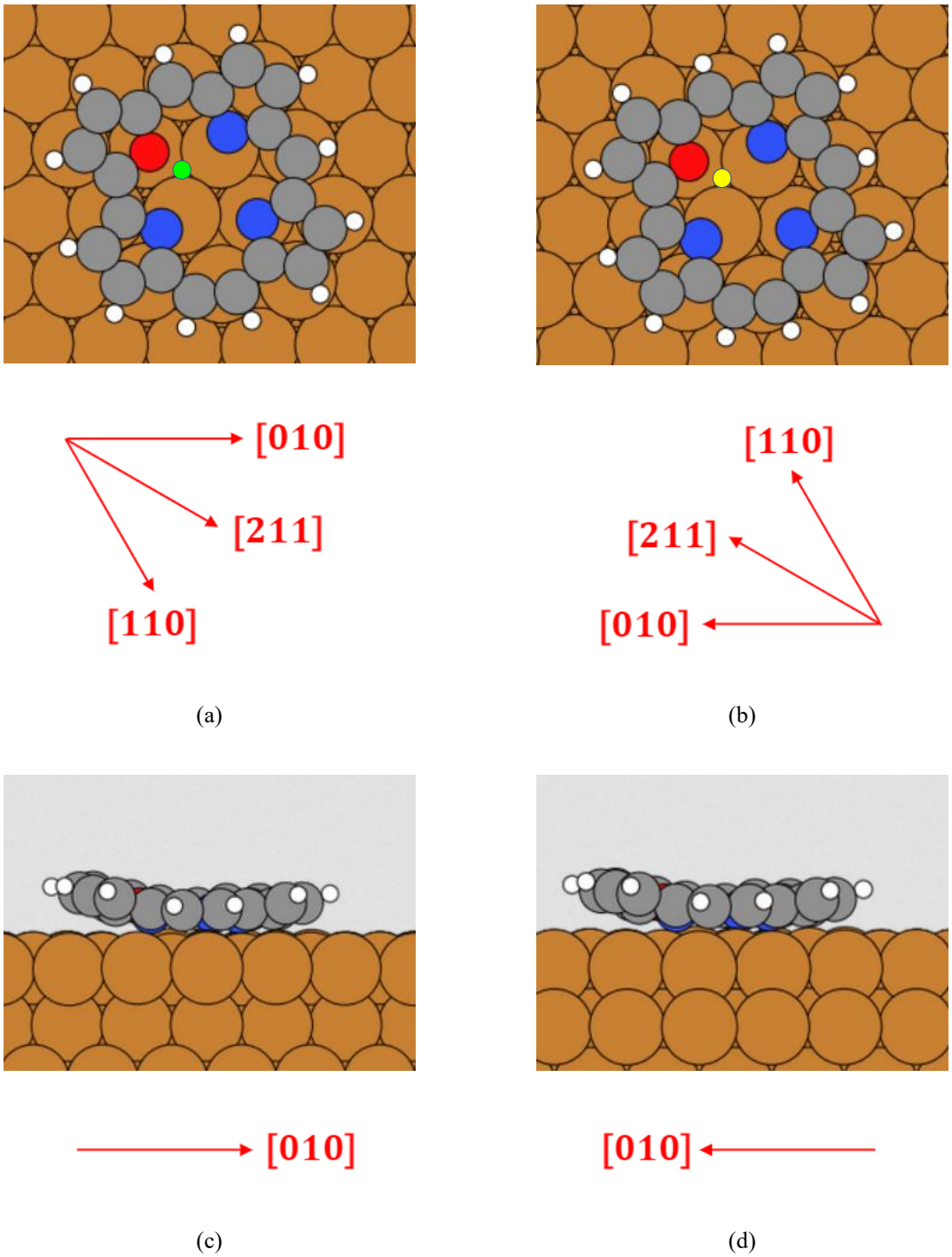


**Figure 6.8:** Top views of the dehydrogenated $\Lambda_{hcp}$ (a) and $\Lambda_{fcc}$ structure (b). The green dot in (a) is centred at the *hcp* site, whereas yellow dot in (b) is centred at the *fcc* site. Shown in (c) and (d) are the side views corresponding to (a) and (b), respectively. The Cu(111) crystallographic directional indices are shown below each schematic by the red arrows.

A common characteristic feature of all the structures in Figs. 6.5 – 6.8 is the bending of the molecule away from the surface. Also, there are no significant changes of the orientations between the adsorbed tautomers and the dehydrogenated molecule. Before presenting and discussing the results for the various interatomic distances of all structures of the adsorbed molecule, we will present and discuss the adsorption energetics summarized in Table 6.5.

| **Tautomer** | $E_{ads}$ (eV) (*hcp*) | $\Delta E_{ads}$ (eV) (*hcp*) | $E_{ads}$ (eV) (*fcc*) | $\Delta E_{ads}$ (eV) (*fcc*) |
|---|---|---|---|---|
| *trans* | -3.69 (-3.78) | 0.00 (0.00) | -3.69 (-3.77) | 0.00 (0.00) |
| *right cis* | -3.68 (-3.77) | 0.01 (0.01) | -3.65 (-3.73) | 0.04 (0.04) |
| *left cis* | -3.63 (-3.72) | 0.06 (0.06) | -3.62 (-3.70) | 0.07 (0.07) |
| OHPc(-H) | -3.04 (-3.13) | 0.65 (0.65) | -3.03 (-3.11) | 0.66 (0.66) |

**Table 6.5:** Calculated adsorption energies $E_{ads}$ and their relative values $\Delta E_{ads}$ for the equilibrium structures of adsorbed OHPc tautomers and dehydrogenated OHPc. The values with and without parentheses were calculated in the (5, 0; -3, 6) and (6 × 6) unit cells, respectively.

The adsorption energies $E_{ads}$ and their relative values $\Delta E_{ads}$ of all structures in Table 6.5 for the (5, 0; -3, 6) and (6 × 6) unit cells show that they are well-converged with system size. There are no significant differences in $E_{ads}$ between the *hcp* and *fcc* adsorption sites in view of the *k*-point sampling error of 0.02 eV. $\Delta E_{ads}$ follows the same trend as the total energies over the tautomers in the gas phase, but the energy differences are reduced substantially. The dehydrogenation energy of the adsorbed *trans* tautomer is given by $\Delta E_{ads}$ = 0.66 eV in Table 6.5. Noteworthy is also the reduction of the dehydrogenation energy by almost a factor of five compared to its gas phase value of $\Delta E$ = 3.02 eV in Table 6.1. The relative thermal population of two levels with an energy difference of $\Delta E_{ads}$ is governed by the Boltzmann factor $\exp(-\Delta E_{ads}/k_B T)$, where $k_B$ is Boltzmann's constant and $T$ is the temperature. Note that in Table 6.5, the smallest difference in $E_{ads}$ is $\Delta E_{ads}$ = 0.01 eV, which is the difference between the *trans* and *right cis hcp* structures. $\Delta E_{ads}$ = 0.01 eV and $T$ = 7 K give a relative population of about $6.35 \times 10^{-8}$.

Thus, an energy difference of 0.01 eV is highly significant at 7 K. The *hcp* and *fcc right cis* structures differ in adsorption energy by 0.04 eV. This is quite a large difference in comparison to the differences between the two *trans*, the two *left cis* and the two dehydrogenated OHPc structures, for which the difference in adsorption energy does not exceed 0.02 eV. An interesting question is whether there would be a thermal population of the *hcp* and *fcc* structures for a given isomer. However, determination of this would require calculation of transfer rates between these two structures. These transfer rates are governed by the energy barrier heights between the structures. These energy barriers were not calculated over the course of this project. Therefore, we cannot currently decide whether we would have a thermal population or not. The calculation of these barriers to determine this would be an important extension of this project.

The interatomic distances for the structures in Table 6.5 are presented below in Tables 6.6 – 6.8. One can see that none of these bonding distance differences are significant enough to explain the large difference in adsorption energy between the *hcp* and *fcc right cis* structures. This means that the reason for this is relatively large energy difference between the two *right cis* structures is quite speculative as there is no data to conclusively suggest why this difference is larger.

| **Site** | **Tautomer** | **$N^1$-Cu (Å)** | **$N^2$-Cu (Å)** | **$N^3$-Cu (Å)** | **O-Cu (Å)** |
|---|---|---|---|---|---|
| *hcp* | *trans* | 2.41 (2.39) | 2.08 (2.08) | 2.12 (2.12) | 2.43 (2.42) |
| | *right cis* | 2.07 (2.06) | 2.04 (2.04) | 2.84 (2.80) | 2.76 (2.74) |
| | *left cis* | 2.06 (2.06) | 2.59 (2.57) | 2.07 (2.07) | 2.62 (2.59) |
| | OHPc(-H) | 2.02 (2.02) | 2.03 (2.03) | 2.04 (2.04) | 2.40 (2.39) |
| *fcc* | *trans* | 2.43 (2.41) | 2.08 (2.08) | 2.11 (2.11) | 2.41 (2.40) |
| | *right cis* | 2.07 (2.07) | 2.05 (2.05) | 2.83 (2.80) | 2.74 (2.72) |
| | *left cis* | 2.07 (2.07) | 2.63 (2.59) | 2.06 (2.07) | 2.60 (2.58) |
| | OHPc(-H) | 2.02 (2.02) | 2.03 (2.03) | 2.04 (2.03) | 2.38 (2.38) |

**Table 6.6:** Calculated nearest neighbour N-Cu and O-Cu interatomic distances for the structures in the *hcp* and *fcc* sites. The $N^1$, $N^2$ and $N^3$ atoms are for the N atoms labelled as '1', '2' and '3' in Fig. 6.1. The N-H distances quoted in red indicate an amine N atom. The values with and without parentheses were calculated in the (5, 0; -3, 6) and (6 × 6) unit cells, respectively.

The molecule-surface bond has been examined using the calculated nearest neighbour N-Cu and O-Cu interatomic distances shown for the $\Lambda_{hcp}$ and $\Lambda_{fcc}$ structures in Tables 6.5 and 6.6, respectively. There are very minor differences between these distances for the two adsorption sites. In all cases the N-H interatomic distances for imine N atoms (N atoms that are not bonded to an H atom) are short, and are about 2.02 – 2.12 Å, whereas the corresponding distances for the amine N atoms (N atoms bonded to a H atoms) are about 0.3 – 0.7 Å larger. Also, the O-Cu distance are a bit larger than the imine N-Cu distances. The bending of the adsorbed molecules is a manifestation of these different bonding distances of the imine and amine N atoms, and the O atoms with the Cu atoms.

The effect of the molecule-surface bond on the intramolecular bonding was examined using the calculated N-N and N-H interatomic distances shown in Table 6.7- 6.8. Also, for these distances, there are very minor differences between these distances for the $\Lambda_{hcp}$ and the $\Lambda_{fcc}$ structures. Compared to the N-N distances in the gas phase there are significant differences in the distances up to about 0.3 Å except for the $N^2$-$N^3$ distances which only show minor changes. In the cases of the *trans* tautomer and the dehydrogenated molecule the ordering between the $N^1$-$N^2$ and the $N^1$-$N^3$ are reversed between the adsorbed and the gas phase molecule.

Furthermore, the difference between the $N^1$-$N^2$ and the $N^1$-$N^3$ distances are dramatically reduced from 0.33 Å to 0.03 Å. The N-H distances for the amine N atoms, as shown in Table 6.8 are essentially the same as in the gas phase. Associated with the significant changes of the N-N distances there are also significant changes of the imine N- H distances upon adsorption, but there is no simple correlation between these two sets of distances. For instance, in the case of the *trans* tautomer, the ordering in magnitude of the imine $N^2$-H and $N^3$-H distances. N-H distances are reversed compared to the $N^1$-$N^2$ and $N^1$-$N^3$ distances.

| Site | Tautomer | $N^1$-$N^2$ (Å) | $N^1$-$N^3$ (Å) | $N^2$-$N^3$ (Å) |
|---|---|---|---|---|
| *Hcp* | *trans* | 3.08 (3.09) [$N^1$] | 3.17 (3.17) [$N^1$] | 3.96 (3.96) |
| | *right cis* | 3.17 (3.17) | 3.14 (3.14) [$N^3$] | 3.96 (3.95) [$N^3$] |
| | *left cis* | 3.09 (3.09) [$N^2$] | 3.27 (3.27) | 4.00 (3.98) [$N^2$] |
| | OHPc(-H) | 3.12 (3.12) | 3.27 (3.27) | 4.00 (3.98) |
| *Fcc* | *trans* | 3.08 (3.08) [$N^1$] | 3.18 (3.18) [$N^1$] | 3.98 (3.97) |
| | *right cis* | 3.17 (3.17) | 3.14 (3.14) [$N^3$] | 3.95 (3.95) [$N^3$] |
| | *left cis* | 3.10 (3.09) [$N^2$] | 3.27 (3.27) | 4.02 (4.00) [$N^2$] |
| | OHPc(-H) | 3.12 (3.12) | 3.27 (3.27) | 4.00 (4.00) |

**Table 6.7:** Calculated N-N interatomic distances for the structures in the *hcp* and *fcc* sites. The amine N atoms are labelled in red and in brackets. The $N^1$, $N^2$ and $N^3$ atoms are for the N atoms labelled as '1', '2' and '3' in Fig. 6.1. The values with and without parentheses were calculated in the (5, 0; -3, 6) and (6 × 6) unit cells, respectively.

| Site | Tautomer | $N^1$-H (Å) | $N^2$-H (Å) | $N^3$-H (Å) |
|---|---|---|---|---|
| *Hcp* | *trans* | 1.03 (1.03) | 2.50 (2.51) | 2.37 (2.37) |
| | *right cis* | 2.29 (2.29) | 3.06 (3.04) | 1.03 (1.03) |
| | *left cis* | 2.52 (2.52) | 1.03 (1.03) | 3.01 (3.00) |
| *Fcc* | *trans* | 1.03 (1.03) | 2.50 (2.50) | 2.39 (2.39) |
| | *right cis* | 2.29 (2.28) | 3.04 (3.04) | 1.03 (1.03) |
| | *left cis* | 2.52 (2.52) | 1.03 (1.03) | 3.02 (3.01) |

**Table 6.8:** Calculated N-H interatomic distances for the structures in the *hcp* and *fcc* sites. The $N^1$, $N^2$ and $N^3$ atoms are for the N atoms labelled as '1', '2' and '3' in Fig 6.1. The distances quoted in red indicate an amine N atom. The values with and without parentheses were calculated in the (5, 0; -3, 6) and (6 × 6) unit cells, respectively.

In Subsection 6.3.3, topographical STM images are simulated for the $A_{hcp}$ and the $A_{fcc}$ equilibrium structures. These are then compared to the experimental STM images.

6.3.3: Simulation of STM Images and Comparison to Experiment

All the simulated and experimental STM images were obtained at a sample bias voltage of + 0.1 V. The simulated topographical STM images for the tautomers shown in Figs. 6.5 – 6.8 are shown below in Fig. 6.9.

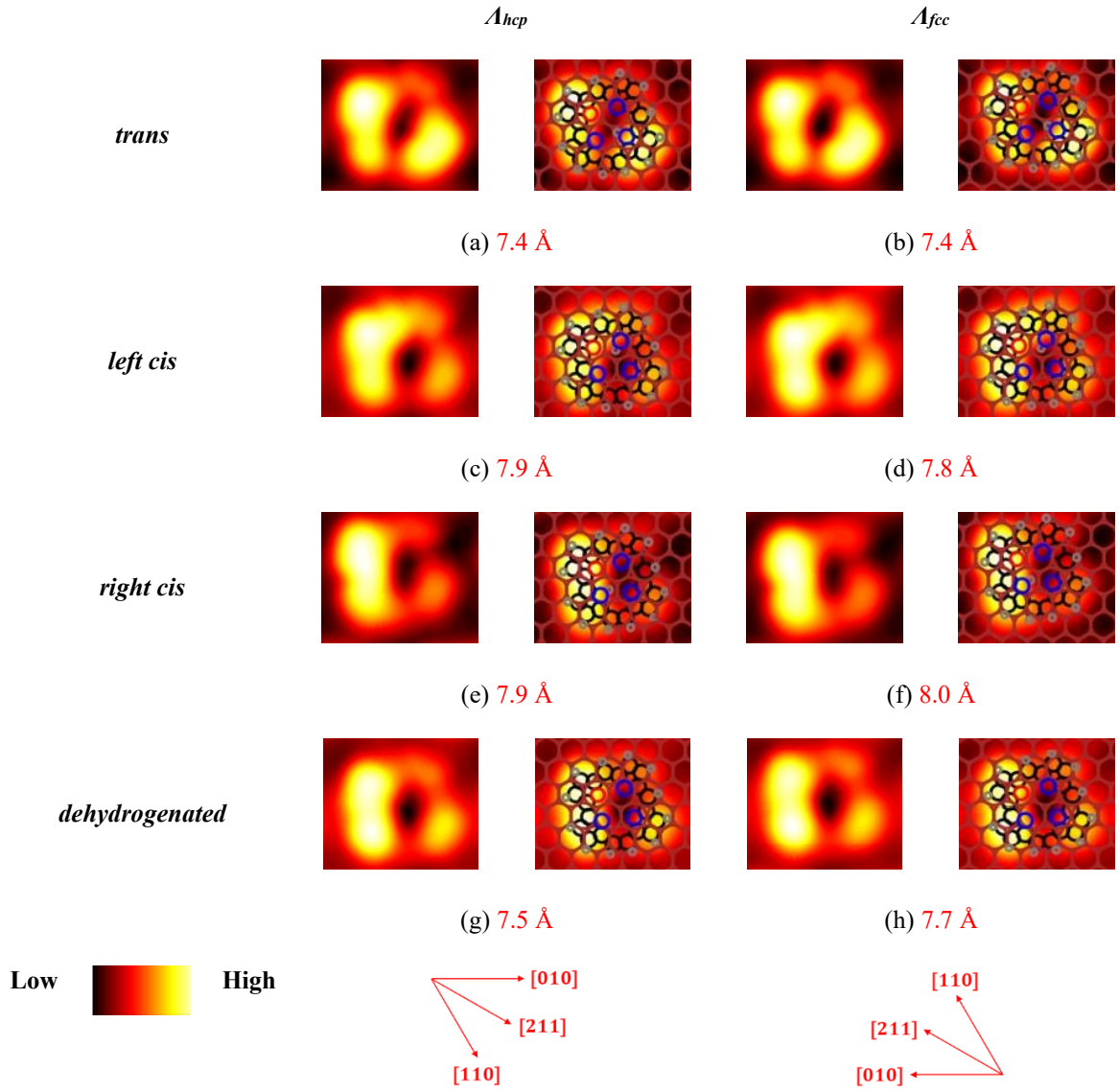


**Figure 6.9:** Simulated topographical STM images of the $\Lambda_{hcp}$ and $\Lambda_{fcc}$ structures. Each RHS image is the same as the LHS, but with superposition of the molecule and Cu(111) top layer. The average tip-surfaces heights are labelled in red. The 'low-high' spectrum shows the relative tip-surface heights. The Cu(111) crystallographic directional indices are shown by the red arrows below (g) and (h), for the $\Lambda_{hcp}$ and $\Lambda_{fcc}$ structures, respectively. The C, Cu, H, N and O atoms are shown by black, brown, grey, blue and red rings, respectively.

The experimentally observed, topographical STM image of a OHPc molecule following deposition on the surface at a substrate temperature of 7 K is shown in Fig. 6.10 (a). The image in (a) matches closely with the simulated image of the *trans* tautomers in Fig. 6.9 (a – b), both in shape and orientation with respect to the [211] surface direction. This match suggests that the experimental image corresponds to a *trans* tautomer, which is corroborated by the molecule being the most stable molecule in the gas phase. The experimental image in (b) closely matches the simulated image of the *right cis* tautomers in Fig. 6.9 (e – f). Finally, the experimental image in (c) has a less convincing match with the simulated image of the dehydrogenated molecule in Fig. 6.9 (g – h).

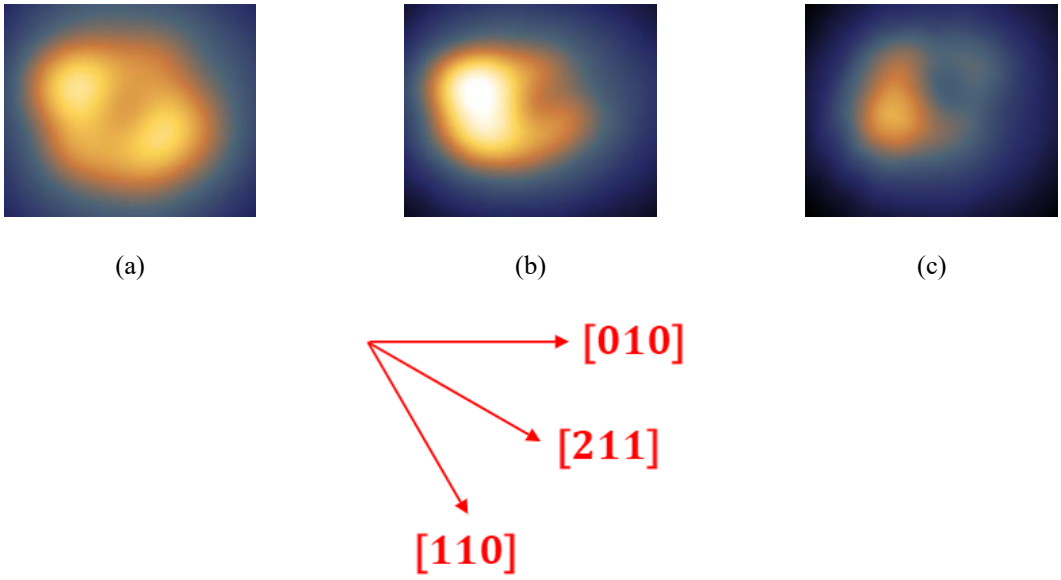


**Figure 6.10:** Experimental topographical STM images of (a) OHPc, (b) the switched OHPc and (c) the dehydrogenated OHPc adsorbed on the Cu(111) surface. The Cu(111) crystallographic directional indices are shown below by the red arrows. (STM images provided by L. Grill and S. Jaekel).

In the next section, we will show that the proposed assignment of the observed tautomers is corroborated by the calculated energy barriers between the *trans* and the *cis* tautomers.

6.3.4: Calculated Energy Barriers between Tautomers

Here we present the calculated energy barriers for hydrogen transfer between the different tautomers and discuss the results in relation to experiments. The potential energy barriers were obtained by calculating minimum energy paths (MEPs) using the climbing image – nudged elastic band (CI-NEB) method as detailed in Section 6.2. $\Delta D_{\mathrm{H}}$ as given by Eq. (3.92) gives the MEP length for the H atom during the transfer between the *trans* and *cis* tautomers. However, it was important to see whether the rest of the molecule moved significantly during the transfer. This motion is described by $\Delta D_{\mathrm{Mol}}$, as given by Eq. (3.91). The values of $\Delta D_{\mathrm{Mol}}$ were found to be considerably more significant than those of $\Delta D_{\mathrm{H}}$. Hence, $\Delta D_{\mathrm{Mol}}$ is that which describes the path length on the barrier plots of Figs. 6.11 – 6.13. Firstly, the gas phase MEPs and barriers are illustrated below in Fig. 6.11.

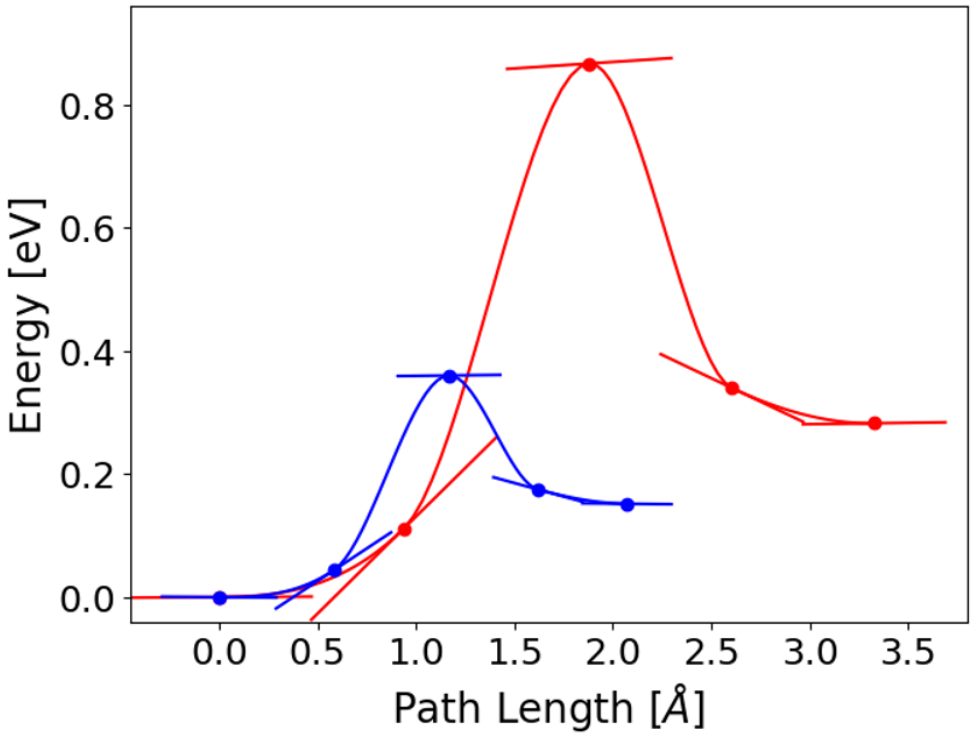


**Figure 6.11:** Calculated MEPs from the *trans* to *left cis* (red) and *trans to right cis* (blue) tautomers of the OHPc molecule in the gas phase. The images and the calculated energy gradients along the MEP are indicated by solid circles and bars, respectively. The *trans* structure is the leftmost point in both the blue and red graphs. The *left cis* and *right cis* structures are represented by the rightmost point in the blue and red graphs, respectively. The transition structure for each calculated MEP is represented by the saddle point in either graph. Both MEP lengths, $\Delta D_{\mathrm{Mol}}$, were calculated by use of Eq. (3.91).

Secondly, the barriers and MEPs for the *trans* to *left cis* transitions are illustrated below in Fig. 6.12.

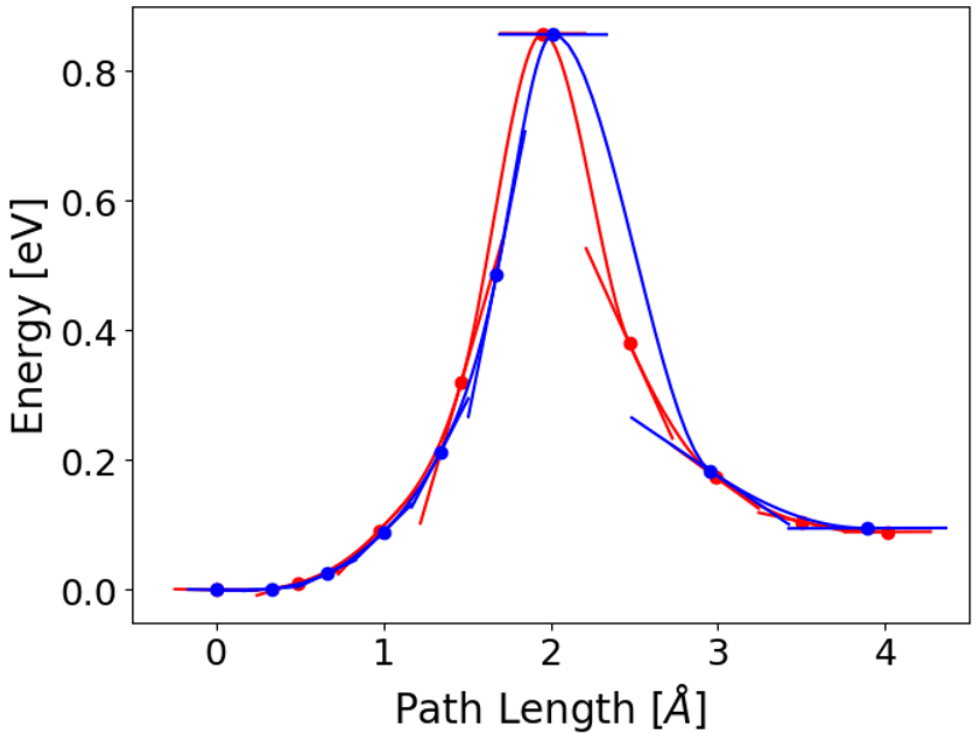


**Figure 6.12:** Calculated MEPs for *trans* to *left cis* of the OHPc molecule on the Cu(111).surface for the *hcp* case (red) and the *fcc* case (blue). The images and the calculated energy gradients along the MEP are indicated by solid circles and bars, respectively. The *trans* and *left cis* structures are represented by the leftmost and rightmost points, respectively, in both the red and blue graphs. The transition structure for each calculated MEP is represented by the saddle point in either graph. Both MEP lengths, $\Delta D_{\mathrm{Mol}}$, were calculated by use of Eq. (3.91).

Finally, the barriers and MEPs for the *trans* to *right cis* transitions are illustrated below in Fig. 6.13.

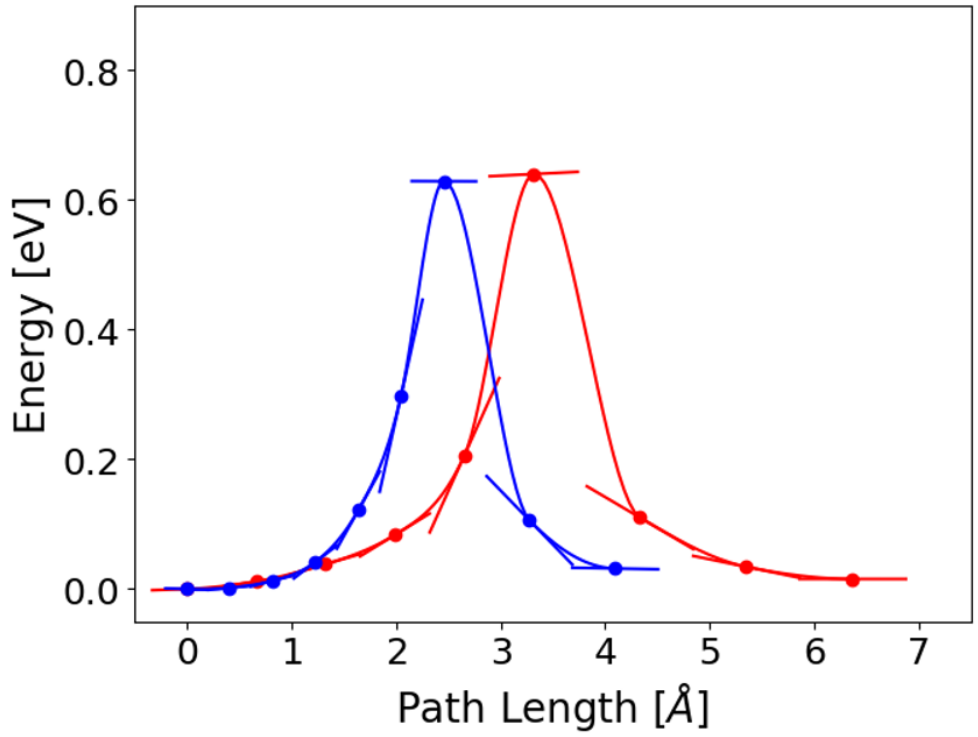


**Figure 6.13:** Calculated MEPs for *trans* to *right cis* of the OHPc molecule on the Cu(111).surface for the *hcp* case (red) and the *fcc* case (blue). The images and the calculated energy gradients along the MEP are indicated by solid circles and bars, respectively. The *trans* and *right cis* structures are represented by the leftmost and rightmost points, respectively, in both the red and blue graphs. The transition structure for each calculated MEP is represented by the saddle point in either graph. Both MEP lengths, $\Delta D_{\mathrm{Mol}}$, were calculated by use of Eq. (3.91).

Further details about the barriers of Figs. 6.11- 6.13 are summarized below in Table 6.9.

| State | Site | Final Tautomer | $E^*$ (eV) | $E^*_{ZPE}$ (eV) | $\Delta D_H$ (Å) | $\Delta D_{Mol}$ (Å) |
|---|---|---|---|---|---|---|
| Gas Phase | | *left cis* | 0.87 | | 1.7 (2.1) | 3.3 |
| | | *right cis* | 0.36 | | 1.0 (1.2) | 2.1 |
| Adsorbed | *hcp* | *left cis* | 0.86 | 0.71 | 1.6 (1.9) | 4.0 |
| | | *right cis* | 0.64 | 0.50 | 1.2 (1.5) | 6.3 |
| | *fcc* | *left cis* | 0.86 | 0.71 | 1.6 (1.9) | 3.9 |
| | | *right cis* | 0.63 | 0.49 | 1.1 (1.5) | 4.1 |

**Table 6.9:** Calculated energy barriers for hydrogen transfer from *trans* to *cis* tautomers of OHPc in the gas phase and adsorbed on the Cu(111) surface. The potential energy barriers are given by $E^*$, whereas the zero-point-energy corrected energy barrier for the H atom is given by $E^*_{ZPE}$. The length of the straight path of the H atom between the two tautomers is given by $\Delta D_H$, whereas the value within the parenthesis gives the MEP length for the H atom. In the latter case, $\Delta D_H$ was calculated by use of Eq. (3.92). $\Delta D_{Mol}$ is the MEP path length as calculated by including all atoms in the molecule, but not the substrate, as calculated by use of Eq. (3.91).

The calculated MEPs for hydrogen transfer from *trans* to *left cis* and *right cis* tautomers in the gas phase were shown in Fig. 6.11. $E^*_{ZPE}$ is not shown in Table 6.9 for the gas phase MEPs. This is because these values were not required for the subsequent discussions. Only an indirect MEP for hydrogen transfer between the *left cis* and *right cis* tautomers via the *trans* tautomer was found in the CI-NEB calculations. As shown by the resulting potential energy barriers $E^*$ in Table 6.9, $E^*$ is less than one half for hydrogen transfer from *trans* to *right cis* than from *trans* to *left cis.* This trend correlates with the relative energies of the *right cis* and *left cis* tautomer with respect to the *trans* tautomer in Table 6.5 but also as shown in Tab1e 6.9, the shorter straight path length from *trans* to *right cis* of the H atom than from *trans* to *left cis.*

This behaviour of these path lengths is expected from the discussion of the interatomic distances in the Subsection 6.3.2. The curvature of the MEP of the H atom is small as shown by the lengths $\Delta D_{\mathrm{H}}$ of the MEP for the H atom in Table 6.9, which are only slightly longer than the straight paths of the H atom. The full path lengths for the MEP including all atoms, as shown in Fig. 6.11, are larger than the MEP of the H atom, which shows that the H transfer involve substantial motion of the other atoms in the molecule. The reason why the MEP length differed significantly in the two *trans* to *right cis* NEB calculations. Namely, $\Delta D_{\mathrm{Mol}} = 6.4$ Å and 4.1 Å for the *trans* to *right cis* configurations in the *hcp* and *fcc* structures, respectively. It is suspected that this is due to the fact that the difference in adsorption energy between the *hcp* and *fcc right cis* structures was substantial in comparison to the other *hcp* and *fcc* structures for a given isomer in Table 6.5, namely by 0.04 eV. The problem is that a reason for this difference in adsorption energy is speculative. Therefore, a good starting point for further investigation is why the two *right cis* configurations differed by 0.04 eV, as this may be likely to yield some insight into explaining the substantial difference in $\Delta D_{\mathrm{Mol}}$ for the *trans* to *right cis* MEPs in comparison to the other much smaller differences in $\Delta D_{\mathrm{Mol}}$ for a given isomer.

The calculated MEPs for the H transfer between the adsorbed *trans* and *cis* tautomers are shown in Figs. 6.12 and 6.13. The resulting potential energy barriers $E^*$ were shown in Table 6.9. These barriers are the same for the *hcp* and *fcc* adsorption sites except for a tiny difference of about 0.01 eV between these two sites for the H transfer from *trans* to *right cis.* The result that $E^*$ is about the same from *trans* to *left cis* tautomer, both in the gas phase and for the adsorbed species, and that $E^*$ is about twice as large from the adsorbed *trans* to *right cis* tautomer than in the gas phase are somewhat surprising in the view of the behaviour of $\Delta E_{\mathrm{ads}}$ and $\Delta D_{\mathrm{H.}}$ $E^*$ follows the trend of $\Delta E_{\mathrm{ads}}$ but $\Delta E_{\mathrm{ads}}$ is much smaller than the corresponding $\Delta E$ in the gas phase as shown in Table 6.1. $\Delta D_{\mathrm{H}}$ has very similar values for the H transfer both in the gas phase molecule and in the adsorbed molecule. The full MEP lengths that include all atoms for the H transfer between the adsorbed tautomers are larger, especially for transfer from *trans* to *right cis,* than between the tautomers in the gas phase. This difference is not due to the motions of the substrate atoms during the H transfer since the MEP lengths $\Delta D_{\mathrm{Mol}}$, excluding the substrate atoms in Table 6.9, are found to be the same as for the full MEPs lengths.

In the STM experiments by Grill and Jaekel,[26] they were able to switch reversibly between the *trans* and a *cis* tautomer by inelastic electron tunnelling. At fixed bias, the switching rate was found to be linear in the tunnelling current corresponding to a one-electron process. The threshold bias for switching was found to be 0.75 V. The assignment that the switched *trans* tautomer corresponds to the *right cis* tautomer from a comparison of experimental and calculated STM images in Subsection 6.3.3 is corroborated by the potential energy barrier being substantially lower by about 0.2 eV for hydrogen transfer from *trans* to *right cis* than from *trans* to *left cis.* A direct comparison of the observed threshold bias with the calculated energy barrier requires a consideration of the change in zero-point energies (ZPEs), between the *trans* tautomer and the transition structures. The calculated N-H stretch vibrational energy is about 400 meV and the loss of this mode at the transition structure suggest that the ZPE can have an important effect on the energy barrier.

The changes in ZPEs between the trans tautomer and the transition structures were estimated by calculating the corresponding changes of vibrational energies while keeping all atoms except the H atom fixed in the calculation of vibrational modes. The presence of a single mode with an imaginary vibrational energy at the saddle points of the MEPs indicates that they are proper transition structures. This means that the MEPs are likely to be physically viable. The resulting ZPE corrected energy barriers $E^*_{ZPE}$ are shown in Table 6.9. The barriers are reduced by about 0.14 eV. The energy barrier for the H transfer from the *trans* to the *right cis* tautomer is reduced to 0.50 eV and the excitation energy of the fundamental of the N-H mode would still be insufficient to overcome this barrier. However, an excitation energy of 0.75 eV would just overcome the ZPE corrected energy barrier of about 0.71 eV for H transfer from the *trans* to the *left cis* tautomer. Since the calculated N-H stretch vibrational energy in the harmonic approximation is about 0.4 eV, this threshold bias suggests that the hydrogen transfer proceeds by the excitation to the first overtone of this mode. Note that the energy of the first overtone is expected to be less than twice the energy of the fundamental due to the anharmonicity of the N-H stretching vibration.

## 6.4: Conclusion

In conclusion, *trans* OHPc was the most stable tautomer in both the gas phase and the adsorbed configuration. The gas phases were planar, but all tautomers showed bending away from the Cu(111) surface. These structural changes as well as the adsorption energy values are indicative of chemisorption. All the adsorbed tautomers and dehydrogenated molecules did not have significant orientation differences between them with respect to the surface, with the $N^1$-O axis aligned closely with the [211] direction.

There were also no significant differences in adsorption energetics or geometry for a given tautomer in either the $\Lambda_{hcp}$ or $\Lambda_{fcc}$ configuration. So, the adsorption site appeared to not greatly affect adsorption energetics or geometry. This is likely to indicate that only the only important interaction was that between the top layer of the Cu(111) surface and the molecule. This would explain why the *trans* molecules experimentally observed by STM were observed to be aligned closely with the [211] direction, but sometimes orientated at $180^0$ to each other.

The trends of adsorption energy were the same trends as that of the gas phase total energies in that *trans* was the most stable, followed by *right cis*, then *left cis*. However, the differences in the gas phase energies were much greater than the differences in adsorption energies. The dehydrogenation energy was also reduced by almost a factor of five in comparison to that of the gas phase.

The topographical features of the simulated STM images corroborated this close alignment of the $N^1$-O axis aligned with the [211] direction, with simulated images for a given tautomer being almost identical for each of the $\Lambda_{hcp}$ or $\Lambda_{fcc}$ cases. The agreement between theory and experiment for the *trans* STM images were very good, as was that for the *right cis* images. There was poor agreement between theory and experimental images for the *left cis* case. The agreement between theory and experimental images for the dehydrogenated molecules was also not great. Therefore, one can say with some degree of confidence that both the $\Lambda_{hcp}$ and the $\Lambda_{fcc}$ *trans* STM images could be assigned to the experimental *trans* image. Similarly, one can also say that both the $\Lambda_{hcp}$ and the $\Lambda_{fcc}$ *right cis* STM images could be assigned to the experimental *cis* image. It would have been potentially useful to improve the STM image simulation (especially for the dehydrogenated molecules). In principle, one could have introduced an explicit atomistic model for the tip and use a real tip wavefunction in the Bardeen approximation for tunnelling. However, the problem with this is that the STM tip characteristics were not known in detail.

We currently do not have an explanation for the difference in adsorption energy between the two *right cis* structures or the difference in $\Delta D_{\mathrm{Mol}}$ between the two *trans* to *right cis* MEPs. However, it was suspected that the difference in $\Delta D_{\mathrm{Mol}}$ was due to the aforementioned difference in adsorption energy. Further work would be required to confirm or refute this. The calculated potential energy barriers also support the assignment from a comparison between the calculated and observed STM image that the adsorbed molecules following the deposition on the surface at a substrate temperature of 7 K, correspond to the *trans* tautomers. This tautomer was found to be the most stable tautomer in the gas phase.

The relatively large energy barriers for hydrogen transfer from the *trans* to *cis* tautomers makes the adsorbed *trans* tautomer kinetically stable at this substrate temperature and prevents a thermal equilibration among the various tautomers. For a typical attempt frequency of $10^{13}$ $s^{-1}$, a temperature of 7 K and an energy barrier of 0.6 – 0.9 eV, the Arrhenius rate law would give a *trans* to *cis* conversion rate of about $10^{-420}$ – $10^{-635}$ $s^{-1}$. In the gas phase, the *cis* molecules would start to have a a sizeable population when the thermal energy $kT$ is about equal to energy difference between the *cis* and *trans* states. This would be when $kT \sim 0.15 – 0.28$ eV which corresponds to $T \sim 1700 – 3200$ K.

We were not able to determine whether there would be a thermal population of the *hcp* and *fcc* structures for a given isomer. This would be a useful extension of the work done so far for this project. An interesting question is whether there would be a thermal population of the *hcp* and *fcc* structures for a given isomer. However, determination of this would require calculation of transfer rates between these two structures. These transfer rates are governed by the energy barrier heights between the structures. These energy barriers were not calculated over the course of this project. Therefore, we cannot currently decide whether we will have a thermal population or not. The calculation of these barriers to determine this would be an important extension of this project.

## 6.5: References


[1] J. T. Hynes, J. P Klinman, H. H Limbach and R. L. Schowen, Hydrogen-Transfer Reactions; Wiley-VCH, 2007.

[2] R. J. McMahon, *Science*, **299**, 833–834, 2003, DOI: 10.1126/science.1080715.

[3] R. J. Shannon, M. A. Blitz, A. Goddard, and D. E. Heard, *Nat. Chem.*, **5**, 745–749. 2013, DOI: 10.1038/nchem.1692.

[4] J. P. Klinman and A. Kohen, *Annu. Rev. Biochem.*, **82**, 471–496, 2013, DOI: 10.1146/annurev-biochem-051710-113623.

[5] R. P Bell, *The Tunneling Effect in Chemistry*; Chapman and Hall, 1980.

[6] P. J. Taylor, G. van der Zwan, and Liudmil Antonov, *Tautomerism*, Ed. L. Antonov, Weiley-VHC, 2013.

[7] W. F. Rowe, Jr., R. W. Duerst, and E. Bright Wilson, *J. Am. Chem. Soc.,* 98, 4021– 4023, 1976.

[8] T. Carrington, Jr. and W. H. Miller, *J. Chem. Phys.*, **84**, 4364–4370, 1986, DOI: 10.1063/1.450058.

[9] X. Meng, J. Guo, J. Peng, J. Chen, Z. Wang, J.-R. Shi, X.-Z. Li, E.-G. Wang, and Y. Jiang, *Nat. Phys.*, **11**, 235–239, 2015, DOI: 10.1038/nphys3225.

[10] M. Koch, M. Pagan, M. Persson, S. Gawinkowski, J. Waluk and T. Kumagai, *J. Am. Chem. Soc*., **139**, 12681–12687, 2017, DOI: 10.1021/jacs.7b06905.

[11] L. J. Lauhon and W. Ho, *Phys. Rev. Lett.,* **85**, 4566–4569, 2000, DOI: 10.1103/PhysRevLett.85.4566.

[12] E. Vogel, M. Kocher, H. Schmickler, and J. Lex, *Angew. Chem. Int. Ed*., **25**, 257–259, 1986, DOI: 10.1002/anie.198602571.

[13] J. Waluk, *Chem. Rev.*, **117**, 2447–2480, 2017, DOI: 10.1021/acs.chemrev.6b00328.

[14] P. Fita, L. Grill, A. Listkowski, H. Piwonski, S. Gawinkowski, M. Pszona, ´ J. Sepioł, E. Mengesha, T. Kumagai, and J. Waluk, *Phys. Chem. Chem. Phys.*, **19**, 4921–4937, 2017, DOI: 10.1039/C6CP07955E.

[15] T. Kumagai, J. N. Ladenthin, Y. Litman, M. Rossi, L. Grill, S. Gawinkowski, J.Waluk and M. Persson, *J. Chem. Phys.*, **148**, 102330, 2018, DOI: 10.1063/1.5004602.

[16] T. Kumagai, F. Hanke, S. Gawinkowski, J. Sharp, K. Kotsis, J. Waluk, M. Persson, and L. Grill, *Phys. Rev. Lett.*, **111**, 246101, 2013, DOI: 10.1103/PhysRevLett.111.246101.

[17] T. Kumagai, F. Hanke, S. Gawinkowski, J. Sharp, K. Kotsis, J. Waluk, M. Persson, and L. Grill, *Nat. Chem.*, **6**, 41–46, 2014, DOI: 10.1038/nchem.1804.

[18] J. N. Ladenthin, L. Grill, S. Gawinkowski, Sh. Liu, J. Waluk, and T. Kumagai, *ACS Nano*, **9**, 7287–7295, 2015, DOI: 10.1021/acsnano.5b02147.

[19] H. Böckmann, S. Liu, J. Mielke, S. Gawinkowski, J. Waluk, L. Grill, M. Wolf, and T. Kumagai, *Nano Lett.*, **16**, 1034–1041, 2016, DOI: 10.1021/acs.nanolett.5b04092.

[20] J. N. Ladenthin, T. Frederiksen, M. Persson, J. C. Sharp, S. Gawinkowski, J. Waluk, and T. Kumagai, *Nat. Chem.*, **8**, 935–94, 2016, DOI: 10.1038/nchem.2552.

[21] P. Liljeroth, J. Repp, and G. Meyer, *Science*, **317**, 1203–1206, 2007, DOI: 10.1126/science.1144366.

[22] A. Sperl, J. Kröger, and R. Berndt, *Angew. Chem. Int. Ed.*, **50**, 5294–5297, 2011, DOI: 10.1002/anie.201100950.

[23] W. Auwarter, K. Seufert, F. Bischoff, D. Ecija, S. Vijayaraghavan, S. Joshi, ¨ F. Klappenberger, N. Samudrala, and J. V. Barth, *Nat. Nanotech*., **7**, 41–46, 2012, DOI: 10.1038/nnano.2011.211.

[24] J. Kügel, A. Sixta, M. Böhme, A. Krönlein, and M. Bode, *ACS Nano*, **10**, 11058–11065, 2016, DOI: 10.1021/acsnano.6b05924.

[25] J. Kügel, M. Leisegang, M. Böhme, A. Krönlein, A. Sixta, and M. Bode, *Nano Lett.*, **17**, 5106–5112, 2017, DOI: 10.1021/acs.nanolett.7b02419.

[26] Private communication.

[27] G. Kresse and J. Furthmüller,. *Phys. Rev. B: Condens. Matter Mater. Phys.*, 1996, **54**, 11169– 11186, DOI: 10.1103/PhysRevB.54.11169.

[28] G. Kresse and D. Joubert, *Phys. Rev. B: Condens. Matter Mater. Phys.* 1999, **59**, 1758– 1775, DOI: 10.1103/PhysRevB.59.1758.

[29] M. Dion, H. Rydberg, E. Schröder, D. C. Langreth, and B. I. Lundqvist, *Phys. Rev. Lett.*, 2004, **92**, 246401-246404, DOI: 10.1103/PhysRevLett.92.246401.

[30] G. Roman-Pérez and J. M. Soler, *Phys. Rev. Lett*., 2009, **103**, 096102, DOI: 10.1103/PhysRevLett.103.096102.

[31] K. Berland and P. Hyldgaard, *Phys. Rev. B: Condens. Matter Mater. Phys.*, 2014, **89**, 035412, DOI: 10.1103/PhysRevB.89.035412 .

[32] L. Gharaee, P. Erhart and P. Hyldgaard, *Phys. Rev. B*, 2017, **95**, 085147, DOI: 10.1103/PhysRevB.95.085147.

[33] J. Tersoff and D. R. Hamann, *Phys. Rev. Lett.*, 1983, **50**, 1998 – 2001, DOI: 10.1103/PhysRevLett.50.1998.

[34] N. Lorente and M. Persson, *Faraday Discuss.*, 2000, **117**, 277-290, DOI: 10.1039/B002826F.

[35] G. Mills, H. Jónsson and G. K. Schenter, *Surf. Sci.*, 1995, **324**, 305– 337, DOI: 10.1016/0039-6028(94)00731-4.

[36] G. Henkelman, B. P. Uberuaga and H. A. Jónsson, *J. Chem. Phys.* 2000, **113**, 9901– 9904, DOI: 10.1063/1.1329672.

[37] D. Sheppard, R. Terrell and G. Henkelman, *J. Chem. Phys.*, **128**, 134106, 2008, DOI: 10.1063/1.2841941.

[38] S. Smidstrup, A. Pedersen, K. Stokbro and H. Jónsson, *J. Chem. Phys.* 2014, **140**, 214106, DOI: 10.1063/1.4878664.

# Chapter 7

## Concluding Remarks

The work in this thesis has covered three distinct projects, namely a flipping reaction of formaldehyde on Cu(110), surface-mediated enantiomeric separation of flurbiprofen on Cu(110) and the tautomerization of 22-oxa-hemiporphycene on Cu(111). The results of each of these systems are described in the conclusions of Chapters 4 – 6. However, a few important results will be highlighted once again here along with suggested ways of extending these projects.

### Insights into a Flipping Reaction of Adsorbed Formaldehyde on Cu(110)

A low symmetry species of formaldehyde ($\eta_3$) was found to be the only viable candidate structure that would explain the experimentally observed flipping reaction on the Cu(110) surface. The magnitudes of the adsorption energies are relatively small, less than 1 eV and their magnitudes increase with the elongation of the C=O bond length. Unlike the earlier study of this adsorption system by Sakong and Groß, this study accounted for dispersion interactions by use of van der Waals exchange-correlation functionals. The MEP of $\eta_3$ occurred by means of an azimuthal rotation of the $CH_2$ group. An interesting extension of this project that time did not allow, would be to calculate the energy barriers between the $\eta_2$ structure and both $\eta_1$ and $\eta_3$.

## Chiral Separation of Racemic Flurbiprofen on Cu(110)

STM experiments indicated that when a racemic (*RS)* mixture of flurbiprofen (FBF) adsorbed onto the Cu(110) surface, enantiomerically pure islands are formed such that each island contains only two rotation domains with only one boundary at the domain wall. Molecules either side of the boundary were oriented at 180$^{o}$ to each other.

The *cis* and *trans* gas phases were almost degenerate ($\Delta E$ = 3 meV). However, upon adsorption to the surface, the *trans* configuration of FBF was clearly preferred. All differences for adsorbed molecules were governed by both molecule-surface and molecule-molecule interactions. Van der Waals energetic contributions were found to be that which governed the intermolecular interactions. These interaction energies between the molecules in the monolayer were found to force the *R*- and *S*-enantiomers into geometries with substantial energy differences, explaining the chiral selectivity. At the rotation domain boundary, it was found that the 96 arrangement was so repulsive that it would be very unlikely to form. Instead, either 66 stacking or the formation of a 69 rotation domain boundary would have been preferred.

However, experimental STM indicated that at the boundary, 69 or 96 structures would have been present, and not 66. The calculated energetic preference of 69 over 96 was conclusive enough to indicate with a degree of confidence that at the domain boundary, the dimer pairs were in the 69 configuration. As previously mentioned in the conclusion of Chapter 5, 6969…6969 arrangements would be unlikely to form because such an arrangement would contain 96 configurations, which would be energetically unfavourable. This helped to explain why the experimental STM showed that only one rotation domain boundary was formed per enantiomerically pure island of adsorbed flurbiprofen. As mentioned in Chapter 5, it was suspected at that the enhanced stability was due to a 69 case, allowing F-H hydrogen bonding across the boundary. So, further investigation into hydrogen bonding enhancing the 69 stability at the domain boundary would be potentially useful. One suggested way of doing this would be using Monte Carlo techniques to simulate how the molecular geometry and interactions change in real time as the molecules adsorb into the 69, 66 and 96 arrangements. This would be likely to give an even more comprehensive picture of the interactions at the rotation domain boundary.

**Tautomerization of Oxa-hemiporphycene Adsorbed to Cu(111)**

It was found that the gas phase energetics explained why the *trans* tautomer was that which was mostly observed upon deposition of the molecule to the Cu(111) surface at 7 K. The adsorption energetics and geometry indicated a preferred molecular alignment along the [211] direction and that the adsorption site upon the surface did not matter significantly at all. In other words, for each tautomer the molecular structure and adsorption energetics of the $\Lambda_{hcp}$ and $\Lambda_{fcc}$ were similar. The only significant difference was the orientation with respect to the surface, i.e. each $\Lambda_{hcp}$ structure was orientated at 180° with respect to its $\Lambda_{fcc}$ counterpart. For a given tautomer, the $\Lambda_{hcp}$ and $\Lambda_{fcc}$ STM features were almost identical.

The calculated energy barriers supported much of the experimental findings. One essential extension to this project would be to deduce a reason for the comparatively large difference in adsorption energy for the two *right cis* structures. This would then potentially yield an explanation for the comparatively large difference in MEP length in the *trans* to *right cis* NEB calculations. Another interesting extension of this project might be to further investigate why the dehydrogenation energy of the adsorbed structures was about five times lower than that of the gas phase. The question as to whether there would be a thermal population of the *hcp* and *fcc* structures for a given isomer is currently unresolved. This would be a useful extension of the work done so far for this project.

# Acknowledgements

There are many people who have helped me along the way during this journey. However, I would like to that my primary and secondary PhD supervisors, Prof. M. Persson and Dr. M. S. Dyer, respectively, for all their input over the past few years. Their assistance, experience and knowledge were invaluable. I would also like to thank the following experimental collaborators whose contributions were crucial for the original work presented in this thesis:

- R. Raval, C. L. Pang and S. Haq at the University of Liverpool
- C. Lin, M. Rossi and T. Kumagai at the Fritz-Haber Institute of the Max-Planck Society
- L. Grill, J. Waluk and S. Jaekel at the University of Graz

I acknowledge the computer time allocated on ARCHER and THOMAS at the MMM hub partially funded by EPSRC (EP/L000202, EP/P020194) through the Materials Chemistry Consortium. This time was invaluable for achieving many of the results of this thesis.

I thank Cliff Addison and his colleagues for keeping the computer clusters running efficiently at the University of Liverpool, as well as for their timely responses to resolving any computational issues.

I thank my friends Tom Cobb and Gareth Morris for their cogent advice and support over the course of my PhD.

# APPENDIX A

## Appendix to Chapter 4

### A.1: Convergence Tests

Convergence tests were done for adsorption energy, $E_{ads}$, with respect to both *k*-point grid and $E_{cut}$. For these convergence tests, the initial (non-optimized) structure used was [*top*, 0°, in], resulting in the $\Lambda_7$ final (optimized) structure. $E_{ads}$ was calculated by use of Eq. (4.2). The calculated error estimation in $E_{ads}$, is denoted *by* $\Delta E_{ads}$.

#### A.1.1: Convergence with Respect to *K*-Points

This *k*-point convergence test was done for $E_{cut}$ = 400 eV. The results of this convergence test are shown below in Table A.1.

| ***k*-Point Grid** | $E_{ads}$ **(eV)** | $\lvert\Delta E_{ads}\rvert$ **(eV)** |
|---|---|---|
| (6 × 6 × 1) | -0.426 | 0.008 |
| (7 × 7 × 1) | -0.431 | 0.005 |
| (8 × 8 × 1) | -0.435 | 0.001 |
| (9 × 9 × 1) | -0.434 | 0.000 |

**Table A.1.** Convergence of $E_{ads}$ with respect to *k*-point grid. $|\Delta E_{ads}|$ is the magnitude of the difference between a value of $E_{ads}$, and the most converged value of $E_{ads}$ with the (9 × 9 × 1) *k*-point grid.

### A.1.2: Convergence with Respect to $E_{cut}$

Here, it was necessary to see how the value of $E_{ads}$ for the (6 × 6 × 1) *k*-point grid, would change with respect to variation in $E_{cut}$. The results for this $E_{cut}$ convergence test are shown below in Table A.2.

| $E_{cut}$ (eV) | $E_{ads}$ (eV) | $\lvert\Delta E_{ads}\rvert$ (eV) |
|---|---|---|
| 400 | -0.426 | 0.004 |
| 500 | -0.422 | 0.000 |
| 600 | -0.422 | 0.000 |

**Table A.2.** Convergence of $E_{ads}$ with respect to $E_{cut}$, using the (6 × 6 × 1) *k*-point grid. $|\Delta E_{ads}|$ is the magnitude of the difference between a value of $E_{ads}$, and the most converged value of $E_{ads}$ which is 600 eV.

### A.1.3: Summary

In Table A.1, all values of $\Delta E_{ads}$ are below 0.01 eV. The adsorption energetics of Chapter 4 could all be adequately compared at this level of precision. Therefore, in Chapter 4, the (6 × 6 × 1) *k*-point grid was used to sample the (2 × 3) cell. The (4 × 6) cell was sampled with a (3 × 3 × 1) *k*-point grid. This sampling would also have an estimated precision of 0.01 eV. This is because both situations for the (2 × 3) and (4 × 6) cells had the same *k*-point density. One can see from Table A.2 that $E_{ads}$ changes very little with increasing $E_{cut}$. Therefore, the least computationally expensive value of $E_{cut}$ = 400 eV was used for the modelling in Chapter 4.

## A.2: Comparison of the $\Lambda_4(\eta_1)$ and $\Lambda_5$ Structures

Here it is shown why the $\Lambda_4(\eta_1)$ configuration is the relevant equilibrium structure, and not the $\Lambda_5$ configuration. The $\Lambda_4(\eta_1)$ and $\Lambda_5$ configurations are shown below in Fig. A.1.

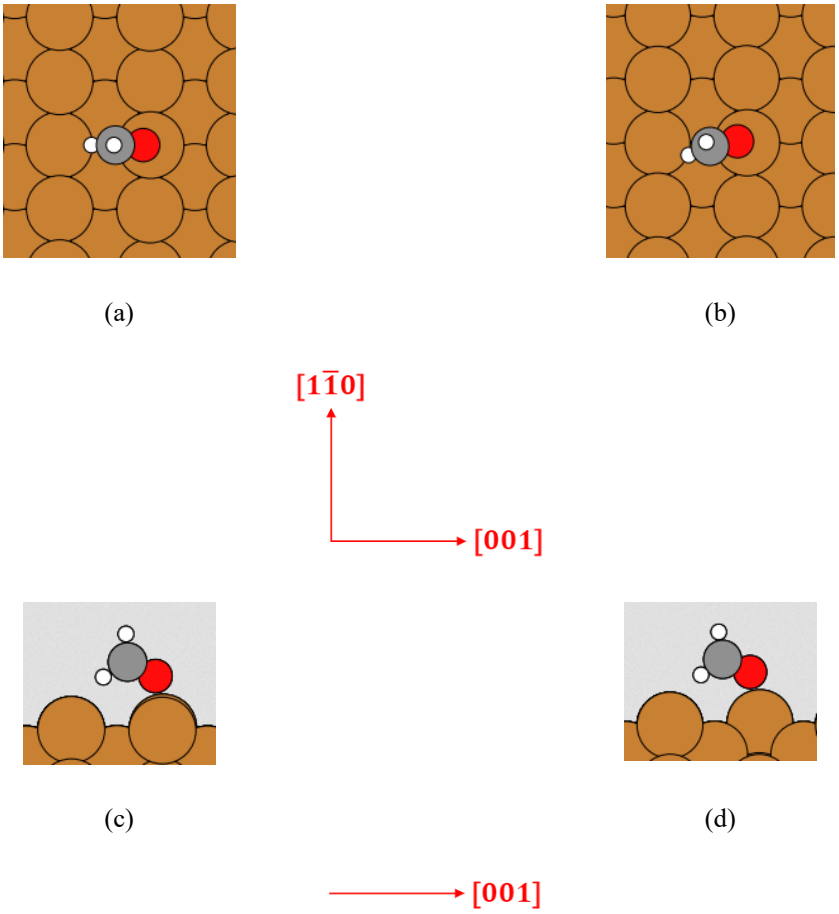


**Figure A.1:** Shown in (a) and (b) are the top views of $\Lambda_4(\eta_1)$ and $\Lambda_5$ configurations, respectively. Shown in (c) and (d) are the side views corresponding to (a) and (b), respectively. $E_{ads}$ = -0.52 (-0.55) eV for both $\Lambda_4(\eta_1)$ and $\Lambda_5$. The values of $E_{ads}$ with and without parentheses were calculated in the (2 x 3) and (4 x 6) cells, respectively.

The values of $E_{ads}$ are the same for both configurations in Fig. A.1. A further investigation into this was required. This is done by means of an NEB calculation to find the minimum potential energy curve between the $\Lambda_4(\eta_1)$ and $\Lambda_5$ configurations. This is shown below in Fig. A.2.

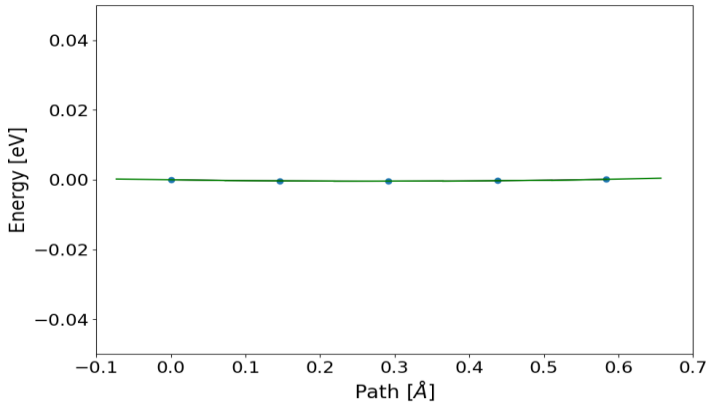


**Figure A.2:** Calculated minimum potential energy curve between $\Lambda_4(\eta_1)$ and $\Lambda_5$ as calculated from three images using the nudged elastic band (NEB) method. The leftmost and rightmost points of this graph represent the energy for the $\Lambda_4(\eta_1)$ and $\Lambda_5$ configuration, respectively. All the other points represent the intermediate structures between $\Lambda_4(\eta_1)$ and $\Lambda_5$.

Fig. A.2 shows that the potential energy curve between $\Lambda_4(\eta_1)$ and $\Lambda_5$ is very flat. The adsorption energetics of Fig. A.1 and the potential energy curve of Fig. A.2 indicate that there is very little difference between the $\Lambda_4(\eta_1)$ and $\Lambda_5$. In fact, the only significant differences between the $\Lambda_4(\eta_1)$ and $\Lambda_5$ structures, are in the low energy vibrational modes Firstly, the differences in energy of each vibrational mode of these two structures, are displayed below in Table A.3.

| Mode Number | $\Lambda_4(\eta_1)$ (meV) | $\Lambda_5$ (meV) | Percentage Difference |
|---|---|---|---|
| 0 | 3.5 | 2.5 | 33.33 |
| 1 | 5.6 | 4.8 | 15.39 |
| 2 | 7.1 | 9.4 | 27.88 |
| 3 | 21.6 | 21.0 | 2.82 |
| 4 | 24.7 | 24.8 | 0.40 |
| 5 | 26.7 | 27.5 | 2.95 |
| 6 | 132.1 | 131.5 | 0.46 |
| 7 | 148.2 | 147.9 | 0.20 |
| 8 | 175.6 | 175.5 | 0.06 |
| 9 | 200.1 | 199.9 | 0.10 |
| 10 | 340.8 | 339.7 | 0.32 |
| 11 | 361.2 | 361.2 | 0.00 |

**Table A.3:** The energies of the $\Lambda_4(\eta_1)$ and $\Lambda_5$ structures. The percentage difference between each energy is shown. Percentage differences greater than 15% are shown in red.

Secondly, the differences in wavenumber of each vibrational mode of the $\Lambda_4(\eta_1)$ and $\Lambda_5$ structures, are displayed below in Table A.4.

| Mode Number | $\Lambda_4(\eta_1)$ (cm$^{-1}$) | $\Lambda_5$ (cm$^{-1}$) | Percentage Difference |
|---|---|---|---|
| 0 | 28.0 | 19.9 | 33.82 |
| 1 | 45.3 | 38.8 | 15.46 |
| 2 | 57.2 | 76.2 | 28.49 |
| 3 | 174.0 | 169.2 | 2.80 |
| 4 | 199.1 | 199.9 | 0.40 |
| 5 | 215.0 | 221.7 | 3.07 |
| 6 | 1065.3 | 1061.0 | 0.41 |
| 7 | 1195.1 | 1193.0 | 0.18 |
| 8 | 1416.6 | 1415.8 | 0.06 |
| 9 | 1613.7 | 1612.2 | 0.09 |
| 10 | 2748.4 | 2739.8 | 0.31 |
| 11 | 2913.3 | 2913.5 | 0.00 |

**Table A.4:** The wavenumbers of the $\Lambda_4(\eta_1)$ and $\Lambda_5$ structures. The percentage difference between each energy is shown. Percentage differences greater than 15% are shown in red.

One can see from Tables A.3 and A.4 that the only significant differences in energy and wavenumber (greater than 15%) are in red. All other percentage differences are less that about 3%. The values of $E_{ads}$, ZPE and important bonding distances of the $\Lambda_4(\eta_1)$ and $\Lambda_5$ structures are shown below in Table A.5.

| | $\Lambda_4(\eta_1)$ | $\Lambda_5$ |
|---|---|---|
| **$E_{ads}$ (eV)** | -0.52 (-0.55) | -0.52 (-0.55) |
| **ZPE (eV)** | 0.72 (0.73) | 0.72 (0.73) |
| **C-Cu (Å)** | 2.95 (2.95) | 2.94 (2.95) |
| **H-Cu (Å)** | 2.44 (2.50) | 2.43 (2.53) |
| **O-Cu (Å)** | 2.06 (2.05) | 2.06 (2.05) |
| **C-H$^1$ (Å)** | 1.12 (1.12) | 1.12 (1.12) |
| **C-H$^2$ (Å)** | 1.11 (1.11) | 1.11 (1.11) |
| **C=O (Å)** | 1.23 (1.23) | 1.23 (1.23) |

**Table A.5**: $E_{ads}$ and ZPE and important nearest-neighbour bonding distances of the $\Lambda_4(\eta_1)$ and $\Lambda_5$ structures. Values with and without parentheses were calculated in the (2 × 3) and (4 × 6) cells, respectively.

The H-C-H angles of the ($\eta_1$) and $\Lambda_5$ structures are shown below in Table A.6.

| **Structure** | **H-C-H Angle (o)** |
|---|---|
| $\Lambda_4(\eta_1)$ | 119.0 (119.0) |
| $\Lambda_5$ | 118.9 (119.0) |

**Table A.6**: The H-C-H angle of the $\Lambda_4(\eta_1)$ and $\Lambda_5$ structures. Values with and without parentheses were calculated in the (2 × 3) and (4 × 6) cells, respectively.

One can see from Tables A.5 and A.6 that there is no appreciable difference between any of the quantities shown for the $\Lambda_4(\eta_1)$ and $\Lambda_5$ structures. Moreover, as the significantly different vibrational energy modes were of low energy, it is reasonable that the comparisons drawn between $\Lambda_4(\eta_1)$ and $\Lambda_6(\eta_3)$ in Chapter 4 were valid. In Chapter 4, $\Lambda_6(\eta_3)$ was confirmed to the likely flipping structure. This is due to the low energy barrier calculated by NEB, and the good agreement between the simulated STM image of the $\Lambda_6(\eta_3)$ as compared to the $O_{pb}$ STM image. The latter was experimentally established to be the flipping species.

## A.3: Minimum Energy Path between $\Lambda_4(\eta_1)$ and $\Lambda_6(\eta_3)$

Here it is shown why flipping between the $\eta_3$ mirror reflected configurations was favoured over flipping between $\Lambda_4(\eta_1)$ and $\eta_3$. The calculated minimum energy path between $\Lambda_4(\eta_1)$ and $\Lambda_6\,\eta_3$ is shown below in Fig. A.3.

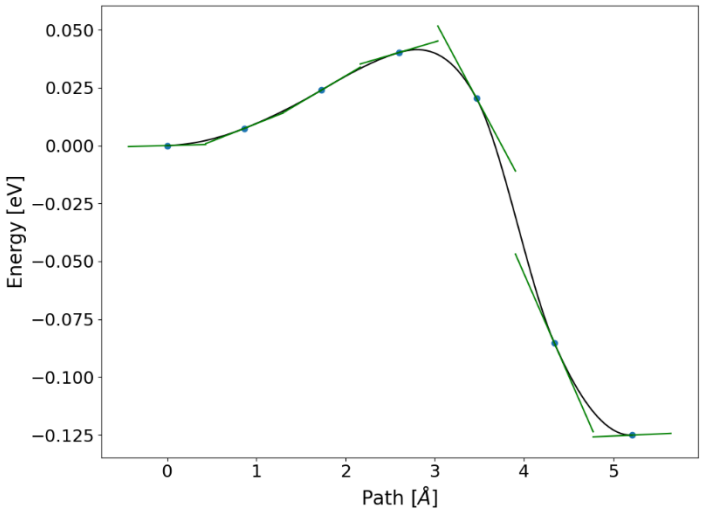


**Figure A.3:** Calculated minimum energy path (MEP) between $\eta_1$ and $\eta_3$ as calculated from five images using the nudged elastic band method. The $\eta_1$ structure occurs at the leftmost point of the graph. The $\eta_3$ structure occurs at the rightmost point. All the other points represent the intermediate structures along the MEP. The calculated potential energy barrier is 0.041 eV.

The calculated energy barrier of 0.041 eV in Fig. A.3 is 24% larger than that of 0.025 eV for mirror-reflected $\eta_3$ flipping as shown in Fig. 4.3 (b). Therefore, $\eta_1$ to $\eta_3$ flipping is less energetically favourable than mirror-reflected $\eta_3$ flipping. This is further evidence in favour of the assignment of $\eta_3$ to the flipping species, $O_{pb}$.

## A.4: Estimation of the Tunnelling Rate with the WKB Approximation

The one-dimensional WKB approximation was used to estimate the tunnelling rate, *R*, between the two mirror-reflected structures of $\eta_1$ and $\eta_3$ as

$$R = \nu \exp\left(-2\int_{\tilde{s}_1}^{\tilde{s}_2} \sqrt{2V(\tilde{s}) - E}\, d\tilde{s}\right). \tag{A.1}$$

In Eq. (A.1), $\nu$ is the frequency of the vibrational mode at the equilibrium position along MEP and $V(\tilde{s})$ is the potential energy curve along the MEPs, as parameterized by the isoinertial (mass-scaled coordinates) path length $\tilde{s}$ and the energy $E = \frac{1}{2}\hbar\nu + V_{\mathrm{eq}}$. The relationship between the isoinertial line element $d\tilde{s}$, and the line element *ds*, is given by

$$d\tilde{s} = \sqrt{\sum_i m_i \left(\frac{dx_i}{ds}\right)^2}\, ds \tag{A.2}$$

In Eq. (A.2), $x_i$ are Cartesian coordinates for the atoms of masses $m_i$. The effectively barrier height, $D_{\mathrm{eff}}$ is given by

$$D_{\mathrm{eff}} = E_{\mathrm{a}} - \frac{\hbar\nu}{2}, \tag{A.3}$$

where $E_{\mathrm{a}}$ is the activation energy.

## A.5: Schematics of the Formaldehyde in the (2 × 3) and the (4 × 6) Unit Cells

The periodic images of the $\eta_3$ structure in the (2 × 3) and (4 × 6) surface unit cells are shown below in Fig. A.4. This structure is used as an example to illustrate the surface periodicity of these cells diagrammatically.

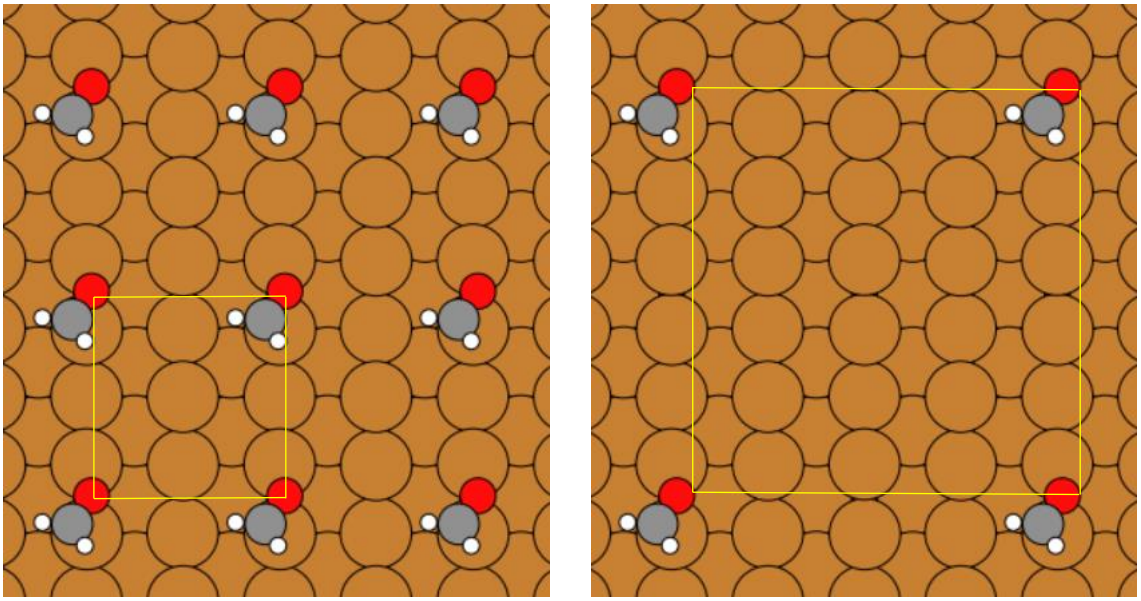

**Figure A.4:** Surface periodicity of $\eta_3$ structure in the (2 × 3) (a) and the (4 × 6) surface unit cell (b).

# APPENDIX B

## Appendix to Chapter 5

### B.1: Convergence Tests

Convergence tests were done for adsorption energy, $E_{ads}$, with respect to both *k*-point grid and $E_{cut}$. These convergence tests were done in both the (1 × 1) and (3 × 2) cells. The convergence tests in the (1 × 1) and (3 × 2) cells for the [*S*, *cis*, monolayer] and chain *trans*-69 structures, respectively. $E_{ads}$ was calculated by use of Eq. (5.2). The calculated error estimation in $E_{ads}$, is denoted by $\Delta E_{ads}$.

#### B.1.1: Convergence with Respect to *K*-Points

These *k*-point convergence tests were done for $E_{cut}$ = 400 eV. The results of the convergence test for the (1 × 1) are shown below in Table B.1.

| ***k*-Point Grid** | **$E_{ads}$ (eV)** | **$\lvert\Delta E_{ads}\rvert$ (eV)** |
|---|---|---|
| (3 × 6 × 1) | -3.079 | 0.019 |
| (4 × 8 × 1) | -3.097 | 0.001 |
| (5 × 10 × 1) | -3.114 | 0.016 |
| (6 × 12 × 1) | -3.098 | 0.000 |

**Table B.1:** Convergence of $E_{ads}$ with respect to *k*-point grid for the [*S*, *cis*, monolayer] structure. $|\Delta E_{ads}|$ is the magnitude of the difference between a value of $E_{ads}$, and the most converged value of $E_{ads}$ with the (6 × 12 × 1) *k*-point grid.

The results of the convergence test for the (3 × 2) cell, are shown below in Table B.2.

| ***k*-Point Grid** | $E_{ads}$ **(eV)** | $\lvert\Delta E_{ads}\rvert$ **(eV)** |
|---|---|---|
| (2 × 2 × 1) | -3.114 | 0.003 |
| (3 × 3 × 1) | -3.108 | 0.009 |
| (4 × 4 × 1) | -3.111 | 0.006 |
| (5 × 5 × 1) | -3.115 | 0.002 |
| (6 × 6 × 1) | -3.117 | 0.000 |

**Table B.2:** Convergence of $E_{ads}$ (per molecule) with respect to *k*-point grid for the *trans*-69 chain structure. $|\Delta E_{ads}|$ is the magnitude of the difference between a value of $E_{ads}$, and the most converged value of $E_{ads}$ with the (6 × 6 × 1) *k*-point grid.

### B.1.2: Convergence with Respect to $E_{cut}$

Here, it was necessary to see how the value of $E_{ads}$ for the both the (1 × 1) and (3 × 2) cells, would change with respect to variation in $E_{cut}$. The results for the $E_{cut}$ convergence tests for the (1 × 1) cell are shown below in Table B.3.

| $E_{cut}$ **(eV)** | $E_{ads}$ **(eV)** | $\lvert\Delta E_{ads}\rvert$ **(eV)** |
|---|---|---|
| 400 | -3.079 | 0.004 |
| 500 | -3.078 | 0.003 |
| 600 | -3.075 | 0.000 |

**Table B.3:** Convergence of $E_{ads}$ with respect to $E_{cut}$, for the (1 × 1) cell and (3 × 6 × 1) *k*-point grid. $|\Delta E_{ads}|$ is the magnitude of the difference between a value of $E_{ads}$, and the most converged value of $E_{ads}$ which is 600 eV.

The results for the $E_{cut}$ convergence tests for the (3 × 2) cell are shown below in Table B.4

| $E_{cut}$ (eV) | $E_{ads}$ (eV) | $\lvert\Delta E_{ads}\rvert$ (eV) |
|---|---|---|
| 400 | -3.115 | 0.004 |
| 500 | -3.113 | 0.002 |
| 600 | -3.111 | 0.000 |

**Table B.4:** Convergence of $E_{ads}$ with respect to $E_{cut}$, for the (3 × 2) cell and (5 × 5 × 1) *k*-point grid. $|\Delta E_{ads}|$ is the magnitude of the difference between a value of $E_{ads}$, and the most converged value of $E_{ads}$ which is 600 eV.

### B.1.3: Summary

In Table B.1, all values of $\Delta E_{ads}$ are below 0.02 eV. The adsorption energetics of Chapter 5 could all be adequately compared at this level of precision. Therefore, in Chapter 5, the (3 × 6 × 1) *k*-point grid was used to sample the (1 × 1) cell. The (3 × 1) cell was sampled with a (3 × 2 × 1) *k*-point grid. For the (3 × 1) cell, it would also be reasonable to estimate the same precision as for the (1 × 1) cell. This is because both situations for the (1 × 1) and (3 × 1) cells had the same *k*-point density.

In Table B.2, all values of $\Delta E_{ads}$ are below 0.01 eV. In Chapter 5, some of values of $E_{ads}$ (per molecule) in the (3 × 2) cell were very close to each other (~0.01 eV). In order to balance both computational expense and the precision required for insights into these close values of $E_{ads}$, the (5 × 5 × 1) *k*-point grid was used.
One can see from Tables B.3 and B.4 that $E_{ads}$ changes very little with increasing $E_{cut}$. Therefore, the least computationally expensive value of $E_{cut}$ = 400 eV was used for the modelling in Chapter 5.

## B.2: The Other Dimer Footprints in the (3 × 1) Cell

### B.2.1: The 69 and 96 Dimer Footprints

The 180° rotation of one molecule with respect to another in the 69 and 96 configurations breaks the $C_2$ symmetry of the (3 × 1) cell. For this reason, two footprints with the same ($x$, $y$) designation, can in fact be different from one another. In order to eliminate any ambiguity, all *trans* footprints (except the 69 and 96 equilibrium structures), are shown below in Fig. B.1. Only the *trans* configuration is shown because a given *cis* footprint would appear as the same footprint to the corresponding *trans* structure, except that the intermolecular F-H orientation would be reversed relative to that of the *trans* configuration. For example, if a *cis* and a *trans* configuration had the same footprint and say that the *cis* footprint is in a 69 arrangement, then the corresponding *trans* footprint would be 96, (and vice versa).

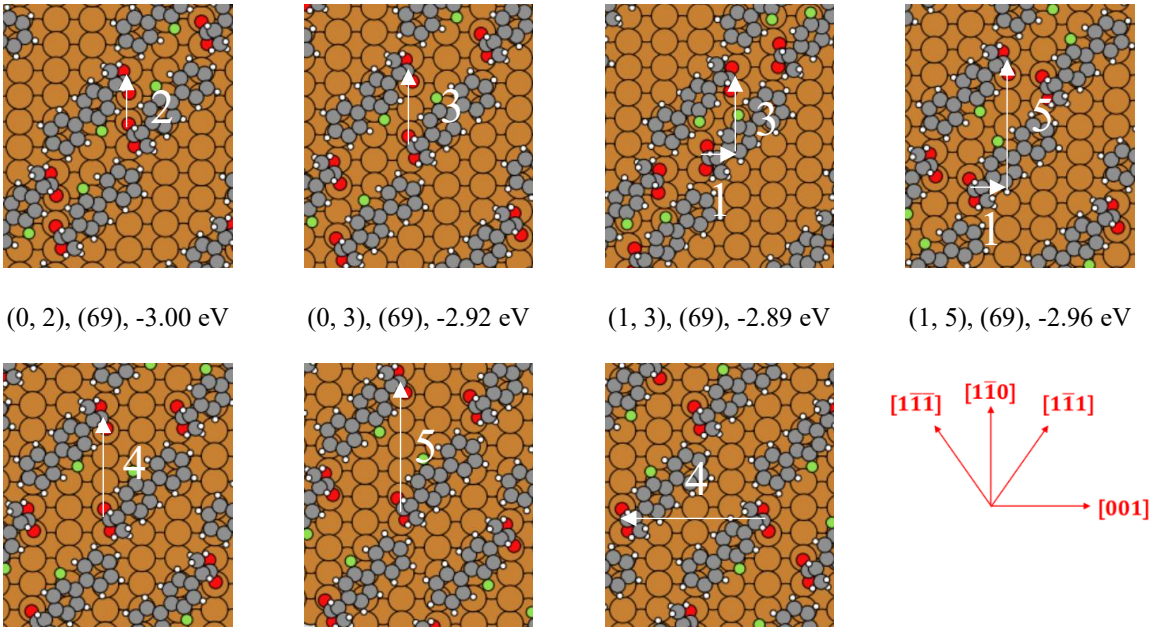


(0, 2), (69), -3.00 eV | (0, 3), (69), -2.92 eV | (1, 3), (69), -2.89 eV | (1, 5), (69), -2.96 eV

(0, 4), -2.89 eV* | (0, 5), -2.83 eV* | (-4, 0), -2.92 eV*

**Figure B1:** The other (non-equilibrium) *trans*-69 dimer footprints that were optimized in the (3 × 1) cell. The leftmost molecule in a dimer pair is defined relative to the rightmost molecule. The origin is centered on bridge site under the chiral centre of the right most molecule and the ($x$, $y$) coordinates are defined by counting top layer copper atoms in horizontal and vertical directions, respectively, to the bridge site under the leftmost molecule. The 69 signatures, as well as the $E_{ads}$ values are also labelled with each footprint. All the *trans*-96 footprints were already shown in Chapter 5. Due to large intermolecular distancing, footprints labelled with '*' cannot be clearly assigned as either '69' or '96'.

The footprints and adsorption energetics of all the 69 and 96 configurations of *cis*- and *trans*-FBF that were optimized in the (3 × 1) cell, are shown below in Table B.5.

| **Footprint** | $E_{ads}$ (*cis*) (eV) | $E_{ads}$ (*trans*) (eV) |
|---|---|---|
| **(0, 2)** | -2.89 (96) | -3.00 (69) |
| **(0, 3)** | -2.86 (96) | -2.92 (69) |
| **(1, 3)** | -2.79 (96) | -2.89 (69) |
| **(1, 4)** | -2.98 (96) | -3.07 (69) |
| **(1, 5)** | -2.87 (96) | -2.96 (69) |
| **(-3, 0)** | -2.73 (69) | -2.88 (96) |
| **(-4, -1)** | -2.85 (69) | -2.89 (96) |
| **(0, 4)** | -2.84* | -2.89* |
| **(0, 5)** | -2.77* | -2.83* |
| **(-4, 0)** | -2.86* | -2.92* |

**Table B.5:** Displayed are the values of $E_{ads}$ for the 69 and 96 footprints, for both the *cis* and *trans*-*S*-FBF configurations in the (3 × 1) cell. The '69' or '96' assignment is shown next to each footprint, except those marked with '*'. These footprints cannot be assigned as either '69' or '96' due to the large intermolecular distances. The equilibrium 69 and 96 energetics are labelled in red. The error in $E_{ads}$, $\Delta E_{ads}$ was 0.02 eV. The difference in $E_{ads}$ for the *trans* (-3, 0) and (-4, 1) footprints is less than $\Delta E_{ads}$. Therefore, both these footprints were considered as *trans* 96 equilibrium structures.

## B.2.2: The 66 Dimer Footprints

Unlike for the 69 and 96 footprints, the $C_2$ symmetry is not broken for the 66 footprints. Therefore, one could create the footprints without any ambiguity, using the convention for (-1, 2) in Chapter 5. The exhaustive set of 66 footprints and their values of $E_{ads}$ are displayed below in Table B.6.

| **Footprint** | $E_{ads}$ (*cis*) (eV) | $E_{ads}$ (*trans*) (eV) |
|---|---|---|
| **(-1, 1)** | -2.08 | -2.90 |
| **(-1, 2)** | -2.94 | -3.06 |
| **(-1, 3)** | -2.90 | -2.98 |
| **(-2, 0)** | -2.83 | -3.01 |
| **(-2, 1)** | -2.84 | -2.94 |
| **(-2, 2)** | -2.85 | -2.93 |

**Table B.6:** Displayed are the values of $E_{ads}$ for the *cis* and *trans*-*S*-FBF 66 footprints in the (3 × 1) cell. The values of $E_{ads}$ of the equilibrium structures are labelled in red.

## B.3: The Experimental Reflection Absorption Infrared Spectra (RAIRS)

Fig. B.2 shows the RAIRS which indicated that the COOH groups of *RS*-FBF deprotonated to $COO^-$ (carboxylate groups) upon adsorption to the Cu(110) surface.

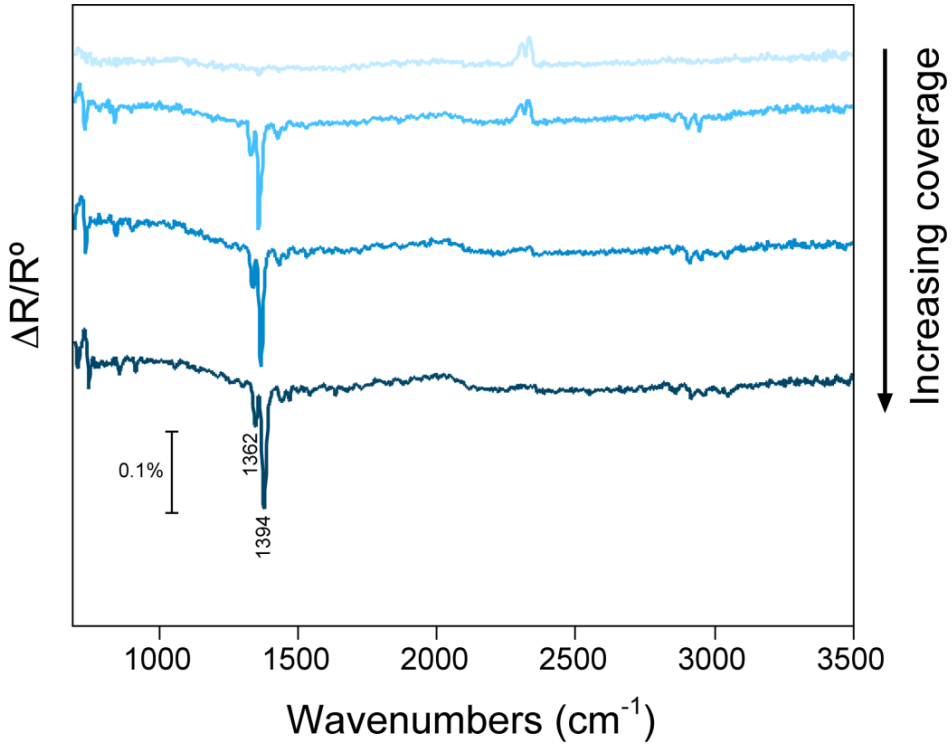


**Figure B.2:** Successive RAIRS collected from a clean Cu(110) surface exposed to *RS*-FBF. The exposure times for each spectrum (going from top to bottom) are 0, 3, 7 and 11 minutes. The intensity of the signal is given by $\Delta R = R^o - R$. The relative absorbance is given by $\Delta R/R^o = (R^o - R)/R^o$, where $R$ is the reflectance of the system with the adsorbate present, and $R^o$ is the reflectance without.
(Spectra and information provided by C. L. Pang, S. Haq and R. Raval).

In Fig. B.2, the key feature is the growth with exposure of the 1394 $cm^{-1}$ peak, which can be assigned to a symmetric carboxylate stretch, $\nu_s(COO^-)$. A peak for the C=O vibration would be at ~1750 $cm^{-1}$. However, one can see that this is absent from the spectra in Fig. B.2. This means that the deprotonation of the molecules occurs at the Cu(110) surface.

# APPENDIX C

## Appendix to Chapter 6

### C.1: Convergence Tests

Convergence tests were done for adsorption energy, $E_{ads}$, with respect to both $k$-point grid and $E_{cut}$. These convergence tests were done in both the (5, 0; -3, 6) and (6 × 6) cells. In both unit cells, the convergence tests were done for the $\Lambda_{hcp,\ trans}$ structure. $E_{ads}$ was calculated by use of Eq. (6.4). The calculated error estimation in $E_{ads}$, is denoted by $\Delta E_{ads}$.

#### C.1.1: Convergence with Respect to $K$-Points

These $k$-point convergence tests were done for $E_{cut}$ = 400 eV. The results of the convergence test for $\Lambda_{hcp,\ trans}$ in the (5, 0; -3, 6) and (6 × 6) cells, are shown below in Tables C.1 and C.2, respectively.

| **$k$-Point Grid** | **$E_{ads}$ (eV)** | **$\lvert\Delta E_{ads}\rvert$ (eV)** |
|---|---|---|
| (2 × 2 × 1) | -3.564 | 0.114 |
| (3 × 3 × 1) | -3.775 | 0.097 |
| (4 × 4 × 1) | -3.641 | 0.037 |
| (5 × 5 × 1) | -3.687 | 0.009 |
| (6 × 6 × 1) | -3.654 | 0.024 |
| (7 × 7 × 1) | -3.674 | 0.004 |
| (8 × 8 × 1) | -3.691 | 0.013 |
| (9 × 9 × 1) | -3.678 | 0.000 |

**Table C.1:** Convergence of $E_{ads}$ with respect to $k$-point grid for the $\Lambda_{hcp,\ trans}$ structure in the (5, 0; -3, 6) cell. $|\Delta E_{ads}|$ is the magnitude of the difference between a value of $E_{ads}$, and the most converged value of $E_{ads}$.

In Table C.1, all values of $\Delta E_{ads}$ are below 0.02 eV for *k*-point grids of (7 × 7 × 1) and (8 × 8 × 1). In Chapter 6, the $\Lambda_{hcp,\ trans}$ and $\Lambda_{hcp,\ right\ cis}$ energies in the (5, 0; -3, 6) cell differed by ~0.01 eV. Unfortunately, this is less than the 0.02 eV estimated error in $E_{ads}$. The computational expense increased dramatically with increase in *k*-point grids size. For the (5, 0; -3, 6) cell in Chapter 6, the (8 × 8 × 1) grid was used for the DFT calculations. This grid was used to compromise between both computational expense and precision for the NEB calculations.

| ***k*-Point Grid** | $E_{ads}$ **(eV)** | $\lvert\Delta E_{ads}\rvert$ **(eV)** |
|---|---|---|
| (2 × 2 × 1) | -3.651 | 0.111 |
| (3 × 3 × 1) | -3.934 | 0.172 |
| (4 × 4 × 1) | -3.854 | 0.092 |
| (5 × 5 × 1) | -3.773 | 0.011 |
| (6 × 6 × 1) | -3.880 | 0.118 |
| (7 × 7 × 1) | -3.744 | 0.018 |
| (8 × 8 × 1) | -3.743 | 0.019 |
| (9 × 9 × 1) | -3.757 | 0.005 |
| (10 × 10 × 1) | -3.743 | 0.019 |
| (11 × 11 × 1) | -3.756 | 0.006 |
| (12 × 12 × 1) | -3.776 | 0.014 |
| (13 × 13 × 1) | -3.762 | 0.000 |

**Table C.2:** Convergence of $E_{ads}$ with respect to *k*-point grid for the $\Lambda_{hcp,\ trans}$ structure in the (6 × 6) cell. $|\Delta E_{ads}|$ is the magnitude of the difference between a value of $E_{ads}$, and the most converged value of $E_{ads}$ with the (13 × 13 × 1) *k*-point grid.

## C.1.2: Convergence with Respect to $E_{cut}$

Here, it was necessary to see how the value of $E_{ads}$ for the both the (5, 0; -3, 6) and (6 × 6) cells, would change with respect to variation in $E_{cut}$. The $E_{cut}$ convergence tests for the (5, 0; -3, 6) and (6 × 6) cells, are done with the (8 × 8 × 1) and (12 × 12 × 1) *k*-point grids, respectively. Firstly, the results of the $E_{cut}$ convergence test for $\Lambda_{hcp,\ trans}$ in the (5, 0; -3, 6)' and (6 × 6) cells, are shown below in Tables C.5 and C.6, respectively.

| $E_{cut}$ (eV) | $E_{ads}$ (eV) | $\lvert\Delta E_{ads}\rvert$ (eV) |
|---|---|---|
| 400 | -3.689 | 0.003 |
| 500 | -3.686 | 0.000 |
| 600 | -3.686 | 0.000 |

**Table C.5:** Convergence of $E_{ads}$ with respect to $E_{cut}$, for the $\Lambda_{hcp,\ trans}$ structure in the (5, 0; -3, 6) cell with the (8 × 8 × 1) *k*-point grid. $|\Delta E_{ads}|$ is the magnitude of the difference between a value of $E_{ads}$, and the most converged value of $E_{ads}$ which is $E_{cut}$ = 600 eV.

| $E_{cut}$ (eV) | $E_{ads}$ (eV) | $\lvert\Delta E_{ads}\rvert$ (eV) |
|---|---|---|
| 400 | -3.776 | 0.007 |
| 500 | -3.769 | 0.000 |

**Table C.6:** Convergence of $E_{ads}$ with respect to $E_{cut}$, for the $\Lambda_{hcp,\ trans}$ structure in the (6 × 6) cell with the (12 × 12 × 1) *k*-point grid. $|\Delta E_{ads}|$ is the magnitude of the difference between a value of $E_{ads}$, and the most converged value of $E_{ads}$ which is $E_{cut}$ = 500 eV.

## C.1.3: Summary

Tables C.1 – C.4 indicate that the best estimated error in *k*-points of 0.02 eV, was obtained by use of the (8 × 8 × 1) and (12 × 12 × 1) *k*-point grids for the (5, 0; -3, 6) and (6 × 6) cells, respectively. However, the estimated adsorption energy precision of 0.02 eV, was adequate for some useful conclusions to be made in Chapter 6. One can see from Tables C.5 – C.6 that $E_{ads}$ changes very little with increasing $E_{cut}$. Therefore, the least computationally expensive value of $E_{cut}$ = 400 eV was used for the modelling in Chapter 6.

C.2: Schematics of the OHPc in the (5, 0; -3, 6) and the (6 × 6) Unit Cells

The $\Lambda_{hpc,\ trans}$ structure is used as an example in Fig. C.1 below, in order to illustrate the surface periodicity of the (5, 0; -3, 6) and the (6 × 6) unit cells.

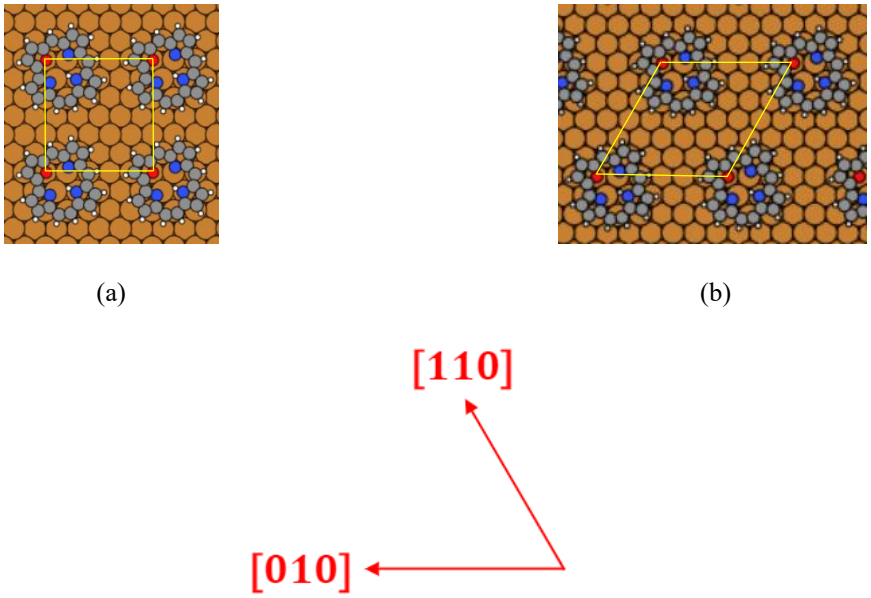


**Figure C.1:** Surface periodicity of the $\Lambda_{hpc,\ trans}$ OHPc molecule in the (5, 0; -3, 6) (a) and the (6 × 6) (b) surface unit cell (b). The Cu(111) crystallographic directional indices are shown by the red arrows.